

Multichannel Intracardiac Electrogram Analysis to Estimate the Depolarisation Wavefront Propagation

Supporting Diagnostics and Treatment of Atrial Fibrillation

Zur Erlangung des akademischen Grades eines

DOKTOR-INGENIEURS

von der Fakultät für

Elektrotechnik und Informationstechnik
des Karlsruher Instituts für Technologie (KIT)

genehmigte

DISSERTATION

von

M.Tech. Bhawna Verma

geb. in New Delhi

| | |
|-----------------------------|---------------------------------|
| Tag der mündlichen Prüfung: | 23. Mai 2017 |
| Referent: | Prof. Dr. rer. nat. Olaf Dössel |
| Korreferent: | Prof. Dr. med. Claus Schmitt |

Eidesstattliche Erklärung

Ich versichere wahrheitsgemäß, die Arbeit selbstständig angefertigt, alle benutzten Hilfsmittel vollständig und genau angegeben und alles kenntlich gemacht zu haben, was aus Arbeiten anderer unverändert oder mit Abänderungen entnommen wurde.

Karlsruhe, den 6.7.2017

Zusammenfassung

Kardiale Arrhythmien sind Störungen des Herzrhythmus, welche von unregelmäßigem Herzschlag kommen. Vorhofflimmern ist die am weitesten verbreitete Herzrhythmusstörung und ist mit zunehmendem Alter weiter verbreitet. Thromboembolische Ereignisse und Störungen der Hämodynamik können als Begleiterscheinungen von Vorhofflimmern (AFib) auftreten und eine signifikant gesteigerte Morbidität und Mortalität zur Folge haben. Die Behandlung von AFib erfolgt mit Medikamenten und zudem mit Hilfe der Katheterablation. Im Zuge der Ablation versuchen Ärzte die Bereiche arrhythmogenen Substrats zu lokalisieren. Danach werden kleine Ablationsnarben im Herzgewebe erzeugt, welche die Ausbreitung abnormaler elektrischer Erregungen im Herzen unterdrücken sollen. Die Erfolgsraten dieser Prozedur erreichen bis zu 70% nach zwei oder drei Ablationen.

Im Zuge diese Arbeiten wurden die Regionen arrhythmogenen Substrats lokalisiert, und die Details der Erregungsausbreitung über dieses Substrat wurden bestimmt. Im Verlauf dieser Arbeit wurden klinische Daten, experimentelle Daten und Simulationen für die Analyse genutzt. Simulationen wurden genutzt um die lokale Aktivierungszeit (LAT) auf klinischen Anatomien zu bestimmen. Experimentelle Daten wurden mit Hilfe eines Elektrodenpatches von einem Hund Herzen erfasst. Klinische Daten wurden mit Hilfe eines elektroanatomischen Mappingsystems im Rahmen klinischer Routineuntersuchungen aufgezeichnet.

Die aufgezeichneten Daten wurden einer Vorverarbeitung unterzogen um messtechnische und geometrische Artefakte wie das ventrikuläre Fernfeld (VFF) oder hoch- und niederfrequentes Rauschen zu unterdrücken. Eine Vielzahl von Merkmalen wurden aus den vorbearbeiteten Daten gewonnen. Dies waren die Bestimmung des Stimulationsprotokolls, die Abschätzung der Dauer der fraktionierten Aktivität, die Korrelation der Morphologie, Spitzen-zu-Spitzen Amplitude, Bestimmung der QRS Komplexe, lokale Aktivierungszeit, die Bestimmung einer stabilen Katheterposition und die Markierung der Region des arrhythmogenen Substrats. Die Methode zur Bestimmung von Richtung und Geschwindigkeit der Erregungsausbreitung wurde bestimmt. Ein grafisches Nutzerinterface (GUI) wurde entwickelt zur Bestimmung der Ausbreitungsgeschwindigkeit und darauf basierender regionaler Analyse. Simulierte Daten wurden genutzt um die Leistungsfähigkeit der entwickelten Algorithmen zu beurteilen. Zur Simulation der LAT auf klinischen Anatomien wurde die fast marching Methode (FaMaS) genutzt. In diesen Simulationen war die goldene Wahrheit für eine Beurteilung der Parame-

terabschätzung bekannt.

Ein umsichtiger und erfolgreicher Versuch wurde unternommen, um Muster und Geschwindigkeit der Erregungsausbreitung auf dem Vorhof zu bestimmen. Dies wurde auf Basis der LAT Zeit und stabiler Katheterpositionen durchgeführt. Interessante Regionen wurden zudem als wahrscheinliche Regionen eines arrhythmogenen Substrats im linken Vorhof markiert. Dies wurde auf Grundlage mehr als eines Merkmals und visueller Beurteilung deren Verteilung im Vorhof durchgeführt. Für die stimulierten Daten wurde die Aktivität der S1 und S2 Erregung verglichen um Änderungen in der Erregungsausbreitung abzuschätzen. Die Auswertung der experimentellen Daten wurde in Kooperation mit internationalen Partnern aus den USA durchgeführt. Für verschiedene Szenarien wurden dabei Richtung und Muster der Erregungsausbreitung abgeschätzt. Die zeitliche und räumliche Informationen der vorgeschlagenen Method war dabei genau kontrolliert.

Mit den Auswertemethoden aus dieser Arbeit können die wahrscheinliche Region des arrhythmogenen Substrats und der Verlauf der Erregungsausbreitung auf dem Vorhof für Vorhofflimmern und Vorhofflattern bestimmt werden. Diese können dem behandelnden Arzt bei der Planung der Ablationstherapie und erfolgreicher Durchführung helfen.

Acknowledgments

This thesis was conducted at the Institute of Biomedical Engineering (IBT), Karlsruhe Institute of Technology (KIT), in close collaboration with the Medizinische Klinikum IV from the Städtisches Klinikum Karlsruhe. I sincerely thank all persons who contributed to the success of the presented research.

First and foremost, I want to express my sincere and deepest thanks to Prof. Dr. rer. nat. Olaf Dössel for giving me the opportunity to work in a stimulating environment and for supporting my ideas during the course of my research work. Furthermore, I would like to thank Prof. Dr. Claus Schmitt for the interest in my work and his referee on the thesis.

I would like to express my deep gratitude to Dr. Armin Luik for data recording at the clinic as well as valuable discussions regarding the clinical perspective with respect to the analysis done during the course of this research. A big thanks goes to Dr.-Ing. Tobias Oesterlein for his support during my doctoral research time. He is the best room-mate cum friend cum discussion partner with whom I shared, besides frequent technical discussions, many nice moments on the fourth floor, and also for the joint supervision of one student. I kindly thank all my former and current colleagues at the IBT for providing valuable feedback on my research activities and for critically proofreading this manuscript. Special thanks to Dr. Ing. Axel Loewe, Dipl.-Math. Lukas Baron, M. Sc. Yilun Su, M. Sc. Stefan Pollnow, Dipl.- Ing. Gustavo A. Lenis and Dr. Ing. Matthias Keller.

I would also like to thank Dr. Jason Ng for introducing me to the experimental data and my gratitude for an excellent collaboration. I want to thank him for hosting me at Northwestern University, Chicago, USA. I would like to thank Benedikt Ebener for doing his Bachelor thesis under my co-supervision.

At last, I want to thank my parents and family for supporting me throughout my studies and during the course of this thesis. It's their support that I left my country and came to this beautiful country to fulfil my dream. The big thanks go to my sister Nidhi, my brother Kanishk and my friend Parth C. Kalaria for their patience and support, especially in difficult times. I would also like to thank my friend Devesh Yadav, Nitish Tripathi and Veenu Kamra for always being there for me at all the time. I would also like to thank my friends Kumar

Ghosh, Kamlesh for helping during the writing towards my PhD completion.

The research leading to the results has received funding from Deutscher Akademischer Austauschdienst. I would also like to thank DAAD for supporting my research.

Contents

| | |
|---|------------|
| Abstract | i |
| Acknowledgments | iii |
| Abbreviations | ix |
| 1 Introduction | 1 |
| 1.1 Motivation | 1 |
| 1.2 Aim | 2 |
| 1.3 Structure of Thesis | 3 |
| <hr/> | |
| I Fundamentals | 5 |
| <hr/> | |
| 2 Clinical Fundamentals | 7 |
| 2.1 The Heart | 7 |
| 2.2 Electrophysiology of the Heart | 8 |
| 2.3 Electrical Conduction | 11 |
| 2.4 EP Studies and Ablation Procedure | 13 |
| 2.5 Electroanatomical Mapping Systems | 14 |
| 2.6 Strength-Duration Curve | 20 |
| 3 Simulation Fundamentals | 23 |
| 3.1 Bidomain and Monodomain Simulation Models | 25 |
| 3.2 Fast Marching Simulation Method | 26 |
| 4 Signal Processing Fundamentals | 29 |
| 4.1 Fourier Transform | 29 |
| 4.2 Wavelet Transform | 33 |
| 4.3 Principle Component Analysis | 33 |
| 4.4 Non Linear Energy Operator | 35 |
| <hr/> | |
| II Developed Methods | 39 |

| | | |
|-----------|--|------------|
| 5 | Generation of Simulated Data | 41 |
| 5.1 | Fast Marching Simulation | 42 |
| 6 | Introduction to the Clinical Cases | 49 |
| 6.1 | Clinical Recordings | 51 |
| 6.2 | Filtering Techniques | 58 |
| 7 | Preprocessing of Clinical Data | 63 |
| 7.1 | Valve Cutting | 64 |
| 7.2 | Coverage Map | 65 |
| 7.3 | Artefact Removal | 66 |
| 7.4 | Spatial Analysis | 68 |
| 7.5 | Triangular Mesh Refinement | 71 |
| 7.6 | Morphological Correlation between Segment Data and Rovtraces | 74 |
| 7.7 | Location of Unipolar and Bipolar Electrograms | 76 |
| 8 | Stimulus Protocol | 79 |
| 8.1 | Stimulus Protocol used with the Clinical Cases | 79 |
| 8.2 | Analysis of Stimulus Protocol Data | 81 |
| 9 | Feature Determination | 85 |
| 9.1 | QRS Complex Detection | 85 |
| 9.2 | Atrial Activity Detection | 87 |
| 9.3 | Ventricular Far Field Removal | 89 |
| 9.4 | Fractionation Duration | 92 |
| 9.5 | Morphological Correlation | 94 |
| 9.6 | Peak-to-Peak Amplitude | 95 |
| 9.7 | Local Activation Time | 96 |
| 9.8 | Arrhythmogenic Region of Interest | 102 |
| 9.9 | Finding Stable Catheter Positions | 103 |
| 9.10 | Extraction of Time Variant Features | 106 |
| 10 | Conduction Velocity | 107 |
| 10.1 | Existing CV Estimation Methods | 109 |
| 10.2 | Proposed CV Estimation Method | 118 |
| 10.3 | CV Estimation for Simulated Cases | 128 |
| 10.4 | CV Estimation for Clinical Cases | 131 |
| 11 | Graphical User Interface | 141 |
| 11.1 | Conduction Time Analysis | 141 |
| 11.2 | Regional CV Estimation | 145 |

| | |
|---|------------|
| 12 Canine Data | 149 |
| 12.1 Introduction | 149 |
| 12.2 CV Estimation for Simulated Data | 153 |
| 12.3 CV Estimation for Canine Data | 156 |
| <hr/> | |
| III Results | 157 |
| <hr/> | |
| 13 Simulated Data Results | 159 |
| 13.1 Homogeneous Propagation Simulation | 160 |
| 13.2 Heterogeneous Propagation Simulation | 162 |
| 13.3 Biatrial Simulation | 164 |
| 14 Feature Extraction | 167 |
| 14.1 Catheter Coverage | 168 |
| 14.2 Location Specific Analysis | 169 |
| 14.3 Extraction of the Selected Segment | 169 |
| 14.4 Mesh Refinement | 171 |
| 14.5 Curvature of the Atrial Geometry: 2D/3D analysis | 173 |
| 14.6 Correlation between Bipolar and Unipolar Electrograms | 174 |
| 14.7 QRS Complex Detection | 175 |
| 14.8 Atrial Activity Detection | 176 |
| 14.9 Peak-to-Peak Value Estimation | 177 |
| 14.10 Fractionation Duration | 179 |
| 14.11 Morphological Correlation | 182 |
| 14.12 LAT Determination | 182 |
| 14.13 Region of Interest Determination | 186 |
| 15 Stimulus Protocol Results | 189 |
| 16 Estimated Conduction Velocity | 193 |
| 16.1 CV Estimation for Simulated Data | 194 |
| 16.2 Effect of Grid-Size and Noise on CV Estimation | 203 |
| 16.3 Comparison of Polynomial Fit and the Modified Triangulation Method | 206 |
| 16.4 CV for Clinical Data | 206 |
| 16.5 Comparison for S1-S2 Triggered Depolarisation Waveforms | 213 |
| 16.6 Comparison of Estimated CV with Statistical Parameters | 215 |
| 16.7 CV Comparison for Simulated and Clinical Data | 217 |
| 17 Canine Data Results | 219 |
| 17.1 CV Estimation for Simulated Data | 220 |
| 17.2 CV Estimation for Canine Data | 221 |
| <hr/> | |
| IV Discussion and Conclusion | 227 |

| | |
|---|------------|
| 18 Discussion and Conclusion | 229 |
| 18.1 Discussion | 229 |
| 18.2 Conclusion | 231 |
| A Appendix | 233 |
| A.1 Appendix A | 233 |
| A.2 Appendix B | 235 |
| References | 237 |
| List of Publications and Supervised Theses | 247 |

Abbreviations

| | |
|--------------|---|
| AFib | atrial fibrillation |
| AFlut | atrial flutter |
| AP | action potential |
| AV | atrio-ventricular |
| BB | Bachmann bundle |
| bpm | beats per minute |
| BSPM | body surface potential maps |
| CA | catheter ablation |
| CFAE | complex fractionated atrial electrogram |
| CS | coronary sinus |
| CT | computed tomography |
| CV | conduction velocity |
| DFT | discrete Fourier transform |
| EA | early activation |
| EAM | electroanatomical mapping |
| EGM | intracardiac electrogram |
| EP | electrophysiology |
| FaMa | fast marching |
| FaMaS | fast marching simulation |
| FD | fractionation duration |
| GUI | graphical user interface |
| HP | high pass |
| IQR | inter quartile ratio |
| IVC | inferior vena cava |
| LA | left atrium |
| LAA | left atrial appendage |
| LAT | local activation time |
| LEMRI | late enhancement magnetic resonance imaging |
| LP | low pass |
| LV | left ventricle |
| MRI | magnetic resonance imaging |
| MV | mitral valve |
| NLEO | non-linear energy operator |

| | |
|-------------|------------------------------|
| P2P | peak-to-peak |
| PCA | principal component analysis |
| PLA | posterior left atrium |
| PV | pulmonary vein |
| RA | right atrium |
| RAA | right atrial appendage |
| RF | radio frequency |
| RV | right ventricle |
| SN | sino-atrial node |
| SR | sinus rhythm |
| STFT | short time Fourier transform |
| SVC | superior vena cava |
| TV | tricuspid valve |
| VFF | ventricular far field |
| WT | wavelet transformation |

Introduction

1.1 Motivation

Cardiac arrhythmias also known as cardiac dysrhythmia is the group of condition associated with irregular heart rate and rhythm. It causes life threatening conditions and is also considered to be one of the major cause of death in western world. Atrial arrhythmia is the most common cardiac arrhythmia [1] [2]. The burden of atrial fibrillation (AFib) rises with increasing age. The number of patients suffering from the cardiac diseases increases with progressing age [1] [3]. The European study group quantifies that AFib development risk is 23% for women and 25% for men [4]. Approximately 100,000 new cases of atrial flutter (AFlut) are being recorded per year in USA alone [5]. In Germany itself around 1 million people are affected from AFib. The overall social burden within Germany is approximately 3 billion euros per year [6] [7]. Although AFib is not lethal itself it accounts for various secondary life threatening problems such as formation of thrombi causing strokes etc. The chaotic excitation propagation during AFib prevents the heart from the regular (homogeneous) contractions and therefore obstructs the blood pumping mechanism. The very first step is to manage the AFib with the anti-arrhythmic and anti-coagulation drugs. If this fails, ablation procedure is then the preferred method. In this lesion lines are created directing the electrical signals to the appropriate path within the heart.

During catheter ablation procedure the cardiac excitation patterns are first analysed measuring intracardiac electrograms with multiple catheter electrodes inside the heart [8]. Over the period of time, this procedure has become a preferred method to treat AFib [9]. Although successful strategies exist to treat paroxysmal AFib, the cure of persistent AFib is still challenging. The first breakthrough in the ablation procedure came when Haissaguerre and colleagues proposed the pulmonary vein (PV) isolation. They proposed that 94% of AFib episodes originate in PVs and through PV isolation 62% success rate was achieved with proximal AFib cases. After this the PV isolation became and remained the most commonly used intervention treatment to cure AFib. In case this does not work, the patients need to go

for other ablations in which depending on the physicians either the rotor ablation is done, or the complex fractionated atrial electrogram (CFAE) ablation is done. The success rate of AFib ablation is correlated strongly to the experience of the electrophysiologist. However, the success rates reported for ablation interventions are still moderate and a major portion of patients need to undergo several interventions before the arrhythmia is cured [2] [10].

A lot of research is going on to understand the mechanisms behind the AFib and AFlut cases. The atrial substrates properties also affect the depolarisation wavefront propagation on the atrium. Various electroanatomical mapping systems are also being used to get the global and local depolarisation propagation patterns in order to understand the propagation on the 3D anatomical structures. The parametric analysis like the CFAE mapping, rotor mapping, phase mapping etc. are under analysis as well. But the analysis and parametric study choice depends on the understanding of the researcher and the physician. Therefore, it is believed that an automatic classification and the propagation pattern information (local and global) can assist the physicians and can guide not so experienced physicians in understanding the mechanisms and behaviour of the depolarisation wavefront. Along with this it is also important that the relevant information are presented to the physicians in a quick and easy interpreting way. The available 3D mapping systems could be used to get the data for analysis and then the results could be externally provided to the physicians. As a motivation to this thesis, the clinical electrograms were recorded from the available 3D electroanatomical mapping (EAM) systems and then the depolarisation propagation information (local and global) was provided as an output. Finally, the clinical outcome of new analysing methods should be discussed with physicians and tested in a clinical environment. The discussion with physicians is an important step in inventing new methods, as the needs of clinical practice and the clinical utility have to be regarded. The propagation pattern analysis could give an insight into the region pertaining fibrillation giving the mechanisms underlying the atrial substrates. This way, additional computer based analysis of atrial electrograms could reduce examination times and improve success rates of AFib ablation. Thus, the patients burden and the overall treatment costs can be significantly reduced.

1.2 Aim

To analyse the intracardiac signals based on the depolarisation wavefront propagation pattern, the analysis of the spatiotemporal information using the data obtained from the mapping system was done. For 2D experimental data and 3D clinical data, the parametric analysis was done that selects stable catheter positions, finds the local activation time (LAT), considers the wall contact and calculates all CV estimates within the area covered by the catheter. A method was also presented and validated which calculates the CV for moving catheter and changing wall contact. During the course of this research the major challenges that are addressed and analysed using the atrial electrograms, are the following:

- Develop the algorithm to analyse and understand the propagation pattern on the atrial geometry
- Develop the technique to mark the region of interest based on the critical sites (estimated by analysing the parameters such as LAT, fractionation duration (FD), morphological correlation etc.)
- Evaluate the LASSO catheter movement and wall contacts inside the atrium
- Develop the graphical user interface (GUI) for conduction velocity (CV) estimation and regional analysis of the atrium.
- Apply the new methods on clinical cases to push medical investigations of atrial fibrillation and to mark the region with slow and fast conduction pattern.

1.3 Structure of Thesis

Part **I** briefly introduces the clinical, simulation and the mathematical fundamentals:

- **Chapter 2** gives an overview of the medical background, electrophysiology and the electrical conduction in the heart. This also recapitulates the information about the electroanatomical mapping systems and the ablation procedures.
- **Chapter 3** outlines the simulation fundamentals that are available and required to understand the simulations done as a part of this research.
- **Chapter 4** introduces the mathematical and signal processing methods used for analysing the intracardiac data.

Part **II** covers and outlines the methods for data processing and visualisation which were developed or applied during this research:

- **Chapter 5** describes the homogeneous and heterogeneous depolarisation wavefront simulations for the 2D and 3D data.
- **Chapter 6** introduces the clinical data and the information extracted from the electroanatomical mapping system.
- **Chapter 7** discusses the various preprocessing steps involved before taking the intracardiac electrograms for further analysis.
- **Chapter 8** introduces the stimulus protocol that has been used for analysis of 2D as well as the 3D data.
- **Chapter 9** describes the various parameters analysed and used to find the region of interest on the clinical 3D geometries.
- **Chapter 10** introduces the CV estimation method developed as a part of this research that is capable of taking the various catheter shapes and differential wall contacts to give the local and global CV.
- **Chapter 11** demonstrates the GUI developed during the course of this thesis.

- **Chapter 12** introduces and also describes the experimental data used for 2D CV estimation

Part **III** explains the results obtained and applied in this research work:

- **Chapter 13** describes the results of the homogeneous and heterogeneous depolarisation wavefront simulations for the 2D and 3D data.
- **Chapter 14** addresses the various results obtained after processing the respective parameter.
- **Chapter 15** discusses the stimulus protocol results.
- **Chapter 16** represents the estimated CV for flutter as well as fibrillation case mapped during sinus rhythm.
- **Chapter 17** describes the results obtained from the experimental (canine) data.

Part **IV** presents the discussion and conclusion in support to the already presented estimates.

- **Chapter 18** summaries the thesis. The discussion and conclusion of the research work is presented in this chapter.

Appendix A.1 displays the comparison of the estimated CV and the peak-to-peak (P2P) amplitudes for the S1 and S2 triggered activities.

Appendix A.2 displays the comparison of the estimated CV and the FD of the activation complexes resulted from the S1 and S2 triggers.

PART I

FUNDAMENTALS

Clinical Fundamentals

This chapter describes the clinical fundamentals that are essential to understand the analysis done during the research presented in this thesis. The general overview over the anatomy and physiology of the heart along with the introduction to the current procedures used to cure atrial fibrillation (AFib) and atrial flutter (AFlut) are presented. Since during this research, the intracardiac electrograms were analysed, therefore, the basics behind the electrocardiogram measurement and the mapping system are discussed in this chapter.

2.1 The Heart

Human heart is a four chamber muscular organ that pumps the oxygenated blood to the entire body. It sits behind the sternum and rib cages and is enclosed in a protective double membraned sac called pericardium [11]. The heart is in the middle of the thorax with its apex pointing to the left. The size of the heart is about the size of the closed fist i.e around 12 *cm* by 8 *cm* in length and breadth. The four chambers of the heart are namely left ventricle (LV), right ventricle (RV), left atrium (LA) and right atrium (RA). The RA and RV together are referred as the right heart, while LA and LV as the left heart.

The heart functions as a pump to provide a continuous flow of blood throughout the body. Figure 2.1 represents the anterior view of human heart. The deoxygenated blood enters the RA through superior vena cava (SVC) and inferior vena cava (IVC). At the same time, the coronary sinus (CS) also returns the deoxygenated blood from the myocardium to the RA. With the contraction of the RA, the blood is pumped to the RV through tricuspid valve (TV). As the RV contracts, the TV closes and the blood is pumped into the lungs via pulmonary vein (PV). The carbon dioxide is exchanged for oxygen in the lungs using the capillaries in the lungs with the diffusion process. The blood then returns to the LA using PVs. After this the blood is pumped to the LV using mitral valve (MV). The blood is finally pumped to the body using aortic valve for systematic circulation. The heart gets its share of oxygenated

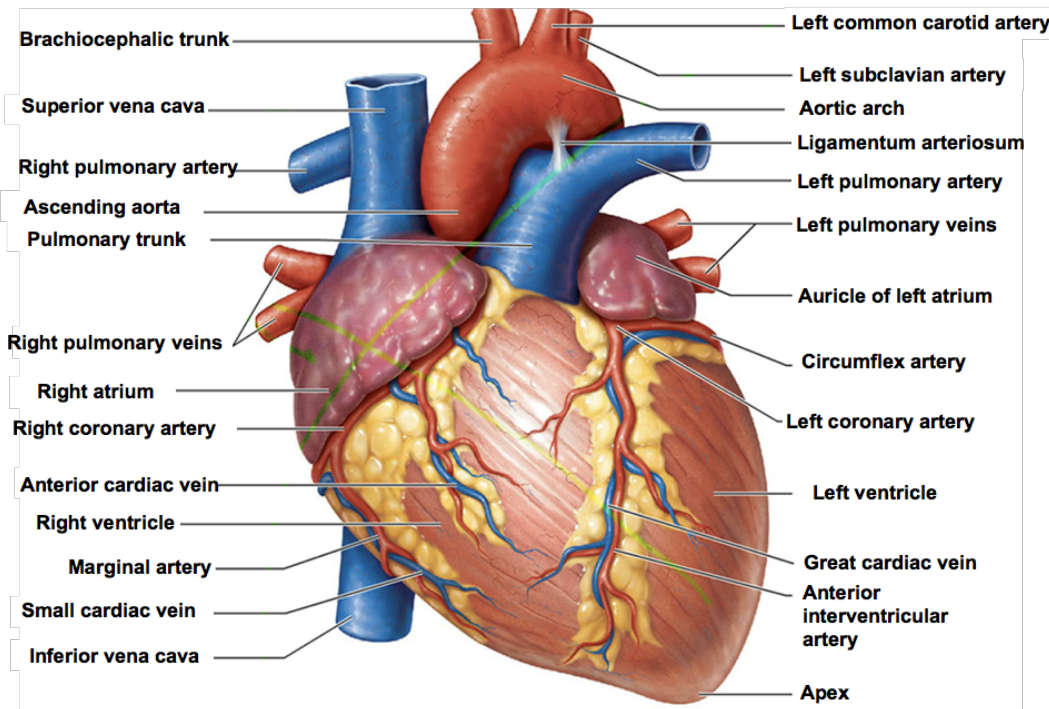


Figure 2.1: The anterior view of the human heart. (www.astoundsurround.com)

blood using the coronary arteries.

The wall of the heart is made up of three different types of layers namely epicardium, myocardium and endocardium. The outer most layer is called the epicardium, next to it is the myocardium and the inner most layer is the endocardium. Different regions of the heart have different thicknesses. The ventricular walls are thicker than the atrial walls. The septum and the left ventricular free walls are thicker than the right ventricular walls. It is due to the fact that the pressure required at the LV is much higher since the blood is to be circulated to the entire body unlike the RV where the blood is to be pumped to the pulmonary circulation. Every heart has a slightly different anatomy which makes it difficult to produce a common model locating (demonstrating) the different tissue present in the heart. The electrophysiology behind the heart functioning is explained in the next section.

2.2 Electrophysiology of the Heart

At the intracellular level, the cardiac excitation propagation behaviour could be analysed using the cardiac electrophysiology. The electric activation in the heart muscle cell is because of the movement of ions present in the cells. The three ions that effects the electric current are sodium (Na^+), potassium (K^+) and calcium (Ca^{2+}). The cardiac myocytes are excitable in nature. During resting phase the ions maintain a constant transmembrane voltage of -80 mV

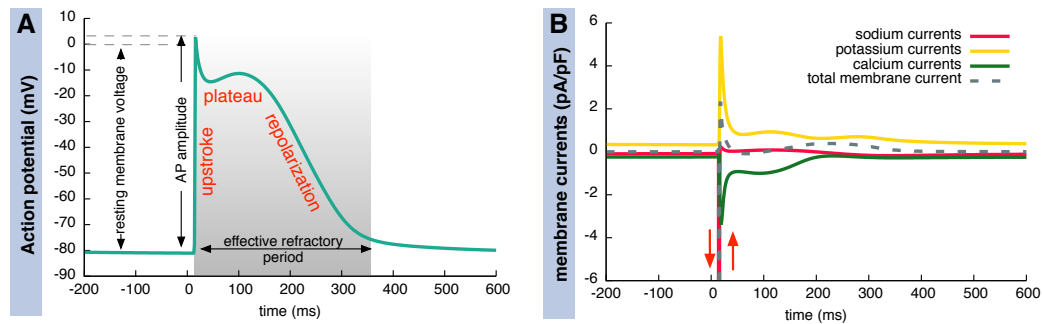


Figure 2.2: The course of the transmembrane voltage V_m during a cardiac AP with its different phases (A) and the membrane currents carried by the different ions (B). The sodium current reaches an amplitude of ≈ -70 pA/pF. The calcium exchange with the sarcoplasmic reticulum is not considered. Courses were computed using the Courtemanche et al. model [12]. Figure inspired by [13].

to -90mV . The extracellular potential is around 90mV higher than the intracellular potential. The action potential (AP) amplitude is the amount of potential increase from the resting potential value due to the trigger. Figure 2.2 represents the course of the transmembrane potential and the membrane currents when the cell is triggered.

As soon as the threshold voltage is reached (due to a trigger), the transmembrane voltage (V_m) suddenly increases caused by the opening of the Na^+ gates. This is represented by the upstroke in Figure 2.2a. After some milliseconds, Na^+ channels are deactivated and the influx of Ca^{2+} ions from the extracellular space prolongs the AP, this is represented by the plateau phase. And after this the outward K^+ ion movement repolarises the membrane voltage to the resting potential, represented as repolarisation in Figure 2.2a.

During this time the Na^+ channels cannot be reactivated unless the repolarisation is completed, which makes the cell refractory during the AP course. This is represented by the effective refractory period (Figure 2.2a). This means that second excitation can not be triggered before the first AP is completed. The cardiac muscle is made up of various types of cells, which behave differently and have different action potential curves and effective restitution period. If the cell is fully depolarised it can not be energised again. It is in the absolute refractory period. As soon as the membrane potential falls to below -50mV , the cell can be triggered again. In this relative refractory period, the cell may indeed be excited, but the newly formed AP is not as pronounced and shorter, compared to the AP as excited from the idle state of the cell. The different waveforms for each of the specialised cells found in the heart are represented in Figure 2.3. The latency shown approximates the one that is normally found in the healthy heart. Therefore there exist heterogeneity in the types of tissue present in the heart and their behaviour. Other aspect that affects the depolarisation wavefront propagation is the presence of fibrosis.

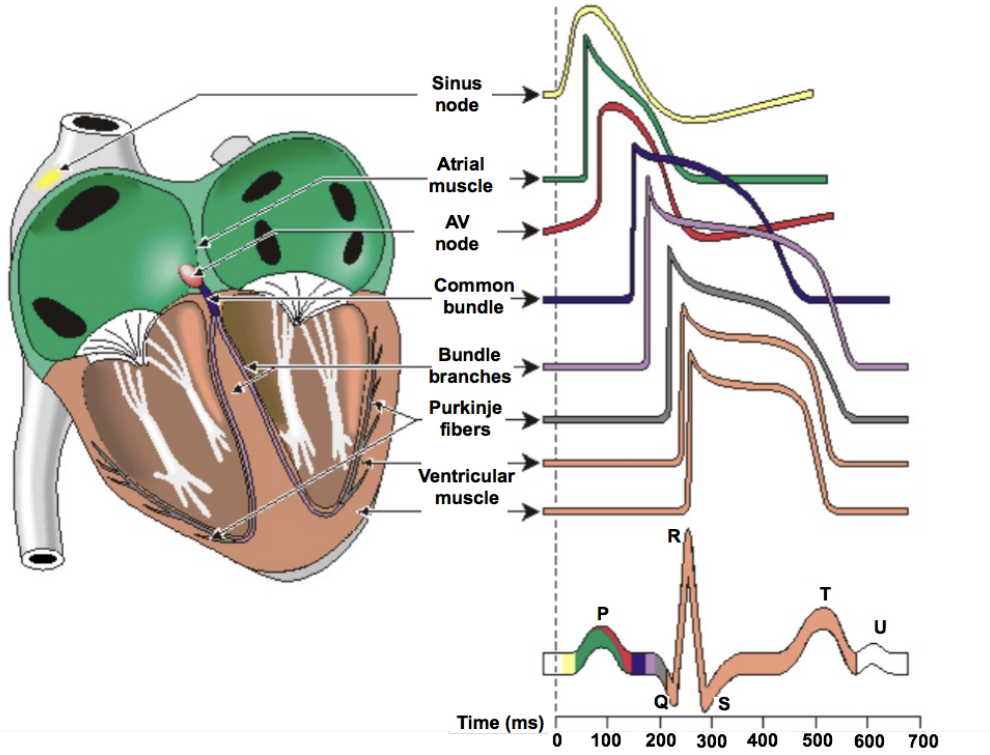


Figure 2.3: Representation of the specialised cell waveforms on the heart contributing to the electro-physiology of the heart [14].

The cells are connected to each other via a low resistance pathway, called gap junctions. The space between cells is very restrictive. There exist two types of intercellular currents namely intracellular currents and extracellular currents. This results in the parallel propagation of both intracellular and extracellular currents [15]. Therefore using the condition $I_i + I_o = 0$, it could be stated that $I_i = -I_o$, and thus,

$$\frac{\partial \phi_i}{\partial x} = -I_i r_i, \quad \frac{\partial \phi_o}{\partial x} = -I_o r_o \quad (2.1)$$

$$\frac{\partial \phi_i}{\partial x} = -I_o r_i, \quad \frac{\partial \phi_o}{\partial x} = -I_o r_o \quad (2.2)$$

where, ϕ_i and ϕ_o are the intracellular and extracellular potentials while, I_i and I_o are the intracellular and extracellular currents, r_i and r_o are the axial resistances per length. Solving the above equations, by integrating x from 0 to infinity, we can determine the extracellular

potential as

$$\phi_i = r_i \int I_o dx, \text{ and, } \phi_o = r_o \int I_o dx \quad (2.3)$$

$$V_m = (r_i + r_o) \int I_o dx \quad (2.4)$$

$$\phi_i = \frac{r_i}{r_i + r_o} V_m \quad (2.5)$$

$$\phi_o = \frac{r_o}{r_i + r_o} V_m \quad (2.6)$$

where, V_m is the transmembrane voltage. The excitation from a depolarised cell to its neighbouring cell spreads via the intercellular currents through the gap junctions. Therefore, it is said that the conductivity of the gap junction is an important factor for estimating the speed of depolarisation wavefront also called as the conduction velocity (CV). Since all the cardiac cells are electrically coupled to each other, therefore, the heart is considered to be an electrical syncytium. This means that the whole myocardium could be excited with an external trigger anywhere on the heart [16].

Therefore, it is stated that the AP curve represents the changes in the membrane potentials due to the movement of ions across the cell membrane of the heart cells. These are initiated by the cells present in the sino-atrial node (SN). Unlike other cells, the cardiac cells are not initiated by the nervous activities. The action potential curve represents the depolarisation and repolarisation due to the changes in the ion concentrations. The electrical conduction of the heart is explained in the next section.

2.3 Electrical Conduction

The cardiac cells making the SN have unstable resting potentials and are self depolarising. Other cardiac cells found in the atrio-ventricular (AV) node are capable of creating a delay in the excitation. The SN is the primary and natural pacemaker of the heart and is located sub-epicardially in the RA, close to the orifice of the SVC. The pumping of the heart is synchronised by the propagation of depolarisation wavefront on the heart and the rate is influenced by the neural system. The nerve signals enters the heart from the vagus nerve and also from the nerve arising from the sympathetic trunk. These nerves do not control the heart rate but they influence the rate to some extent.

The normal cardiac rhythm starts from the SN as represented in Figure 2.4. The cardiac depolarisation and repolarisation could as well be seen from the *ECG* signal. The heart function in *ECG* signals is represented by the *P* wave, *QRS* complex and the *T* wave terminology. Table 2.1 also represents the events corresponding to the depolarisation wavefront propagation on the heart with respect to time, CV and the associated intrinsic frequencies. The electrical

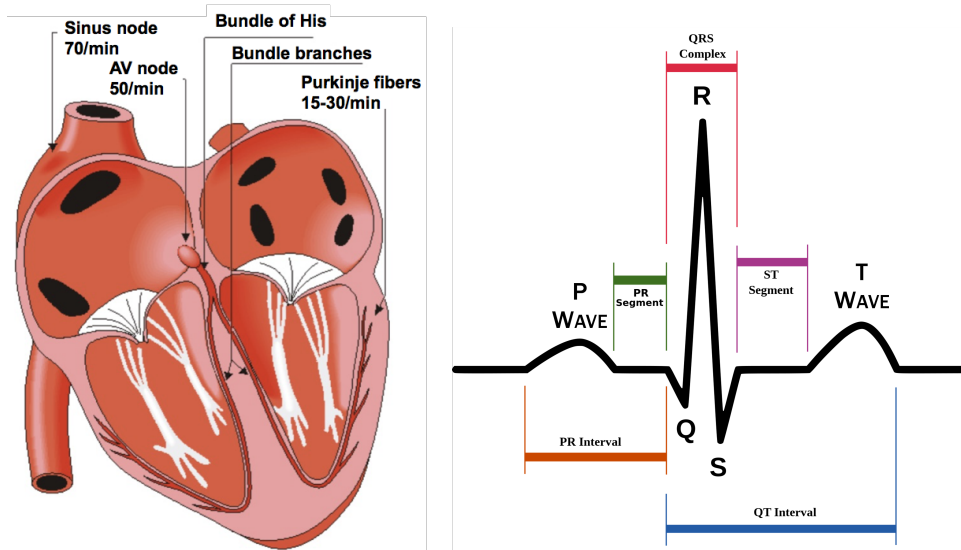


Figure 2.4: Representation of a) the cardiac conduction system [14]. b) The ECG signal corresponding to one cycle of the cardiac conduction.

Table 2.1: Electrical conduction in human heart. Representation of the events corresponding to the depolarisation wavefront propagation on the heart with respect to time, CV and the associated intrinsic frequencies [17] [18].

| Location in the heart | Event | Time (ms) | ECG terminology | Conduction velocity (m/s) | Intrinsic frequency (Hz) |
|--------------------------------|----------------------|-----------|--------------------|---------------------------|--------------------------|
| SN node, RA, LA, | impulse generated | 0 | P_{onset} | 0.05 | 70-80 |
| AV Node | depolarization | 5.85 | P | 0.8- 1.0 | |
| bundle of his, bundle branches | arrival of impulse | 50 | P-Q | 0.02- 0.05 | |
| Purkinje fibers | departure of impulse | 125 | Interval | 1.0-1.5 | 20- 40 |
| | activated | 130 | | 1.0-1.5 | |
| | activated | 145 | | 3.0-3.5 | |
| endocardium | activated | 150 | | 0.3(axial) | |
| Septum | | 175 | | | |
| Left Ventricle | depolarization | 190 | QRS | 0.8 | |
| epicardium | | 225 | | | |
| LV | depolarization | 250 | | | |
| RV | depolarization | | | | |
| epicardium | | | | | |
| LV | repolarization | 400 | T_{onset} | | |
| RV | repolarization | | | 0.5 | |
| endocardium | | | | | |
| LV | repolarization | 600 | T | | |

activity from the SN node propagates in the form of a depolarisation wavefront causing the atrium to contract (represented by *P* wave in the *ECG* signal). The depolarisation wavefront enters the LA via Bachmann bundle (BB), so as to get the synchronised movement of the atria. The depolarisation wavefront (electrical activity) reaches the AV node as represented in Table 2.1 and Figure 2.4. The AV node lies at the bottom of RA in the atrioventricular septum, the boundary between the electrically isolated atrium and ventricles. There is a delay provided at the AV node. The depolarisation wavefront from there on travels through

the ventricles along the bundle of His to the left and right bundle branches. The signals inside the ventricles are carried out by the Purkinje fibres that are capable of transmitting the electric trigger to the heart muscle. The depolarisation of the ventricle and the repolarisation of the atria is represented by the *QRS* complex in the *ECG* signal. The *T* wave represents the repolarisation of the ventricles. Depending upon the type of tissue, the depolarisation wavefront propagation speed also changes resulting into a synchronised pumping of the heart, that in-turn results into a synchronised heart beat. The various CVs associated with different locations and tissue types of the heart are mentioned in Table 2.1.

During the normal sinus rhythm (SR), the heart rate is around 60bpm to 100bpm (beats per minute (bpm)). The depolarisation wavefront propagation speed called as conduction velocity (CV), in human atrium ranges from 0.51m/s to 1.20m/s except in some specific tissue types such as BB where it is extremely fast. The depolarisation wavefront travels through the intracellular space between cells in myocardium. The CV is greater along the myocyte orientation. During AFlut the heart rate is around 200bpm to 350bpm and during AFib it is around 350bpm to 600bpm . Also after a certain point in time AFlut can change to AFib, if not treated. The extremely fast excitation of the atria during AFib leads to shortened AP.

The overall depolarisation propagation pattern could be observed on the atrium by combining together the respective propagation on the different cells. This yields to the propagation in one prominent direction. Depending upon the substrate properties, presence of slow and fast conducting regions, ectopic foci, dominant frequency regions, the depolarisation wavefront direction varies and contributes to the overall propagation pattern.

2.4 EP Studies and Ablation Procedure

Cardiac arrhythmias are problems associated with irregular heart rate and rhythm. As first treatment, the drug therapy is used to get SR back. In case the drug therapy fails, then the physician treats the patients in the electrophysiology (EP) labs. The procedure is performed by using the different types of catheters inserted via venous access to record and analyse the intracardiac electrograms. Besides the diagnostics in the EP lab, after analysing the electrograms, the catheter ablation can be performed to damage the pro-arrhythmic substrates. The most commonly used catheter ablation (CA) techniques are the radio frequency (RF) ablation [19] and the cryothermal ablation [20].

Various shapes and size of catheters with different number of recording electrodes are available now-a-days for electroanatomical mapping and recording. During the mapping procedure, a standard mapping catheter with 8 to 10 electrodes is placed in the CS artery. It cover a large region around the MV in the LA. This catheter records the signals from both the LA and the LV. The other mapping catheters are the 10 and 20 pole LASSO catheter (or

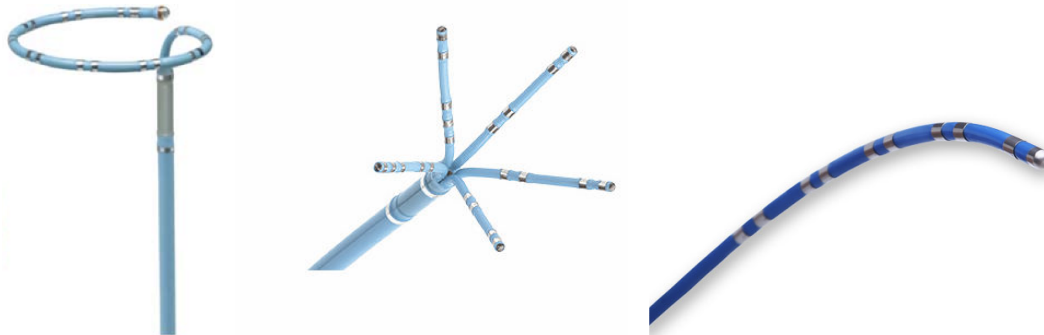


Figure 2.5: Representation of various catheters used during electroanatomical recordings. a) 20 Pole LASSO catheter, b) PentaRay catheter and c) ablation catheter. (www.medicaexpo.com)

Basket catheter, ORION catheter) and the ablation catheter. The catheter used during the procedure also depends on the familiarity and choice of the physician. Figure 2.5 represents few of the mainly used catheters available for mapping.

For RF ablation, a high frequency current of 300kHz to 1000kHz is inserted to the tip of the ablation catheter [21] [22]. The high density of the high frequency current at the tip of the catheter causes local resistive heating of the tissue in a radius of about 2mm [8]. To form a scar lesion by irreversible cellular death, the tissue must be heated up to at least 50°C for around 60seconds . However great care is to be taken, since the temperature should not exceed 70°C to avoid thromboembolic complications. Therefore, the tip temperature and the impedance are constantly monitored. Unlike the RF ablation, the cryothermal ablation is performed by delivering a refrigerant (usually liquid nitrogen is used for this purpose) through the catheter shaft [8]. In this the tissue is damaged by cooling. The benefits of this procedure over the RF ablation is under study [23]. The typical target of the procedure are the PV, complex fractionated atrial electrogram (CFAE) locations, re-entry path or the sites of the focal activities [24]. The aim of these procedures is to get the SR back. However, this is not achieved in 100% cases. The success rate depends a lot on locating the arrhythmogenic substrate. The next section of this chapter deals with the various electroanatomical mapping (EAM) systems available that are of great help to map and to get the successful ablation procedure done.

2.5 Electroanatomical Mapping Systems

After drug therapy, the catheter ablation procedure has evolved as the curative measure for various rhythm disturbances [25] [26] [27]. Electroanatomical mapping (EAM) is the technological advancement to facilitate the efforts to cure the rhythmic disturbances. Several EAM systems utilising various technologies are available to facilitate the mapping

and ablation procedures. During the catheter ablation procedure with the use of the 3D electroanatomical mapping systems the radiation exposure has been reduced considerably. There are a variety of EAM systems available which could be used for different applications and therefore, must be chosen depending upon the requirements. These requirements could be to obtain the local activation time (LAT) map, CFEA map, the cardiac geometry, the anticipated arrhythmia or it could be the compatibility of the system with adjunctive tools (such as ablation catheters and diagnostic) and also the operator's familiarity with the selected system. While these systems could offer great assistance during the EP procedure, their inappropriate application can substantially hamper the mapping efforts and procedural success. Therefore, these systems should not replace careful interpretation of data and strict adherence to electrophysiology principles.

The EAM systems are capable of recording the intracardiac electrical activities (using various catheters) in terms of the unipolar as well as bipolar electrograms along with their spatial information and the body surface potential maps (BSPM). The 3D chambers could be constructed using the spatial information and when applied properly, the accurate determination of the arrhythmias could be located. Therefore, it can be stated that the success rate of the procedure depends a lot on the experience and expertise of the physician. The EAM systems allow the positioning and manipulation of the catheter without fluoroscopic guidance radiation dose, along with less significant effects on procedural duration and success rates [28] [29] [30]. The electrical and the magnetic phenomenon are used while mapping with the EAM systems. There are a lot of catheters available that could be combined with the system to generate the electrograms and could in-turn help in chamber reconstruction. While mapping, the resolution of the map depends highly on the coverage possibilities of the catheter in use.

The location and temporal references are selected during the procedure. The timing reference could be at any arbitrarily selected recording (for example, intracardiac electrograms or surface ECG signals). During procedure, the intracardiac electrograms are often selected as the timing reference because they are more consistent in appearance and precise in timing than surface ECG recordings. There are a number of EAM systems available accomplishing this task. Some of them are namely

1. Biosense CARTO system
2. EnSite NavX mapping system
3. Non-contact mapping system
4. Real time position management system

A brief introduction to these mapping system is given in the next section .

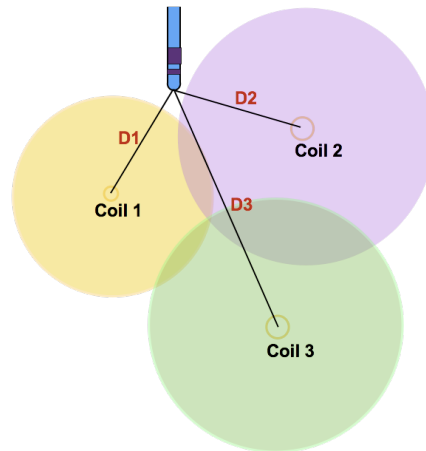


Figure 2.6: Illustration demonstrating operation of the Biosense CARTO electroanatomical mapping system. Three separate coils (coil 1, coil 2 and coil 3) emit a low-level magnetic field. The field strength from each coil is measured by a sensor within the tip of a specialised mapping/ablation catheter, and its position relative to each coil is then triangulated. The ablation catheter presented has the sensor in its tip.

2.5.1 Biosense CARTO System

The CARTO mapping system (Biosense, Diamond Bar, CA, USA) is an advanced technology that utilises the electromagnetic technology delivered from three separate coils in a locator pad beneath the patient, to create the real-time 3D map of the cardiac structure. The CARTO system uses low frequency magnetic fields that are calibrated and computer controlled. The low level magnetic field of 5×10^{-6} Tesla to 5×10^{-5} Tesla is utilised during the mapping. From each of the three coils, the strength of the magnetic field is detected by using the location sensors embedded proximal to the tip of the mapping catheter as represented in Figure 2.6.

During the therapeutic CA procedure, physicians insert the catheter through a small incision in the groin where it is then weaved up to the heart through a blood vessel in the leg or from the arm. It is to be noted that the strength of the magnetic field measured by the sensors on the tip of the catheter is a function of the distance between them. Using these information, the location of the catheter is determined in space [31]. Once it reaches the heart, the mapping catheter can be moved along chamber's surface to record local endocardial activation times for recording the local activities, along with recording the location points, to generate a 3D geometry. The system is designed to help electrophysiologists to navigate inside the heart. The tip of the ablation catheter is also capable of delivering the RF energy that is utilised to ablate the selected regions for creating the ablation lines. Depending on the site, the RF energy could be delivered to specific locations of the heart wall to produce scar lesions in order to block faulty electrical impulses causing heart rhythm disorders.

Some validation studies have shown that the system has good accuracy in navigating to single points, in returning to prior ablation sites, and also in creating a desired length of ablation line [32]. The key features of the CARTO system includes:

- Accurate representation of the chamber geometry and the capability to generate the activation maps.
- Capability to record the important landmarks, area of scar and also the vessels.
- Capability to record the ablation lesion locations facilitating the ablation lines.
- Capability to enables accurate visualisation of multiple catheters in the heart.
- Non-fluoroscopic mapping system allowing clinicians to rapidly create a map of the heart with CT like resolution during the ablation procedure.

2.5.2 EnSite NavX Mapping System

The EnSite NavX and the EnSite Velocity mapping system are from Endocardial Solutions, St. Jude Medical Inc., St. Paul, MN, USA. Similar to the CARTO system, the NavX system is also capable of displaying 3D positions of multiple catheters utilising the electromagnetic phenomenon. The difference between the two systems is that instead of magnetic fields, electric currents are utilised in the EnSite systems during the endocardial mapping. The 3D map is generated by applying a low-level $5.6kHz$ current through orthogonally-located skin patches. At each electrode, the impedance and the voltage are recorded that is generated from the applied current. It allows to record their distance from each skin patch, and ultimately their location in space, are triangulated with the help of a reference electrode. Thus, in this manner, the 3D images of the catheter are displayed. By moving the mapping catheters inside the atrium, the chamber geometries are constructed along the endocardial surface.

Various studies have demonstrated the feasibility and benefits when the EnSite NavX system is used in conjunction with conventional mapping strategies [33]. In one study the significant reductions in radiation dosage and time (procedural and fluoroscopy) was observed along with comparable success achieved in PV isolation [34]. The EnSite NavX system has the following strengths:

- The ability to simultaneously display multiple catheter positions in real-time. Figure 2.7 represents one such example.
- Accurate representation of cardiac anatomy.
- Its compatibility with any EP catheter.
- Ability to map and record up to 128 electrodes.
- Ability to generate the LAT map and the CFEA map.

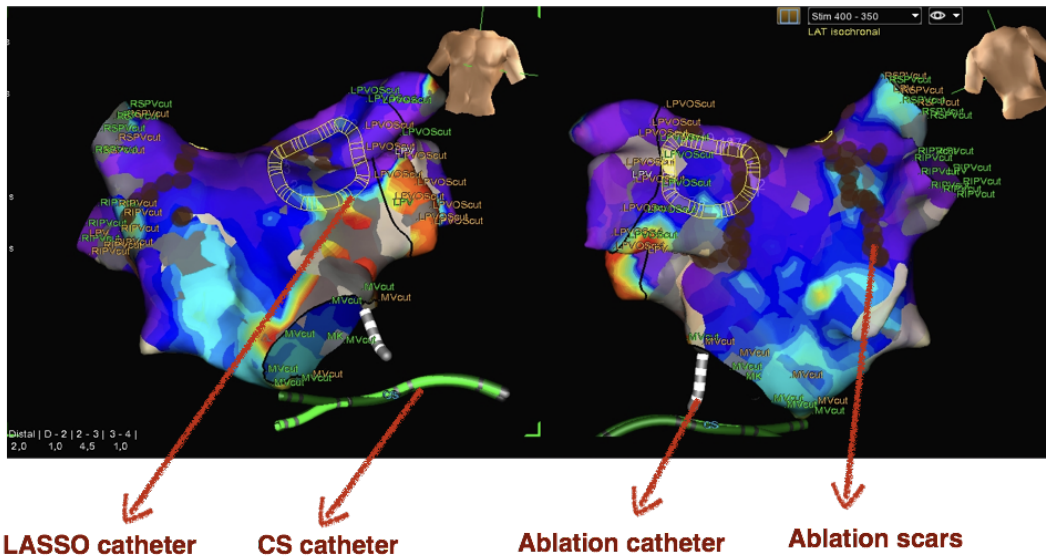


Figure 2.7: Screenshot from the velocity mapping system representing the various catheters, the annotations on the atrium and the created scar lines respectively.

With this system, huge data (more than 10 GB from 2 hours of recording) can be recorded for analyses that could also be done on later point in time. Along with this, the unipolar as well as bipolar electrograms can be recorded along with other spatiotemporal signals. The distal electrode recordings are more reliable compared to the proximal since that is more likely to be in contact with the endocardium. This is because of the fact that amplitude of the bipolar electrogram is maximum during parallel propagation to the axis of recording electrodes, while amplitude reduces when propagation is perpendicular to the electrodes. On proximal electrode wavefront targets at an angle and recordings are influenced by catheter orientation relative to tissue [35]. Disadvantages of the EnSite system includes limited utility against non-sustained arrhythmias. During mapping, the inaccurate recognition of complex anatomical structures can be observed unless careful contact mapping is performed in such areas [36].

2.5.3 Non-Contact Mapping System

The non-contact mapping system by EnSite, Endocardial Solutions Inc., St. Paul, MN, USA utilises a multi-electrode array to simultaneously record multiple areas of endocardial activation [37] [38]. Figure 2.8 represents the non-contact mapping catheter by St. Jude Medical. The multi-electrode array is an inflatable balloon with 64 electrodes on its surface. This catheter rapidly collects real-time cardiac electrical information and translates it into 3D iso-potential map. This tool simplifies the diagnostic procedures by calculating around 3,000 electrical data points in a single heartbeat. Therefore, a relatively high density map can be generated.

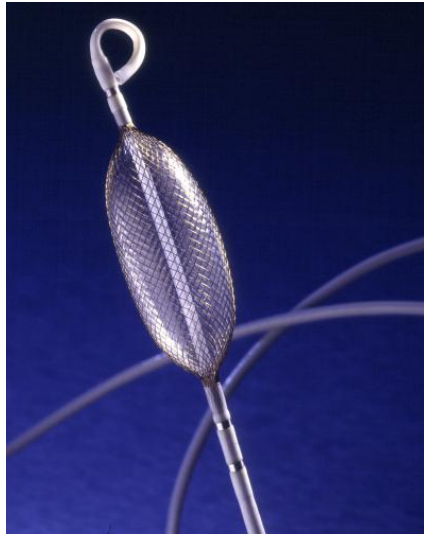


Figure 2.8: Representation of the non contact mapping catheter by St. Jude Medical [40].

Similar to the EnSite Velocity mapping system, the 3D localisation of the electrodes is achieved by applying a low-level 5.6kHz current. The chamber geometry can be reconstructed by manipulating the mapping catheter within the area of interest and the corresponding electrical iso-potentials can be plotted on the endocardial surface [37] [39].

With this mapping modality, the acquisition of multiple endocardial electrograms from a single beat makes it quite useful for mapping the non-sustained arrhythmias, rhythm disturbances and ectopic beats that are poorly tolerated. The limitation of this includes the inaccuracy of electrogram timing and morphology at greater distances from the catheter along with the difficulty in positioning the balloon, and inaccuracy in reconstructing certain features of chamber geometry.

2.5.4 Real Time Position Management System

The real time position management system is introduced by Cardiac Pathways, Sunnyvale, CA, USA. This system employs ultrasound ranging to localise reference and mapping catheter positions as explained in [41]. In this case the two reference catheters contain an ultrasound transducer along their shaft. One of them is typically situated in the RA, CS, or RV and the other one is the mapping catheter. In this the continuous ultrasound energy of 558.5kHz is emitted by a separate ultrasound transmitting and receiving device. This energy is received by the transducers housed within the reference and ablation catheters and the time required to receive this signal is converted to distance. The advantage of this system is the real-time location of ablation and reference catheters, the capability of repositioning reference catheters to their original location and the ability to demonstrate the degree of catheter deflection. This system at the same time has limitations in recording anatomic

features between separate cardiac structures. This may lead to distortion of cardiac geometry, and the need to use specific reference and ablation catheters equipped with ultrasound transducers.

2.6 Strength-Duration Curve

As explained in the section 2.2, the self excitable tissue in the SN initiates the regular depolarisation wavefront on the atrium. This triggering on the myocardium excites the adjacent tissue and the process goes on. The depolarisation wavefront can also be triggered by applying an external stimulus. This section deals with the basics behind this stimulation process.

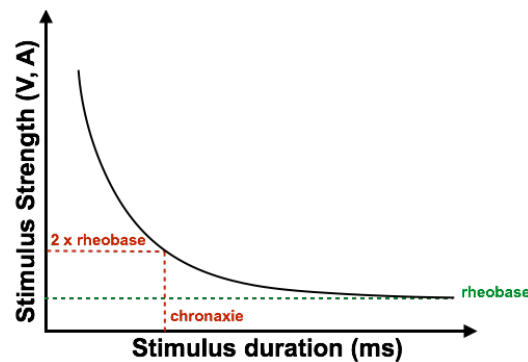


Figure 2.9: Strength duration curve [42].

For applying the external stimulus anywhere on the cardiac tissue, a minimum amount of energy expressed in terms of voltage, current, energy or charge is given to the myocardium through the electrode. By applying this energy, a depolarisation wavefront gets initiated from the location of stimulation and propagates through the connecting cells because of the changes in the ion concentration that triggers the ions in the adjacent cells. A special curve called the **strength-duration curve** [42] explains the interdependence of the stimulus strength and the stimulus duration in activating the tissue. This curve was discovered by G. Weiss in 1901 and is represented in Figure 2.9. It could be clearly observed that with the stimulus strength i.e., expressed in terms of voltage or current, the ability to create an action potential changes. The total number of tissue that gets activated by the stimulus depends on the stimulus strength and the duration for which the stimulus is applied for. The depolarisation wavefront travels on the atrium in terms of the flow of electrical charge due to the ion concentration changes. As a measure of stimulus strength, both or either of voltage or current could be interchangeably used. That is why, there exist proportionality between the amount of charge transferred (current (I) and times (t)) which is related to the strength duration (D) as expressed by the Weiss equation. b relates to the Rheobase value and c relates

to the Chronaxie value.

$$Q_{min} = b(D + c) = I_{min} \cdot D \quad (2.7)$$

$$I_{min} \cdot t = \frac{Q_{min} \cdot t}{D} \quad (2.8)$$

$$I_{min} = b \left(1 + \frac{c}{D} \right) \quad (2.9)$$

As specified in the strength-duration curve above, Rheobase is the minimum strength (i.e., current or voltage amplitude) applied for very long duration, in order to result into a depolarisation threshold that could start the propagation by providing a threshold of action potential. In other words, Rheobase is also expressed as the least voltage or current needed to depolarise the heart for a long time pulse duration. Mathematically, Rheobase could also be expressed as the slope of the graph as specified in the Weiss equation (Equation 2.7 to Equation 2.9). The other parameter in the curve is called as the Chronaxie. It is the shortest pulse duration required to depolarise the heart at a voltage equal to twice the Rheobase. In simple words, it is the stimulus duration that produces a response when the stimulus strength is set to exactly at double Rheobase. The amount of energy applied to get the depolarisation wavefront in the clinical cases under consideration was given from the CS catheter in order to get the propagation over the atrial geometry after the SR.

Simulation Fundamentals

This chapter describes the basics about the cardiac excitations using the simulation models. The in-silico model helps in getting the idealised clinical scenarios for research and parametric analysis purpose. Cardiac simulation is done to model electrical excitation propagation in human heart. There exist various models simulating cardiac electrophysiology that can compute the transmembrane potential, currents, ion concentration etc. for specific types of tissue. Usually these models contain a set of coupled differential equations used to get the simulation of the activation of the human atrial cells. In a review article by Wilhelms et al. the different types of simulation models were explained and compared [43]. The fundamentals involved with the simulation starts with the understanding of the basic concepts of the computational models of cardiac electrophysiology. The various mechanisms involved (from cell level to tissue level and for the whole body scale) in the cardiac excitations are explained using the mathematical expressions in simulation environment.

In 1952, the first electrophysiological cell model was presented by A. L. Hodgkin and A. F. Huxley [44]. This was based on the voltage clamp experiment on the axons of the giant squid. It contained a mathematical description of the ionic mechanism underlying the electrophysiological phenomenon. In 1962, approximately after 10 years, the first mathematical model of cardiac electrophysiology including pacemaker activities was published by D. Noble [45]. But the first models of human atrial electrophysiology were published in 1998 by Courtemanche et al. [12] and Nygren et al. [46]. Courtemanche et al. effectively developed a working model of the human atrial action potential (AP) from the Luo-Rudy model which was based on guinea pig ventricular cells [12].

The Courtemanche et al. model is a useful model of the AP based on the ionic current data due to the changes in the calcium (Ca^{2+}), potassium (K^+) and sodium (Na^+) ions [12]. The schematic of various current flow as given by this model is represented in Figure 3.1. A mathematical description was provided by this model describing the electrical behaviour of human atrial myocyte by calculating the ion concentrations, ionic currents, bindings to

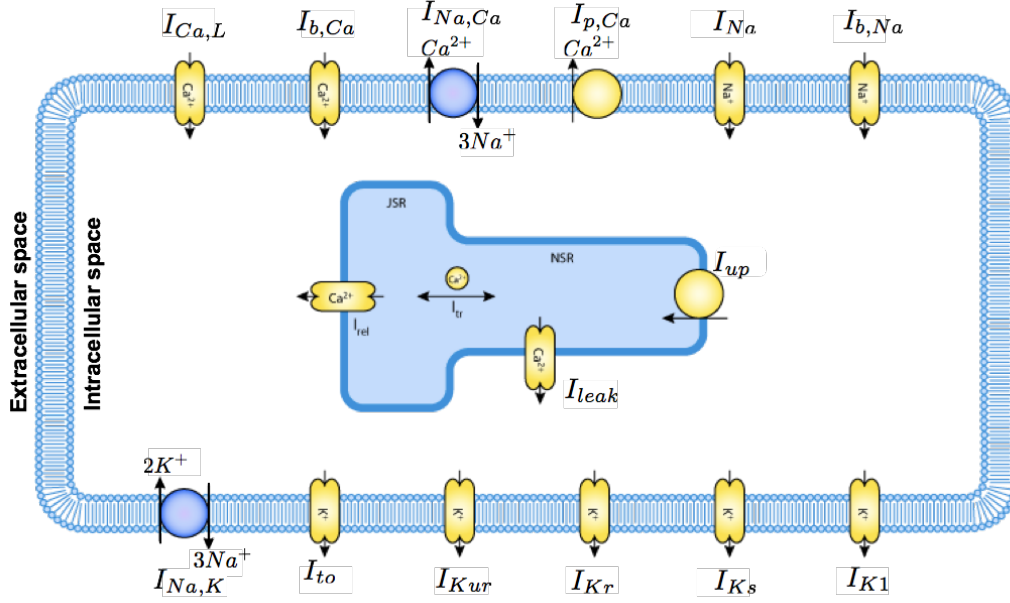


Figure 3.1: Representation of the schematic of the Courtmanche-Ramirez-Nattel model of the atrial electrophysiology. The calcium (Ca^{2+}), potassium (K^+) and sodium (Na^+) ion currents altered during re-modelling causes the changes in the ionic currents are represented. Figure modified from www.cellml.org.

intracellular structures, and the transmembrane voltages. The ordinary differential equation was expressed as the sum of ionic currents and the externally applied stimulus currents.

$$\frac{dV_m}{dt} = \frac{-(I_{ion} + I_{stim})}{C_m} \quad (3.1)$$

where, I_{stim} is the externally applied stimulus currents, V_m is the transmembrane voltage, I_{ion} is the net ionic current across the cell membrane given as

$$I_{ion} = I_{Na} + I_{K1} + I_{to} + I_{Kur} + I_{Kr} + I_{Ks} + I_{Ca,L} + I_{p,Ca} + I_{NaK} + I_{NaCa} + I_{b,Na} + I_{b,Ca} \quad (3.2)$$

These are the various ionic currents involved. These are defined as the product of the channel conductivity g_x and the ion specific Nernst voltage weighted with a product of the gating variable defined as Ohms law:

$$I_x = g_x(V_m - E_{Nernst,x}), \quad (3.3)$$

where, $E_{Nernst,x}$ is the Nernst voltage of the specific ion, g_x is the ion channel conductivity, γ_i describes the kinetic behaviour of the ion channel. It is the product of the maximum conductivity of channels carrying I_x currents. In terms of the gating variable it is defined as,

$$g_x = \hat{g}_x \prod_i \gamma_i \quad (3.4)$$

where \hat{g}_x is the maximum conductivity. Since the channels have open and closed state, therefore the gating variables are defined by the first order differential equation as

$$\frac{d\gamma_i}{dt} = \alpha_{\gamma_i}(1 - \gamma_i) - \beta_{\gamma_i}\gamma_i \quad (3.5)$$

The rate constant variables α and β represent the transition between open to closed gating and are also dependent on the transmembrane voltage. The various atrial structures show differences in cell electrophysiology [47] [48]. A detailed review of this is also presented by Schotten et al. in [49].

At cellular level the atrial muscle contains the myocyte cells within the extracellular matrix. Within the intracellular spaces these have gap junctions with which they are electrically connected to each other. Therefore, if there is a change in one cell current or the V_m , this is transferred to the connected cells resulting into the spread of a depolarisation wavefront. The conductivity is greater along the myocytes. Between the extracellular and intracellular spaces, there exist an anisotropic behaviour. The excitation propagations could be described mathematically using various monodomain and bidomain simulation models as explained in the next section.

3.1 Bidomain and Monodomain Simulation Models

The above stated expressions were used to simulate the propagation at the cellular level. These in-silico models are used for simulating the excitation propagation on tissue and organ level using the bidomain model and its simplification called as the monodomain model as far as excitation propagation is concerned. These models are used to describe the reaction diffusion process and the ionic current behaviour. The excitation sequences are described by the so called reaction diffusion model. The bidomain model deals with the intracellular and extracellular spaces, using the Poisson equations, while the monodomain model deals with the intracellular currents through the gap junctions. The bidomain and the monodomain model also proved to be suitable for complex excitation patterns including the wave break [50]. For simpler activation patterns, the fast marching (FaMa) scheme based on the Eikonal equation can provide reasonable activation sequences at significantly reduced computational cost [51] [52] [53].

Poisson's equations for bidomain models is expressed in terms of intracellular potentials (ϕ_i), extracellular potentials (ϕ_e), intracellular conductivity tensors σ_i , extracellular conductivity tensors σ_e , cell to volume ration (β) and externally applied current (I_{si}) [54]. Therefore, conductivity and the currents in the intracellular and extracellular spaces can be defined as:

$$\nabla \cdot (\sigma_e \nabla \phi_e) = -\beta I_m - I_{se} \quad (3.6)$$

$$\nabla \cdot (\sigma_i \nabla \phi_i) = \beta I_m - I_{si} \quad (3.7)$$

The transmembrane current (I_m) is expressed in terms of the membrane capacitance (C_m) and sum of ionic currents (I_{ion}) across the cell membrane as

$$I_m = C_m \frac{dV_m}{dt} + I_{ion} \quad (3.8)$$

The intracellular and the extracellular conductivity tensors can be expressed using the anisotropy ratio k . If this (k) is equal for both the spaces, then the conductivity (σ_i) can be expressed as ($k\sigma_e$). This also allows to get the simplified version of the bidomain model, i.e, called as the monodomain model.

$$\nabla \cdot (\sigma_i \nabla V_m) = (k+1) \cdot \beta \left(C_m \frac{dV_m}{dt} + I_{ion} + I_{stim} \right) \quad (3.9)$$

$$\nabla \cdot (\sigma \nabla V_m) = \beta \left(C_m \frac{dV_m}{dt} + I_{ion} \right) \quad (3.10)$$

$$\sigma = \left(\frac{\sigma_e \cdot \sigma_i}{\sigma_e + \sigma_i} \right) \quad (3.11)$$

The monodomain and bidomain models coupled with models of the cardiac electrophysiology and can reflect the reaction-diffusion processes in the human heart. A detailed description of the bidomain model and its simplification as the monodomain model can be found in [55]. Since the monodomain model is faster compared to the bidomain model, therefore it is used more commonly in the atrial modelling.

3.2 Fast Marching Simulation Method

The various biophysical models simulate the ion diffusion through the membrane. And since these are based on the ion concentrations, therefore these requires various input parameters and high resolution of the atrial models. These many parameters and requirements makes them computationally expensive and not suitable for clinical use. For example, the cellular automaton is a rule based simulation tool developed at IBT that generates electrical propagation in the heart [56]. But, unlike this the Eikonal model simulates the cardiac excitation by calculating the activation time of all the nodes. For fast marching simulation (FaMaS) the Eikonal equation is solved.

In simulation environment also, the spread of the depolarisation wavefront is because of the changes in the ion concentration triggered from one end. There are various biophysical models that can simulate the ion diffusion through the membrane. To get a smooth and good simulation, it is required to have a high resolution atrial model along with other input parameters. Usually the simulation is computationally expensive and time consuming. With the monodomain, reaction diffusion it is also possible to capture the behaviour of the complex excitation patterns, but that is on the expenses of a large computational time. On the other hand, the much simpler Eikonal based model can be used to simulate the cardiac excitation without reflecting the diffusion process [51]. The Eikonal equation can govern the spread of the depolarisation wavefront from the trigger point by calculating the activation time for all the nodes present and connected, for the given geometry at a low computational cost. For FaMaS, the Eikonal equation was solved with the approximated parameters and using the given physiological information. Once the triggering point is manually defined on the

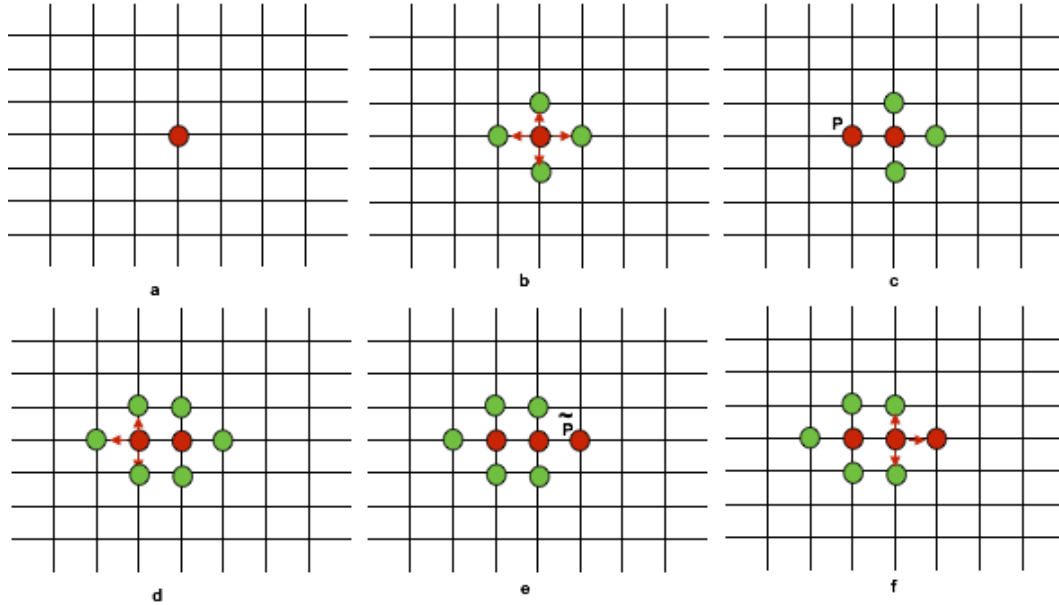


Figure 3.2: Illustration of Fast Marching method. Red are the known nodes and green are the trial nodes. a) Starting point. b) The time of all the adjacent nodes is calculated. c) The node with smallest time is made the known node. d) The adjacent trial nodes time is calculated. e and f) The procedure goes on like this [57].

triangulated grid surface, than with the progressing time, the speed function (F) is always positive. Therefore, the wavefront propagation is defined by the direction along the normal to the surface and F . Thus, the propagation of the wavefront can be approximated by the Eikonal equation that is a non linear partial differential equation and is expressed as

$$|\nabla F| = 1 \quad (3.12)$$

The spread function is defined at each and every node as the activation time. Solving the Eikonal equation, is a method to simulate the cardiac excitation over the given geometry. Therefore, for simulating the atrial excitation, the surface triangular mesh was taken as one of the inputs. Several iterations over the given mesh result into the solution of the Eikonal equation.

In case of a common quadratic mesh composed of N^2 nodes approximately N^2 iterations are required. This leads to a complexity of $O(N^4)$ [58]. While the FaMa method considers the adjacent nodes and the least time stamp as an input, it can solve the Eikonal equation with one iteration. In this, the node with the known time stamp is taken as the starting point and the calculation starts from this node. All the adjacent nodes are called trial nodes and their time stamps are calculated. This has also been demonstrated and explained in Figure 3.2. Therefore, for the equidistant $N \cdot N$ mesh, the complexity is reduced to only $O(S \cdot N)$, where S is the computing time of a sorting algorithm to sort the trail nodes. The FaMaS algorithm interpolates the distance of several adjacent nodes and thus considers the topology, unlike Dijkstra which calculates the distance only on the basis of the edge weights. The FaMa

is capable of solving the Eikonal equation on equidistant and triangulated surfaces. An extension to the FaMa scheme allowing to include multiple wavefronts has been done by Sermesant et al. [59].

Signal Processing Fundamentals

The research work presented deals with the multichannel intracardiac electrogram analysis to estimate the depolarisation wavefront propagation. The intracardiac clinical electrograms under analysis were recorded in the time domain. Those were the continuous signals discretised with the sampling rate of $2kHz$ and $1kHz$. The analysis of these intracardiac signals was done in time domain as well as in the frequency domain. This chapter deals with the signal processing fundamentals used during the presented research work.

During the course of this thesis, the signal processing techniques such as non-linear energy operator (NLEO), principal component analysis (PCA), high pass (HP) and low pass (LP) filtering were used. This part gives a brief introduction to these techniques one after the other.

4.1 Fourier Transform

The intracardiac electrograms obtained using EnSite Velocity mapping systems were recorded in time domain. The time domain as well as the frequency domain analysis were done to extract the useful information from the obtained electrograms. The time domain analysis can give the information such as event occurrence while the frequency domain analysis can also give the important information such as noise and artefacts present in the signals. The Fourier transform can be a very useful tool to analyse the signals in frequency domain. This section gives a brief introduction to the Fourier transformation [60]. The comparison between the time domain and the frequency domain analysis is represented using Figure 4.1.

Using the Fourier transformation, the frequency content of the periodic signal can be analysed. Fourier transform represents the periodic function $f(t)$ by an infinite sum of sines and cosine trigonometric functions, transforming the function of time into the frequencies that make it up. As a result of this, the harmonic frequencies and their amplitudes are obtained and thus

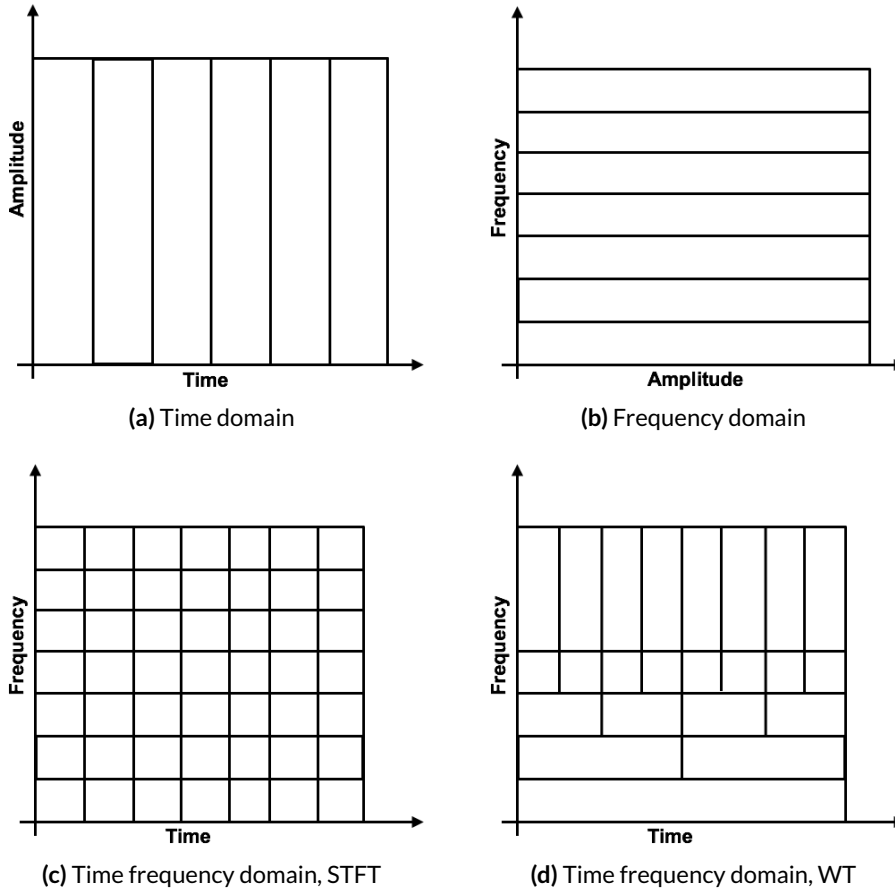


Figure 4.1: Representation of the comparison between the time domain, frequency domain and the time-frequency domain.

it is also called as the frequency domain representation of the original signal. The periodic function can be composed of these harmonics.

$$f(t) = \frac{a_0}{2} + \sum_{k=1}^{\infty} \left(a_k \cos(2\pi \frac{k}{T} t) + b_k \sin(2\pi \frac{k}{T} t) \right) \quad (4.1)$$

Therefore, in terms of Fourier series, the function $f(t)$ can be decomposed as represented in Equation (4.1), where a_k and b_k are the Fourier coefficients and T represents the cycle duration of $f(t)$. The exponential definition of the Fourier series is as represented in Equation (4.2).

$$f(t) = \sum_{-\infty}^{+\infty} c_n e^{jn\omega t} \quad (4.2)$$

$$c_n = \frac{1}{T} \int_0^T f(t) e^{-jn\omega t} dt \quad (4.3)$$

where c_n is the complex amplitude of $f(t)$.

4.1.0.1 Continuous Fourier Transform

The Fourier transform pair is the most general form of a periodic and continuous time signal. To analyse this the cycle duration is set to $T \rightarrow \infty$. Thus the Fourier integral is obtained as

$$\lim_{T \rightarrow \infty} (\frac{c_n T}{T}) = F(j\omega) \quad (4.4)$$

The limit is the spectral density, and $\omega = 2\pi f$. Therefore, this could be represented as

$$f(t) = \int_{-\infty}^{+\infty} F(f) e^{2j\pi f t} df \quad (4.5)$$

$$F(f) = \int_{-\infty}^{+\infty} f(t) e^{-2j\pi f t} dt \quad (4.6)$$

From Equation (4.5) and Equation (4.6) the duality between the time domain and the frequency domain can be observed as illustrated. Since this notation closely relates to the signal representation in both the domains, therefore, this is preferred in signal processing.

4.1.1 Discrete Fourier Transform

The discrete Fourier transform converts a finite sequence of equally spaced samples of a function into an equivalent length sequence of equally spaced samples of discrete time. The Fourier transform is a complex valued function of frequency. In order to analyse in the discrete environment using computers, the signals as well as their spectrum needs to be discrete [61]. A signal say $x(t)$ could be discretised with the sampling frequency of f_A (sampling time T_A). Let the time-discrete representation of signal $x(t)$ be x_k i.e.,

$$x(t)|_{t=kT_A} = x(kT_A) =: x_k \quad (4.7)$$

where k is an integer within the range of $-\infty < k < +\infty$, but since there are N number of sample values, therefore the limit of k is $0 < k < N - 1$. The discrete Fourier transform can thus be defined as

$$X_n = DFT\{x_k\} = \sum_{k=0}^{N-1} x_k e^{-2j\pi kn/N} \quad (4.8)$$

And similarly the inverse discrete Fourier transform can be defined as

$$x_k = IDFT\{X_n\} = \frac{1}{N} \sum_{n=0}^{N-1} X_n e^{2j\pi kn/N} \quad (4.9)$$

The complexity of the discrete Fourier transform (DFT) is dependent on the signal length (N), and is $O(N^2)$. The computational cost of the DFT can be reduced to $N \log(N)$ using the symmetry and periodicity. Fast Fourier transform (FFT) is the family of DFT that is computationally more efficient.

4.1.2 Short Time Fourier Transform

Short time Fourier transform, also called as the short term Fourier transform is a Fourier related transform that is usually used to determine the sinusoidal frequency and phase content of the signal as it changes with time. This gives the information about the frequency content, but loosing a bit of the information about the time at which it has occurred. This is a method to analyse the non stationary signals. Therefore using this method only a short period (defined using the window function) of signals are Fourier transformed unlike the above stated method. For example, $w(t)$ is a window that is non-zero for a short period of time and $f(t)$ is the sample signal to be transformed. Therefore, this signal transformation into the time-frequency domain for only the non-zero part is given as

$$S(w, t) = \int_{-\infty}^{+\infty} s(\tau)w(\tau - t)e^{-j\omega\tau}d\tau \quad (4.10)$$

The window function is an important parameter in short time Fourier transform (STFT), since its quality depends upon the window function. The narrow window function results in poor frequency resolution, while the broader window function results in better frequency resolution. In this case too, the time and frequency domain are inversely proportional to each other given by Equation (4.11).

$$\Delta\omega \cdot \Delta t \leq \frac{1}{2} \quad (4.11)$$

It is also important to note that one cannot simultaneously sharply localise a signal (or function) in both the time and frequency domain. Also it is not possible to get both frequency and time domain resolution as stated by the uncertainty principle.

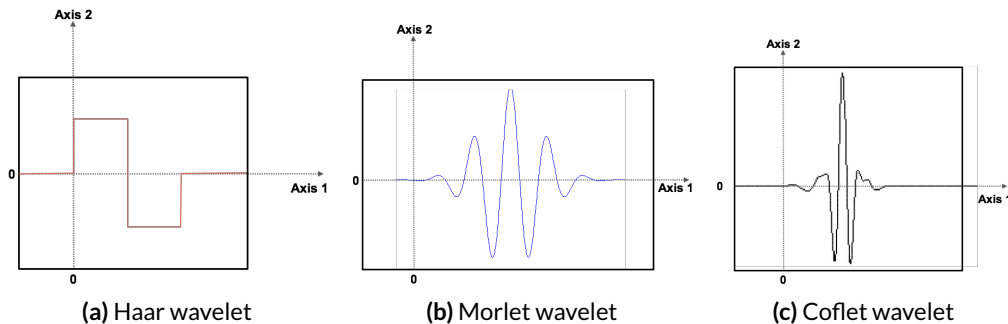


Figure 4.2: Representation of three commonly used wavelets.

4.2 Wavelet Transform

As explained above, the Fourier transform is a powerful tool for data analysis however it does not represent abrupt changes efficiently. This is because the signals are represented using sine and cosine wave which are not localised in time or space. To accurately analyse the signals with abrupt changes, another time-frequency transformation is used that is well localised in time and frequency. A wavelet is the rapidly decaying wave like oscillation that has zero mean and it exists for a finite duration. The Fourier transform used the exponentials, whereas the wavelet transform uses the wavelets. They come in various sizes and shapes. Some of the various wavelets are represented in Figure 4.2. Compared to the STFT above, the wavelet transform gives the frequency content of the signal along with the information of the time at which the particular frequency occurred. Mathematically the wavelet transform is defined as

$$W_x^\Psi(a, b; f(t), \psi(t)) = \frac{1}{\sqrt{|a|}} \int_{-\infty}^{+\infty} x(t) \psi^* \left(\frac{t-b}{a} \right) dt \quad (4.12)$$

The wavelet is defined by the kernel function $\psi(t)$. Any wavelet must fulfil the following condition

$$\int_{-\infty}^{+\infty} \frac{|\Psi(af)|^2}{|f|} df < \infty \quad (4.13)$$

where $\Psi(f)$ represents the Fourier transform of $\psi(t)$. And $\psi(t)$ is called as the mother wavelet.

During the course of this thesis, the Haar wavelet was used for *QRS* complex detection analysis. In wavelet transformation (WT), the wavelet scaling and the time shifting is done. Parameter a represents the scaling and b represents the time shift in the mother wavelet. The scaling function is adjusted in the WT to ensure that the mother wavelet is not changing its energy with $\left(\frac{1}{\sqrt{|a|}} \right)$.

4.3 Principle Component Analysis

The PCA is an important classical tool in the field of signal processing to reduce the number of correlated variables and to classify them into a number of linearly uncorrelated (principle components) variables. Therefore, it could be defined as a data reduction or structure detection method (tool). The reduction in the variables is done preserving all or most of the information. Therefore, the number of principal components needed to represent a signal is less than or equal to the number of original variables or the number of observations. In the

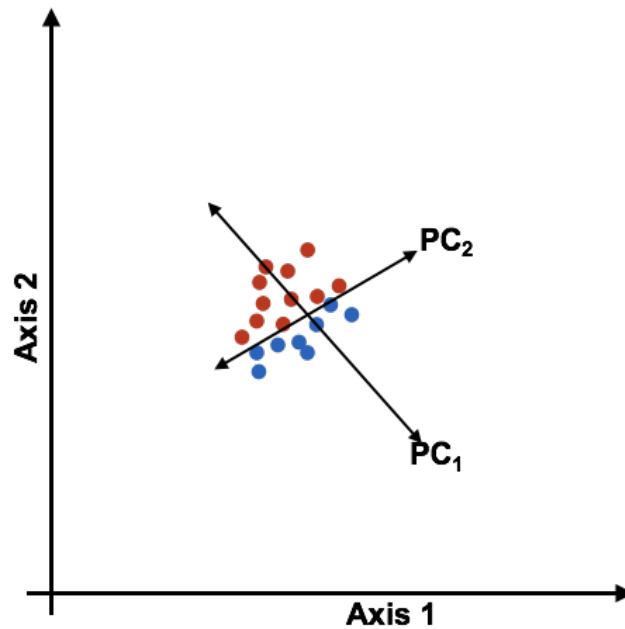


Figure 4.3: Representation of the an example demonstrating the concept of PCA. As represented PCA finds a new orthonormal base so that the variances along the new axis is maximal. Axis1 and Axis2 are the original base, PC_1 and PC_2 are the axis found by the PCA.

PCA, the first principal component covers as much of the variability in the data as possible, and each succeeding component covers as much of the remaining variability as possible. This is achieved by finding an orthogonal transformation to convert a set of observations into the principal components, i.e. transforming the data into a subspace with decreasing covariances over the axis as represented in Figure 4.3.

The PCA method is mathematically defined as an orthogonal linear transformation that transforms the data to a new coordinate system in such a way that the greatest variance by some projection of the data comes to lie on the first coordinate (called the first principal component), the second greatest variance on the second coordinate, and so on. The steps involved in PCA analysis are:

1. Standardise the data.
2. Calculate the covariance matrix.
3. Find the Eigenvalues and Eigenvectors of the covariance matrix.
4. Plot the Eigenvectors / principal components over the scaled data.

This could be demonstrated using an example, considering a sample X with N number of observations defined as $X = [x_0, x_1, x_2, \dots, x_N]$. Using this data, the aim of PCA is to find a new base A for expressing the given data as

$$X = ZA^T \quad (4.14)$$

Using this data matrix, the version X_Z of zero-mean is constructed. This allows to assess the variability from the origin. The solution of this is given by the Eigenvalue decomposition of the observation covariance matrix R of the zero-mean data matrix X_Z .

$$R = X_Z^T X_Z \quad (4.15)$$

For this the Eigenvalue and Eigenvector are determined. The covariance matrix R gives the information of the way in which the axis must be rotated to achieve the minimum covariance between the sample points. The principal diagonal of this matrix R has the variance value, while the rest of the matrix contains the covariances. Any symmetric, non singular, square matrix can be transformed to a diagonal matrix using the expression:

$$L = A^T R A \quad (4.16)$$

where A contains the Eigenvectors of the matrix R , and L is the diagonal matrix with Eigenvalues along the diagonal [60]. The Eigenvalues are sorted in the descending order such as $\lambda_1 \geq \lambda_2 \geq \lambda_3 \geq \dots \lambda_N$ and the same order is with the corresponding Eigenvectors. The PCA solution from this can thus be obtained and the resulting transformation is given by

$$Z_{PCA} = X_Z A \quad (4.17)$$

where Z contains all the principal scores representing the finally transformed data. And A contains the Eigenvectors of R which is the base of new constructed coordinate.

4.4 Non Linear Energy Operator

The non linear energy operator is a method to find the instantaneous energy in the signal such that it can make a sense [62] [63]. As represented by Kaiser et al. the algorithm operates on only three sequential samples of the signal at a time and estimates the instantaneous energy of any signal [62]. To find this energy the simple spring-mass system was used as an example. Using the Newtons second law on the spring mass system, the obtained differential equation is

$$\frac{d^2x}{dt^2} + \frac{k}{m}x = 0 \quad (4.18)$$

The solution to this equation is the simple harmonic motion that is given by $x(t) = A \cos(\omega t + \phi)$, where A is the amplitude, ω is the angular frequency of the oscillation. While the total energy of the system is defined as

$$E = \frac{1}{2}kx^2 + \frac{1}{2}mx^2 \quad (4.19)$$

$$= \frac{1}{2}m\omega^2 A^2 \quad (4.20)$$

or,

$$E \propto A^2 \omega^2 \quad (4.21)$$

This represents that the energy is not only proportional to the amplitude square, but also to the square of the frequencies. Let x_n be the sample of the time discrete simple harmonic oscillation signal with an amplitude A , the digital frequency Ω and phase ϕ . Thus,

$$x_n = A \cos(\Omega n + \phi) \quad (4.22)$$

Considering the other two adjacent signals we get

$$x_{n+1} = A \cos(\Omega(n+1) + \phi) \quad (4.23)$$

$$x_{n-1} = A \cos(\Omega(n-1) + \phi) \quad (4.24)$$

Using the trigonometric identities, it is obtained

$$\cos(\alpha + \beta)\cos(\alpha - \beta) = \frac{1}{2}[\cos(2\alpha) + \cos(2\beta)] \quad (4.25)$$

$$x_{n+1}x_{n-1} = \frac{A^2}{2}[\cos(2\Omega n + 2\phi) + \cos(2\Omega)] \quad (4.26)$$

$$\cos(2\alpha) = 1 - 2\sin^2 \alpha \quad (4.27)$$

$$x_{n+1}x_{n-1} = A^2 \cos^2(\Omega n + \phi) - A^2 \sin^2(\Omega) \quad (4.28)$$

$$x_{n+1}x_{n-1} = x_n^2 - A^2 \sin^2(\Omega) \quad (4.29)$$

Therefore, the energy of the harmonics can be formulated by

$$E_{NLEO} = A^2 \sin^2(\Omega) \approx A^2 \Omega^2 \quad (4.30)$$

This is obtained by approximating $\sin \Omega \approx \Omega$, considered for the frequencies below 1/8 of the sampling frequencies [62]. For this case, the relative error is less than 11%.

Using this concept in the discrete time domain the instantaneous energy can be calculated for the signal with a time stamp of n as

$$E_{NLEO} = x_n^2 - x_{n-1}x_{n+1} \quad (4.31)$$

The three adjacent samples were used to compute the energy of the signal. This operation is termed as the NLEO. It could be observed that the energy is proportional to the squared amplitude and squared frequencies of the signal. In order to get the robust estimation when noise is also present along with the signal, a low pass filtering of the energy was done as described in [64]. To evaluate the local activation time (LAT) and to mark the fractionation duration (FD), from various types of electrograms the NLEO was used throughout this thesis.

PART II

DEVELOPED METHODS

Generation of Simulated Data

Catheter ablation is the well known procedure to treat atrial fibrillation (AFib), if drug therapy fails. The main purpose of this procedure is to get rid of the chaotic depolarisation wavefront propagation pattern over the atrium. As of now the success rate of this procedure is around 50% after first ablation and up to 90% after second or third ablation and depends a lot on the experience and expertise of the physician. As a part of this thesis, the regional and global depolarisation wavefront propagation speed and pattern were estimated. In order to benchmark the CV estimation algorithms, the ground truth was required to find the accuracy and robustness of the algorithms. Since the clinical environments could not be controlled, therefore the simulations were needed. The simulation environment represents the idealistic conditions, which could be controlled and varied as per requirements. Thus, the simulations were performed as a part of this thesis to benchmark the CV estimation algorithms. The various geometries obtained from the electroanatomical mapping system as well as for the biatrial geometry obtained from the simulation environment, were used to analyse the depolarisation wavefront propagation patterns and to study their functional and structural aspects. In the scope of this thesis, various clinical geometries were used for a number of homogeneous and heterogeneous depolarisation wavefront propagation simulations.

At the Institute of Biomedical Engineering (IBT- KIT), there exist solvers for the monodomain and bidomain simulation model, as explained briefly in section 3.1. These were able to mathematically represent the various clinical scenarios. Within the scope of this thesis, the fast marching simulation (FaMaS) method was used to generate the simulated local activation time (LAT) on the clinical geometries. Various homogeneous and heterogeneous propagation simulations were done to obtain different depolarisation wavefront propagation scenarios over the atrium. The parameter called LAT, was later used with the clinical data for regional and global CV estimation. The purpose of the simulation environment is to provide a framework that can reflect the behaviour of the depolarisation wave, as the tissue type varies and as the wavefront propagation speed changes. The controlled simulation provides a platform for benchmarking the algorithm based on the analysis of parameters of the clinical cases. The next section gives a brief introduction of the simulation scenario.

5.1 Fast Marching Simulation

The myocardial tissue is formed of cells of $100\mu m \cdot 10\mu m$ average dimension [65]. All these cells are aligned in dominant direction. These cells contain thousands of ionic channels, which forms the basics of the cardiac electrophysiology. There exist a number of methods trying to imitate the behaviour of these ion channels to get closer to the realistic cardiac electrophysiology. The depolarisation wavefront propagation pattern over the atrium is the reflection of the changes in the ion concentrations as explained in section 2.2. The changes in ion concentration of one cell triggers the changes in the ion concentration of the adjacent cells and this effect is transferred to the other connecting cells too resulting in a depolarisation propagation pattern, also termed as the depolarisation wavefront [66]. This physiological behaviour of the changes in ion concentrations and the depolarisation wavefront propagation is mathematically modelled using simulation. In our case we have used FaMaS method for simulation over the triangulated surfaces. This is because the clinical data obtained using the electroanatomical mapping system typically have the triangular mesh geometry. The details about the FaMaS method are explained in section 3.2 of this thesis. As explained, the Eikonal equation governs the spread of an activation wave in a medium, resulting in a scalar LAT field. As an input to the FaMaS simulation, the predefined speed of the propagation were given to the manually selected regions. The different steps involved in the simulation procedure are as explained below.

Step 1: Importing the clinical geometry from the 3D electroanatomical mapping system and assigning the tissue classes based on the extent of heterogeneity to be introduced.

Step 2: Triangular mesh refinement done to increase the resolution of the geometry. This was done by introducing new nodes into the existing mesh without disturbing the original available triangular mesh. The resolution increment was done in order to get a smooth propagation over the 3D geometry.

Step 3: Manual selection of the trigger node using Paraview (*Paraview version 5.2.0*).

Step 4: Using the input parameters such as triggering node ID, refined triangular mesh, timestamp, tissue type information and the input propagation speed, the simulation was initiated.

Step 6: As an output of the FaMaS, each node was assigned with the LAT value, representing the forward depolarisation propagation pattern starting from the trigger node.

Step 7: This output is imported in MATLAB for further analysis.

These depolarisation propagation simulations were done for homogeneous as well as heterogeneous wavefront propagation over the clinical left atrial geometries in 2D and 3D. The simulation has also been done to obtain the LAT for the high resolution biatrial simulated geometry as explained in the next section.

5.1.1 Homogeneous Propagation Simulation

The term homogeneous in this thesis is used to regard the fact that the atrial surface was assigned one single speed for excitation propagation simulation. Therefore, the LAT at all the nodes were computed using the given propagation speed over the entire geometry. Homogeneous propagation simulation represents the simplest case for the simulated propagation (on a 3D atrial geometry) scenario with no complexity included. These were further divided into two sections namely 1. using the 3D clinical LA geometries, 2. using the 2D triangular patch. Both the cases are described in respective sections below.

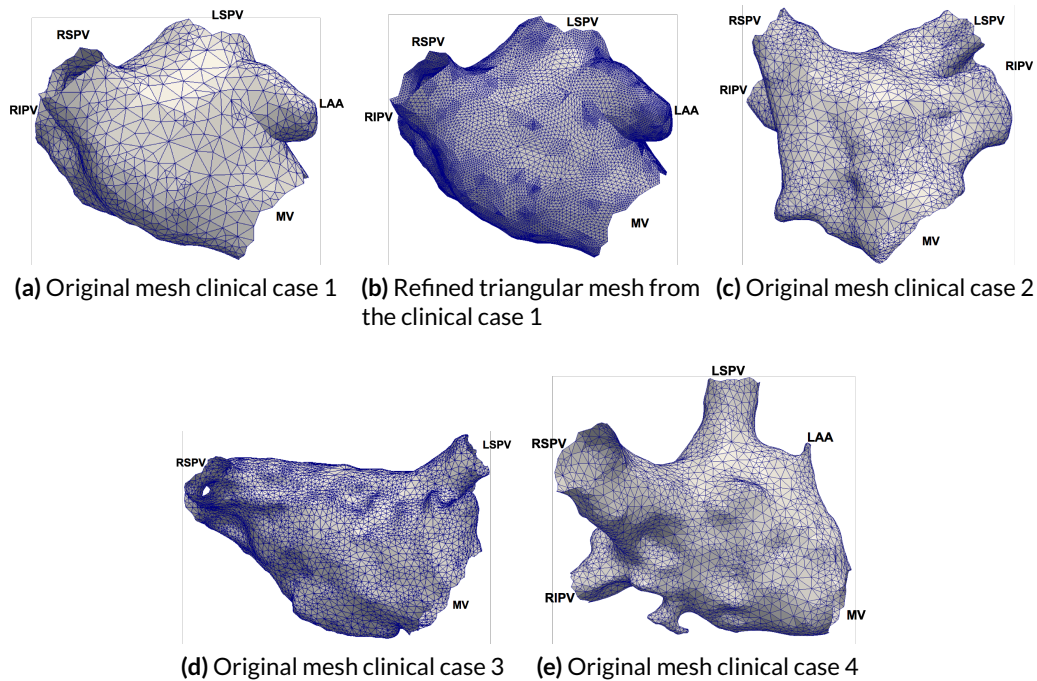


Figure 5.1: The various clinical geometries obtained from the electroanatomical mapping system and used for homogeneous FaMaS to compute the LAT based on given propagation speeds.

5.1.1.1 Using 3D Clinical Left Atrial Geometries

As represented in Figure 5.1 the four clinical LA geometries were used as an input for FaMaS method. Figure 5.1a and b represent the same clinical case but with variable resolution.

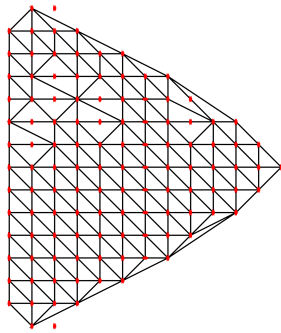


Figure 5.2: Illustration of 2D patch used for FaMa homogeneous propagation simulation to estimate the LAT at all the nodes for the given triangular mesh.

There were 4922 nodes in the original triangular mesh and 21798 in the refined triangular mesh, i.e. approximately four times the original nodes. These were introduced to get the refined triangular mesh and a smooth depolarisation wavefront propagation over the given geometry. The mesh refinement and the artefact removal techniques are explained in chapter 7. Since the FaMaS uses the Eikonal equation therefore, the LAT estimation was done from one node to the other. The triangular mesh refinement was done for all the clinical cases. FaMa simulations were done to get the depolarisation propagation with the known ground truth values with least complexity for the given clinical LA geometries. The given input propagation speed for all the homogeneous cases was $\approx 0.5 m/s$ and is enlisted in Table 5.1. The resulting LAT maps are explained and discussed in the result section (chapter 13) of this thesis.

5.1.1.2 Simulation of a 2D Triangular Patch

This section deals with the second independent simulation scenario. Here, the simulation was done using the spatial information obtained from a patch catheter electrode locations. The catheter had 117 electrodes and their spatial coordinates were used as an input for FaMaS. The input propagation speed of $0.507 m/s$ was used for 2D simulation. The triangular mesh was created using the available vertices information. The trigger was selected manually and the FaMaS simulation was done to get the corresponding temporal (LAT) coordinate. Figure 5.2 represents the 2D patch used for simulation. The red dots represents the various electrodes on the triangular patch catheter. The electrode locations involved in the triangular mesh as the vertices are the ones for which the LATs were computed. This was done because in the experimental scenario, only at these locations, good electrograms with clear activation complexes were recorded. The corresponding simulated LAT results are explained and discussed in chapter 12 of this thesis.

Table 5.1: Various homogeneous and heterogeneous cases used for FaMaS.

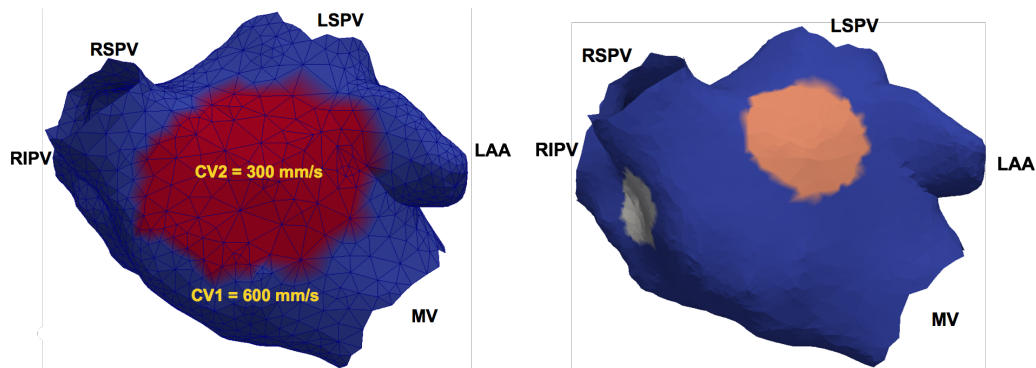
| Serial number | Clinical case | No. of regions with different propagation speed on the atrium | Input propagation speed to get simulated LAT (m/s) | Trigger point location |
|---------------|---------------|---|--|----------------------------|
| 1 | 1 | 1 | 0.507 | Near |
| 2 | 1 | 2 | 0.6 and 0.3 | the |
| 3 | 1 | 4 | 0.6, 0.4, 0.3, 0.2 | BB |
| 4 | 2 | 1 | 0.507 | region |
| 5 | 3 | 1 | 0.507 | |
| 6 | 4 | 1 | 0.507 | |
| 7 | 1 | 4 | 0.2, 0.4, 0.6, 0.8 | |
| 8 | 1 | 1 | 0.507 | Near CS catheter electrode |

5.1.2 Heterogeneous Propagation Simulation

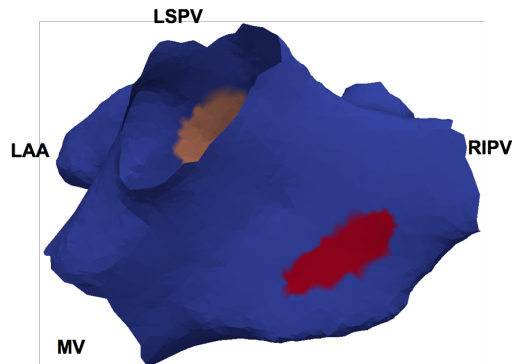
In the heterogeneous propagation case, the depolarisation wavefront travels with different propagation speed in the various manually selected regions on the given clinical geometry. The heterogeneities were included to get closer to the realistic scenarios where the depolarisation wavefront has variable speed in different physiological tissue types. The clinical as well as the high resolution biatrial geometries were used for the heterogeneous LAT simulation using the FaMaS method. The various heterogeneous simulation details are enlisted in Table 5.1. In this section they are categorised in two sections 1. using the clinically obtained LA geometries, 2. using the simulated biatrial geometry, as explained below.

5.1.2.1 Using Clinical Left Atrial Geometries

The heterogeneous depolarisation propagation was simulated using the geometries mapped during the routine clinical procedure. The mapping and recording has been done using the EnSite Velocity mapping system (St. Jude Medical, USA). To introduce heterogeneity and to get the propagation having variable speeds, various regions were manually selected on the atrial geometries. This has been done after importing the clinical geometries in MATLAB (*MATLAB version R2016b*). Figure 5.3 represents the manually selected 2 and 4 regions respectively on one of the clinical geometries. All these regions belong to different tissue classes and were given different propagation speeds as input for LAT simulations. The tissue class annotation and region selection were done purely on the manual basis to get a heterogeneous propagation. These geometries were then imported in Paraview software (*version 9.0*) and the triggers were manually selected. Different permutations and combinations of the speeds were simulated to get different propagation patterns. The results and the propagation patterns obtained from FaMaS simulations are explained in chapter 13.



(a) The clinical geometries with 2 tissue classes having 300 mm/s and 600 mm/s as the FaMaS input propagation speed. (b) Posterior view of the clinical geometry having 4 tissue classes (heterogeneous regions)



(c) Anterior view of the clinical geometry having 4 tissue classes (heterogeneous regions)

Figure 5.3: The various geometries used for heterogeneous FaMa simulations. b and c are the posterior and anterior view of the same clinical case. These are mentioned in row 2 and 3 of Table 5.1. LSPV- left superior pulmonary vein, LIPV- left inferior pulmonary vein, RSPV- right superior pulmonary vein, RIPV- right inferior pulmonary vein, LAA- left atrial appendage, MV- mitral valve.

5.1.2.2 Using Biatrial Simulated Geometries

The single layer high density biatrial geometry obtained by registering the computed tomography (CT) and magnetic resonance imaging (MRI) biatrial data as explained by Krueger et al. in [67], was used with FaMaS method to get the LAT for the depolarisation wavefront propagation over various atrial physiological tissue types. The biatrial geometry was available as a triangular mesh. In the biatrial geometry, different tissue classes were assigned to the various marked regions on the biatrial geometry as represented in Figure 5.4. The tissue classes and the speed given to various regions are enlisted in Table 5.2. Different tissue classes were assigned to the scar tissue, left atrium (LA), right atrium (RA), left atrial appendage (LAA), crista terminalis, pectinate muscle and to the other anatomical regions. These are represented by colour code in Figure 5.4. In order to keep low complexity and less computational time, the blood has been given 0 input propagation speed during this FaMa

Table 5.2: Assigned propagation speeds for various tissue classes used with biatrial geometry for fast marching simulation (FaMaS).

| Serial Number | Tissue class | Atrial region | Simulation 1 assigned input speed (m/s) | Simulation 2 assigned input speed (m/s) |
|---------------|--------------|------------------------|---|---|
| 1 | 32 | Left atrium | 0.2 | 0.2 |
| 2 | 33 | Right atrium | 0.2 | 0.2 |
| 3 | 111 | Left atrial appendage | 0.8 | 0.4 |
| 4 | 112 | Right atrial appendage | 0.8 | 0.4 |
| 5 | 113 | Revitalize scar | 0.8 | 0.4 |
| 6 | 100 | Crista terminalis | 0.4 | 0.8 |
| 7 | 101 | Pectinate muscle | 0.4 | 0.8 |
| 8 | 102 | Bachmann Bundle | 0.8 | 0.8 |
| 9 | 159,160 | Vena cava | 1.2 | 1.2 |
| 10 | 192-199 | Bridge | 0.2 | 1.2 |
| 11 | 166-169 | Pulmonary vein | 0.8 | 1.2 |
| 12 | 155 | Septum | 0.2 | 0.4 |
| 13 | 34 | Sinus node | 0.2 | 0.2 |
| 14 | 9 | Blood | 0 | 0 |

simulation. Two different propagation patterns were simulated for this biatrial geometry. For these simulations the trigger has been selected manually at some arbitrary location in the LA. Since the regions had various propagation speed therefore, the LAT maps were obtained corresponding to the various input propagation speeds on the biatrial surface. The LAT corresponding to different tissue classes and regions on the geometry are discussed and represented in chapter 13 with other simulated LAT maps.

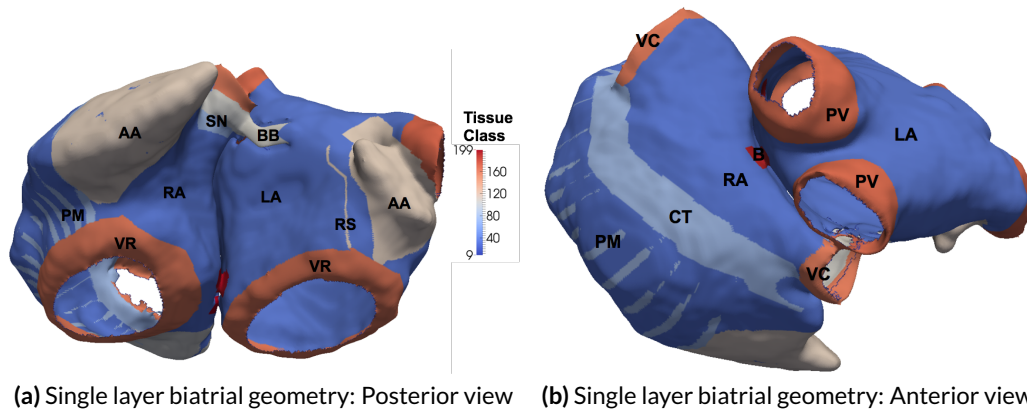


Figure 5.4: The biatrial geometry used for FaMaS heterogeneous LAT simulation. LA- left atrium, RA- right atrium, SN- sinus node, LAA- left atrial appendage, RAA- right atrial appendage, RS- revitalise scar, CT- crista terminalis, PM- pectinate muscle, BB- Bachmann bundle, VC- vena cava, B- bridges, PV- pulmonary vein.

Introduction to the Clinical Cases

Atrial fibrillation (AFib) is one of the most frequently encountered rhythm disorder [68]. It is promoted by irregular conduction in the heart and results into a chaotic depolarisation wavefront propagation pattern. The prevalence of AFib has been doubled during the last decade [69]. Its prevalence varies with age and sex of the patients. Procedures such as catheter ablation, pharmacological control, cardioverters etc. are being used to treat AFib. Catheter ablation is a well-know procedure to control or treat AFib, suggested after drug therapy fails. This is a minimally invasive procedure, in which catheters are guided to the atrial chambers and then recording and ablations are done.

During this minimally invasive procedure and routine clinical mapping, data are acquired using a 3D electroanatomical mapping (EAM) systems. These 3D EAM systems have reduced

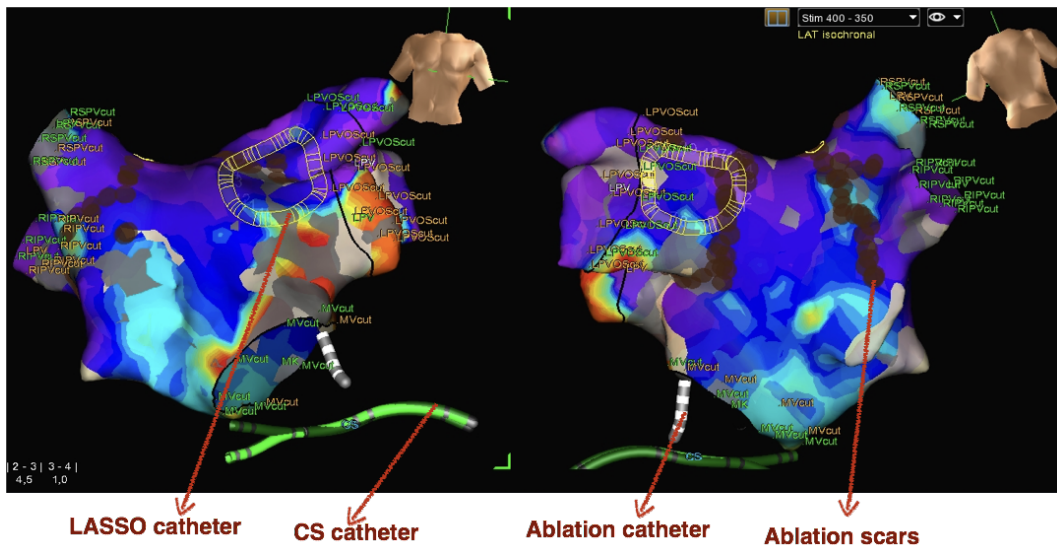


Figure 6.1: The screenshot obtained from EnSite Velocity mapping system, along with different types of catheters present. Various marked valve cuts can be clearly seen. These are later on used for cutting out the region outside of them as explained in the text.

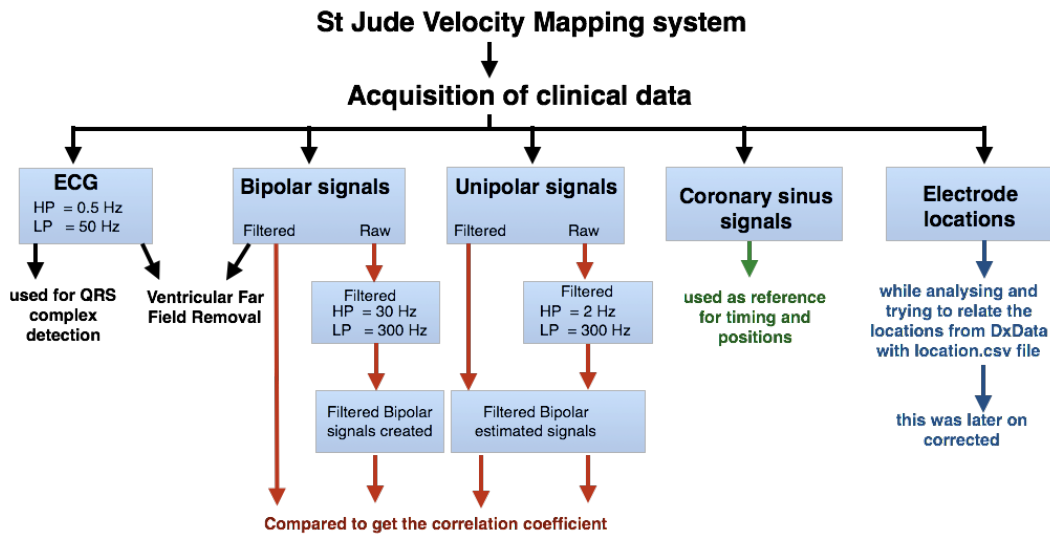


Figure 6.2: Representation of the various data acquired from the EnSite Velocity mapping system. The flowchart represents the processing and feature extractions that have been done using respective data.

the radiation exposure when radio frequency (RF) catheter ablation procedures are being performed by well-trained physicians. To understand the mechanism behind the chaotic propagation of the depolarisation wavefront and to find the best cure, a lot of research has been going on to create various maps for therapeutic and research purposes.

Various in-vivo and in-silico studies are also going on to understand electrophysiological, functional and structural properties of the heart. This could help the physicians and lead to a quantitative electrophysiological parametrisation of the various phenomena inside the heart.

As a part of this research, the estimation of the regional and global depolarisation wavefront propagation pattern and speed on the atria were analysed. But before getting into the details of that, it is important to understand the statistical and fundamental information that could be extracted from the available clinical EAM systems.

As explained in section 2.5, there are various EAM systems available such as CARTO (Biosense Webster, Israel), NavX Velocity (St. Jude Medical, USA), RHYTHMIA (Boston Scientific, USA) and Real Time Position Management system, that could be used for mapping the clinical cases. Depending upon the requirements and availability, a mapping system was selected to map and obtain the clinical data. In our case, the EnSite Velocity mapping system by St. Jude Medical, USA was used to record the data. The recording was done at a frequency of 2.0345 kHz during the routine mapping. The data were recorded with informed consent from the patients at the Städtisches Klinikum Karlsruhe, Karlsruhe.

This chapter is an introduction to the various data that are obtained using the Velocity mapping system. The various catheters used in the data acquisition and processing are 10 pole

Table 6.1: Details of the clinical cases taken into consideration and their respective analysed parameters.

| Clinical case | Type of analysis | Age, weight sex | Catheter used | Atria mapped |
|---------------|----------------------------------|-----------------|---------------|--------------|
| 1 | Spatial and temporal analysis | NA | LASSO | LA, RA |
| 2 | VFF removal | NA | LASSO | LA |
| 3 | Stimulus protocol based analysis | 65, 60, F | 10 pole LASSO | LA |
| 4 | Stimulus protocol based analysis | 60, 65, M | 20 pole LASSO | LA |
| 5 | Stimulus protocol based analysis | 61, 80, M | 10 pole LASSO | LA |
| 6 | Stimulus protocol based analysis | 68, 83, M | 20 pole LASSO | LA |

and 20 pole LASSO catheters, ablation catheter and coronary sinus (CS) catheter. Figure 6.1 represents the screen shoot of one of the recorded cases. All the three catheters can be clearly seen in this screenshot. The ablation lines were marked by red dots and the various valve cuts are also annotated. The data from the mapping system were analysed for different studies and the methods associated with them are explained in chapter 7, 9 and 10. The various data obtained have been listed in the flowchart in Figure 6.2. Various parametric and statistical analysis were done using these clinical information (explained in the upcoming chapters). Table 6.1 gives a brief introduction and overview of the various clinical cases and their respective analysed clinical scenarios. The next section of this chapter explains the various recordings done using the available EAM system.

6.1 Clinical Recordings

In the clinical environment, various types of catheters were used to map the activities in the tissue. These catheters contain electrodes that can reflect the activities in terms of electrograms. These electrograms are measured with respect to the reference electrode. As the depolarisation wavefront approaches the electrode, a positive deflection is observed, while as it goes away, a negative deflection is observed in the unipolar electrograms. A zero is observed when the depolarisation wavefront is exactly beneath the electrode. The difference in extracellular potential from two electrodes is reflected by the electrogram. The two electrodes used are called as the reference and exploring electrode.

During this research, as represented in Figure 6.2, the recording was done using the EnSite Velocity mapping system. This system has the advantage that it is compatible with almost any electrophysiology (EP) catheter and most of the EP lab equipment. The various clinical signals that were recorded and used for analysis as well as the associated feature extraction techniques (as mentioned in the flowchart of Figure 6.2), are explained in chapter 7 to 10.

The sampling rate used for data acquisition could vary for different mapping systems. For example, the sampling rate obtained from the CARTO system was 1 kHz , while in the EnSite Velocity mapping system a sampling frequency of 2 kHz was used. With the EnSite Velocity

mapping system, it is also possible to connect maximum of 2 basket catheters resulting into 128 electrograms at once making the global pattern clearly visible on the cardiac chambers. The recording done depends upon the type of catheter used. As explained in section 2.2, the propagation of the depolarisation wavefront is due to the ion concentration change and is observed as current and voltage changes. This could be mapped by endocardium, epicardium or using body surface potential maps. The EnSite Velocity mapping system was used to map the endocardium of the atrium. These recorded signals were used for various parametric analysis which in-turn could help in benchmarking the respective event occurrences. The various types of clinical signals recorded using the catheters are briefly explained below.

6.1.1 Unipolar Electrograms

In 1934, Frank Wilson developed the Wilson Central Terminal which is used for unipolar electrogram recording [70]. In case of unipolar electrogram recording, the reference electrode is kept at far distance from the heart. The Wilson Central Terminal is obtained by averaging the three active limb electrode voltages measured with respect to the return ground electrode and it is a good approximation of an electrode at far distance. Usually the reference electrode is placed at the Wilson terminal, therefore, it is also considered as the location of zero electrical activity. The exploring electrode (distal or proximal electrodes) gets in contact with the active tissue in the mapping region. Now-a-days, various other places such as CS or the inferior vena cava (IVC) could also be used to place the electrical reference electrode. The catheter in the CS artery is always used for the positional reference.

The unipolar electrograms contain both the near and far fields and measure the voltage on a single electrode. Since the distal electrode is close and in most of the cases in contact with the endocardium, therefore, it is considered to be more reliable. The morphology of the electrogram is associated with the tissue underneath and it changes as the tissue type changes. Healthy tissue gives clear activation, while with arrhythmogenic substrate, a complex morphology of the activation complex is obtained.

As the depolarisation wavefront travels over the cardiac tissue, the exploring electrode senses this change in the form of electrograms. Therefore, the recorded potential difference between the reference and exploring electrodes gives the extracellular potential at the exploring myocardial cells and is a result of the transmembrane currents. Depending upon the speed of the depolarisation wavefront beneath the electrode the duration of the activity on the electrogram changes. Slower the propagation, larger would be the duration observed. In the clinical recording and set up, the signals are always affected by various noise sources.

One such example is represented in Figure 6.3. This recorded unipolar electrogram contains power-line hum, along with baseline wander. During preprocessing stage, all these artefacts were removed by using various filters (explained later in this chapter). After preprocessing

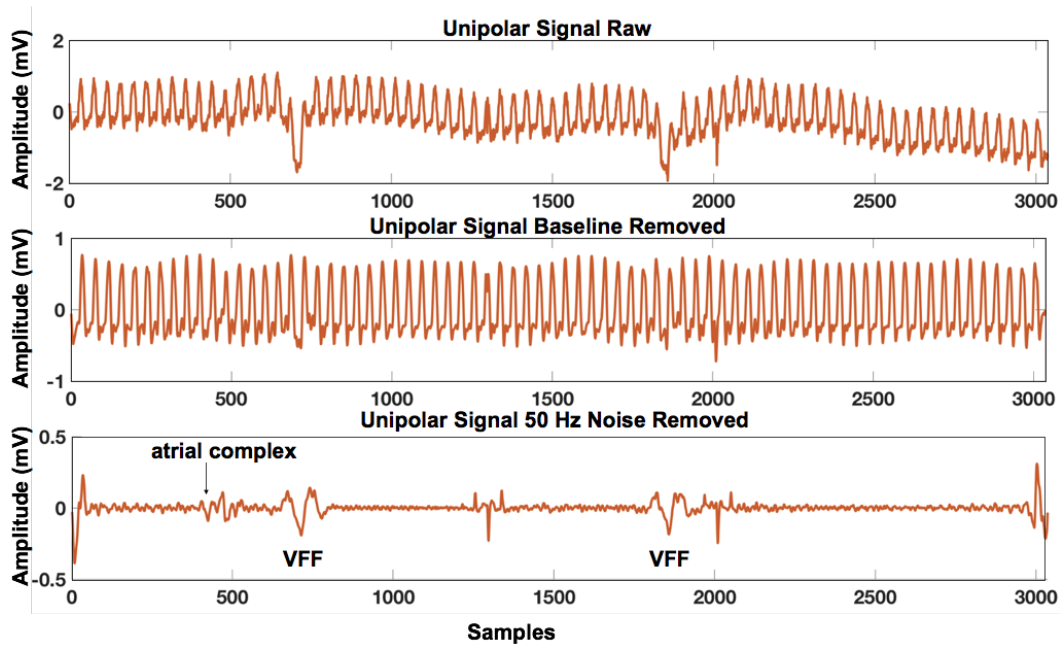


Figure 6.3: Illustration of raw and filtered unipolar signals obtained from the clinic during routine procedure. Recorded at a sampling rate of 2.03 kHz

and artefact removal, the clear activities can be observed. Figure 6.3a is the raw unipolar electrogram of 1.2 second (corresponding to 3036 samples) recorded at a sampling rate of 2.03 kHz . Figure 6.3b is the same electrogram after baseline wander removal and Figure 6.3c is the filtered unipolar electrogram.

In the filtered signals, artefacts such as the ventricular far field (VFF), could still be observed. In Figure 6.3c, the atrial complex and the VFF are marked. Because of the presence of the local artefacts, the bipolar signals are often preferred over the unipolar signals.

6.1.2 Bipolar Electrograms

The unipolar electrograms are obtained by subtracting the potentials between the distal and the reference electrodes. Unlike these, the bipolar electrograms represent the activities obtained between two closely spaced electrodes. That is the bipolar electrograms are the amplified difference of two unipolar signals. The two closely spaced electrodes produce two unipolar electrograms, which give the bipolar electrograms by calculating the algebraic differences between the two.

Since the activities from closely spaced electrodes are subtracted, the bipolar electrograms in ideal situations are free from VFF and common mode noise since $(Unipolar\ Signal\ 1 + VFF) - (Unipolar\ Signal\ 2 + VFF) = Bipolar\ Signal$. This is because subtraction of two unipolar signals results in subtraction of the local artefacts as well as the far field activities.

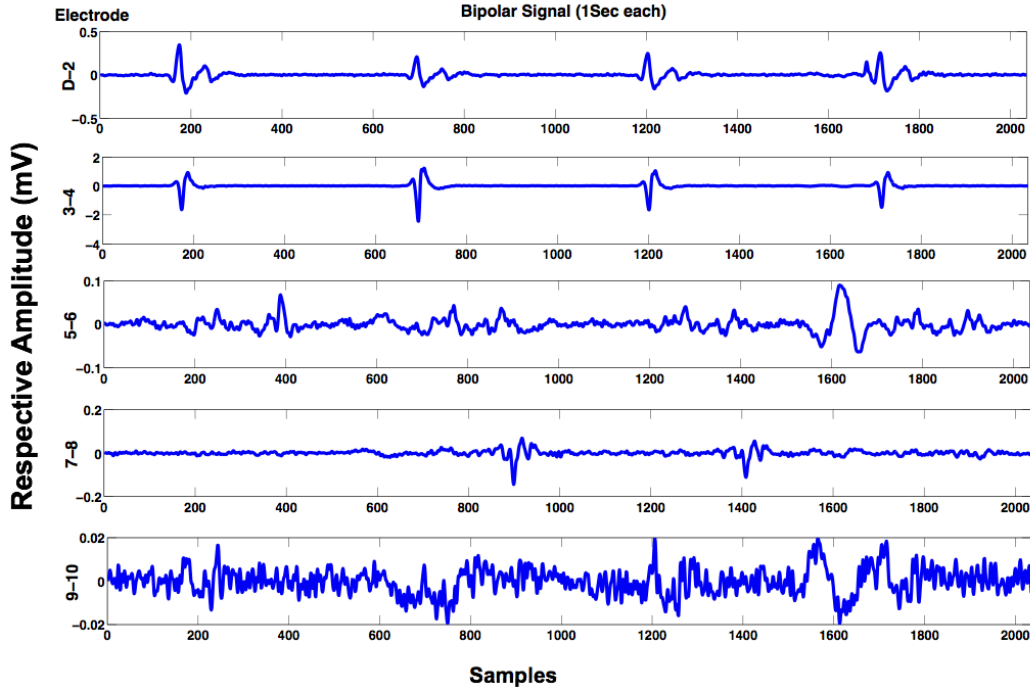


Figure 6.4: Illustration of bipolar electrograms from distal to the proximal electrode obtained using the 10 pole LASSO catheter. The annotations are *a* to *e* for respective electrogram from top to bottom.

Therefore, in bipolar electrograms, better signal to noise ratio is obtained.

The bipolar electrograms approximate the first spatial derivative of the unipolar electrograms. These are influenced by catheter orientation relative to tissue and are dependent on the inter electrode distance. The amplitude is maximum during parallel propagation to the axis of recording electrodes, while amplitude reduces when propagation is perpendicular to the line between the electrodes. Also, the amplitude of the bipolar electrograms decreases as the electrodes get closer.

The bipolar electrogram duration can give a rough estimate of the conduction velocity (CV). This also depends on the orientation of the catheter as well as on the excitation wavefront propagation pattern. Slower conduction between two electrodes, results in widening of the bipolar electrograms. In the scope of this thesis, the bipolar electrograms from the 10 pole and 20 pole LASSO catheters were analysed.

Figure 6.4 represents the bipolar electrograms for a 10 pole LASSO catheter. The combination of unipolar electrodes subtracted to get the bipolar electrograms are $D - 2$, $3 - 4$, $5 - 6$, $7 - 8$, $9 - 10$ as annotated. Clear activation complexes can be observed in the signals obtained by subtracting D and 2^{nd} electrodes unipolar electrograms (Figure 6.4a), and also in the bipolar electrogram obtained by subtracting 3^{rd} and 4^{th} electrodes unipolar electrograms (Figure 6.4b). For the bipolar electrogram obtained by subtracting the 9^{th} and 10^{th} electrodes

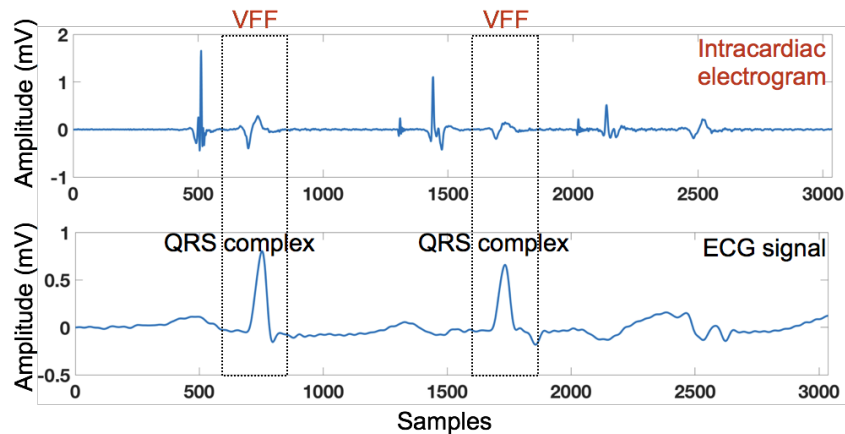


Figure 6.5: Representation of the intracardiac 1.5 second segment along with the *ECG* signal. Both are recorded at the same location. The *QRS* complex of *ECG* signal was used to mark the VFF in the intracardiac signal.

unipolar electrograms (Figure 6.4e), an extremely low amplitude signal is obtained which could be regarded as noise. This is because in this bipolar electrogram the amplitude is $< 0.08\text{mV}$ throughout. Looking at such electrograms, it can be stated that the recorded locations hardly show activity in the tissue beneath the electrode.

From the various clinical cases under analysis, the approximate number of recorded electrograms varied from 300 to 600 (with 1 second to 5 second electrograms at each recorded location) per clinical case using the LASSO catheter.

6.1.3 ECG Signals

Along with the intracardiac signals, the body surface potentials can also be recorded using the EAM system (along with the endocardial intracardiac mapping). The *ECG* records the electrical changes on the skin that result from the electrophysiological pattern of the depolarisation wavefront during cardiac activity. The 12 lead *ECG* signals were also obtained by connecting *ECG* leads with the mapping system.

The *P* wave, *QRS* complex, *T* wave and *U* wave can be denoted corresponding to the depolarisation and repolarisation of the atria and ventricle as explained in section 2.3. If the *ECG* signal is compared with the intracardiac signals, the atrial and ventricular activities corresponding to their depolarisation information can be separated. The *QRS* complex corresponds to the ventricular depolarisation and atrial repolarisation of the heart.

In the scope of this thesis, the *ECG* signal was used to mark the ventricular activities in the clinically obtained atrial electrograms. Figure 6.5 represents the VFF in the intracardiac

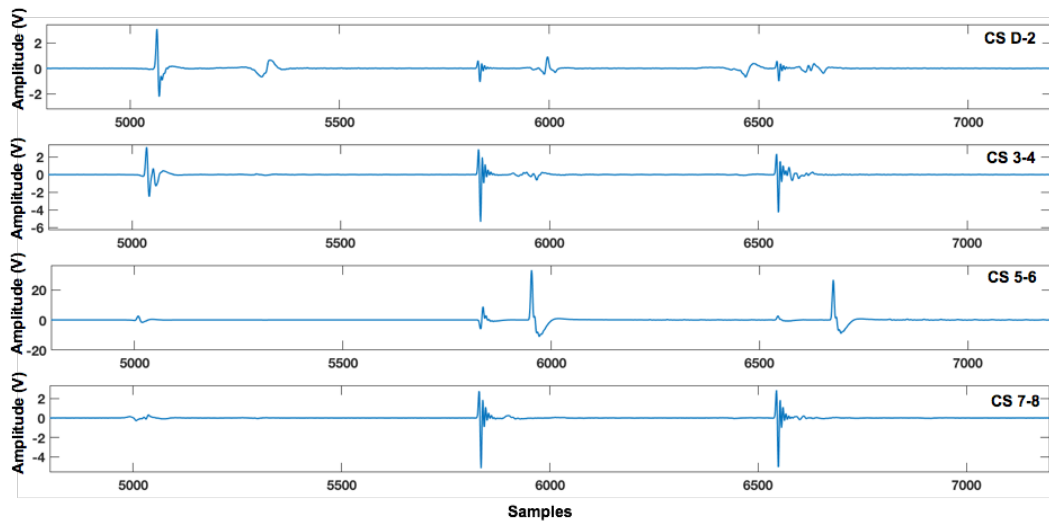


Figure 6.6: Simultaneously recorded CS signal in various leads of the catheter.

electrograms simultaneous to the *QRS* complexes in the *ECG* signals. The *ECG* signals were used to mark the VFF and play a vital role in separating them from the atrial activities. Therefore, in the atrial electrograms, the activities corresponding to the *QRS* complexes can be regarded as corresponding to the VFF. This will be explained in chapter 9 under the section called VFF removal.

6.1.4 CS Signals

The catheters are minimally invasively inserted into the cardiac chambers for endocardial recordings. During the procedure, one catheter is also inserted to the coronary artery and is called as the CS catheter. This is done because it remains stationary during recording (temporally and spatially). Thus, the recordings done by the CS catheter can be used as the temporal reference signal. At times, the CS can also be used as reference electrode (instead of the Wilson terminal) for unipolar electrogram measurement. The reference selection during the procedure can be done by the operator as per interest. In the scope of this thesis, the electrograms obtained from the CS catheter are used as the temporal reference electrograms.

The recordings were done during sinus rhythm (SR). In some of the clinical cases, the analysis was also done using the stimulus protocol data recordings. The stimulus was given using the CS catheter (explained in chapter 10) in terms of voltage and current to the left atrium (LA). For giving the external stimulus, any electrode pair on the CS catheter could be used. In our case CS 3 – 4 and CS 7 – 8 electrodes were used to give the artificial stimuli. The CS signals can also be used to calculate the basic cycle length from the available intracardiac electrograms.

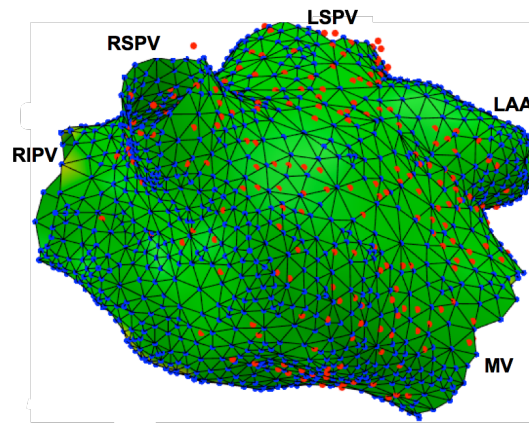


Figure 6.7: Illustration of surface points and the triangular mesh generated for the clinical case using the EnSite Velocity mapping system. Red dots are the points selected by the physician at which the electrograms were recorded.

Figure 6.6 represents an example of bipolar electrograms obtained from the CS catheter. Clear activation complexes of high peak-to-peak (P2P) amplitude can be observed. Out of all the CS bipolar electrograms, any one can be selected and used as a temporal reference during the analysis. The selection of CS reference signal is done depending on the application and the parameter to be studied.

6.1.5 Spatial Location

As discussed in chapter 2, the EAM system provides the electrograms. Along with this, there are possibilities for chamber re-constructions, features to mark anatomical landmarks, display of the various electrograms involved in mapping without using fluoroscopy.

Compared to the other conventional mapping strategies, the EAM system has the distinct ability to reliably allow the catheter positioning. The EnSite Velocity mapping system displays the 3D positions of multiple catheters by applying a low level 5.6Hz current through orthogonally located skin patches. The recorded voltage and impedance at each catheter's electrode generated from this current allows their distance from each skin patch, and ultimately, their location in space, to be triangulated with the help of a reference electrode.

As the catheters move inside the 3D chamber the geometry is generated in the form of a triangular mesh by moving a mapping catheter along the endocardial surface (as represented in Figure 6.1). The recording of the electrograms lasting from 1second to 5seconds can be done at locations selected by the physician. The locations recorded are marked by the physicians. These spatial locations of the electrodes can be used at later stages for analysis. The triangular mesh geometry and the physician selected points are represented in Figure 6.7. Using the LASSO catheter the number of these recorded locations vary from 300 to 600.

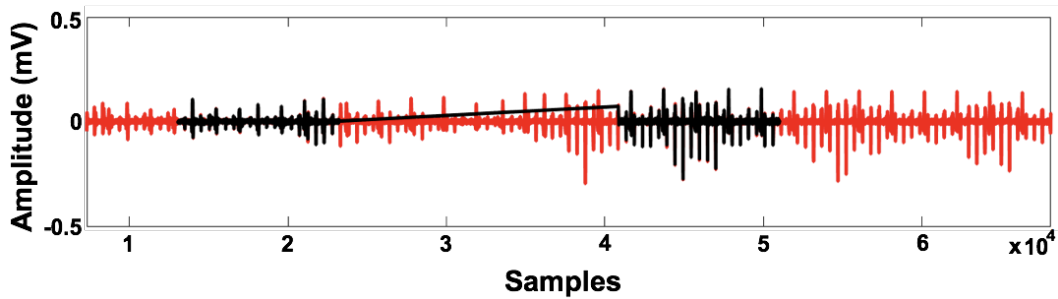


Figure 6.8: Illustration of the segments segregated from the entire data set connected via a straight line.

Higher resolution maps can also be generated using the newly introduced ORION catheter and RHYTHMIA mapping system in combination with automatic point acquisition. The triangular mesh makes the clinical geometry mapped from inside the endocardium while the red dots are the points where all electrograms were measured. With the help of the system, simultaneously multiple catheter positions can be displayed and recorded in real time.

6.1.6 Segment Data

As explained above, during the procedure, the physician can select some recording locations based on their experience and expertise. These recorded electrograms at various locations are termed as the segment data. These segments usually contain the activities that are of interest to the physicians. These may vary from 1 to 5 *seconds*. In the scope of this thesis, these segments were of great interest. These segments could be segregated from the huge data set corresponding to the recording that could last from 30 *minutes* to 4 *hours*.

To extract these segments from the entire dataset various temporal and spatial parameters are taken into consideration. This will be explained in the feature extraction section in chapter 9. One such example of the selected segment from the long dynamic electrogram is represented in the Figure 6.8. The red coloured electrograms are the recorded segments during the procedure while the black colour segments are the ones selected by the physicians during the procedure and these are the ones taken for analysis at later stage.

6.2 Filtering Techniques

When the clinical electrograms are recorded, there are various baseline frequencies, high frequency jitters etc. present. Therefore, filtering is a very important preprocessing step during the intracardiac signal analysis. Depending on the type of clinical cases different filtering frequencies were used to remove the unwanted frequency components. The selection of the filter and the filtering frequencies depends on the type of signal under analysis. The

ECG signals, unipolar signals, bipolar signals use different filtering frequencies. Table 6.2 gives the brief introduction of the frequencies used for the mentioned signals.

6.2.1 ECG Signal Filtering

The surface *ECG* signals are concentrated in the frequency range between 1 Hz to 80 Hz [71]. High resolution *ECG* signals are concentrated between a bandwidth of 0.05 Hz to 300 Hz [72].

In this thesis, the *ECG* signals were used together with the intracardiac signals to find, mark and separate the ventricular activities. The *QRS* complexes were marked using the wavelet technique [73]. During the research the *ECG* signals were taken into consideration for *QRS* complex detection, and analysing the intracardiac signals using the temporal coordinates. The filtering frequencies (2nd order Butterworth filter) used during our analysis were 1 Hz and 80 Hz for high pass (HP) and low pass (LP) filtering.

6.2.2 Unipolar Signal Filtering

Unipolar recordings give the local information of the depolarisation wavefront for the tissue underneath the recording electrode. Along with the electrical activity of the tissue, the electrograms also contain artefacts such as baseline wander, high frequencies jitters etc. The HP and LP filters were used to remove some of these artefacts.

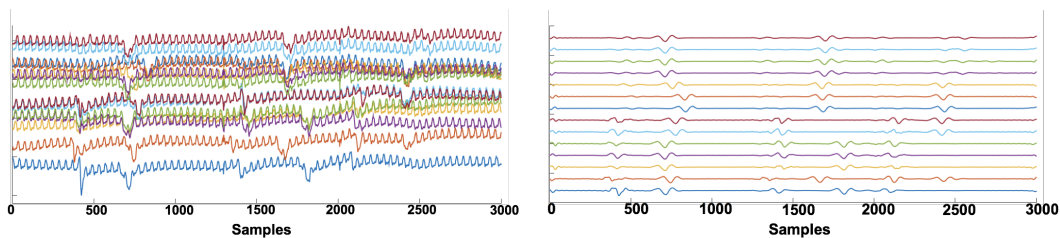


Figure 6.9: The representation of raw and filtered unipolar signals. a) Raw unipolar signals and b) filtered unipolar signals

As represented in Table 6.2, the filtering frequencies used for removing the artefacts from unipolar electrograms were 2 Hz and 300 Hz to remove the unwanted high and low frequency components respectively. Similar to Figure 6.3, Figure 6.9a represents the 14 raw unipolar signals while Figure 6.9b represents the corresponding filtered unipolar signals. The two steps involved in filtering were namely:

1. Removing the baseline wander.

The baseline wander removal in unipolar electrograms was done by using the causal filter

Table 6.2: Filtering frequencies used for various types of signals during analysis. The 2nd order Butterworth filters were used for filtering.

| S.No. | Type of signals | High Pass frequencies (Hz) | Low Pass frequencies (Hz) |
|-------|-----------------------|----------------------------|---------------------------|
| 1 | ECG | 1 | 80 |
| 2 | Unipolar Intracardiac | 2 | 300 |
| 3 | Bipolar Intracardiac | 30 | 300 |

having the HP and LP frequencies of 2Hz and 300Hz respectively.

2. Removing the 50 Hz noise.

The 50Hz noise removal was done by using the notch filter with the frequency of 50Hz . The selected window around 50Hz was of 5Hz to get rid of the 45Hz to 55Hz frequency components.

6.2.3 Bipolar Signal Filtering

The bipolar electrograms were obtained after subtracting the two unipolar electrograms.

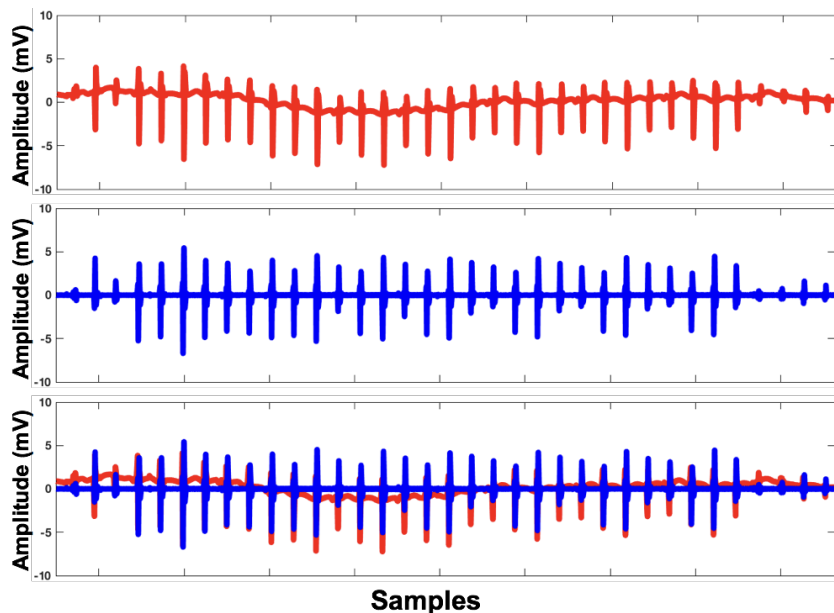


Figure 6.10: Representation of raw (red) and filtered (blue) bipolar electrograms obtained from the EnSite Velocity mapping system.

But there are artefacts present in the bipolar electrograms such as the alternans or jitter or baseline wander etc. Therefore, filtering of the bipolar signals is also required during preprocessing. The filtered and unfiltered bipolar electrograms are demonstrated in Figure 6.10.

Figure 6.10*a* are the raw bipolar electrograms. This signal was filtered using the HP and LP frequencies of 30Hz and 300Hz as mentioned in Table 6.2. Figure 6.10*b* represents the filtered electrogram. Figure 6.10*c* represents the raw and filtered signal together. The difference between the two can be seen clearly.

Preprocessing of Clinical Data

As explained in chapter 7, the intra-atrial electrograms and the geometrical information obtained during the routine clinical procedures were used for the analysis. Based on the experience and expertise, the physicians visually inspect the electrograms and using the various clinical protocols decides the treatment this will be explained in the introduction section of chapter 14. The treatment for atrial fibrillation (AFib) is done using the catheter ablation procedure after the drug therapy failed.

During electroanatomical mapping (EAM) the spatial and temporal information were obtained in terms of the electrograms and the atrial geometries. Different types of catheters can be used for the electrogram recordings. In the scope of this thesis, the catheters used for recording were the 10 pole and 20 pole LASSO catheter, PentaRay catheter, ORION catheter, ablation catheter and the coronary sinus (CS) catheter.

The recorded signals contain the depolarisation wavefront propagation information superimposed with the artefacts. Before further analysis the preprocessing of the signals had to be done and these artefacts were to be removed. Normally preprocessing involves the removal of noise, baseline wander, geometrical artefacts, the no-contact (of electrode with endocardium) signals, alignment of the segments based on the reference signals, and so on-so forth. For the removal of artefacts the various preprocessing steps involved are explained in the next section of this chapter. The most usual preprocessing steps used for almost all the clinical cases under analysis in this thesis are namely:

1. Valve cutting

This was done by manually marking the valve regions on the atrium, while collecting the data from the clinic (as annotated in Figure 6.1). The annotations were marked after the mapping was finished. Once the regions were marked, a MATLAB script was used to remove them. Usually this includes, the pulmonary vein (PV) regions and the mitral valve (MV) region removal, in case of left atrium (LA).

2. Removing the spatiotemporal information of the electrodes lying outside the valve cut region

Once the valves are marked and the region of interest were selected, the location lying outside this region were also removed.

3. High pass and low pass filtering

This was done to remove the unwanted frequency components from the electrogram segments.

4. Removing the power-line hum

At times the power-line hum could be observed in the clinical electrograms because of the connection problem or due to electrodes short circuiting. These were usually very high amplitude artefacts. The baseline wander and the 50 Hz noise (which could be present in the unipolar or in bipolar electrograms) were also removed using the filters. These were also removed during the preprocessing of the clinical electrograms.

5. Including the recorded spatial locations to the obtained geometrical triangular mesh

The recorded locations were included to get the exact interpolation of the local activation time (LAT) over the atrial geometries.

6. Correlating the atrial activities temporally with the CS signals

Since the electrodes in the CS remain stationary throughout the recording, therefore it is used as the reference. The selection of the reference electrode was done from the available CS catheter electrodes.

7. Removing the geometrical artefacts if present

Sometimes the recorded geometry has spatial artefacts that had to be removed during preprocessing stages.

All the above stated steps were done to get the relevant signals to be used for further analysis. The filtering frequencies used for the unipolar and the bipolar recorded signals have already been explained in chapter 6. This chapter deals with valve cutting, coverage map generation, the geometrical artefact removal, reliability check for spatial locations, refinement of the geometry and the morphological correlation between unipolar and bipolar electrograms.

7.1 Valve Cutting

The EAM system provides a feature which allows the user to mark or annotate various regions on the mapped geometries. This can be done after mapping and before exporting the data from the system. This feature was used to manually assign the various markers on the atrial geometry. This part of analysis was done in collaboration with Dr.-Ing. Tobias

Oesterlein. After marking the various regions, the data were imported from the clinical system and analysed using MATLAB (version *MATLAB_R2016b*). Figure 7.1a, represents the annotated regions as *LSPVcut*, *RSPVcut*, *MVcut* and *RIPVcut*.

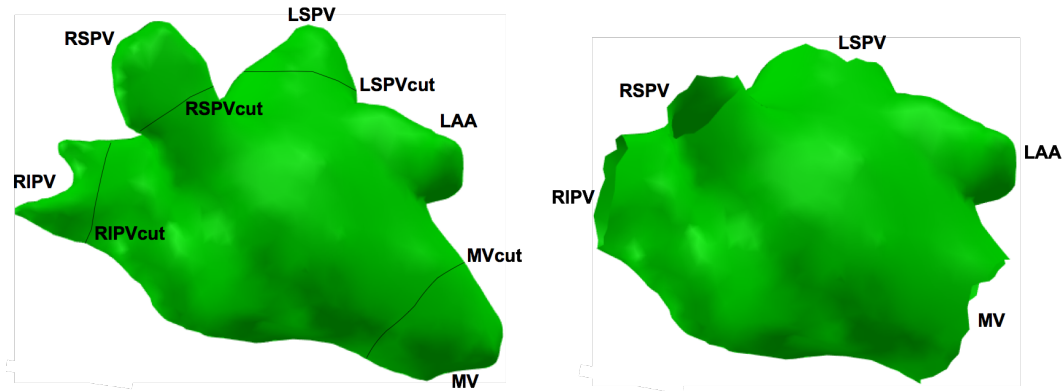


Figure 7.1: a) The electroanatomical geometry with the cut marked on various regions. b) Geometry obtained after valve cut. RIPV- right inferior pulmonary vein, RSPV- right superior pulmonary vein, LSPV- left superior pulmonary vein, LIPV- left inferior pulmonary vein, MV- mitral valve

The manual selection of these regions (only) was done specifically because our analysis was to be done for the endocardial activities inside the atrium. These marked points were used to then separate the PV and the MV regions and to get the geometry as represented in Figure 7.1b. If compared the coverage region between the two geometries (with valve and without valve), it was achieved that all the points with electrograms have a coverage of 99.5%. This coverage map generation is explained in the next section.

7.2 Coverage Map

Once the EAM was done and the data were exported from clinic, the next stage of analysis was done using the spatiotemporal information. The spatial locations and geometries were recorded with respect to a reference location. As the catheter moves inside the geometry, with respect to the reference catheter, the recording catheters moving inside the atrium generate the geometry that is reflected on the screen. Marking various regions the valve cut was done as explained above. At various locations in space, the electrograms were also recorded at a sampling rate of 2.034kHz .

The spatial locations at which the electrograms were obtained using the catheters stable positions were termed as the recorded locations. These locations were then used to compute the coverage map. This was done using the area around each recorded location that was obtained from the moving catheter. Once that was done, the percentage of the net spatial coverage by the catheter inside the endocardium was estimated. The accessibility inside the atrium was also dependent on the type of the catheters used and its (catheters) accessibility

inside the atrium. Depending on these two factors (type of catheters and their accessibility), the coverage map was generated. To generate the coverage map both plays an important role, but to get the coverage map, the acquired points locations were used. The various stable catheter locations are represented in Figure 9.15 to Figure 9.20.

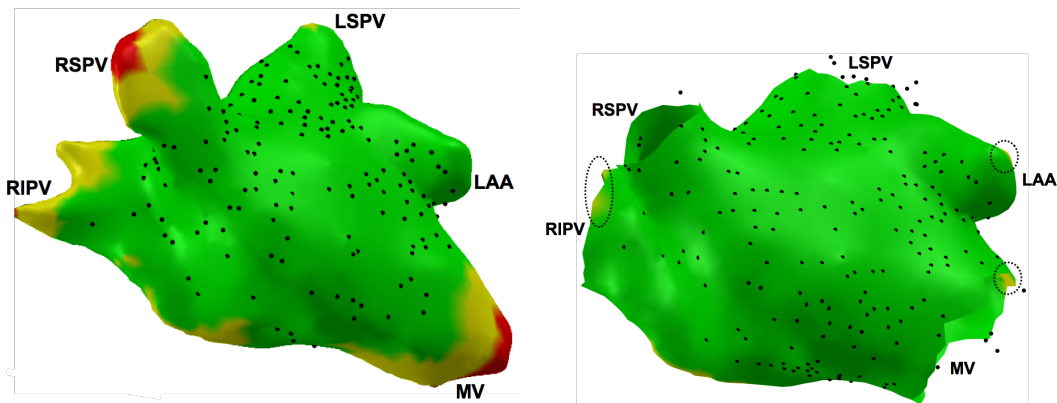


Figure 7.2: Coverage map for the clinical case mapped using 10 pole LASSO catheter. a) Geometry without valve cut. b) Coverage map of the geometry after valve cut.

In order to interpolate the coverage map, the radii around each recorded location was taken into consideration. The nodes on the triangular mesh (making up the geometry) within 5 mm were interpolated as green, from 5 mm to 10 mm were interpolated as yellow and above 10 mm as red. Figure 7.2a, represents the geometry before valve cut. All the recorded locations are represented by black dots. As stated above, the interpolation was done and the coverage map was generated. It can be seen clearly that the entire recording was concentrated to the region inside the atrial chamber as compared to the region within veins. Figure 7.2b represents the interpolation after valve cut. It can be observed that after valve cut all the recorded locations were in the region of interest. The region having least number of recorded locations (marked manually) were removed. A coverage of 99.5% was achieved. The encircled region is the one, where compared to green region less denser recordings were done. The posterior and anterior view of this clinical case is represented later in Figure 14.2.

Thus, it can be stated that with the coverage map the information about the area that the catheter moves in during the recording can be obtained. This map takes all the physician selected (manually) recording points (called as recorded locations) to represent the resolution in various atrial regions.

7.3 Artefact Removal

In the clinical recordings, the spatiotemporal information was obtained and analysed. As observed during the research, the artefacts could be present in the temporal (in electrograms)

or in the spatial (in geometry) form. The artefacts in the electrograms can be regarded as the presence of various unwanted frequency components, which could be present at any level of the recording. These could be because of poor contact, the baseline wander, 50Hz or 60Hz noise, power-line hum, high or low frequency noise, jitters or motion artefacts. The geometrical artefacts were because of wrong estimation of the spatial locations. These could be because of wrong connections, interference between various electrodes, or may be because of incorrect recorded locations. Also the movement of the patients and the changes in the reference catheter positions contribute to the artefacts.

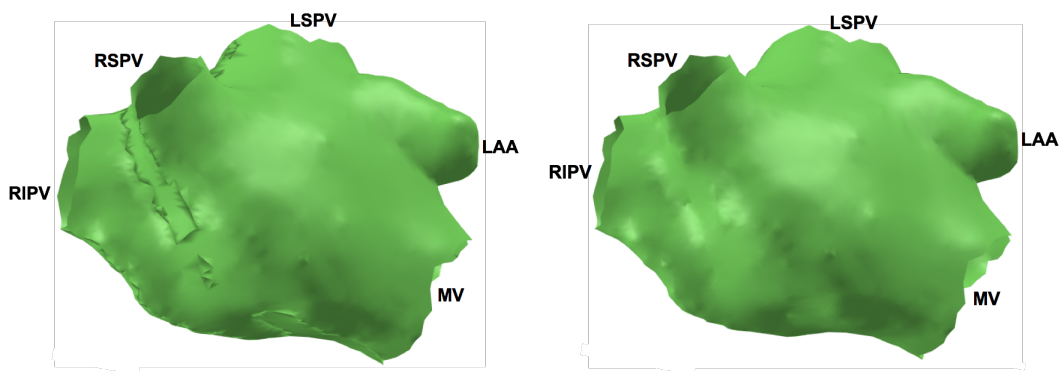


Figure 7.3: The artefacts in clinical cases resulted into the change in normal (perpendicular to the respective triangular face) direction vector in terms of the surface normals. a) Geometry with artefact in terms of surface normal orientation. b) Geometry with surface normal artefact removed.

In electrograms, the artefact removal was done using the signal processing tools such as filters. In this section, the geometrical artefacts are detailed for the cases as represented in Figure 7.3 and Figure 7.4. While generating the clinical geometry or while performing any operation and analysis on the triangular mesh of the geometry it was important to take care of the surface normal. It should be in the outward direction to get a regular geometry. It can be observed that in Figure 7.3a, the distortion in the geometry is present. This was because the surface normals were pointing in the inward direction in the artefact region. These artefacts were obtained while introducing new nodes and faces to the existing triangular geometry. For the original geometry all the normals were pointing outwards so the estimated triangular mesh introduced should also be pointing outwards. These type of geometrical artefacts are not recorded from the system but could appear at any stage of processing. These can be corrected using the blender software or MATLAB. These artefacts were removed and the corrected geometry with all the surface normals pointing outwards are represented in Figure 7.3b.

Figure 7.4 represents the other type of geometrical artefacts (due to incorrect recording) giving realistically false geometry. In this case, one of the recorded location was mapped at a location represented by a notch inside the geometry. The triangular mesh obtained also involved this point in the geometry construction, and therefore, the artefact was obtained.

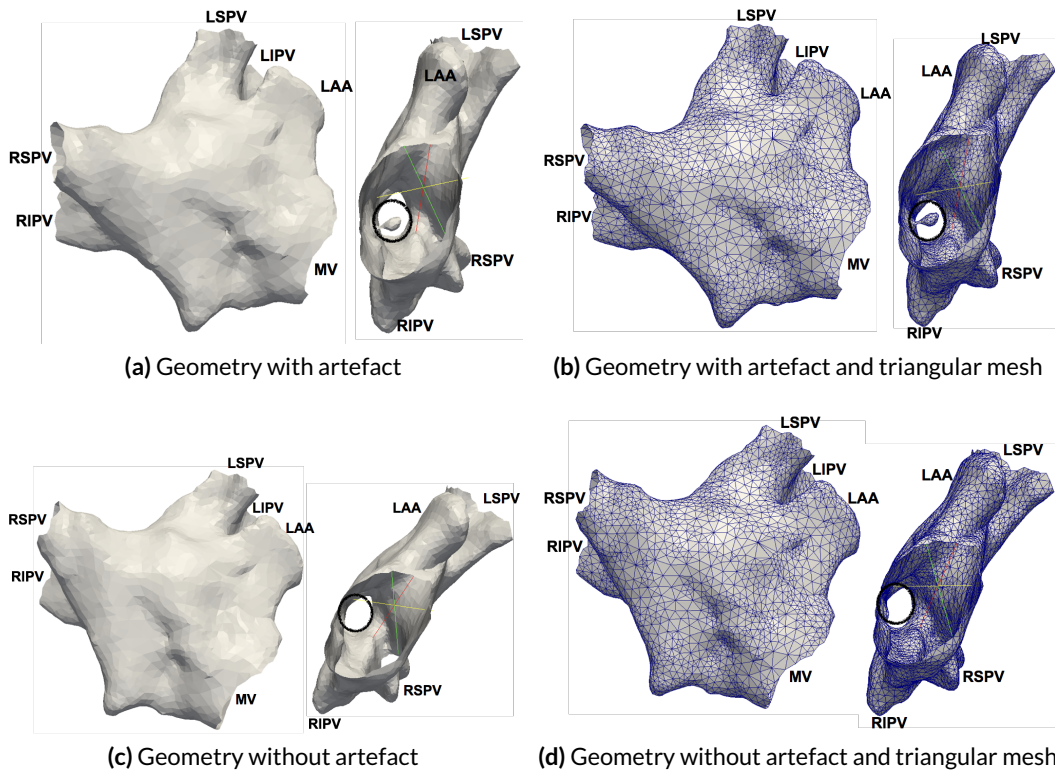


Figure 7.4: Representation of the geometrical artefact (encircled) on one of the clinical case. The presence of the geometrical artefact does account to the triangular mesh as represented.

Figure 7.4 *a* and *b* represents the clinically obtained geometry with and without triangular mesh. This type of geometrical artefacts were removed by deleting the extra recorded locations. This could also done using the blender software during preprocessing. After discarding the realistically false locations, the geometry was retrieved as represented in Figure 7.4 *c* and *d*.

The geometrical artefacts were observed only in one out of the 6 available clinical cases. But this analysis and these observations clearly represented the possibilities to be taken care of during the preprocessing stage for 3D spatiotemporal data analysis.

7.4 Spatial Analysis

As explained in chapter 6, it is possible to extract the electrograms using various types of catheters along with their spatial locations. The EAM system can record the raw as well as filtered unipolar and bipolar intracardiac electrograms along with the CS catheter signals and the *ECG* signals. These recording instants are manually selected by the physicians. The spatial locations are crucial information (similar to the electrograms), since they provide the site of activation on the 3D geometry. This is an extremely important information for

estimation of other parameters such as conduction velocity (CV), which can thereafter be used for analysing the depolarisation propagation pathway. This section deals with the analysis done to find the correlation between the various spatial locations obtained from the mapping system. Doing location specific analysis it is possible to determine the spatial heterogeneity and to dig into the effect of curvature of the atrium.

Along with the electrogram information, the spatial information was also extracted from the mapping system as *rovtracexyz*, *surfxyz* and as *location.csv* file. The triangular mesh information were saved as the *surfxyz* coordinates. The locations of the bipolar electrograms can be extracted from the *rovtracexyz* or from the *location.csv* file. As explained in section 6.1.6, the segment data and the physician selected points (1 *second* to 5 *second* electrogram) are to be extracted from the data set (of up to 4 hour long recording). These 1 *second* to 5 *second* recording segments are termed as the segment data. *Rovtraces* represents the location at which the electrograms were recorded. While the *location.csv* gives the various points on the 3D geometry which were recorded when the physician selects the segment. The analysis was to mathematically correlate the two locations using least square transformation. An attempt was made to find the fit between the available spatial coordinates.

A decision had to be made on the spatial location. This was done to find if the locations could be correlated for further analysis or not. The locations from the *rovtracexyz* and the *location.csv* files were taken as the independent and dependent variables respectively and the constants were calculated. The constants calculated from one set of coordinates were used with the other set of coordinates to benchmark them and to find if the two coordinates fit or not.

$$IndependentVariable = \begin{bmatrix} x_1 & y_1 & z_1 \\ x_2 & y_2 & z_2 \\ \dots & \dots & \dots \\ x_n & y_n & z_n \end{bmatrix}$$

$$DependentVariable = \begin{bmatrix} X_1 & Y_1 & Z_1 \\ X_2 & Y_2 & Z_2 \\ \dots & \dots & \dots \\ X_n & Y_n & Z_n \end{bmatrix}$$

The solution for X , Y and Z for 3D space would be

$$X = \sum_{i=1}^n X_i = a \sum x_i + b \sum y_i + c \sum z_i + nt_x \quad (7.1)$$

$$Y = \sum_{i=1}^n Y_i = d \sum x_i + e \sum y_i + f \sum z_i + nt_y \quad (7.2)$$

$$Z = \sum_{i=1}^n Z_i = g \sum x_i + h \sum y_i + i \sum z_i + nt_z \quad (7.3)$$

Solving these expressions for one coordinate at a time, in order to get the constants a to i as specified in the expression above.

$$X = ax + by + cz + t_x \quad (7.4)$$

$$e = X - ax - by - cz - t_x \quad (7.5)$$

$$e^2 = (X - ax - by - cz - t_x)^2 \quad (7.6)$$

where e is the error. The differentiation with respect to all the constants separately gives us the following expressions

$$\frac{\sum e^2}{da} = 2 \sum (X - ax - by - cz - t_x)(+x) = 0 \quad (7.7)$$

$$\sum Xx - a \sum x^2 - b \sum xy - c \sum xz - t_x \sum x = 0 \quad (7.8)$$

$$\frac{\sum e^2}{db} = 2 \sum (X - ax - by - cz - t_x)(+y) = 0 \quad (7.9)$$

$$\sum Xy - a \sum xy - b \sum y^2 - c \sum yz - t_x \sum y = 0 \quad (7.10)$$

$$\frac{\sum e^2}{dc} = 2 \sum (X - ax - by - cz - t_x)(+z) = 0 \quad (7.11)$$

$$\sum Xz - a \sum xz - b \sum yz - c \sum z^2 - t_x \sum z = 0 \quad (7.12)$$

$$\frac{\sum e^2}{dt_x} = 2 \sum (X - ax - by - cz - t_x)(1) = 0 \quad (7.13)$$

$$\sum X - a \sum x - b \sum y - c \sum z - nt_x = 0 \quad (7.14)$$

Using the above stated equations and expressions, we obtained

$$\sum Xx = a \sum x^2 + b \sum xy + c \sum xz + t_x \sum x \quad (7.15)$$

$$\sum Xy = a \sum xy + b \sum y^2 + c \sum yz + t_x \sum y \quad (7.16)$$

$$\sum Xz = a \sum xz + b \sum yz + c \sum z^2 + t_x \sum z \quad (7.17)$$

$$\sum X = a \sum x + b \sum y + c \sum z + nt_x \quad (7.18)$$

Collectively these could be represented as,

$$\begin{bmatrix} \Sigma Xx \\ \Sigma Xy \\ \Sigma Xz \\ \Sigma X \end{bmatrix} = \begin{bmatrix} \Sigma x^2 & \Sigma xy & \Sigma xz & \Sigma x \\ \Sigma xy & \Sigma y^2 & \Sigma yz & \Sigma y \\ \Sigma xz & \Sigma yz & \Sigma z^2 & \Sigma z \\ \Sigma x & \Sigma y & \Sigma z & n \end{bmatrix} \cdot \begin{bmatrix} a \\ b \\ c \\ t_x \end{bmatrix}$$

Similarly, calculating for Y and Z coordinates

$$\begin{bmatrix} \Sigma Yx \\ \Sigma Yy \\ \Sigma Yz \\ \Sigma Y \end{bmatrix} = \begin{bmatrix} \Sigma x^2 & \Sigma xy & \Sigma xz & \Sigma x \\ \Sigma xy & \Sigma y^2 & \Sigma yz & \Sigma y \\ \Sigma xz & \Sigma yz & \Sigma z^2 & \Sigma z \\ \Sigma x & \Sigma y & \Sigma z & n \end{bmatrix} \cdot \begin{bmatrix} d \\ e \\ f \\ t_y \end{bmatrix}$$

and,

$$\begin{bmatrix} \Sigma Zx \\ \Sigma Zy \\ \Sigma Zz \\ \Sigma Z \end{bmatrix} = \begin{bmatrix} \Sigma x^2 & \Sigma xy & \Sigma xz & \Sigma x \\ \Sigma xy & \Sigma y^2 & \Sigma yz & \Sigma y \\ \Sigma xz & \Sigma yz & \Sigma z^2 & \Sigma z \\ \Sigma x & \Sigma y & \Sigma z & n \end{bmatrix} \cdot \begin{bmatrix} g \\ h \\ i \\ t_z \end{bmatrix}$$

Solving these we get the constants as,

$$Constants = \begin{bmatrix} a & b & c & t_x \\ d & e & f & t_y \\ g & h & i & t_z \\ 0 & 0 & 0 & 1 \end{bmatrix}$$

The importance of this study was to determine the reliability of the location information obtained from the electroanatomical system. The results obtained from this comparison are represented and discussed in section 14.2. These location information were later used during the regional analysis along with the other statistical parameters. Spatial and temporal information are most important to find the curvature of the different regions on the atrium and to find the statistical parameters such as CV.

7.5 Triangular Mesh Refinement

From the electroanatomical mapping system the clinical geometries were obtained as triangular mesh. The relative position of the catheter movement inside the atrium is also mapped with respect to reference location. The vertices of the triangular meshes were sparsely mapped with a median distance between the vertices of the triangular mesh to be around

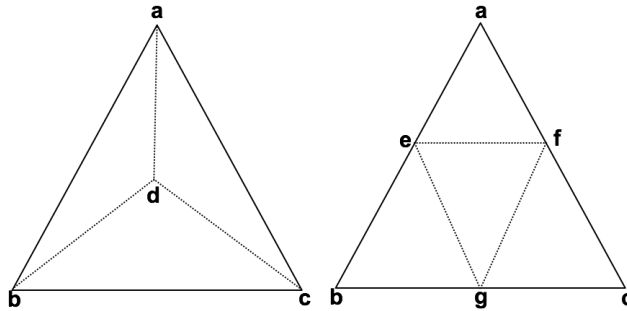


Figure 7.5: Illustration of introducing a new node for mesh refinement. a, b and c are the vertices of the triangular mesh. The centroid of the triangle is represented by point d , while e, f and g are the centre of the respective edge of the triangle. a) Refinement method 1, in which the centroid of individual triangle is added to the mesh. b) 3 new points (centre of each edge) are included as the new nodes and the mesh is refined adding them to the existing mesh.

1 *mm* as represented in the boxplot 1 of Figure 14.5d.

During this research, the CV estimation was done using the clinical geometries along with the simulated LAT. The estimate was also done with clinical geometry and the LAT parameter obtained from the intracardiac electrograms respectively. To get a smooth propagation over the triangulated surface a refined mesh was required. The propagation of the depolarisation wavefront in simulated environment is a discrete phenomenon. Denser the triangular mesh forming the geometry, more smooth the propagation would be. Therefore, a successful attempt was made to make the available triangular mesh more dense by including new points in the existing triangular mesh. This process is referred to as the mesh refinement.

In this section, the mesh refinement method was used to get a finer mesh on the atrial surface geometry is explained. A number of new points were included in the existing mesh so as to get a dense geometry. A couple of iterations were done to reach up to 0.2 *mm* median distance between the vertices of the triangular mesh. The value of 0.2 *mm* was arbitrarily defined as a threshold distance used during the mesh refinement. The triangular mesh refinement made it possible to get the distance between various nodes giving a better approximation of the curvature in various regions of the atrial geometry. This gives a possibility to get a clearer interpolation of the depolarisation propagation pathway over the geometry. As represented in Figure 7.5, there are two different ways used for the mesh refinement namely

1. Taking the centroid and introducing it as a new vertex in the triangular mesh. With this only one node per iteration is added to each triangular face.
2. Taking the centre of each edge and introducing three nodes to the existing face of the triangular mesh. With this three nodes are added to each face of the mesh.

Using both the above stated ways the refinement was done. The distance between two arbitrary nodes of the mesh were estimated using Dijkstra shortest path algorithm as represented in Figure 7.6. Method 2 (introducing the centre of each edge as a new node) gave the better distance over the curvature including the intermediate nodes as compared to the one obtained using Method 1 (introducing the centroid as a new node).

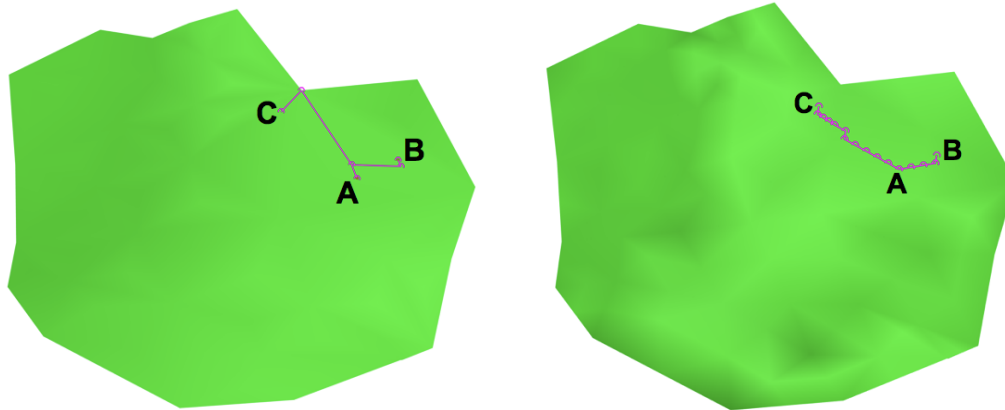


Figure 7.6: As represented in Figure 7.5 there are two ways to include the new nodes to the existing mesh represented on arbitrarily selected atrial patch. This is the illustration of the results obtained after using both the methods. a) Dijkstra shortest path obtained after using the nodes introduced using method 1 (introducing the centroid as a new node) to go from A to B and A to C. b) Dijkstra shortest path obtained after using the nodes introduced using method 2 (introducing the centre of each edge as a new node) to go from A to B and A to C.

During the course of this research, with every iteration (refinement) three new nodes (being the centre of each edge) are included. This was done till the edge length became $< 0.2\text{mm}$ throughout the geometry. Up to 5 iterations were done to achieve this. Since introducing three nodes per iteration (using the centre of each edge) gave better approximation for the distances between the nodes. Therefore, this method of refinement was used throughout the research. The refined mesh was used in 2 applications namely

1. In the simulation environment where the triangular mesh of the geometries were required for LAT evaluation, the refinement was done until the surface points were in the proximity of 0.2mm from the triangular nodes. This was done to bring the surface points (represented by red dots in Figure 7.6) close to the triangular mesh.
2. For the clinical study of CV estimation, the refinement of the triangular mesh was done after including the surface points to the triangular mesh. The refined geometries were also used with the simulation environment to benchmark the CV estimation method. In this method the surface points (marked as red in Figure 7.6) are included in the geometry and then the refinement was done.

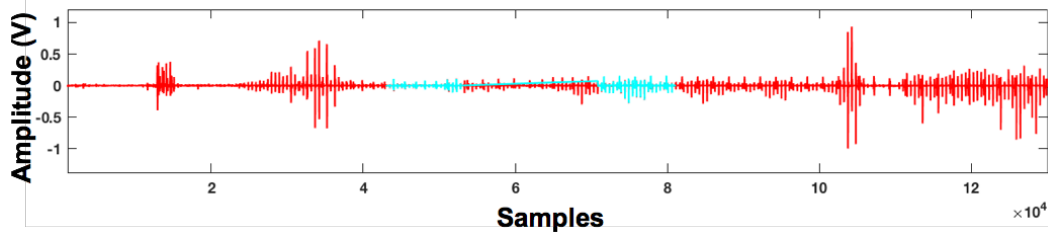


Figure 7.7: Representation of the recorded segment (selected by the physician) superimposed on a 60 second long segment. Red represents the recorded segment and blue represents the physician selected segments.

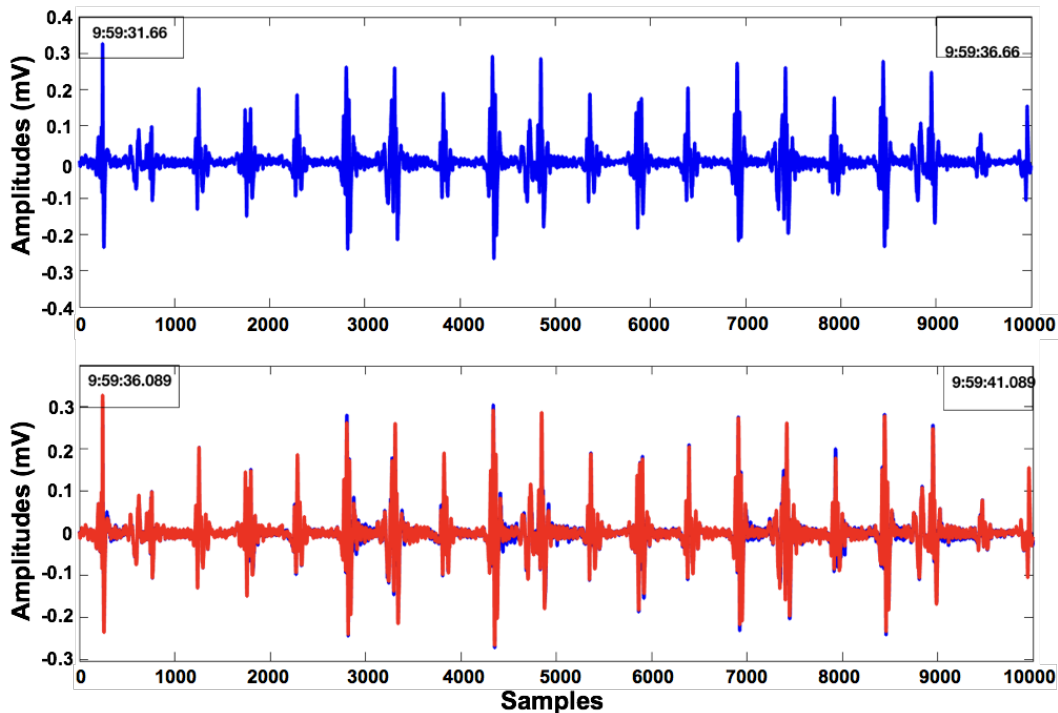


Figure 7.8: Illustration of offset in the segment compared to entire data

The results of mesh refinement are discussed and represented in section 14.4.

7.6 Morphological Correlation between Segment Data and Rovtraces

During the procedure, the recording was done for a couple of hours and the data were collected. From this data, the physician selected segments were extracted using the temporal information. These selected segments were then correlated with each other to find (if there exist any) offset between them in terms of temporal existence. This was done since the

selected segment was later on used for the time and frequency domain analysis. This section deals with the morphological correlation estimation between the segments obtained from the temporal locations selected by the physicians and their existence in the entire dataset. Since the same segment was found from the dataset using temporal information, therefore, using morphological correlation estimation information the offset in time between the two was estimated. Mathematically, the morphological correlation between A and B is defined as

$$\rho = \frac{1}{N-1} \sum_{i=1}^N \left(\frac{A_i - \mu_A}{\sigma_A} \right) \left(\frac{B_i - \mu_B}{\sigma_B} \right) \quad (7.19)$$

where N is the number of scalar observations, μ_A is the mean of A , σ_A is the standard deviation of A , μ_B is the mean of B and σ_B is the standard deviation of B .

The morphological correlation coefficient was calculated to know the linear dependencies between the variables and to find the offset introduced when the mapping was done using *rovtraces* as well as segments.

Figure 7.7 represents a 60second segment, which contains two physician selected segments of 5second each. These segments were found using the time and the correlation coefficients. Figure 7.8 represents that the exact 5second segment found in the recorded dataset with a correlation coefficient of up to 100%. But as represented there existed an offset in time of 4.4seconds. Therefore, it was important to correlate the segments with offset value while segregating them from the entire data set.

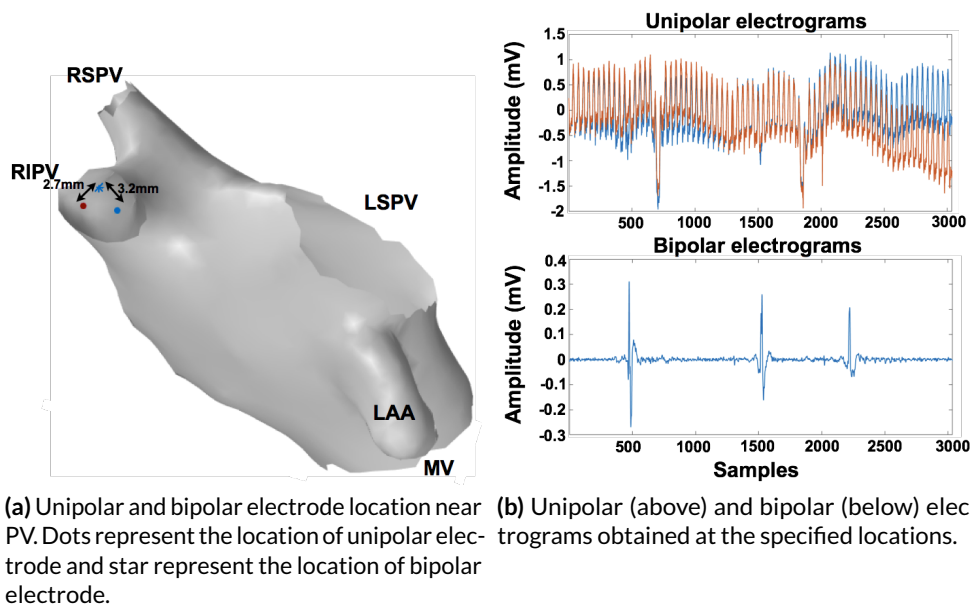
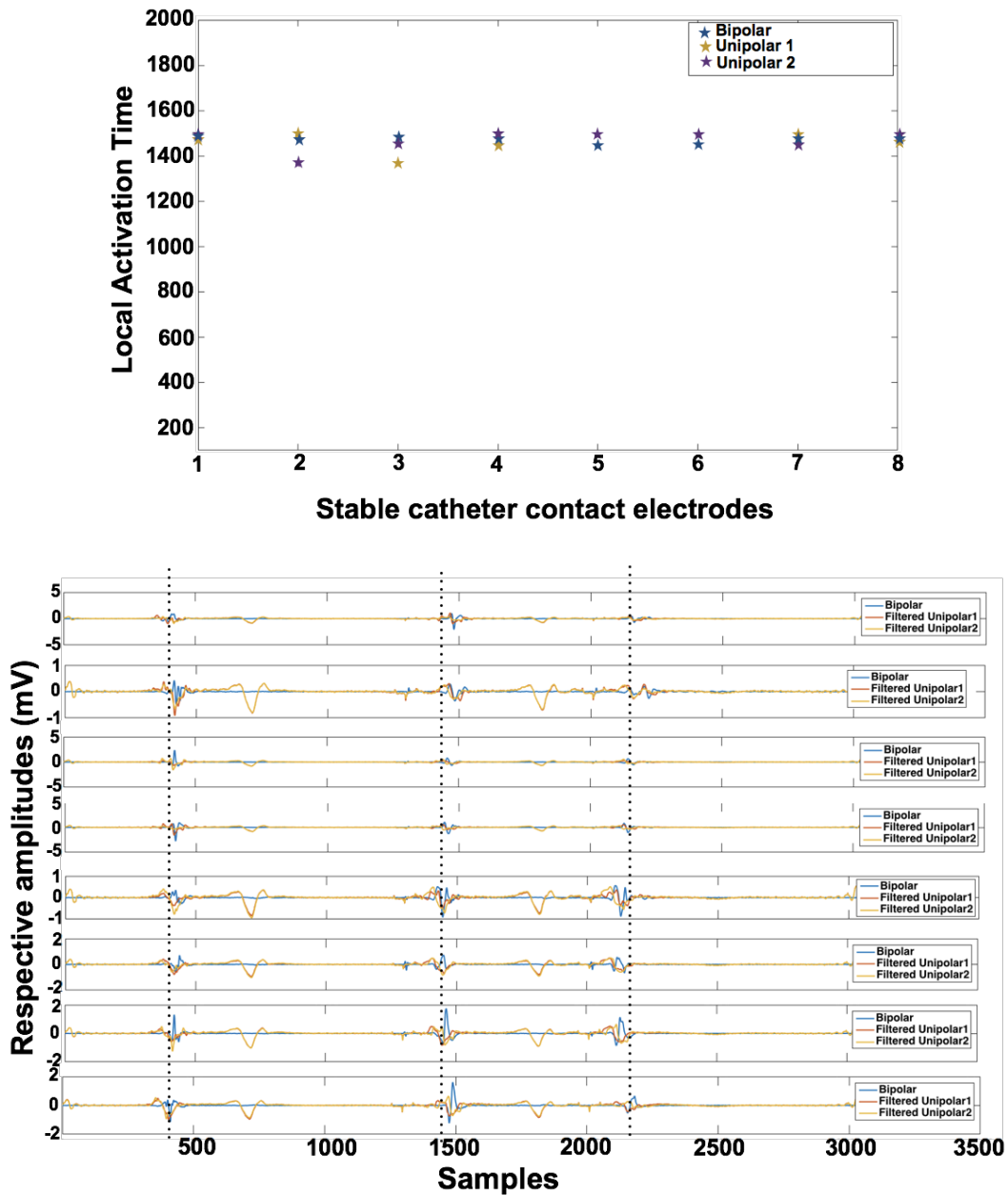


Figure 7.9: Illustration of unipolar electrode and bipolar electrode locations and their temporal information.



(a) For the stable catheter position unipolar and bipolar electrograms giving the LAT at a close proximity marked by dashed lines.

Figure 7.10: Illustration of unipolar electrode and bipolar electrode locations and their temporal information.

7.7 Location of Unipolar and Bipolar Electrograms

The location of the unipolar and bipolar electrograms were obtained from the mapping system. An effort was made to find the distance between the two locations as represented in Figure 7.9. Figure 7.9a represents the unipolar and bipolar electrogram recording at a

location near the pulmonary vein. For one stable catheter position, the unipolar and bipolar distances for all 8 bipolar contact electrode are represented in Figure 7.10a. This shows that the recording location of bipolar signals are in close proximity of 1 mm to 5 mm to the unipolar electrode location. Also in Figure 7.10b, it can be clearly seen that the activation complexes of bipolar and unipolar electrograms have the LAT at the same temporal and spatial locations.

Stimulus Protocol

The human heart beat is triggered by the specialised cells together making the sino-atrial node (SN) at a regular rate of $60bpm$ to $100bpm$ without any external stimulus. Stimulation is the process of applying an external trigger (called stimulus or stimuli) at any location on the heart. The stimulus can be given by providing some energy to electrodes in contact with the endocardium. The depolarisation wavefront initiated from this triggering point thereafter travels over the entire atrium. The time and rate of stimulation also affects the heart contraction. The stimulus protocol used for pacing within the clinical cases under consideration, is a special clinical protocol and is applied from a catheter positioned in the coronary sinus (CS) artery. A small amount of stimulation was done during recording using the pacing protocol in the clinical cases under consideration keeping the safety measures into account. The energy given as the stimulation to the cardiac tissue is defined by the strength-duration curve as explained in section 2.6. The next section explains the stimulus protocol used with the clinical data.

A study by Alessie et al. [74] states that if a rapid pacing stimulation is continued for a longer period in time (around 2 to 3 weeks), it can result into persistent fibrillation. During the course of this thesis, the second type of experimental data was obtained by pacing the canine heart for 6 weeks as explained in chapter 12.

8.1 Stimulus Protocol used with the Clinical Cases

In the course of this thesis, four clinical cases mapped during stimulation were recorded during the routine clinical procedure and were mapped using the EnSite Velocity electroanatomical mapping (EAM) systems with written informed consent of the patients. All the four cases are represented in Figure 8.1. These clinical cases were paced with the special pacing protocol. The stars in Figure 8.1 represent the approximate location from where the depolarisation activity started in the left atrium (LA). Yellow star indicates the location for

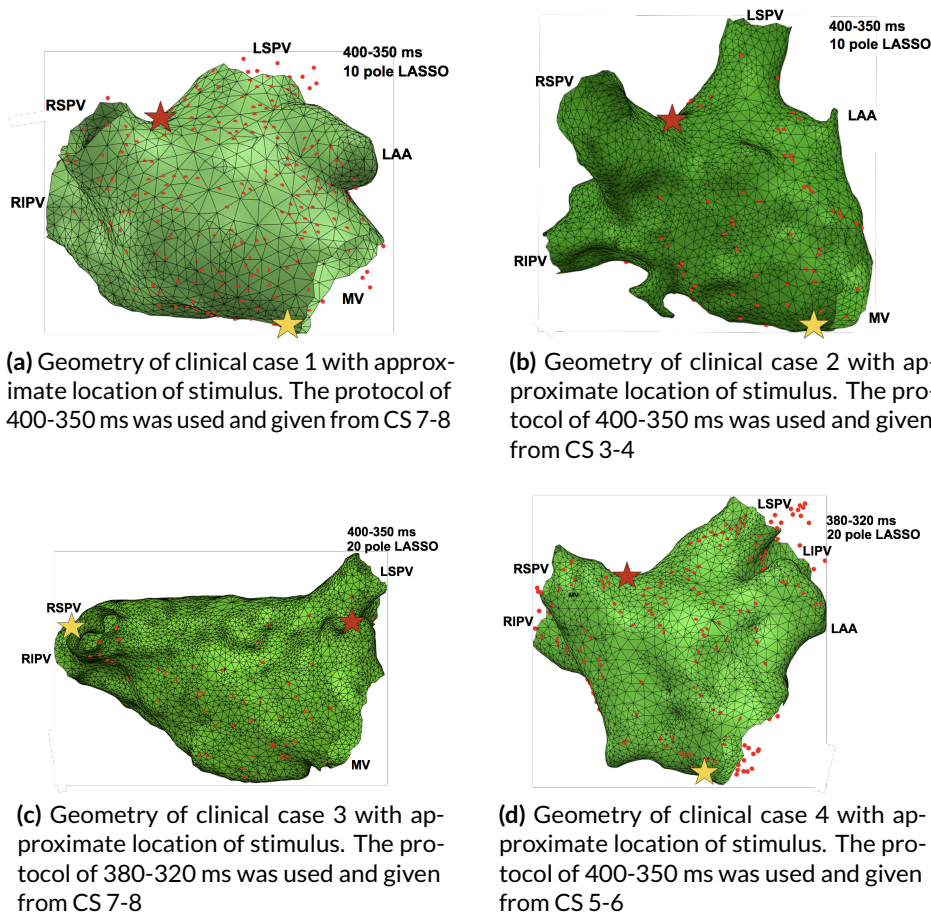


Figure 8.1: Clinical geometries with approximate location of stimulus. These were stimulated using the 400- 350 ms and 380- 320 ms stimulus protocol respectively. Red star represents the approximate location from where the sinus triggered activity enters in LA and yellow star represents the approximate location from where the stimulus was applied using CS catheter electrodes.

CS triggered activities and red star indicates the location near Bachmann bundle (BB) from where the depolarisation wavefront entered the LA during sinus rhythm (SR). The stimulus trigger of these cases were given using the CS catheter. In all the four clinical cases, two stimuli were given always after the SR and at the approximate same location. These stimuli were regarded as $S1$ and $S2$ stimuli. The used stimulus protocol was given at a basic cycle length of 400ms, 350ms, 380ms and 320ms depending on the type of stimulation protocol. The annotation SN is used for the regular depolarisation wavefront initiated from the SN in right atrium. In 3 clinical cases, the basic cycle length of 400ms and 350ms for $SN - S1$ and $S1 - S2$ was chosen respectively. For the fourth clinical case, the basic cycle length was 380ms and 320ms for $SN - S1$ and $S1 - S2$ activities respectively. The signals obtained from the CS catheter containing the three activities are represented in Figure 8.2. For all the 4 clinical cases, the depolarisation propagation resulting from the SN node and from stimulus trigger have been studied and analysed separately. The recording has been done

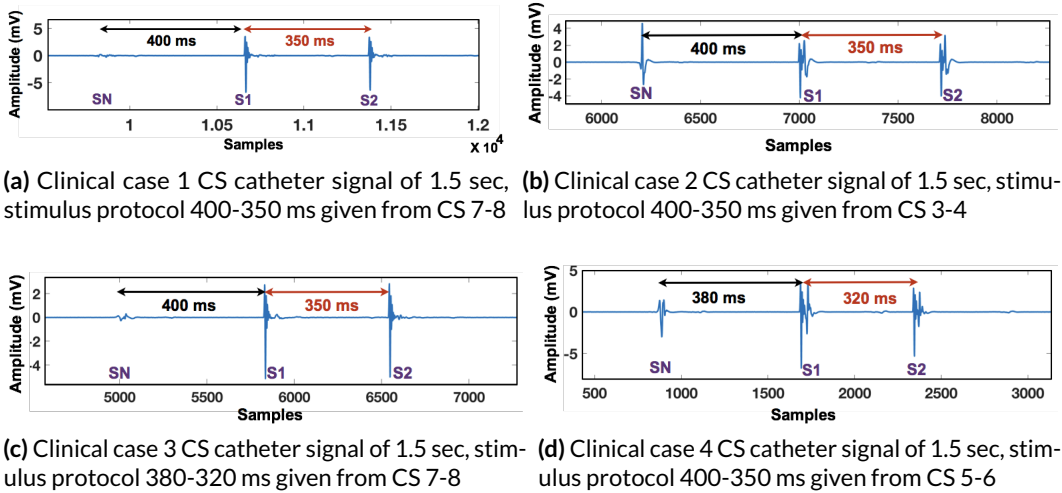


Figure 8.2: CS catheter electrograms used as reference. Also the time course of each stimulation protocol can be seen. Sampling frequency was 2.034 kHz

during the SR and is explained in the next section.

8.2 Analysis of Stimulus Protocol Data

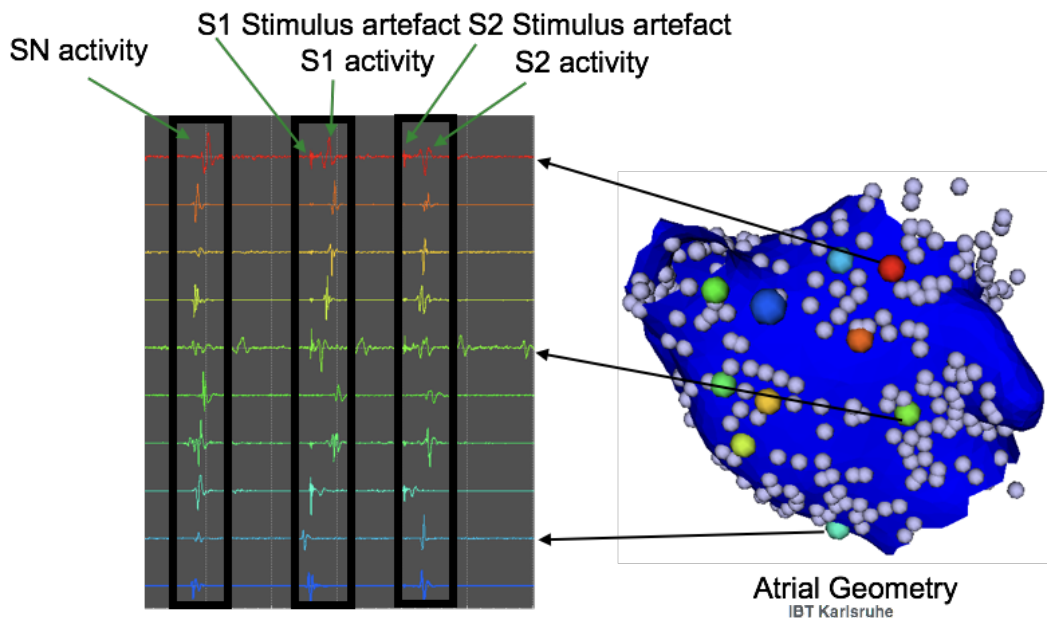


Figure 8.3: Atrial electrograms at different locations. CS catheter used for temporal alignment. All the stimulus artefacts can be seen aligned to each other [75].

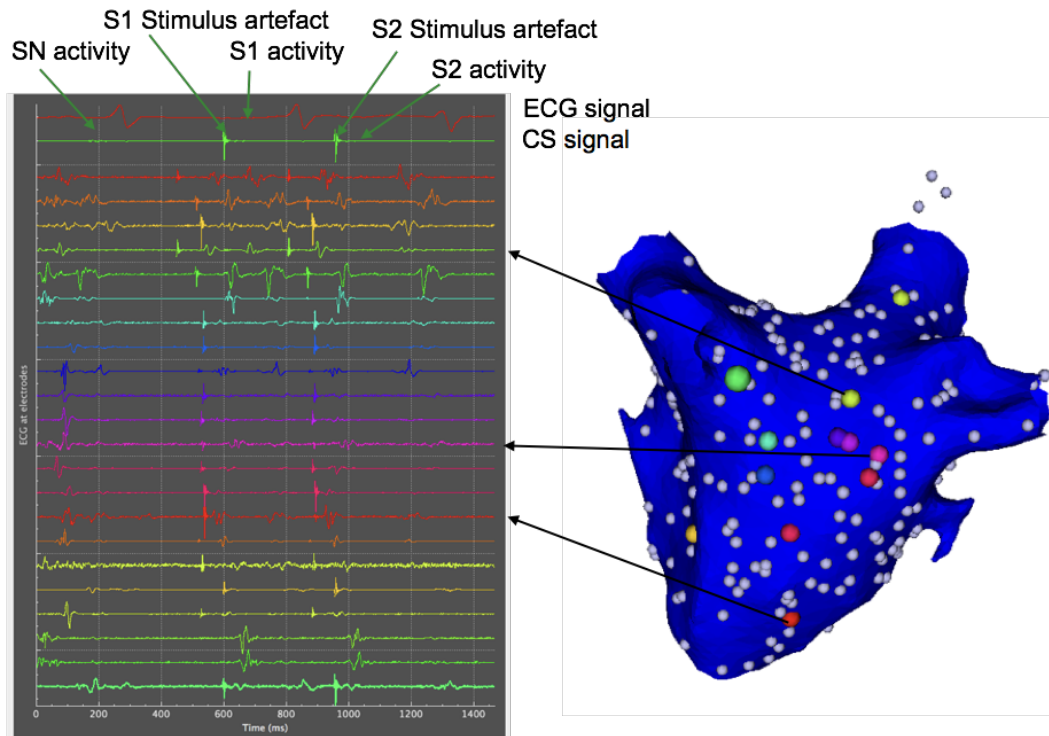
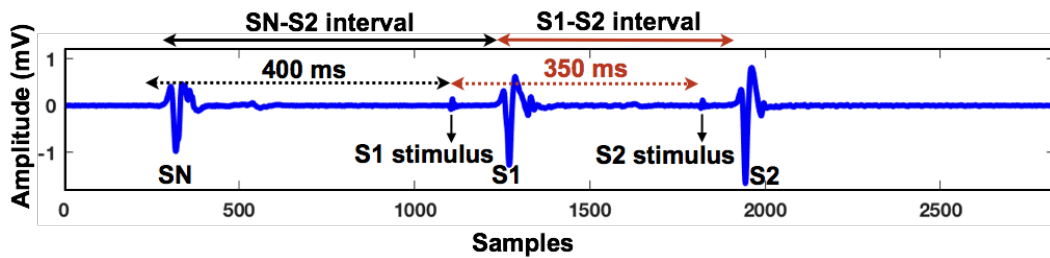


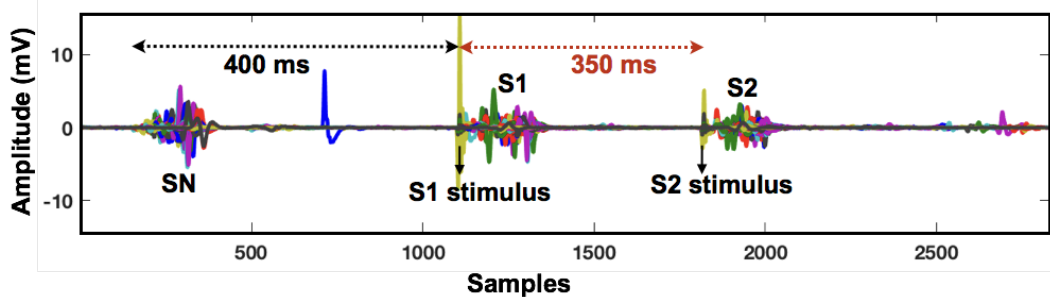
Figure 8.4: Atrial electrograms at different locations, CS catheter used for temporal alignment. All the stimulus artefacts are not aligned in this case since the offset was large [75].

As explained above, the electrograms containing the atrial activities corresponding to SR and the stimulus trigger, were acquired at various locations while mapping the endocardium. Figure 8.3 and Figure 8.4 represent the 1.5 *second* long electrograms at the selected locations for two clinical cases. The pacing protocol was such that every stimulus appeared after the SN activity as annotated. It can be clearly observed in Figure 8.3 and Figure 8.4, that at every location three activities were obtained because of the depolarisation wavefront starting from the SN node and twice because of stimulus applied from the CS catheter. These activities might or might not be aligned with the CS catheter. At the initial stage the segment selection was done. Using the CS catheter signals, the alignment of the activities was done, taking the activity in the CS catheter as reference and the stimulus artefact to be at the same temporal instant. This was done to get the correct estimation of the LAT at each location with respect to the triggering time. Later on these LAT were used for depolarisation wavefront CV estimation. The various annotations on the atrial electrograms were as represented in Figure 8.5. Overlapping the electrograms on one another yields the temporal separation between all the three activities as represented in Figure 8.5*b*. There is a considerable time difference between all the three activities due to different distances between the electrodes.

After aligning the activities and generating the histogram, the spread of LAT over the temporal axis was observed. Figure 8.6 represents the analysis for one of the clinical cases. Figure 8.6*a* represents the histogram for SN – S1 activities, a case in which the stimulus



(a) 1.5 second atrial electrogram from an arbitrary location



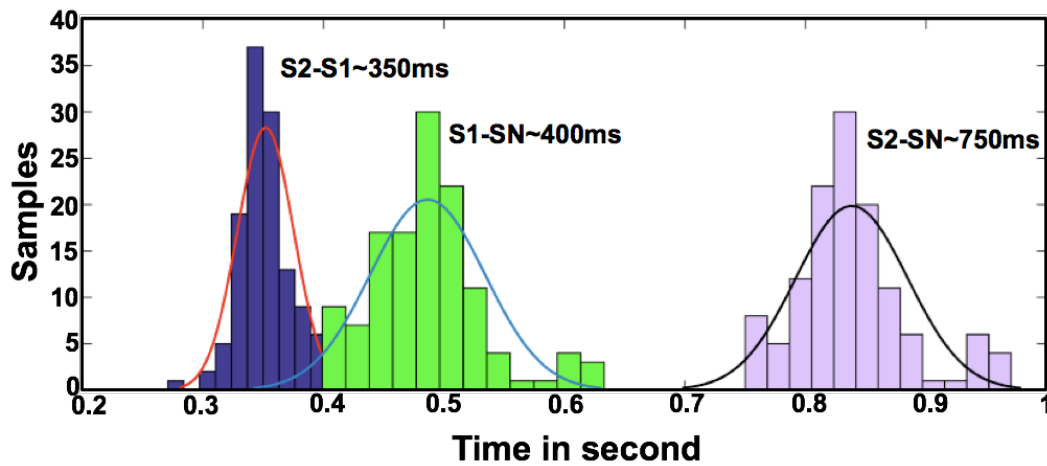
(b) Activities from various locations on heart superimposed on each other

Figure 8.5: Single 1.5 second atrial electrogram from an arbitrary location on the atrium representing the various activation complexes. Also when these activities are superimposed on each other it can be clearly observed that they are temporally apart from each other.

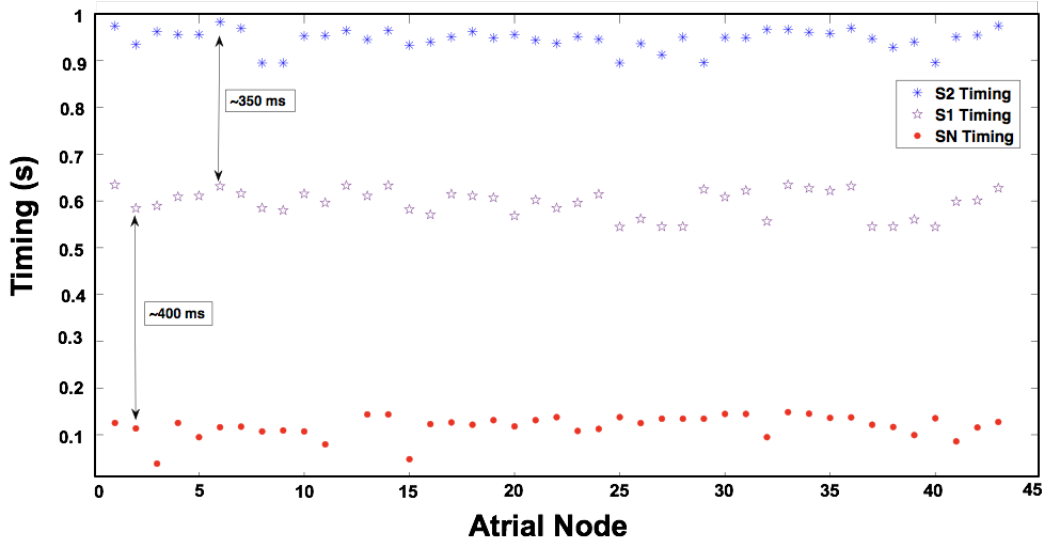
protocol was 400ms. Depending upon the location and wavefront propagation speed, the time taken by the excitation to reach a particular location is always different. Therefore the complexes were obtained around the temporal location of the stimulus. Since the $S1$ activity appeared after SN , and $S2$ activity appeared after $S1$, therefore, the LAT interpolation at all the locations are presented in Figure 8.6b, favouring the same. The data was processed and visualised in MATLAB.

An analysis was done to estimate the morphological correlation between the atrial activity complexes between $SN - S1$ and $S1 - S2$ complexes. The result of this analysis is explained and discussed in section 9.5 of this thesis.

As explained by Allesie et al. in his publication continuous pacing for around 3 weeks can induce permanent fibrillation in the cardiac tissue [74]. This effect has been analysed in the canine data. The canine data was obtained in the normal sinus rhythm and also after 3 weeks of continuous pacing until the heart fails. The electrograms from the canine data have been acquired using the triangular patch catheter and are explained in details in chapter 12 of this thesis.



(a) Histogram representation of the activity timing $SN - S1$, $S2 - S1$ and $S2 - SN$.



(b) The time at which each activity appeared in the 1.5 second segment

Figure 8.6: All the atrial activities appeared one after the other, which can also be observed clearly as represented in *a* and *b*.

Feature Determination

Chapter 6 gave a brief introduction of the clinical data recorded using the EnSite Velocity mapping system. As explained, the recorded intracardiac electrograms contain a lot of information which can be extracted using various signal processing techniques. Feature extraction is a term used to signify the process of extracting the functional or physiological information (as statistical parameters) out of the available data.

The various features extracted from the spatiotemporal information of the intracardiac electrograms can be used for marking the slow conducting regions, scar regions, unhealthy tissue, far fields etc. These features obtained as various electrophysiological parameters can make it easy to understand the various physiological and functional mechanisms of the atrium. The various statistical parameters were extracted, analysed and compared to reach to a final conclusion.

During the course of this research, the feature extraction was done for the data obtained using the EnSite Velocity mapping system and for the canine data obtained using the Unimap system. The various features extracted during this research are briefly demonstrated in the respective section.

9.1 QRS Complex Detection

ECG is the non-invasive procedure to obtain the cardiac activity information and can be acquired fast and easily. In case of emergency, it gives the best measure for decision making in case of heart abnormalities. Within the *ECG* signals, the *QRS* complex gives a good measure of cardiac activity by getting the first impression. The detection of *QRS* complexes is a very tedious job because of the presence of various types of artefacts such as noise, power-line interference, baseline wander or due to the high frequency characteristics that are similar to the *QRS* complexes [76].

The atrial and ventricular activities can be seen clearly in the *ECG* signals depending on the lead used. *QRS* complexes within the *ECG* signals are the most striking waveform present. These contain the three graphical deflections annotated as *Q*, *R* and *S*, corresponding to the depolarisation of the ventricles in human heart. It usually lasts from 0.06 *seconds* to 0.10 *seconds* in normal adult *ECG* trace. Any abnormality corresponding to slower conduction is reflected in the *ECG* signal by widening of the *QRS* complexes.

Alcaraz et al. did the classification of the persistent and paroxysmal atrial fibrillation (AFib), based in the *ECG* recordings [77]. The *QRS* count per minute is also related to the heart rate, and any increase in count is considered as Tachycardia. To obtain the feature called the *QRS* complex, the lead selection is the first step. Not all the leads can give relevant required information.

There exist a number of methods to mark and find the *QRS* complexes from the *ECG* signals. From the various techniques available for *QRS* detection which are based on the digital analysis of the *QRS* complex width, amplitude or slope, some of them are namely:

1. *R* peaks detection [78]
2. Steepest slope of the *R* wave [79]
3. First derivative based *QRS* complex determination [80]
4. Template matching [81]
5. Detection of *ECG* characteristics using wavelet transform [82]

These methods have their respective benefits and limitations at the same time. For example, for a proper *QRS* complex determination, the *R* wave steepest slope method would not be sufficient. Along with the steepest slope, it is required to get the other parameters such as amplitude, width and the *QRS* complex energy [83] [84]. A real time *QRS* complex detection method was proposed by Pan-Tompkin [85]. In this method the detection of *QRS* was done using an appropriate threshold and filtering. The *QRS* complex detector includes linear digital filtering, non linear transformation followed by the decision rule algorithm based on adaptive threshold. A refractory period of 200 *ms* was chosen before detecting the next complex.

In this thesis, the intracardiac atrial electrogram analysis was done. Therefore, it was required to identify the atrial components in the electrograms. The intracardiac signals have complexes corresponding to the atrial activities at the respective recorded location along with the far field effects that could account from ventricular activities or some other location. The various ventricular activities that are reflected in the electrograms (annotated as the far field) are to be removed. For ventricular far field (VFF) removal, the *ECG* signals are compared to the intracardiac signals on temporal basis. The *QRS* complexes in the *ECG* signals correspond to the ventricular activities. In the data recorded using the stimulus protocol stimulation, the VFF was removed by selecting a temporal window of 200 *ms* and using the first highest

peak (estimated using NLEO) after stimulus peak for estimating the atrial complex existence. While for the πCA method, the QRS detection was done using the wavelet based technique [86].

9.1.1 Wavelet Transform for QRS Detection

This work was done in collaboration with Dipl.-Ing. Gustavo Lenis and Dr.-Ing. Tobias Oesterlein. The QRS complexes were marked using the wavelet transform based analysis also called as wavelet transform based QRS detection technique [73] as explained in section 4.2. In this technique, the stationary wavelet transform based QRS detection was done and the well known Haar wavelet was used for decomposition.

$$Th(t) = k.MA\{|D_n(t)|\} \quad (9.1)$$

The absolute value of the detail coefficients $D_n(t)$ located at a frequency band of around $15 Hz$, were used for the QRS detection. An adaptive threshold was applied on the transformed signal. The time and signal dependent threshold was chosen to be a scaled version of a moving average of the transformed signal. In Equation (9.1), MA denotes the operator for the moving average. A variation of the scale parameter k of the threshold signal is run to find the QRS detection that minimised the variance of the duration of the RR intervals predicted.

The results corresponding to the QRS complex detection used for separating the VFF are represented in section 14.7 and section 14.9.

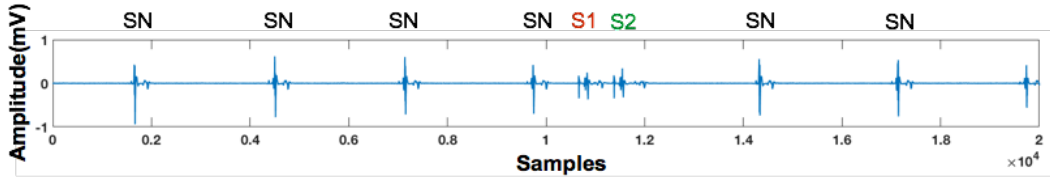


Figure 9.1: Representation of a 10 second long segment containing the SN triggered activities along with the SN, S1 and S2 triggered activity.

9.2 Atrial Activity Detection

In this section, the atrial activity detection analysis from the stimulus protocol data is described. The activation complexes recorded as various deflections in the atrial electrograms represent the propagation of the depolarisation wavefront beneath the recording location. During clinical signal processing and feature extraction, it was important to segregate the activation complexes of interest. This was done after temporally selecting the signals (the ones that are selected by the physicians) from the entire dataset. The analysis of the electrograms

were done for VFF removal, flutter case data analysis, CV estimation and stimulus protocol data analysis.

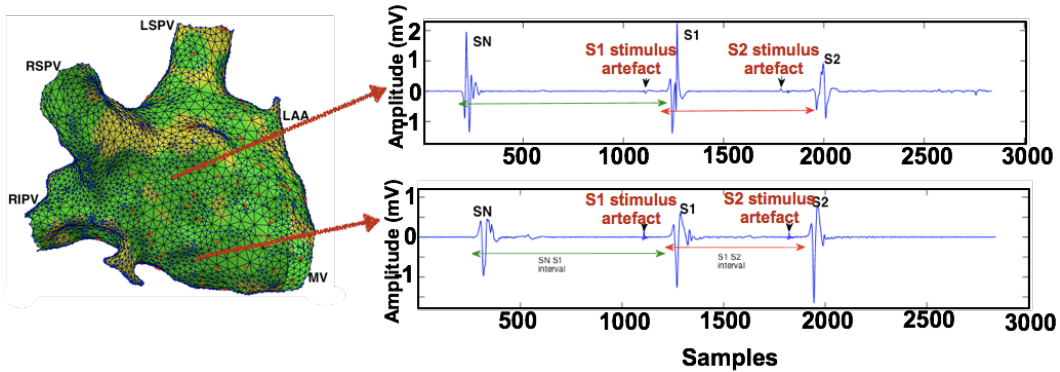


Figure 9.2: Representation of the atrial segments obtained at the two specified locations with clear *SN*, *S1* and *S2* triggered activities as annotated. The location of the respective trigger is represented in Figure 8.1.

Figure 9.1 represents a 10 *second* long data segment recorded at a sampling rate of 2.034 *kHz*. This segment was obtained while recording the stimulus protocol data. The stimulus artefacts and the following activities can be seen clearly (marked as *S1* and *S2* respectively). The atrial surface, the segments with the sinus rhythm (*SR*), *S1* and *S2* activities are segregated at the recorded locations. The stimulus activities *S1* and *S2* were triggered with the stimuli given from the coronary sinus (*CS*) catheter as explained in chapter 8. Since, the stimuli were given during *SR*, therefore, the regular *SR* was observed before the paced sequences. Based on the type of protocol used, the temporal distance between the sino-atrial node (*SN*) activities and the stimulus activities marked as *S1* and *S2* changes. The segments are segregated individually on temporal basis using an automated algorithm written in MATLAB.

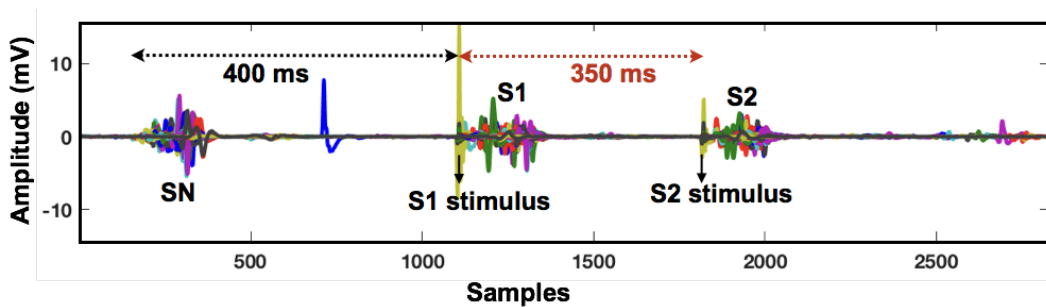


Figure 9.3: Representation of the atrial complexes superimposed on each other, recorded at all the locations of the left atrium for one of the clinical case. For this case as annotated, the stimulus protocol was 400-350 ms. There is significant temporal distance between *SN*, *S1* and *S2* activities.

Figure 9.2 represents the selected atrial segments at two arbitrary locations. At each location the three activities in the individual electrogram can be observed. If the activities at all the locations are taken together and are superimposed on each other, the three clear activation complexes can be obtained and this can be seen in Figure 9.3. There exist considerable temporal distance between *SN*, *S1* and *S2* activities. It can also be observed that the time gap is such that the tissue gets repolarised completely before the next trigger was given. Therefore, the atrial complexes from distinguished triggers can be analysed separately.

9.3 Ventricular Far Field Removal

The intracardiac electrograms recorded during the routine procedures are compromised with artefacts such as baseline wander, power-line hum, high frequency noise etc. These can be removed using various filtering techniques as explained in section 6.2. This is because the frequency range of these components is different from the frequency range of the atrial activities. Another component called the VFF is also present in the atrial intracardiac electrograms. VFF are defined as the far fields corresponding to the electrical activity of the ventricles. These artefacts correspond to the same frequency range as the atrial activities, thus making it difficult to separate using frequency domain analysis.

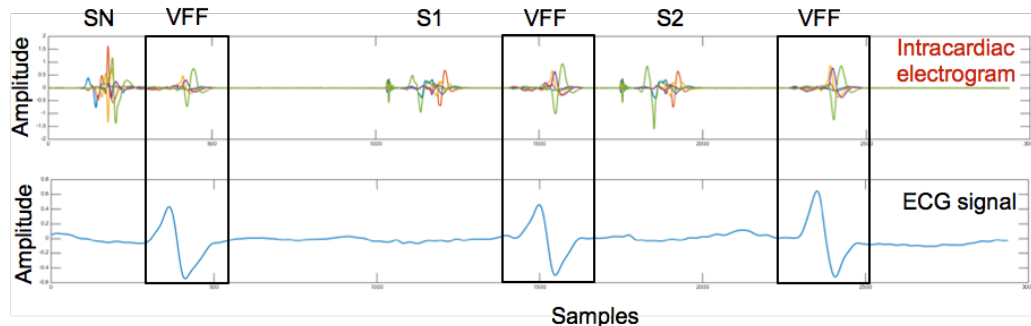


Figure 9.4: VFF marked corresponding to the *QRS* complex of the *ECG* signal.

The atrial activation complexes always appear before the VFF. But in AFib and atrial flutter (AFlut) cases the temporal existence of the VFF is very close to or incorporated into atrial activities as represented in Figure 9.5. Also, the magnitude of the far fields depend upon the recording location. On the electrograms recorded in the atrium, these are stronger near the ventricles, while at locations far from the ventricle, these are small in magnitude.

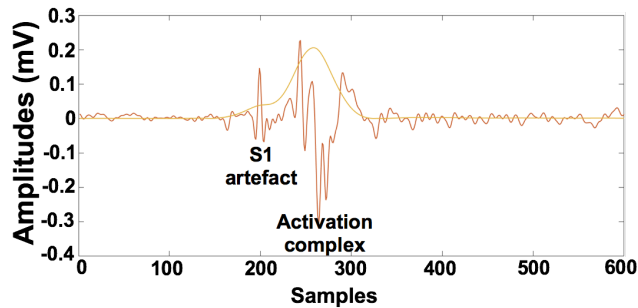


Figure 9.5: The bipolar segment for the S1 triggered activity and the NLEO curve of the segment. The peaks of the two are not clearly separable.

9.3.1 VFF removal in stimulus signals

In the clinical electrograms obtained using the electroanatomical mapping system the VFF were also observed to be present. The presence of VFF could be seen by comparing the intra atrial electrograms with the *ECG* signals. This is because the temporal presence of the ventricular activities in bipolar electrograms coincides with the *QRS* complexes of the *ECG* signals. Therefore, in order to remove the VFF, the *ECG* signals were taken into consideration. One such example of the stimulus protocol data having atrial complexes and the VFF is represented in Figure 9.4.

The amplitudes of the VFF are observed to be comparatively stronger at the locations close to the ventricle such as the mitral valve (MV). There are techniques available for VFF removal such as template matching and subtraction, adaptive ventricular cancellation, independent component analysis [87], principal component analysis (PCA) and periodic component analysis [88] [89].

The removal of VFF in the stimulus protocol data was done using the time domain analysis. A collaborative study was done with Dr.-Ing. Tobias Oesterlein for the VFF removal using π CA method. A brief description of PCA method is done in section 4.3 [90] [91]. PCA is a method to remove the VFF in case of fibrillation. It is a technique in which large data sets are correlated into few principal components having weights. The weights were chosen in such a manner that the principal components become mutually uncorrelated. This technique has been used for *ECG* signal processing. The π CA method is explained briefly below.

9.3.2 π CA method

Within the scope of this project, for VFF removal from AFlut cases the π CA method is introduced. The previous work utilising this method for other applications can be found in [92] [93] [94] dealing with the separation of mother and fetal *ECGs* [95]. This method was used to determine a linear mixing vector called w which maximises the periodicity of the

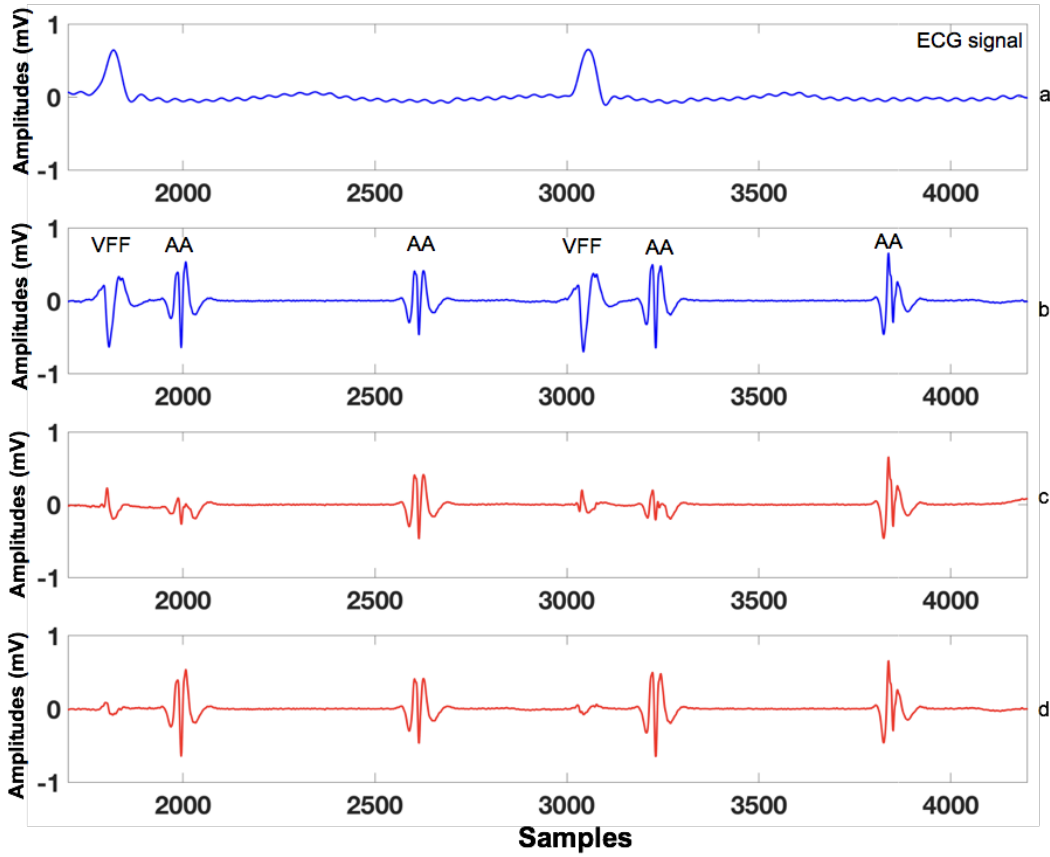


Figure 9.6: Representation of the two cases of original and the reconstructed signals obtained after VFF removal. a) Represents the *ECG* signal, b) represents the intracardiac signal, c) represents the signal to be subtracted and d) represents the VFF removed signal having only the atrial activities.

transformed signal $s(t) = w^T * X(t)$ for a given period τ . The optimisation chosen to solve this problem is

$$\varepsilon(w, \tau) = \frac{\sum_t |s(t + \tau) - s(t)|^2}{\sum_t |s(t)|^2} = 2 \left(1 - \frac{w^T C_{xx}(\tau) w}{w^T C_{xx}(0) w} \right) \quad (9.2)$$

The covariance matrix of $X(t)$ gives the C_{xx} as

$$C_{xx}(\tau) = E_t \{X(t + \tau)X(t)^T\}. \quad (9.3)$$

Using the Rayleigh-Ritz theorem the vector optimal transformation weights w_{opt} to minimise ε can be computed. The linear transformation given by $s(t) = w_{opt}^T * X(t)$ thus results in a signal with optimised periodicity τ . This was applied to the intracardiac electrograms to optimise the periodicity. To make this method to be used for the artefact removal slight modifications were done to this explained method.

During the VFF removal using this method the following steps were involved:

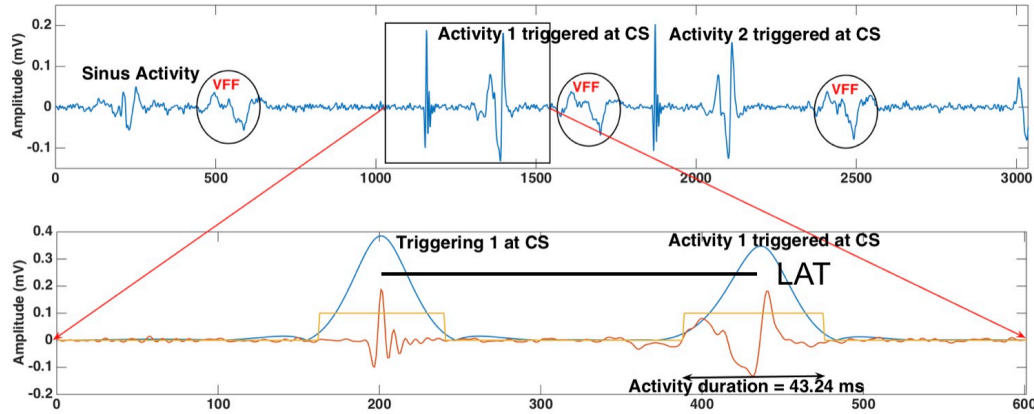


Figure 9.7: Representation of the fractionation duration (also called as the activity duration) for the atrial complexes obtained using the stimulus protocol. 0.1 times the maxima of the NLEO energy was used to get the step function around the activation complexes as represented by the yellow curve. The width of the window gives the activation duration.

1. To all the channels the weights were assigned (with pulse train).
2. In order to approximate the periodicity, the VFF is approximated.
3. An inverse template is formed by all the channels, for an optimal mixing vector w_{opt} .
4. When this inverse is added to the intracardiac electrograms, the VFF could be removed.
5. The resultant electrogram free from VFF can be reconstructed as $AA_{final} = w_{opt}^T * X(t)$.

The detailed explanation of this method is given in [89]. The πCA method is demonstrated and used with the simulated data. Figure 9.6 represents the two cases of original and the reconstructed signals obtained after VFF removal.

9.4 Fractionation Duration

After detecting and segregating the activation complexes, the spread of these activation complexes was estimated. The spread of the complexes was termed as the fractionation duration (FD) also called as the activity duration. The FD estimation was done after removing the noise and no contact signals from the given electrograms.

Figure 9.7 represents one of the electrograms giving clear complexes of the three activities one after the other used for estimating the FD at an arbitrary location on the geometry (also represented in Figure 9.2). The non-linear energy operator (NLEO) was used to get the energy of the activation complexes [64] [96]. The basics of NLEO are explained in section 4.4. The NLEO is defined as

$$E = abs(x_t^2 - x_{t+1}x_{t-1}) \quad (9.4)$$

where x is the sample at time t . The time of maxima of the NLEO obtained after low pass filtering is defined as the local activation time (LAT). To estimate the FD, a step function is generated around the NLEO using an adequately defined threshold. In this research the threshold of 0.1 times the maximum of the NLEO curve was used. To get the regional FD at all the locations, the activities resulting from the SN trigger or from the CS S1 triggered or from S2 trigger were analysed separately and the results were visualised on the atrium to get the regional information.

Higher the fractionation in activation complexes, higher is the possibility of arrhythmogenesis. The unhealthy tissue, slow conducting tissue, arrhythmogenic regions are the ones getting higher FD as compared to the healthy tissue. This is because in the region with arrhythmogeneity the depolarisation wavefront propagates slowly resulting in larger FD value. The results obtained from FD analysis are discussed and represented in chapter 14.

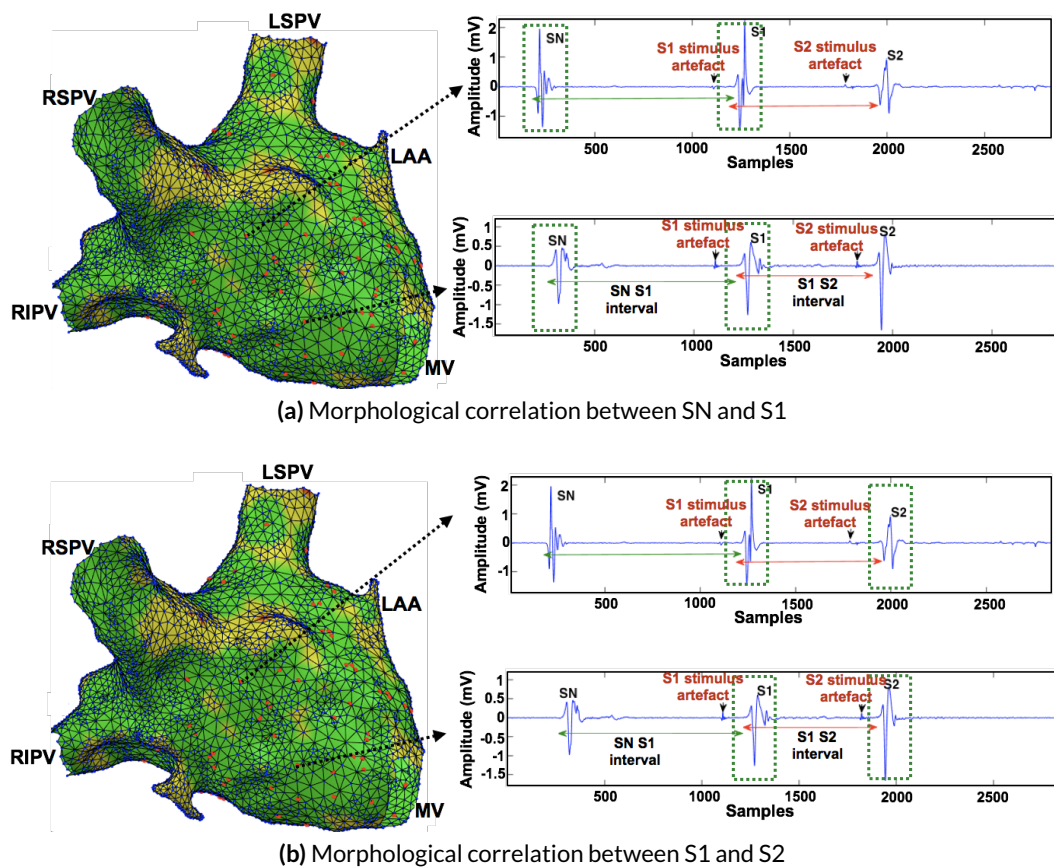


Figure 9.8: Representation of the two cases for which the morphological correlation were estimated.

9.5 Morphological Correlation

As the depolarisation wavefront travels over the atrium, the propagation is recorded in terms of activation complexes using the electrodes on the catheter. Depending on the orientation of the catheter and the angle that the depolarisation wavefront is making with the electrodes, different morphologies of the activation complexes are obtained. In case of electrogram recording over healthy substrate with 90° catheter orientation, as the depolarisation wavefront approaches the electrode, a positive deflection is observed and as it leaves a negative deflection is observed. In case of bipolar electrograms this morphology also changes depending on which pair of electrodes are chosen to get the bipolar electrograms [35]. In the scope of this research, the estimation of the morphological correlation was done for the atrial complexes resulting from the stimulation. The morphological correlation between two signals A and B is defined as

$$\sigma(A, B) = \frac{1}{N-1} \sum_{i=1}^N \left(\frac{A_i - \mu_A}{\sigma_A} \right) \left(\frac{B_i - \mu_B}{\sigma_B} \right) \quad (9.5)$$

where N is the number of scalar observations, μ_A is the mean of A , σ_A is the standard deviation of A , μ_B is the mean of B and σ_B is the standard deviation of B .

Figure 9.8 represents the electrograms obtained from the stimulus protocol data at two locations of the atrium. The morphological correlation between the atrial activities resulting from two stimuli was estimated. The first morphological correlation was estimated between the first and second atrial complex (i.e. SN triggered activities and S1 triggered activities) as marked in Figure 9.8a. This was because as explained in chapter 8, these two activities were originated (triggered) from different location, therefore, these were expected to have a low morphological correlation. Figure 9.8b represents the second morphological correlations case, where the estimation was done between S1 triggered and S2 triggered activities. As explained in section 8.1, these two activities were triggered from the same location (Figure 8.1). It is well known that in healthy cases, the depolarisation wavefront starting from one location but having a time interval between them should take the same pathway and therefore are expected to have similar morphology. Therefore, between S1 and S2 triggered activities, a high morphological correlation was expected.

Changes in the depolarisation wavefront pathways for S1 and S2 triggered activities could possibly be because of the presence of arrhythmogenic substrate. For example, the region of scar might let one depolarisation wavefront pass, while stopping the other. These sort of factors could lead to low morphological correlation values between S1 and S2 triggered activities.

The results obtained for the morphological correlation between $SN - S1$ and $S1 - S2$ triggered activities are represented and discussed in chapter 14.

It is to be noted that sometimes if at both the electrodes the activity arrives at the same time and the wavefront makes the same angle with the electrodes, in the bipolar electrogram a zero is obtained. These recordings are usually not included in the analysis. But most of the cases clear activation complexes were observed for the recorded locations.

9.6 Peak-to-Peak Amplitude

The amplitude of the atrial activities are also associated with the quality of intracardiac signals and with the quality of atrial substrate. The high peak-to-peak (P2P) amplitude is associated with the healthy substrate while low P2P amplitudes are associated with either unhealthy substrates or no contact of the electrode with the active tissue of the atrium.

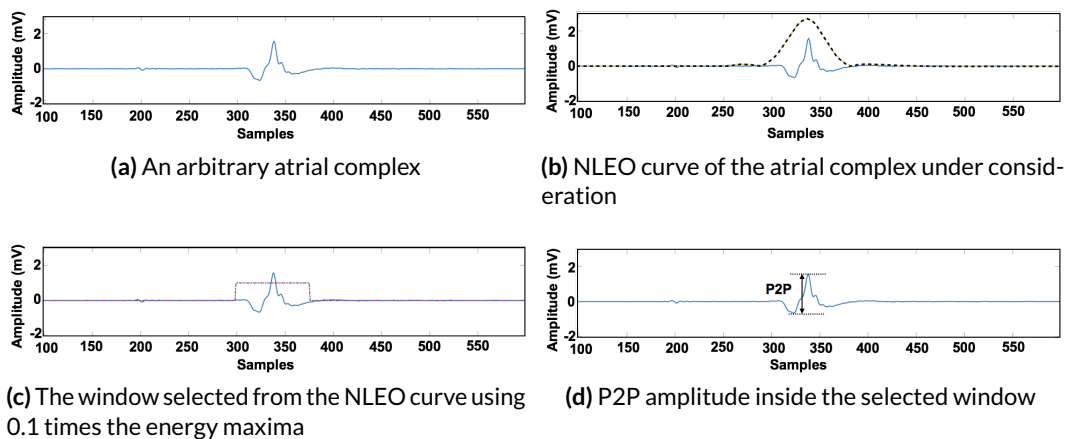


Figure 9.9: Illustration of the peak to peak values estimation for the selected segments. This was done using the NLEO curve.

Similar to FD, the P2P amplitude estimation was also done for the depolarisation wavefronts triggered from SN node and from the CS catheter. To detect the P2P amplitude in the intracardiac electrograms, the atrial activities are marked first. As explained in section 9.2 and as represented step-wise in Figure 9.9, the atrial activation complex presence was marked using NLEO. 0.1 times of the energy maxima was used to get the window around activation complexes. Once the activation complexes are detected, the maximum and minimum amplitudes were subtracted to get the P2P amplitude values within the window around activation

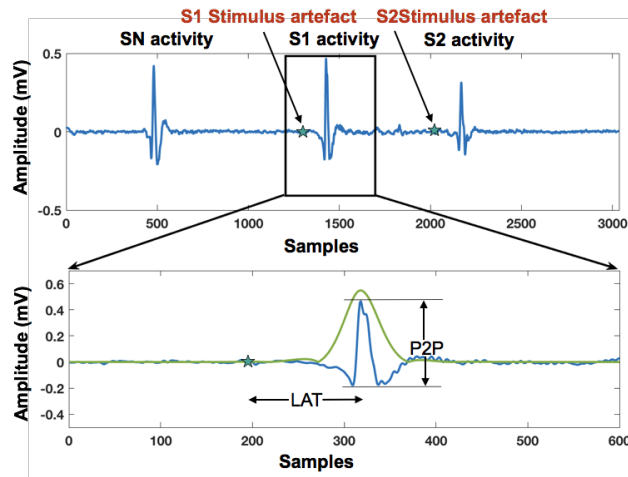


Figure 9.10: Illustration of P2P amplitude and the LAT estimation in the atrial activities for the stimulus protocol data

complexes.

An other illustration of the LAT and P2P estimation for stimulus data is represented in Figure 9.10. For the stimulus protocol data, the three activities (SN triggered, S1 triggered and S2 triggered) are first separated. Then, the NLEO curve was estimated and was used with the individual activities (Figure 9.10b), to estimates the LAT and P2P amplitudes.

The healthy atrial tissue usually shows a greater P2P amplitude compared to the arrhythmogenic tissue. The tissue giving P2P values less that 0.08 mV throughout was considered as noise or no contact signals. Therefore, after the segment selection, the P2P amplitudes were calculated and the decision was taken (to keep or discard the signals) based on the threshold of 0.08 mV P2P amplitude. The results obtained are discussed in the respective section 14.10.

9.7 Local Activation Time

Local activation time (LAT) is one of the most important electrophysiological parameters used to visualise the depolarisation excitation propagation on the cardiac geometry. It is because LAT gives the temporal information about the activation of the tissue underneath the recorded location [97]. LAT can be estimated using the individual clinical signals and can thereafter be used for interpolation on the clinical geometries to get the 3D LAT map.

In this research work, the analysis based on LAT was done with the simulated as well as the clinical environment. In simulation environment the LATs were simulated for the 2D and 3D geometries using the fast marching simulation (FaMaS) tool as explained in chapter 5. The LAT simulation was done for various excitation scenarios (homogeneous and heterogeneous excitation propagation). This was done to get the known excitation patterns and speeds

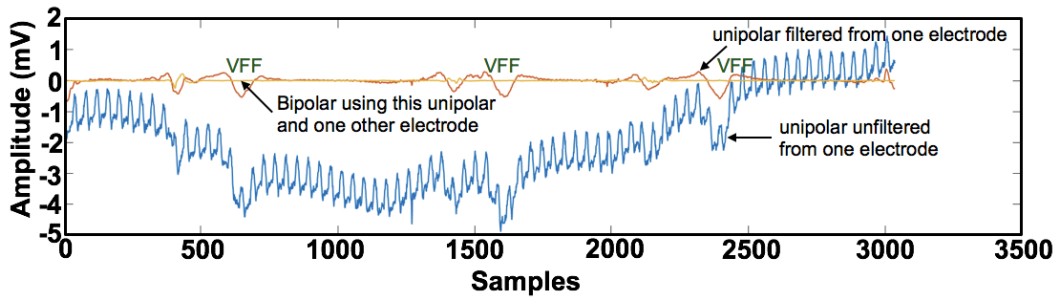


Figure 9.11: Representations of the various signals obtained from the electroanatomical mapping system on a 1.5 second temporal scale, obtained with the sampling rate of 2.0345 kHz.

on the clinical geometry which could later on be used for CV estimation. This was done to benchmark the CV estimation algorithms that were developed as a part of this research. Slight error in LAT can cause huge error in the dependent parameter (such as CV) estimation, therefore, the careful estimation of LAT was very important.

For the clinical scenarios, the estimation of LAT was done using the bipolar as well as unipolar electrograms. These LATs were then used for the estimation of regional and global CV. This in-turn can help in finding and marking the arrhythmogenic substrates (marked as the region of interest in section 14.14) and to find the substrates with slow and fast conducting properties. There exist a number of ways for LAT estimation and determination using unipolar or bipolar electrograms as explained in the next section of this chapter.

As explained in chapter 6, various information can be extracted using the electroanatomical mapping system, which can be used for various statistical parameter analysis. Figure 9.11 represents some of the signals obtained from the electroanatomical mapping system in a temporal window of 1.5 seconds. One of the highly important parameters that can be estimated using the electrograms is the LAT giving the information of the activation at a particular location [98]. These can be calculated using the unipolar as well as the bipolar electrograms. There exists a number of methods for LAT estimation [99] [100] [101]. Few of them are namely:

1. Using the maximum downslope ($-\frac{dV}{dt}$) [102]
2. Using absolute voltage maxima [103]
3. Using maxima of NLEO [64]
4. Using the maximum upslope represented by ($\frac{dV}{dt}$) [104]
5. Minimum voltage [105]

As explained above, LAT giving the information of the time instant at which the depolarisation wavefront crosses the tissue beneath the recording electrode can be defined for both unipolar as well as the bipolar signals. Ndrepepa et al. [106] has explained that the time of the depolarisation wavefront excitation at a particular instant coincides with the time of

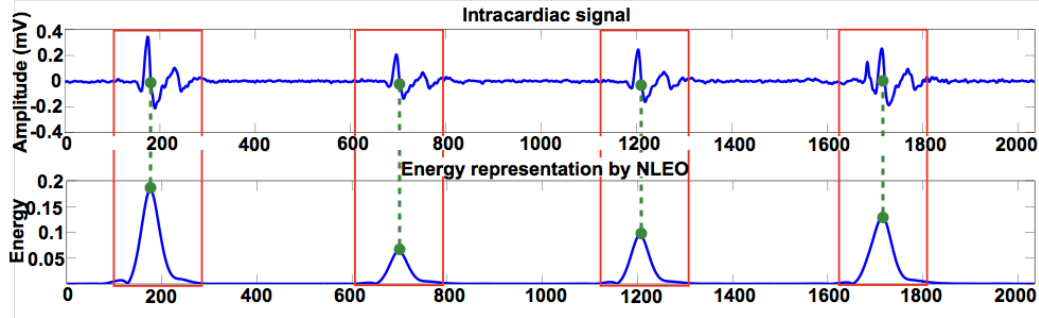


Figure 9.12: Representation of LAT estimation using the NLEO. The maxima of the energy computed for the bipolar electrograms are marked as the LAT.

steepest slope in the unipolar electrograms. Therefore, for LAT annotation using unipolar electrograms the maximum downslope could be taken into consideration. But when the unipolar electrograms contain a lot of noise or has fractionation in the electrograms, then the maximum downslope may not give the exact LAT values. For the fractionated signals, the bipolar electrograms are to be taken into consideration for the LAT determination as explained by Milad El Haddad et al. [107]. The same problem exist while estimating the LAT using the absolute voltage, maximum upslope or using minimum voltage in case of the fractionated electrograms since no clear complexes are obtained from the clinical recordings.

In this research, the LAT estimation was done for the clinical electrograms obtained during the routine mapping of clinical procedure. The cases under analysis were with unhealthy substrates, therefore, the electrograms had a lot of noise and fractionation. Depending on the catheter orientation, the morphology of the signal also changes. As represented in Figure 9.12, the four complexes have different morphologies and activation durations (also called as FD). The unipolar and bipolar electrograms recording was done at a sampling rate of 2.035 kHz. Due to various artefacts and long FD for some complexes, the method adopted in this research work was the NLEO for clinical data LAT estimation [64]. The NLEO is defined as

$$E = \text{abs}(x_t^2 - x_{t+1}x_{t-1})$$

where x is the sample at time t . The maxima of NLEO obtained after low pass filtering is marked as the LAT. As represented in Figure 9.12, the maxima of the NLEO as annotated by green dots were marked as the LATs of the respective atrial complex.

The annotation of LAT can also be done from the unipolar electrograms. The unipolar electrograms are compromised due to the presence of local artefacts, baseline wander and high frequency noise. Therefore in our case, the bipolar electrograms were used for analysis since these give better signal to noise ratio.

The LAT estimation was also done for the clinical cases obtained for paced and non-paced scenarios. The LAT estimation for the paced scenario is explained here while the LAT

estimation was also done for the experimental data obtained by the regional high density mapping of the canine heart as explained in section 12.1. From these high density maps, the bipolar and unipolar electrograms were recorded and later on used for the LAT estimation (using the NLEO). The detailed description of the canine data is done in chapter 12. The next section explains the LAT estimation for the paced sequence data.

9.7.1 LAT Determination for Paced Scenario

During the course of this thesis, two types of clinical data sets were analysed namely:

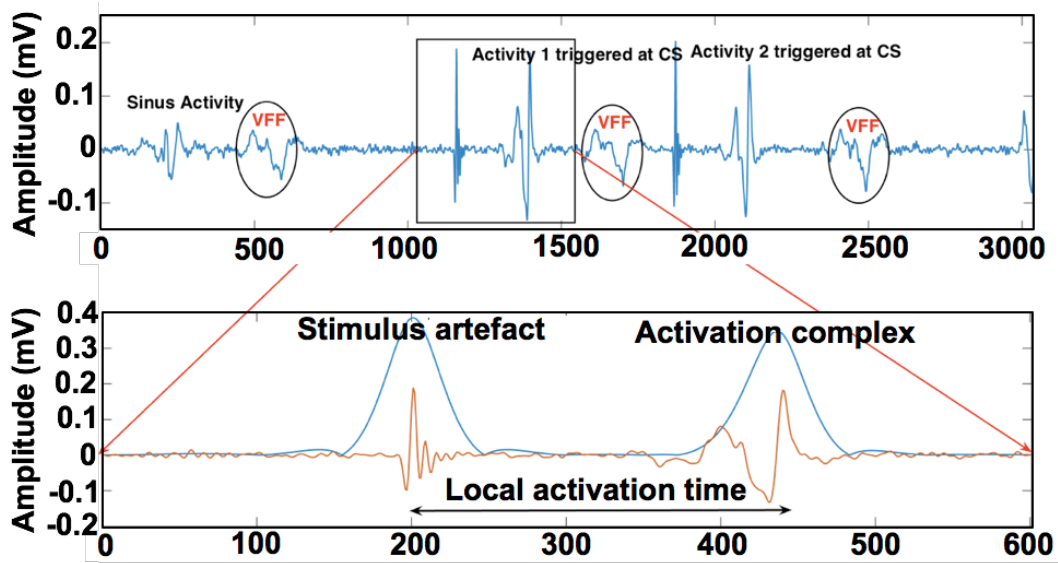
1. Signals with stimulus protocol (paced scenario)
2. Signals without stimulus protocol (non-paced scenario)

Figure 9.12 represents the signals recorded during SR and for the cases when no stimulus was given to the myocardial tissue. Figure 9.13 represents the electrogram, when the recording was also done during SR but when the stimulus triggers were applied from the CS catheter.

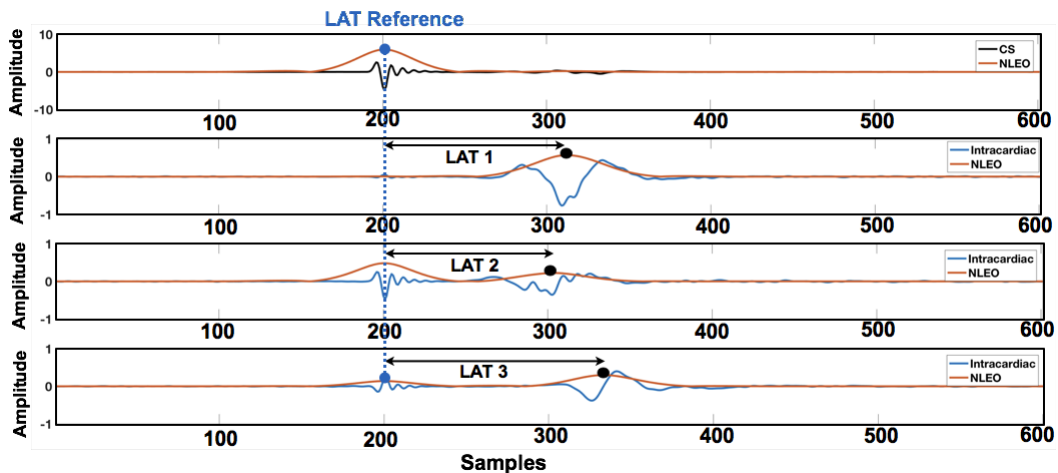
The stimulus protocol was used, such that the depolarisation wavefront was triggered twice from one specific location (as represented in Figure 8.1) in the left atrium (LA) along with the SN node triggering. The various excitation propagations were possible such that the depolarisation wavefront that is triggered from the sinus node (SN) and the other one is the depolarisation wavefront started from the external trigger given from the electrodes inside the atrium. Once triggered, the depolarisation wavefront covers the entire atrium and the LAT represents the time of activation of the respective location.

In the stimulus protocol data after preprocessing, the alignment of the stimulus artefacts were done with respect to CS catheter signals. The atrial complexes were then separated and used for LAT estimation as represented in Figure 9.13. The stimulus trigger was taken as the reference and from there the time of the atrial activity complexes were marked as LAT as represented in Figure 9.13*b*. As represented in Figure 8.1, the stimuli were given from the CS catheter and the normal SN trigger was also present. Therefore, three depolarisation excitations were analysed in respective clinical case. It has also been observed that individual activities (SN, S1 and S2 triggered) took different times to cover the atrial geometries. The LATs for the individual excitation wave to travel the atrium for two clinical cases are stated in Table 9.1 and the same could be observed in the histogram in Figure 8.6.

In this research, the LAT estimation and the LAT difference between S1 and S2 triggered depolarisation wavefront was used to analyse the fact that these depolarisation wavefronts took different pathways and times to travel over the atrium. This could be related and linked to the arrhythmogeneity presence on the atrium. The probable region of arrhythmogeneity is



(a) Representation of the electrogram obtained for the paced scenario and the LAT annotation at an arbitrary location for the depolarisation excitation triggered from the CS catheter

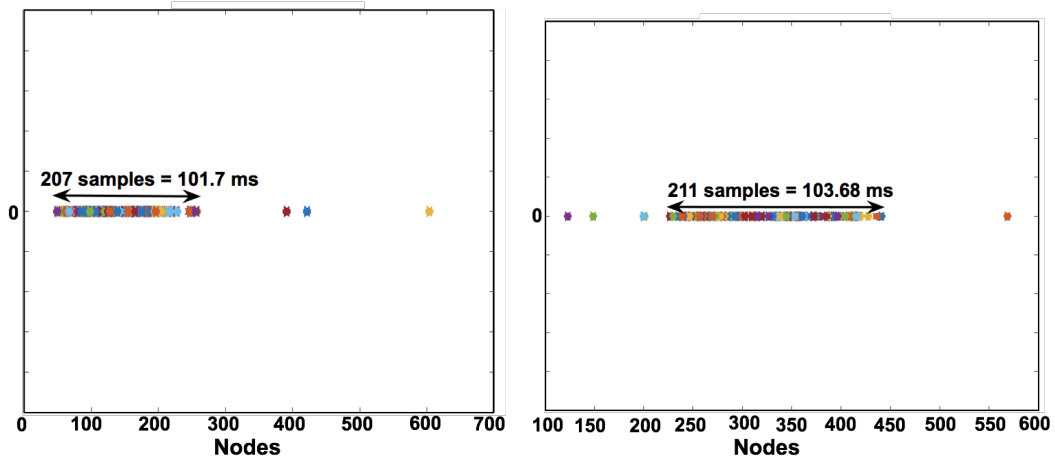


(b) Representation of the stimulus artefact alignment and LAT estimation at various locations computed with respect to the stimulus temporal location. This also represents that the various locations got depolarised at various instants

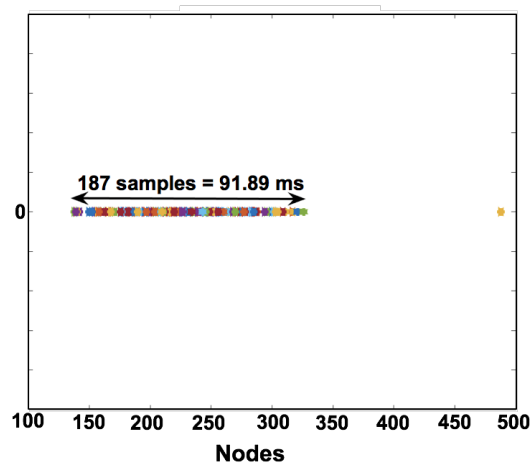
Figure 9.13: Representation of LAT time estimation in the paced scenario electrograms.

represented in Figure 14.17. There exist LAT differences for S1 and S2 triggered activities. The colour code is the interpolation of the LAT difference at respective locations on the atrium. Figure 9.14 represents that all the activities took from 90ms to 140ms to travel over the atrium, which is a realistic value. All the results obtained after LAT estimation and their visualisation have been discussed in the result in section 14.13.

In these signals (for paced scenario data), the LAT estimation was done after separating the activation complexes corresponding to the respective depolarisation wavefronts. The NLEO



(a) Activity span taken by the depolarisation wavefront triggered by SN (b) Activity span taken by the depolarisation wavefront triggered by stimulus S1



(c) Activity span taken by the depolarisation wavefront triggered by stimulus S2

Figure 9.14: LAT span by individual activities on the atrium in case of the paced scenario.

Table 9.1: Time taken by various activities to travel over the atrium for sinus node triggering and the CS triggering respectively for two clinical cases (annotated as S1 trigger and S2 trigger).

| Clinical case | Sinus trigger (ms) | S1 trigger (ms) | S2 trigger (ms) |
|---------------|--------------------|-----------------|-----------------|
| 1 | 97.78 | 88.94 | 90.90 |
| 2 | 101.71 | 103.68 | 91.89 |

curve was then used along with the threshold of 0.1σ to mark the activation complexes. The samples size between the maxima of NLEO of stimulus artefact, from the maxima of NLEO for the atrial complexes was called as the LAT of the respective location.

As we go close to the stimulus trigger location, the temporal distance between the atrial complexes and the trigger location decreases. Also at these locations, it was difficult to

separate the pacing artefact from the atrial activities, using bipolar electrograms alone. This was because no clear NLEO curve maxima's were obtained as represented in Figure 9.5. Therefore, to get the LAT near the stimulus trigger location, it was important to combine the unipolar and bipolar activities analysis to get the LAT. This has been explained in the work published and discussed in the paper [108].

9.7.2 Local Activation Time for Canine Data

Chapter 12 explains the canine data obtained using a 2D patch catheter at two locations namely left atrial appendage (LAA) and posterior left atrium (PLA) of the canine atrium. The recording was done during SR and also after inducing fibrillation. The 2D patch catheter with 117 electrodes was used for recording. At each electrode a 10*second* long electrogram segment was recorded. These electrogram segments were used for LAT estimation as well as for CV estimation. The electrograms obtained were pre-processed for the artefact removal before LAT estimation. For these electrograms, the NLEO was used for marking the activation complexes and for estimating the LAT values. Figure 12.2 represents the various LATs marked over the 10*second* long electrogram segment. In the canine data, alternans were observed. In our analysis, the LAT of the alternans were not used in CV estimation.

9.8 Arrhythmogenic Region of Interest

The atrium is heterogeneous in nature. Different tissue (which differ in functional and physiological properties) combine together to make the atria. Based on the parameters such as LAT, P2P, morphological correlations and FD the probable region of arrhythmogenic substrates can be marked as the region of interest on the atrium. As stated above and represented in the result section in chapter 14, for each parameter individually, the statistical and parametric analysis of the regions was used to find the arrhythmogeneity. The statistical parameters were combined together to match if they point to the common area or not.

These arrhythmogenic areas are the regions where the FD is comparatively larger (i.e. $> 50ms$) along with the LAT differences between stimulus S1 triggered and S2 triggered activities plus the low P2P amplitudes. The activities from the two stimuli S1 and S2 (started from the same location), in the healthy heart should take the same pathway to cover the atrium. Any change in the pathway could be because of the slow conduction region, scar tissue, or might be due to higher fibrosis. This work was presented in [109] [110]. In this study, the presence of arrhythmogenic substrates was marked for the paced scenario clinical cases, by analysing the LAT, depolarisation wavefront propagation pattern and correlation coefficients.

positions of the catheter were obtained. The various catheter contact electrode positions over the atrial geometry are represented in Figure 9.15 to Figure 9.20.

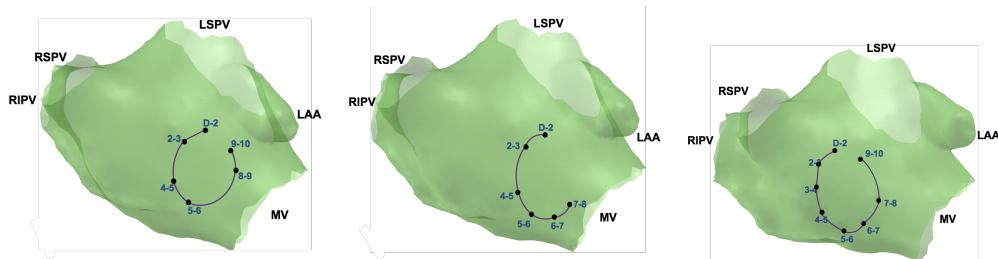


Figure 9.16: Stable catheter positions near MV (posterior view) obtained after preprocessing. Note the change in the catheter shape and position. Also the number of contact electrodes is changing.

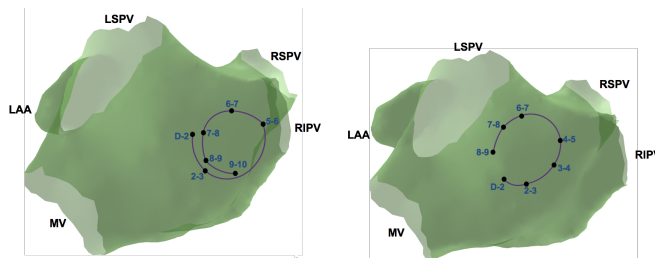


Figure 9.17: Stable catheter positions near MV (anterior view) obtained after preprocessing. Note the change in the catheter shape and position. Also the number of contact electrodes is changing.

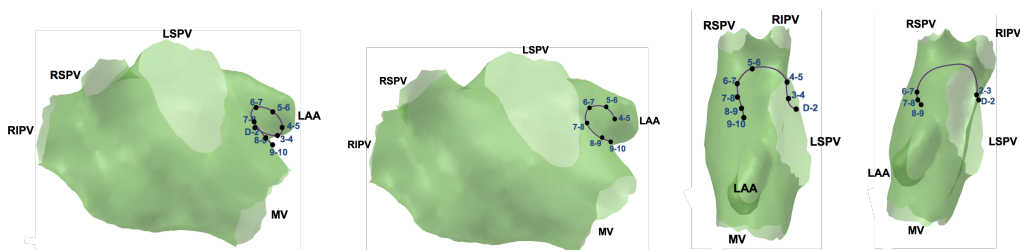


Figure 9.18: Stable catheter positions near LAA and roof obtained after preprocessing. Note the change in the catheter shape and position. Also the number of contact electrodes is changing.

Figure 9.15 to Figure 9.18 represent the stable catheter positions at various anatomical locations. The bipolar locations of the electrodes which were in contact with the endocardium are only represented. This was done because at these locations good quality (P2P amplitude of activation complexes $> 0.08\text{ mV}$) were obtained after preprocessing. The shape and the size of the contact electrodes can be seen clearly to be changing over the period of time. It can also be seen that for the clinical cases, the recording was done using the 10 pole LASSO catheter. The posterior, anterior and the roof placement of the catheter give an insight into

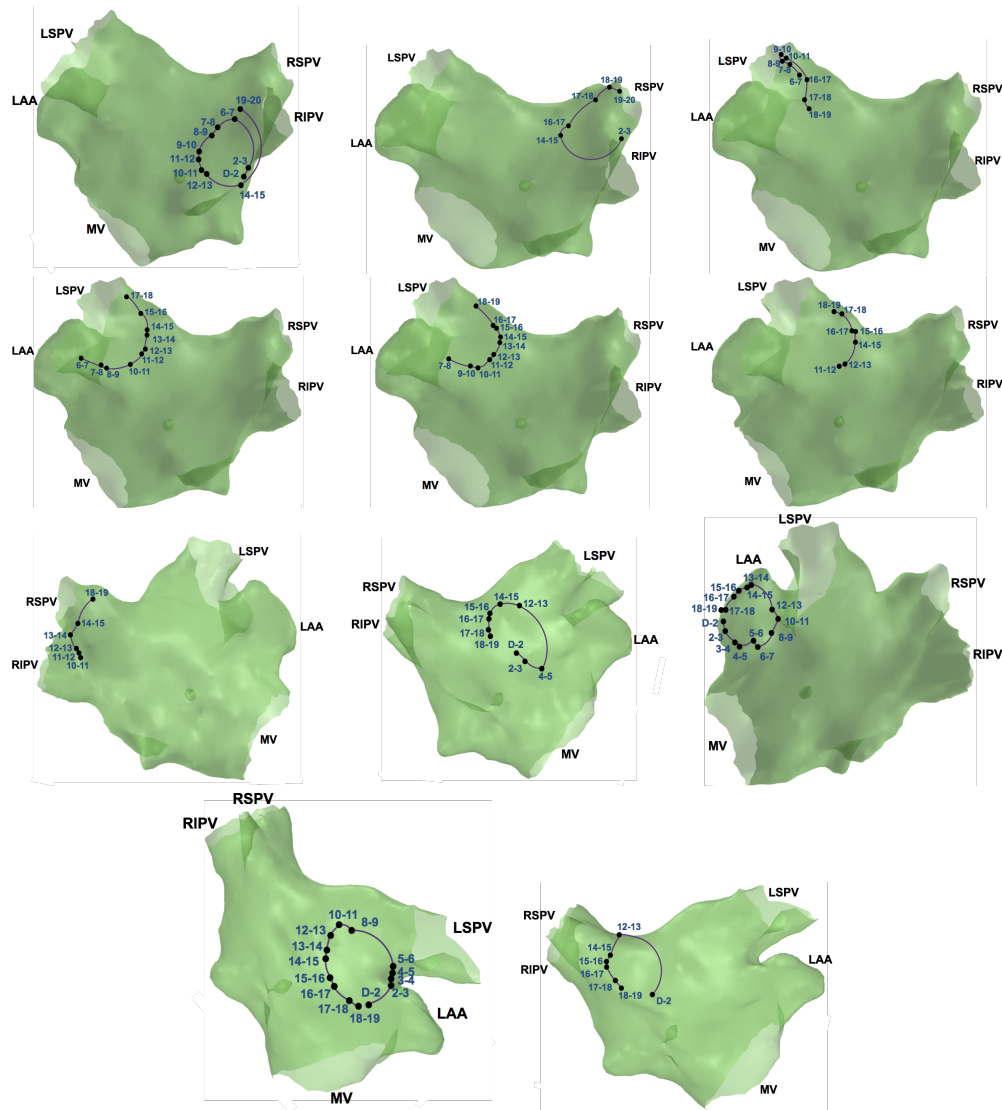


Figure 9.19: Stable catheter positions obtained after preprocessing for clinical case 2 near veins. Note the change in the catheter shape and position. Also the number of contact electrodes is changing. Posterior View, Anterior View, Catheter placed on the roof and catheter in the appendage area. The contact on posterior anterior could also be observed for a 20 pole LASSO catheter.

how the catheter was moved while the clinical recordings were done.

Similarly in Figure 9.19 and Figure 9.20 the various stable catheter positions can be seen for the second clinical case. In this case, a 20 pole LASSO catheter was used for mapping. The recording was done for anterior, posterior, roof and the appendage region as represented.

As explained in section 10.3, for estimating the CV of the depolarisation wavefront, all these stable catheter positions were taken into consideration.

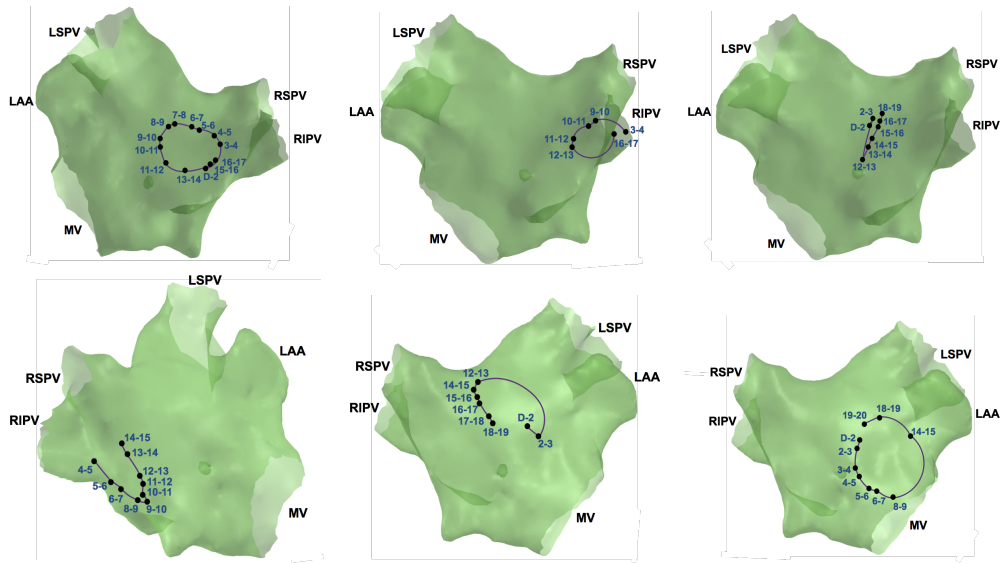


Figure 9.20: Stable catheter positions obtained after preprocessing for clinical case 2. Note the change in the catheter shape and position. Also the number of contact electrodes is changing. Posterior view, Anterior view, catheter placed on the roof and catheter in the appendage area. The contact on posterior anterior could also be observed for a 20 pole LASSO catheter.

9.10 Extraction of Time Variant Features

In the intracardiac electrograms the useful information were extracted based on the temporal occurrence and spatial locations of the atrial activities represented by electrograms on the 3D electroanatomical geometry. The features extracted were namely conduction velocity (CV), LAT, FD etc. In the active segment 3 kinds of activities were present.

1. No activity/ Baseline /Zero voltage
2. Single atrial activation duration ($10\text{ms} - 30\text{ms}$)
3. Fractionated activity over long period $> 50\text{ms}$

These were explained above and the results are discussed in chapter 18. Looking at the statistical parameters, a decision could then be made. For example, the coverage map and the stable catheter positions can give information about the mapped region. Along with FD and P2P value, the CV magnitude and direction vectors can give the information about the excitation pattern of the wavefront.

Conduction Velocity

The atrium is anisotropic and heterogeneous in nature. Therefore, the regional substrate analysis is important to get the physiological and pathological understanding of the atrium. The anisotropies are the result of fibre orientations and the heterogeneities are due to the presence of fibrosis and various tissue types. Patients suffering from atrial fibrillation (AFib) or atrial flutter (AFlut) additionally show heterogeneities and anisotropies due to the presence of various degrees of fibrosis and functional blocks [111]. For better understanding of the regional substrate, parameters such as tissue fibrosis, intracardiac electrogram (EGM) fractionation as well as the depolarisation wavefront propagation patterns are under analysis [112] [113] [111] [114]. Research has been going on in order to understand the mechanism of cardiac arrhythmias resulting from various heterogeneities [115]. To understand the mechanisms behind the atrial electrophysiology and to understand the mechanisms of phenomena such as AFib and AFlut, computer modelling can play a vital role [50] [116].

In clinic, the patients suffering from AFib or AFlut are initially treated with drugs. If not successful, they are examined in the electrophysiology (EP) lab, by introducing the multichannel catheters inside the heart for minimally invasive catheter ablation treatment. The endocardial mapping is done by placing the multichannel catheters and measuring the electrograms and the electrodes locations with respect to a reference location. During this procedure, depending on the system and catheter used, different types of maps such as LAT maps, low voltage maps, complex fractionated signals maps can be generated for understanding the on going phenomenon [75].

The understanding of the regional behaviour of the atrial substrate is important for better diagnosis and ablation planning in interventional cardiology. For this the understanding of the global and regional substrate could be an important analysis. CV is an important quantitative electrophysiological parameter describing depolarisation wavefront's propagation speed and pattern. Since the propagation depends on the substrate, this parameter could provide important information about the underlying tissue. It has been observed that the conduction velocity (CV) is reduced in arrhythmogenic areas, particularly for AFib or AFlut

cases [117]. The remodelling leads to a globally reduced CV and fibrosis causes a locally reduced CV [118] [119]. The first step of the minimally invasive catheter ablation is the pulmonary vein (PV) isolation [120]. After PV isolation, basically four strategies have been proposed

1. CFAE ablation,
2. rotor and focal source ablation,
3. low voltage ablation,
4. fibrotic tissue ablation based on late enhancement magnetic resonance imaging (LEMRI).

This entirely depends upon the expertise and experience of the physicians. It is important to identify regions which are supposed to be the slow depolarisation propagating regions [121]. To know more about the atrial substrate and the pattern and speed with which the depolarisation wavefront is propagating, the CV estimation is required.

Research has been going on in order to understand the depolarisation propagation pattern at various levels. With the advancements of various technologies, from optical mapping to signal processing to the usage of various patch catheters mapping the regional depolarisation propagation and the CV estimation, this has become an important research topic during last few decades. This research deals with the signal processing and the electrogram analysis for the estimation of the depolarisation wavefront propagation speed and pattern called as the CV.

The in-vivo and in-vitro studies using small patch catheters and involving endo- or epicardial mapping gives an insight into the regional CV patterns on atrial substrates. Several articles have been published dealing with the determination of regional CV, but none of them deals with the changing catheter shape and wall contact. There are various methods available estimating the CV, such as cosine fit [122] [123], triangulation [124], finite difference technique [125] [126], polynomial fit [127], but all of these address idealised scenarios. These methods have their limitations when it comes to the clinical cases, which makes it difficult to use them for regional CV estimation in the clinical environment and for procedure planning [128] [129]. A brief explanation of these available methods will be presented in the following sections of this chapter. Their limitations and the need of a new method that can deal with the real scenarios will be discussed.

In AFib there is a chaotic depolarisation wavefront propagation pattern while in AFlut there is a repetitive depolarisation propagation pattern. Since the two show different behaviour different assumptions are to be taken into consideration to analyse the depolarisation propagation patterns for respective scenario. It is because of the fact that the propagation pattern is not the same for all triggers even if they are given at the same spatial location. The propagation over the anisotropic and heterogeneous atrium and the pattern keeps on changing with progressing time [127].

During the ablation procedures and endocardial mapping, the shape and the number of electrodes in contact to the endocardial surface of the catheter that records the electrophysiological activities in terms of intracardiac electrograms, changes. This change is done voluntarily by the physicians based on their experience and expertise. This change in the catheter shape and electrode contact makes it difficult to quantify and estimate the CV for clinical electrophysiological cases.

In the already existing methods for CV estimation, the cosine fit takes the circular catheter shape and planar wavefront into consideration, therefore these cannot be used for regional CV estimation except for few idealistic cases [122] in clinical context. Due to the dynamic catheter movement, the different stable catheter positions are to be taken into consideration while calculating the regional CV. The method to calculate the local CV on the 3D atrial endocardium for different catheter shapes and changing number of contact electrodes is still unknown. Therefore, in this work a method is proposed that takes the 3D geometry, the curvature of the atrial surface and the bipolar endocardial EGM into consideration to calculate the local CV for the different stable catheter positions obtained from an electroanatomical mapping system. The algorithm was verified using simulated data generated using the FaMaS method [57]. The proposed method for CV estimation is a robust way to calculate regional CV propagation pattern for arbitrary catheter shapes. The correlation between CV and the fractionation duration (FD) (duration of the atrial complex) as well as the peak-to-peak (P2P) values were calculated and presented in the result section. In this work, a reliable CV estimation was done, which can help the physicians during ablation, to understand the region specific wavefront propagation in the atria.

10.1 Existing CV Estimation Methods

From the existing methods, the CV estimation methods that can be used in clinical scenarios are explained in this section with their benefits and drawbacks with respect to the clinically obtained electroanatomical mapping data. Methods such as optical mapping techniques for CV estimation etc. were not of interest since the analysis was focused on the CV estimation using the spatiotemporal information obtained from an electroanatomical mapping system. Thus, these are not a part of discussion in this thesis.

10.1.1 Polynomial Fit Method

Bayly et al. [130] introduced the CV estimation using 2D spatial and temporal coordinates in year 1998. After this, Barnette et al. [127] introduced the method for 3D CV estimation in year 2000. The method was applied to the experimental data of canine myocardium using the space time coordinate information obtained by mapping the epicardium at 396 – 466

sites. In this along with the 3D spatial information, the temporal information called the local activation time (LAT) were expressed as a quadratic polynomial fit with spatial (x, y, z) and temporal (t) coordinates, as expressed in the equation:

$$t = ax^2 + by^2 + cz^2 + dxy + exz + fyz + gx + hy + iz + j \quad (10.1)$$

To solve the fit, all the 10 coefficients (from a to j) are to be determined. To obtain all the 10 coefficients, in ideal situation 10 spatiotemporal locations are required with no (spatial or temporal) dependencies between the nodes. But, since there exist a dependency between the nodes, more than 10 points are required to solve the fit. A minimum of about 20 points in the fitting region are desired in order to estimate all ten coefficients from sampled data that also include noise. In order to determine the CV using the spatial and temporal information, the gradient can be calculated in closed form, from the polynomial fit. The partial derivative is used to solve the quadratic expression, due to simultaneous changes in the coordinates. The partial derivative of t with respect to x, y and z coordinate cannot be used to get the propagation speed. As proposed by Barnette et al., the CV estimation was done using the partial derivatives as expressed in equations below:

$$\frac{dx}{dt} = \frac{\partial x}{\partial t} + \left(\frac{\partial x}{\partial y}\right) \left(\frac{\partial y}{\partial t}\right) + \left(\frac{\partial x}{\partial z}\right) \left(\frac{\partial z}{\partial t}\right) \quad (10.2)$$

$$\frac{dy}{dt} = \frac{\partial y}{\partial t} + \left(\frac{\partial y}{\partial x}\right) \left(\frac{\partial x}{\partial t}\right) + \left(\frac{\partial y}{\partial z}\right) \left(\frac{\partial z}{\partial t}\right) \quad (10.3)$$

$$\frac{dz}{dt} = \frac{\partial z}{\partial t} + \left(\frac{\partial z}{\partial x}\right) \left(\frac{\partial x}{\partial t}\right) + \left(\frac{\partial z}{\partial y}\right) \left(\frac{\partial y}{\partial t}\right) \quad (10.4)$$

The partial derivative of time with respect to x, y and z coordinates gives a linear dependency on the spatial coordinates:

$$t_x = \frac{\partial t}{\partial x}, \quad t_y = \frac{\partial t}{\partial y}, \quad t_z = \frac{\partial t}{\partial z} \quad (10.5)$$

$$t_x = 2ax + dy + ez + g \quad (10.6)$$

$$t_y = 2by + dx + fz + h \quad (10.7)$$

$$t_z = 2cz + ex + fy + i \quad (10.8)$$

The wavefronts surfaces are assumed to be orthogonal and because of this the CV components were defined to be related as given in expressions:

$$CV_y = \frac{t_y}{t_x} CV_x \quad (10.9)$$

$$CV_z = \frac{t_z}{t_x} CV_x \quad (10.10)$$

This gives the CV vector components along x , y and z axis to be:

$$CV_x = \frac{dx}{dt} = \frac{t_x}{t_x^2 + t_y^2 + t_z^2} \quad (10.11)$$

$$CV_y = \frac{dy}{dt} = \frac{t_y}{t_x^2 + t_y^2 + t_z^2} \quad (10.12)$$

$$CV_z = \frac{dz}{dt} = \frac{t_z}{t_x^2 + t_y^2 + t_z^2} \quad (10.13)$$

where N is the number of fits. Each node i contributes to N number of fits and all these fits are referenced to a reference point j . The weighted sum is calculated by the number of fits each node is involved in, respectively. Its contribution is taken into consideration for final CV value calculation at the node i :

$$w_{ji} = \frac{1}{LRMSE_j * D_{ji}} + \frac{3}{RMSE_j} \quad (10.14)$$

$$CV_x^i = \sum_{j=1}^{N_i} CV_x^j * w_{ji} \quad (10.15)$$

$$CV_y^i = \sum_{j=1}^{N_i} CV_y^j * w_{ji} \quad (10.16)$$

$$CV_z^i = \sum_{j=1}^{N_i} CV_z^j * w_{ji} \quad (10.17)$$

$$CV^i = \sqrt{(CV_x^i)^2 + (CV_y^i)^2 + (CV_z^i)^2} \quad (10.18)$$

RMSE is the root mean square error of the fit, while the linear root mean square error (LRMSE) is the RMSE of its linear part. D_{ji} is the distance between active sites of the fit which also takes the spatiotemporal window size ($x_{win}, y_{win}, z_{win}, t_{win}$) of fit j into account. The RMSE and LRMSE provide a measure between the measured time $t_{ji,meas}$, and the calculated times $t_{ji,calc}, t_{ji,calc,lin}$. The latter is the time calculated using only the linear part of the fit equation:

$$\begin{aligned} D_{ji} &= \sqrt{(x_i - x_j)^2 + (y_i - y_j)^2 + (z_i - z_j)^2 + (t_i - t_j)^2} \\ &\quad + 0.5 * \sqrt{x_{win}^2 + y_{win}^2 + z_{win}^2 + t_{win}^2} \\ t_{ji,calc} &= ax^2 + by^2 + cz^2 + dxy + exz + fyz + gx + hy + iz + j \\ t_{ji,calc,lin} &= gx + hy + iz + j \end{aligned} \quad (10.19)$$

Limitations

In real clinical environment data recording is done using different types of clinical multi-channel catheters but activation times at 20 points are rarely available. This method was similar to Bayly et al. [130]. Bayly introduced the method for 2D plane and Barnette modified that and did polynomial fit for the 3D plane with an accuracy of 1 to 2% in CV

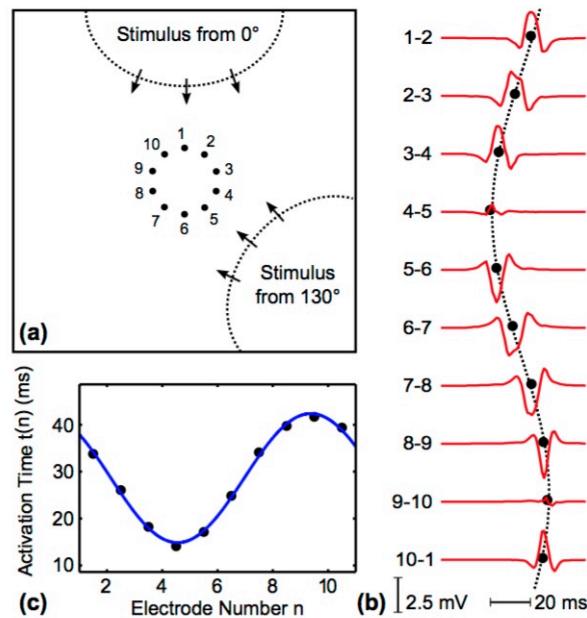


Figure 10.1: Simulation and analysis of intracardiac EGMs in a tissue patch. (a) Schematic patch setup. The circular mapping catheter with 10 electrodes was placed in the centre of the patch. All angles were measured clockwise relative to electrode 1 that was aligned with the y-axis. 36 stimuli were initiated at 10° intervals. Two example stimuli at 0° and 130° are illustrated. (b) Simulated bipolar EGMs (potential differences between neighbour electrodes) for the 130° stimulus. Black dots represent the detected activation times. The fitted cosine curve is marked with a dotted line. (c) Detailed plot of activation times as a function of electrode number. The times were assigned to half-integer electrode numbers as bipolar EGMs were analysed. [122]

vector estimation. In this work, the author has benchmarked this method and data using simulations. These simulation were idealistic to the highly dense recordings which is not the case during clinical recordings. Using clinical multichannel catheters, the recording is done by the physicians mainly using catheters such as LASSO or PentaRay. These are the majorly used catheters for electroanatomical endocardial mapping. With these the activation times at 20 points within the close proximity are rarely available simultaneously. This makes it difficult to use the polynomial fit method for the regional CV calculation. Barnette et al. in the paper described the limitations in the region with curvature, collision of wavefronts, block, insufficient number of points and ill condition of fitting problems. This brings the need of a new method that can take less given spatial temporal locations and still give a good estimate of the regional CV vector information.

10.1.2 Cosine Fit Method

In year 2010, at the Institute of Biomedical Engineering, KIT, Weber et al. [122] did a quantitative analysis of electrophysiological data. A method called cosine fit has been developed to calculate CV and the depolarisation wavefront incidence direction for a single

wavefront passing through the circular mapping catheter. This method states that for a perfectly circular arrangement of electrodes (for e.g. in the LASSO catheter) and a plane wavefront, the activation time depicted from the electrograms and for all electrodes line by line shows a cosine shape. In this fit, the phase of the cosine tells the direction and the amplitude gives the speed of the depolarisation wave. In this method the activation time in each channel is determined and then the cosine data model is fitted to the detected activation times. The detection of the activation times is done from the EGMs using NLEO as proposed by Kaiser et al. [62]. The cosine function depicting the activation pattern in the catheter electrodes is defined as:

$$t(n) = t_c - A \cdot \cos[\phi(n) - \phi_o] \quad (10.20)$$

where, t_c is the centre of the activation time and is the base line of the cosine function as represented in Figure 10.1. Parameter A in the above expression represents the amplitude of the fitted cosine. ϕ_n is the angle at which the electrode is placed, ϕ_o corresponds to the phase shift of the electrode with earliest activation. If the parameter γ represents the offset between two neighbouring electrodes, then $\phi = \gamma(n + 1)$ and the activation time expression is represented as

$$t(n) = t_c - A \cdot \cos[\gamma(n - 1) - \phi_o] \quad (10.21)$$

$$Local\ CV = \frac{r}{A}. \quad (10.22)$$

where r is the catheter radius and A is the cosine amplitude. The validation was done by Weber for patch data as represented in Figure 10.1.

Limitations

This method is limited to the idealistic condition of a single planar wavefront passing through the circular mapping catheter which is only possible on the posterior or anterior wall of the atrium, where the curvature is more or less planar. But during routine mapping procedure, getting a circular catheter shape and the planar wavefront at these locations is very unlikely. As explained, depending on the area of mapping and recording, the physicians voluntarily keeps on changing the catheter shape and size. As a result of it the number of electrodes in contact with the endocardium keeps on changing to get a better coverage of the atrium. Therefore, in those realistic scenario to get the idealistic conditions for CV calculation as given by Weber et al. is difficult and very unlikely. Also the orientation of the electrodes keeps on changing with the catheter shape and size. This method cannot deal with any other catheter shape except the circular one. This method can also not be used in the wavefront collision region. The circular shape of the catheter and the plane wave assumption obviously are strong restrictions of the method. Therefore, a method is required that can take the various catheter shapes and contact electrodes into consideration for CV estimation.

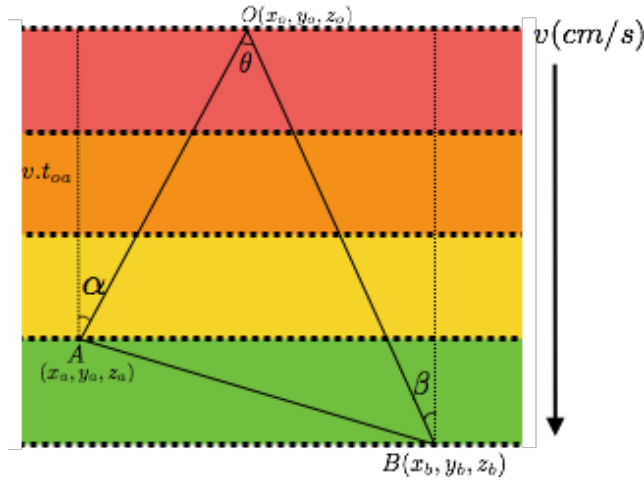


Figure 10.2: Schematic representation of a triad of three endocardial points, marked as O, A, and B. v represents wavefront propagation velocity [124].

10.1.3 Triangulation Method

The method of triangulation was proposed by Kojodjojo et al. in year 2006 [124]. In this method, a triad of points is considered and defined in 2D plane and the principle of triangulation is applied. The assumption is made that the 20 adjacent points get activated by the same wavefront and the LAT difference is more than 3 ms. The considered triads can form equilateral or non-equilateral triangles. The selection of the points is done as per the choice of the operator. The spatial and temporal information at each involved node in the triad is used for CV estimation. The trigonometric formulas used for CV estimation were:

$$\cos \alpha = \frac{v \cdot t_{oa}}{OA} \quad (10.23)$$

$$v = \frac{OA}{t_{oa}} \cos \alpha \quad (10.24)$$

Using the trigonometric formulas for the triangle represented in Figure 10.2, the angles can be expressed as

$$\cos \beta = \frac{v \cdot t_{ob}}{OB} = \cos(\theta - \alpha) \quad (10.25)$$

$$\frac{v \cdot t_{ob}}{OB} = \cos \theta \cos \alpha + \sin \theta \sin \alpha \quad (10.26)$$

$$v = \frac{OB}{t_{ob}} (\cos \theta \cos \alpha + \sin \theta \sin \alpha) \quad (10.27)$$

Combining the above equations results in,

$$\frac{OB}{t_{ob}}(\cos\theta\cos\alpha + \sin\theta\sin\alpha) = \frac{OA}{t_{oa}}\cos\alpha \quad (10.28)$$

$$\tan\alpha = \frac{\frac{t_{ob}OA}{t_{oa}OB} - \cos\theta}{\sin\theta} \quad (10.29)$$

$$\cos\theta = \frac{(OA)^2 + (OB)^2 - (AB)^2}{2(OA)(OB)} \quad (10.30)$$

The Euclidean distances between points are calculated as

$$OA = \sqrt{(x_a - x_o)^2 + (y_a - y_o)^2 + (z_a - z_o)^2} \quad (10.31)$$

$$OB = \sqrt{(x_b - x_o)^2 + (y_b - y_o)^2 + (z_b - z_o)^2} \quad (10.32)$$

$$AB = \sqrt{(x_a - x_b)^2 + (y_a - y_b)^2 + (z_a - z_b)^2} \quad (10.33)$$

Limitations

This method is used for CV estimation using the spatial and temporal locations given in the form of triads. The assumption is that all the three points must lie on the same plane irrespective of the triad being equilateral or not. But during the electroanatomical mapping in clinical scenarios, the information obtained is in terms of various recorded locations. The plane that is defined by the three points of the triad might not be a good approximation of the real endocardial surface. Also, the triad made using the recorded locations might not belong to the same plane, in particular for larger distances of the electrodes like in LASSO catheter or PentaRay catheter. If assumed in the same plane, the euclidean distance obtained is not the one taken by the depolarisation propagation wavefront to cover the atrium, yielding wrong CV estimation. Therefore, it is difficult to use this method with the available clinical scenarios. In real cases the voluntary recording is done moving the catheter along the endocardial wall. Along with this, in the clinical data the atrial surface has a strong curvature in some regions and it is difficult to get the triads points from the recorded locations, for example in the pulmonary vein or isthmus region. Also during the recording, the number of recorded locations is less compared to the vertices of the generated triangular mesh. Therefore, this method can also not be used as it is for CV estimation for the clinical cases of low density mapping (example, LASSO catheter mapping) where the catheter moves and the contact with the atrial endocardium changes. Thus, there was a need to find a method for CV estimation that can take into consideration the moving catheter shape, changing number of contact electrodes and sparse recorded locations on the endocardium.

10.1.4 Polynomial Fit for Circular Wavefront

This approach of polynomial fit for circular wavefront was proposed by Roney et al. in the year 2014 [128]. This is an extended approach to include circular wavefronts originating

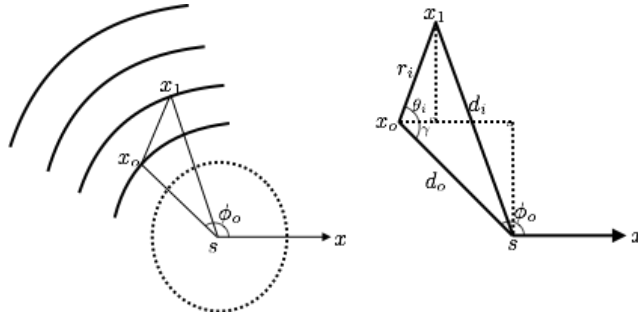


Figure 10.3: Circular point source at s measured at an arbitrary arrangement of recording points x_i . Local radius of curvature d_i computed for each electrode. Length r_i is the distance to the earliest activated electrode x_0 [128].

from focal sources and to various catheter geometries. Roney et al. developed automated algorithms to rapidly identify CV from multipolar catheter data with any arrangement of electrodes, whilst providing estimates of wavefront direction and focal source position, which can guide the catheter towards a focal arrhythmic source as represented in Figure 10.3.

In this, the plane of best fit is computed for all the available electrode locations in terms of 3D coordinates. The points are orthogonally projected on this plane. The activation time at any point x_i is expected to be defined by the expression:

$$\hat{t}_i = T + \frac{\|x_i - s\|}{v} \quad (10.34)$$

The equation can be expressed in terms of a known point x_o and unknown angle ϕ_o as well as the radius of curvature. From Figure 10.3, we can clearly get the expression using cosine rule, as

$$d_o = \|x_o - s\| \quad (10.35)$$

$$d_i^2 = d_o^2 + r_i^2 - 2d_o r_i \cos(\theta_i + \gamma) \quad (10.36)$$

$$= d_o^2 + r_i^2 - 2d_o [(x_i - x_o) \cos \phi_o + (y_i - y_o) \sin \phi_o] \quad (10.37)$$

$$\hat{t}_i = \beta_o + \beta_i \sqrt{(\beta_2^2 + \beta_3^2) + 2(\beta_2 X_i + \beta_3 Y_i) + Z_i} \quad (10.38)$$

$$\hat{t}_i = \gamma_o + \gamma_1 X_i + \gamma_2 Y_i \quad (10.39)$$

Here, $X_i = x_i - x_o$, $Y_i = y_i - y_o$ and similarly $Z_i = z_i - z_o$ and $\beta = [T, v^{-1}, d_o \cos \phi_o, d_o \sin \phi_o]^T$.

Limitations

This method deals with the estimation of CV towards the focal arrhythmic sources for planar and circular waves only. The collision of wavefronts will produce spurious results using this algorithm. This method also has limitations when artefacts are present. This also has limitations in case of arrhythmogeneity and anisotropies of the tissue underneath. Other than for these focal arrhythmic regions, this method cannot be used. Therefore, for the

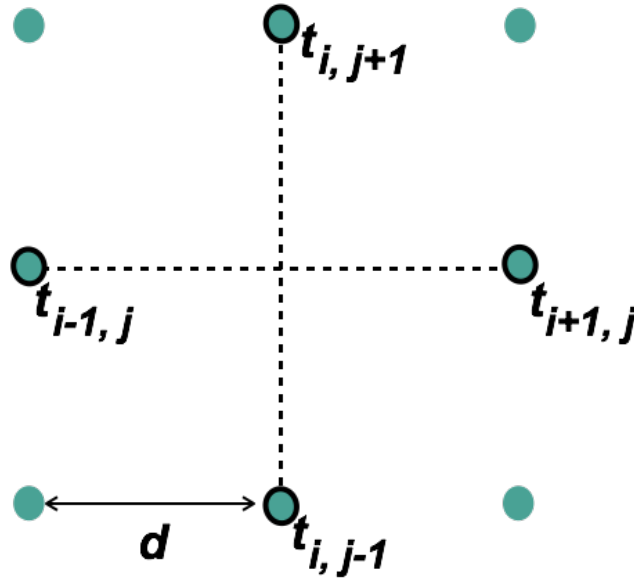


Figure 10.4: Finite element method representation. [132]

data obtained using the routine clinical mapping, a new regional and global CV calculation method is required.

10.1.5 Finite Element Method

This deals with the CV calculation in 2D using data obtained by cardiac optical mapping [131]. In this method the vertical and the horizontal activation gradient are computed using first order finite difference stencils as represented in Figure 10.4 and expressions below.

$$G_x = \frac{1}{2} \left[\frac{t_{i+1,j} - t_{i,j}}{d} + \frac{t_{i,j} - t_{i-1,j}}{d} \right] i \quad (10.40)$$

$$= \frac{t_{i+1,j} - t_{i-1,j}}{2d} i \quad (10.41)$$

$$G_y = \left[\frac{t_{i,j+1} - t_{i,j-1}}{2d} \right] i \quad (10.42)$$

The CV is given by magnitude $|u|$ and direction \hat{n} ,

$$|u| = \frac{1}{|G_A|} \quad (10.43)$$

$$= \frac{1}{\sqrt{G_x^2 + G_y^2}} \quad (10.44)$$

$$\hat{n} = i \frac{G_x}{\sqrt{G_x^2 + G_y^2}} + j \frac{G_y}{\sqrt{G_x^2 + G_y^2}} \quad (10.45)$$

$$u = |u|\hat{n} = i \frac{G_x}{G_x^2 + G_y^2} + j \frac{G_y}{G_x^2 + G_y^2} \quad (10.46)$$

Limitations

Being the optical mapping data and 2D approach, this method does not deal with the estimation of CV using the spatiotemporal locations that are obtained during the routine clinical mapping procedures. Therefore, during the course of this thesis, this method was not used and implemented. A new approach is yet to find regarding the regional and global CV estimation for the LASSO data that can deal with the moving catheter along with changing number of contact electrodes.

10.1.6 Other Methods

The above stated are some of the existing CV estimation methods. There exist certain more methods and scenarios such as represented by Latcu et al. in [133] where he dealt with the flutter case and the isthmus region specifically. Other than these, there exist the methods that either considers the time difference and the spatial distance in 2D plane [134]. Radial basis function and the maximum likelihood estimation was also one of the ways to calculate the CV vectors. These methods also deal with data in the form of EGMs giving temporal information of the respective spatial coordinate for the depolarisation wavefront propagation, yielding the requirement of a new CV estimation method.

10.2 Proposed CV Estimation Method

CV estimation can be used as a very important electrophysiological information for the regional as well as global understanding of the atrial substrate and to get the depolarisation wavefront propagation pattern over the cardiac tissue. As explained in the previous section, there exist a number of methods for CV estimation, but they have limitations with respect to the clinical scenarios. During the ablation procedure, one of the primary steps is the endocardial mapping. During this mapping procedure, the physicians voluntarily move the catheter inside the atrium. Depending on the mapping regions, the shape and orientation of

the catheter changes. As the catheter moves and the atrial dynamics varies, the electrodes on the catheter change their contact with the myocardial layer.

In the introduction part of this thesis (electroanatomical mapping and data recording section), it is explained how the spatiotemporal information along with the endocardial EGMs were extracted from the mapping system. These spatiotemporal information were then used to get the catheter contact electrodes specifications. As the catheter moves inside the atrial chambers, its shape changes as the physicians try to get good coverage by moving it in all the directions. Electrograms were recorded showing good P2P amplitude and clear atrial complexes, at specific locations, and these catheter locations were called as the stable catheter positions. At these locations the electrograms from 1 *second* up to 5 *seconds* could be recorded. For the dynamic catheter movement, the different stable catheter positions were taken into consideration to estimate the regional CV.

Due to the non ideal situations, it is difficult to estimate the CV with the already existing methods. None of the previously presented articles and methods deal with changing catheter shapes as well as changing wall contact. The functional and physiological heterogeneities, such as the 3D curvature of the geometry and the low density of recorded locations makes it difficult to get perfect conditions for CV estimation. This makes it very difficult to quantify and calculate the CV for clinical electrophysiological cases. The above proposed methods were used for CV estimation in various scenarios, but when it comes to clinical cases due to heterogeneities and non ideal scenarios, it was difficult to use any of the existing methods. In this thesis, a method is proposed that takes the 3D geometry, the curvature of the atrial surface and the endocardial EGM into consideration to calculate the local CV for different stable catheter positions obtained from the electroanatomical mapping system. The algorithm was verified using simulated data that have been generated using the FaMaS method [57] [129]. The proposed method can be used with the various clinical scenarios. It can help the physicians during ablation planning by giving the region specific information about the depolarisation wavefront propagation speed and pattern on the atrium.

From the electroanatomical mapping system two of the input modalities are the triangular mesh (i.e, the geometry) and the activation times at various locations (extracted from the clinical EGMs). These two modalities are obtained using various feature extraction techniques after preprocessing. Therefore, to estimate the regional and global CV, these two information are used as input. The proposed CV estimation method was divided into three approaches. The diagrammatic workflow of CV estimation in 3 stages is presented in Figure 10.5 and Figure 10.6. In the workflow, for a particular case, T represents the number of vertices in the triangular mesh that is obtained from the electroanatomical mapping system while recording the data during routine procedure. L represents the number of locations for which the temporal information is available (i.e, the recorded locations in case of clinical data) and

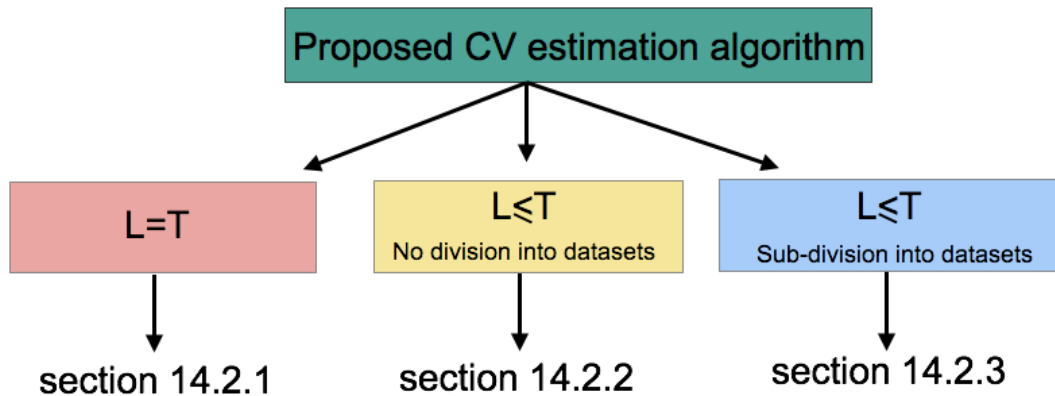


Figure 10.5: Three different formulations of the proposed modified triangulation method for CV estimation. The sections mentioned above are the sections of the chapter in which the particular case is explained. T represents the number of vertices in the triangular mesh that was obtained from the electroanatomical mapping system. L represents the number of locations for which the temporal information was available (i.e., the recorded locations in case of clinical data) and D represents the dataset (if the recorded locations are divided into data sets).

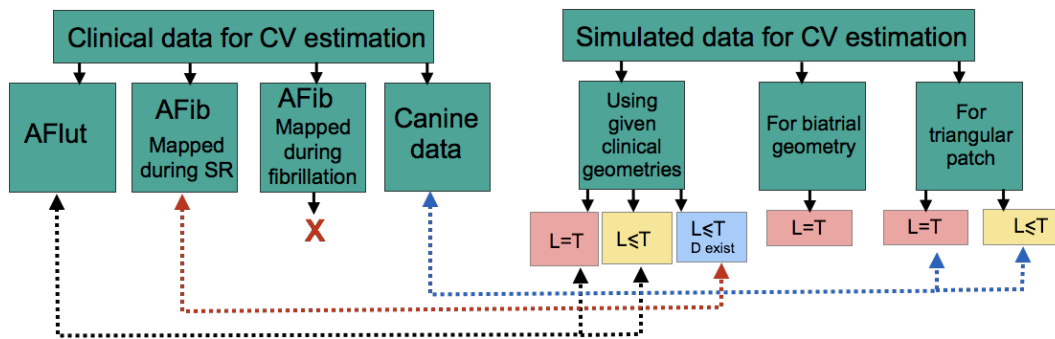


Figure 10.6: CV estimation for simulated and clinical cases. The links in the both parts represents the relation between the clinical scenarios that are simulated for benchmarking the CV estimation algorithm.

D represents the sub division of datasets (if the recorded locations are divided into data sets).

1. When the spatial and temporal information were given for all the nodes making the 3D geometry with triangular mesh, for CV estimation (i.e., $L=T$).
2. Using a selected dataset (spatiotemporal information) instead of using all the vertices with their activation times, for CV estimation. At this stage, the intermediate vertices were taken into consideration for estimation of the distances between two nodes of the given dataset (i.e., $L \leq T$ and there is no sub division into smaller datasets).
3. Using the clinically obtained stable catheter contact electrodes locations and the LAT values extracted from the EGMs, for CV estimation. The electroanatomical 3D geometries and the EGMs were obtained using the clinical electroanatomical mapping systems (i.e.,

$L \leq T$ and a subdivision into smaller datasets is done).

The CV estimation of the simulated data was done to evaluate the performance of the algorithm, before using it with the clinical data. Thus, the CV estimation for simulated cases (section 10.3 and as represented in Figure 10.6) is explained before the clinical data (section 10.4 and as represented in Figure 10.6). In the next section the three different formulations (as represented in Figure 10.5) of the modified triangulation method for CV estimation are explained.

10.2.1 CV Estimation when all Nodes have SpatioTemporal Coordinates

At this stage of CV estimation the inputs were the spatiotemporal coordinates available at all the nodes of the triangular mesh (i.e., $L=T$). All the triads involved in the 3D mesh were taken into consideration to estimate the CV. Figure 10.7a represents the triangular meshes and the 3D geometry. The modified triangulation method was used for the estimation of the speed and direction of the propagating depolarisation wavefront as explained mathematically. All the vertices of the triangular mesh were used along with their respective activation times. The vertices of the individual triangles (being equilateral or non-equilateral) were assumed to be in the same plane, making an angle α and β respectively with the CV vector. Taking all the triangular faces one after the other, the CV estimation was done for the entire 3D geometry. As represented in Figure 10.7, the velocity was assumed to be in an arbitrary direction and then the various angles were calculated using the given spatial coordinates and using the trigonometric formulas. The rotational matrix was constructed to give the direction of temporal coordinate progression in space.

As explained above, the analysis was done assuming the points making a triad to be in the same plane. The coordinate with least temporal value was assigned as O and the other two were assigned as A and B . In a particular triad, the nodes were selected such that the point O of Figure 10.7b was the one with least LAT out of the three considered for the respective triad. This was as represented in Figure 10.7b, the triangles are taken one after the other and the nodes annotation changes. The node O shifts from one triangle to other and the CV magnitude and directions were estimated and plotted for each triad. The inclination of each distance vector with the velocity vector was assumed to be at an angle α and β . Let, the coordinates of the three points be (x_o, y_o, z_o) , (x_a, y_a, z_a) and (x_b, y_b, z_b) for O , A and B respectively. The length of each edge can be calculated as:

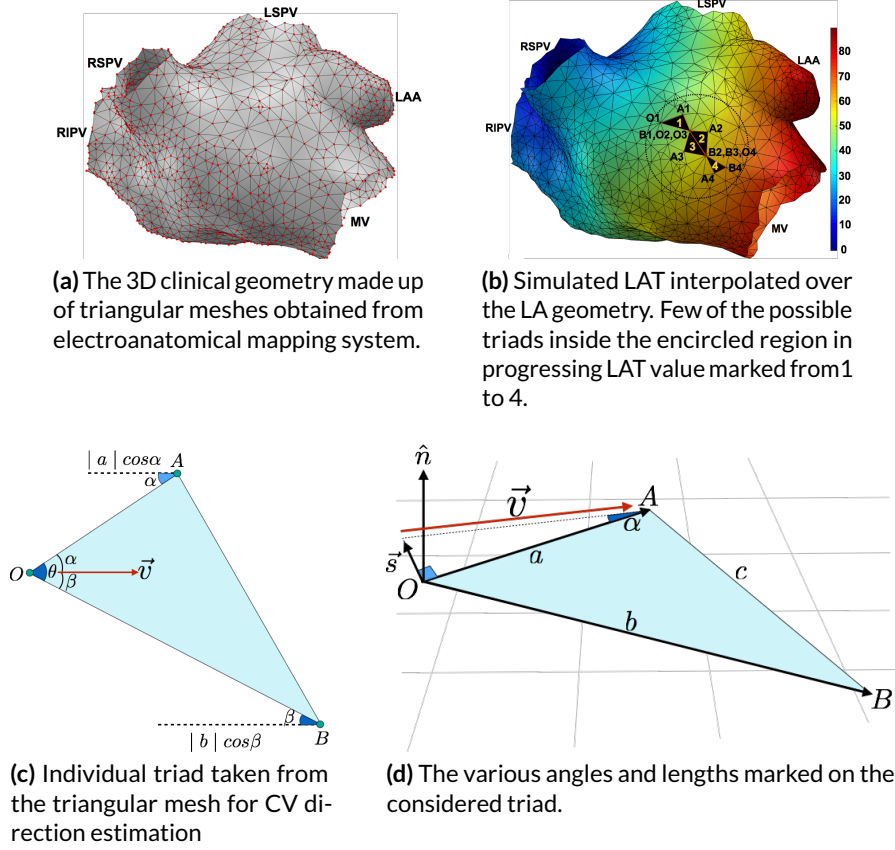


Figure 10.7: Representation of the triangulation method for CV estimation using all nodes [124]. The points of triad were assumed to be in the same plane. The selection of triad is represented for the encircled region in b . The velocity is arbitrarily assumed making an angle α and β with the triad points.

$$|a| = \sqrt{(x_a - x_o)^2 + (y_a - y_o)^2 + (z_a - z_o)^2} \quad (10.47)$$

$$|b| = \sqrt{(x_b - x_o)^2 + (y_b - y_o)^2 + (z_b - z_o)^2} \quad (10.48)$$

$$|c| = \sqrt{(x_a - x_b)^2 + (y_a - y_b)^2 + (z_a - z_b)^2} \quad (10.49)$$

where, a , b and c are the edge lengths respectively. Using the trigonometric formulas of the triangle, the velocity vector was defined as,

$$\cos \alpha = \frac{v \cdot t_{oa}}{|a|} \quad (10.50)$$

$$\mathbf{v} = \frac{|a|}{t_{oa}} \cos \alpha \quad (10.51)$$

The velocity vector was making an angle β with the vector OB , having an edge length of b ,

$$\begin{aligned}\cos \beta &= \frac{v \cdot t_{ob}}{|b|} = \cos(\theta - \alpha) \\ \frac{v \cdot t_{ob}}{|b|} &= \cos \theta \cos \alpha + \sin \theta \sin \alpha\end{aligned}\quad (10.52)$$

$$\mathbf{v} = \frac{|b|}{t_{ob}}(\cos \theta \cos \alpha + \sin \theta \sin \alpha)\quad (10.53)$$

Combining the above equations to get the angles,

$$\frac{|b|}{t_{ob}}(\cos \theta \cos \alpha + \sin \theta \sin \alpha) = \frac{|a|}{t_{oa}} \cos \alpha\quad (10.54)$$

$$\alpha = \tan^{-1} \left(\frac{\frac{t_{ob}|a|}{t_{oa}|b|} - \cos \theta}{\sin \theta} \right)\quad (10.55)$$

$$\cos \theta = \frac{(|a|)^2 + (|b|)^2 - (|c|)^2}{2(|a|)(|b|)}\quad (10.56)$$

The direction vectors were calculated on rotational basis. The direction perpendicular to the cross product of $\hat{\mathbf{a}}$ and $\hat{\mathbf{b}}$ gives the CV vector $\hat{\mathbf{v}}$.

$$\hat{\mathbf{n}} = \hat{\mathbf{a}} \times \hat{\mathbf{b}}\quad (10.57)$$

$$\hat{\mathbf{v}} = R \times \hat{\mathbf{n}}\quad (10.58)$$

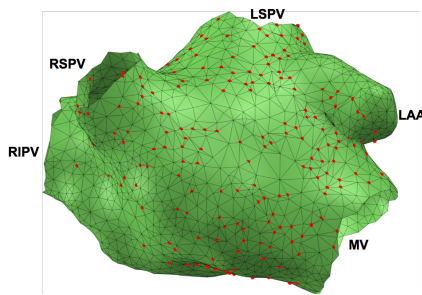
Unlike the triangulation method, the rotational matrix R was defined as

$$R = \begin{bmatrix} \cos \alpha + n_x^2(1 - \cos \alpha) & n_x n_y(1 - \cos \alpha) - n_z \sin \alpha & n_x n_z(1 - \cos \alpha) + n_y \sin \alpha \\ n_y n_x(1 - \cos \alpha) + n_z \sin \alpha & \cos \alpha + n_y^2(1 - \cos \alpha) & n_y n_z(1 - \cos \alpha) - n_x \sin \alpha \\ n_z n_x(1 - \cos \alpha) - n_y \sin \alpha & n_z n_y(1 - \cos \alpha) + n_x \sin \alpha & \cos \alpha + n_z^2(1 - \cos \alpha) \end{bmatrix}$$

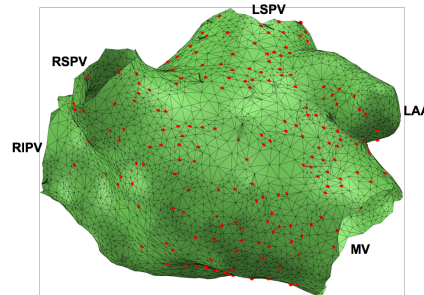
In the course of this research, at this stage, the simulated LATs were used as an input for the CV estimation at all the vertices of the triangular mesh. This was because in simulations, a high resolution map can be generated. This was a preliminary stage for estimating the CV using the spatiotemporal coordinates. During simulation the triangular mesh obtained from the electroanatomical mapping system were used as input. The LATs were computed at all the nodes using the FaMaS as explained in chapter 5 of this thesis. All the clinical geometries were imported and processed using MATLAB. To get denser geometries, mesh refinement was done introducing intermediate nodes before LAT simulation. The details of the mesh refinement and the simulation has been explained in section 7.5. These generated LAT maps had mesh resolutions that is done twice with approximately 1400 and 55000 numbers of nodes, depending upon the density of nodes of the triangular mesh. Some of the LAT maps used for CV calculation using all the vertices of the triangular mesh are represented in Figure 13.1, Figure 13.2, Figure 13.4 and Figure 13.7. The magnitude and the directions of the estimated CV are represented and discussed in the result section of this thesis.

This case was used for CV estimation of the AFlut cases. The implementation for this method with the flutter case for CV estimation was done in MATLAB and the results are described and discussed in the result section of this thesis.

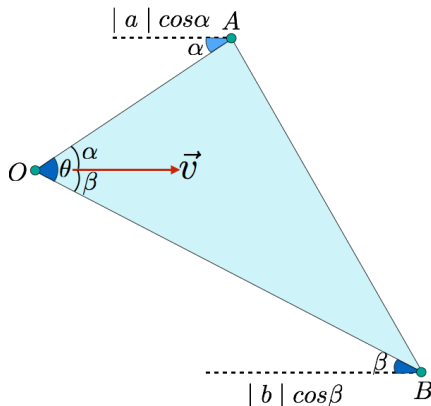
10.2.2 CV for Nodes with Selected SpatioTemporal Coordinates



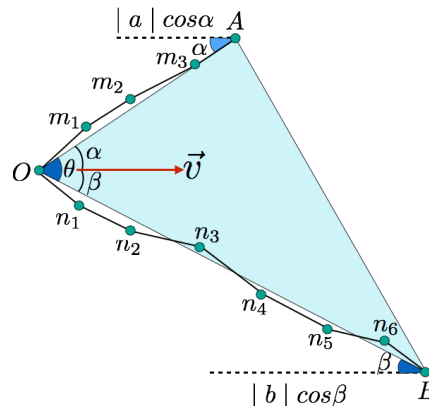
(a) Triangular mesh on the clinical geometry. Number of nodes with temporal information (marked with red dots) is smaller than the triangular mesh vertices.



(b) Refined geometry after introducing new nodes. The location with the temporal information remained unaltered but are also included in the triangular mesh as vertices.



(c) Triangulation method representation for a triad



(d) Modified triangulation method representation. Intermediate nodes were included to get the distances covered by propagating wavefront from one node to the other, involved in the triad.

Figure 10.8: Representation of the modified triangulation method, that involves the intermediate nodes to get the distances covered by propagating wavefront from one node to the other. Unlike in [124] the points in triad might or might not lie on the same plane.

Unlike the previous case, where all the vertices of the triangular mesh had the temporal coordinate value (called LAT), there were cases when only some of the vertices have the temporal coordinate (i.e., $L \leq T$ with no division of data). Since the physicians use mapping catheters such as LASSO, PentaRay etc. in the clinical environment the mapping was done by voluntarily moving the catheter inside endocardium, ending up in the triangular mesh and with recorded electrograms at some of these nodes. These electrograms were used to get the LAT. In these realistic situations, the CV estimation was done using nodes with selected

spatiotemporal coordinates. Therefore, this was closer to the clinical situations, when the recording locations were smaller than the number of the vertices of the triangular mesh. As represented in Figure 10.8a, the number of triangular polygons which form the geometry was much larger than the locations (marked by red dots) with the temporal information. These vertices marked as red dots had spatiotemporal coordinates and were used in the triads for CV estimates. All the other nodes of the surface mesh were used for estimating the distances between the nodes involved in the triad to get a closer estimation of the distances over the geometry. **In this, the modified triangulation method estimates the angular information considering the triads formed using the nodes (with temporal information) to be in the same plane, while to get the distance between nodes (of the selected triad), the Dijkstra shortest path algorithm was used.** This method does the global as well as regional CV estimation. The rotation matrix also works as expressed by the equation in the previous section since to get the direction vector the angular information was used and the points on the triad were assumed to belong to one plane.

In this, since the distance via the intermediate nodes was used, the refinement was an important factor to get the distance along the curvature of the geometry. An accuracy of 0.2mm was achieved by up to 5 iterations. With each iteration 3 new nodes were introduced in the existing face of the triangular mesh. This means adding one node at the centre of each edge as explained in the mesh refinement section of this thesis. For the above stated case, the refined geometry is represented in Figure 10.8b. The CV estimation was done as presented in Figure 10.8d. The mathematical equations used after the preprocessing step are as explained below.

To get the angular information the three points are assumed to be in the same plane and therefore the trigonometric formulas yield:

$$\alpha = \tan^{-1} \left(\frac{\frac{t_{ob}|a|}{t_{oa}|b|} - \cos \theta}{\sin \theta} \right) \quad (10.59)$$

$$\cos \theta = \frac{(|a|)^2 + (|b|)^2 - (|c|)^2}{2(|a|)(|b|)} \quad (10.60)$$

$$\hat{n} = \hat{a} \times \hat{b} \quad (10.61)$$

$$\hat{v} = R \times \hat{n} \quad (10.62)$$

$$R = \begin{bmatrix} \cos \alpha + n_x^2(1 - \cos \alpha) & n_x n_y(1 - \cos \alpha) - n_z \sin \alpha & n_x n_z(1 - \cos \alpha) + n_y \sin \alpha \\ n_y n_x(1 - \cos \alpha) + n_z \sin \alpha & \cos \alpha + n_y^2(1 - \cos \alpha) & n_y n_z(1 - \cos \alpha) - n_x \sin \alpha \\ n_z n_x(1 - \cos \alpha) - n_y \sin \alpha & n_z n_y(1 - \cos \alpha) + n_x \sin \alpha & \cos \alpha + n_z^2(1 - \cos \alpha) \end{bmatrix}$$

To get the magnitude of the CV, we need to go over the intermediate nodes (including all of them) to get the appropriate distance travelled by the waveform to cover the atrium. Therefore in Equation 10.64, parameter b was replaced by B , and the CV magnitude was defined as

Algorithm 10.1 The triangulation in 3D for CV calculation for respective dataset.

if $size(VerticesInDataset, 2) > 3$ **then**

For $Triangle = 1 : end$ (10.66)

$O =$ node with min LAT From Triangle 1 (10.67)

 Define A and B (10.68)

$T_o =$ LAT for O (10.69)

 Determine T_a and T_b (10.70)

$$\alpha = \tan^{-1} \left(\frac{\frac{t_{ob}|a|}{t_{oa}|b|} - \cos \theta}{\sin \theta} \right) \quad (10.71)$$

$$\cos \theta = \frac{(|a|)^2 + (|b|)^2 - (|c|)^2}{2(|a|)(|b|)} \quad (10.72)$$

$$\hat{n} = \hat{OA} \times \hat{OB} \quad (10.73)$$

$$|B| = |\overrightarrow{On_1}| + \sum_{N=2}^{N=n} |\overrightarrow{n_{N-1}n_N}| + |\overrightarrow{n_nB}| \quad (10.74)$$

$$|CV| = \frac{|B|}{t_{ob}} (\cos \theta \cos \alpha + \sin \theta \sin \alpha)$$

$$\overrightarrow{CV} = \hat{R} \times \hat{n} \quad (10.75)$$

end for loop (10.76)

end if

$$|B| = |OB| = Distance_{via\ intermediate\ nodes} \quad (10.63)$$

$$\mathbf{v} = \frac{|B|}{t_{ob}} (\cos \theta \cos \alpha + \sin \theta \sin \alpha) \quad (10.64)$$

$$\mathbf{B} = |\overrightarrow{On_1}| + \sum_{N=2}^{N=n} |\overrightarrow{n_{N-1}n_N}| + |\overrightarrow{n_nB}| \quad (10.65)$$

All the intermediate nodes n_1 to n_6 and m_1 to m_3 might or might not lie on the same plane. They are part of the triangular mesh that makes up the 3D electroanatomical geometry.

10.2.3 CV for Selected Datasets with given SpatioTemporal Coordinates

As the catheter moves during the electroanatomical mapping, inside the atrium, the contact of the catheter electrodes and the endocardium surface keeps changing. This leads to variable catheter configurations inside the atrium. This was the reason why the CV estimation method must be able to deal with various catheter shapes and changing wall contact. This was basically regional CV estimation using the temporal and spatial information obtained after

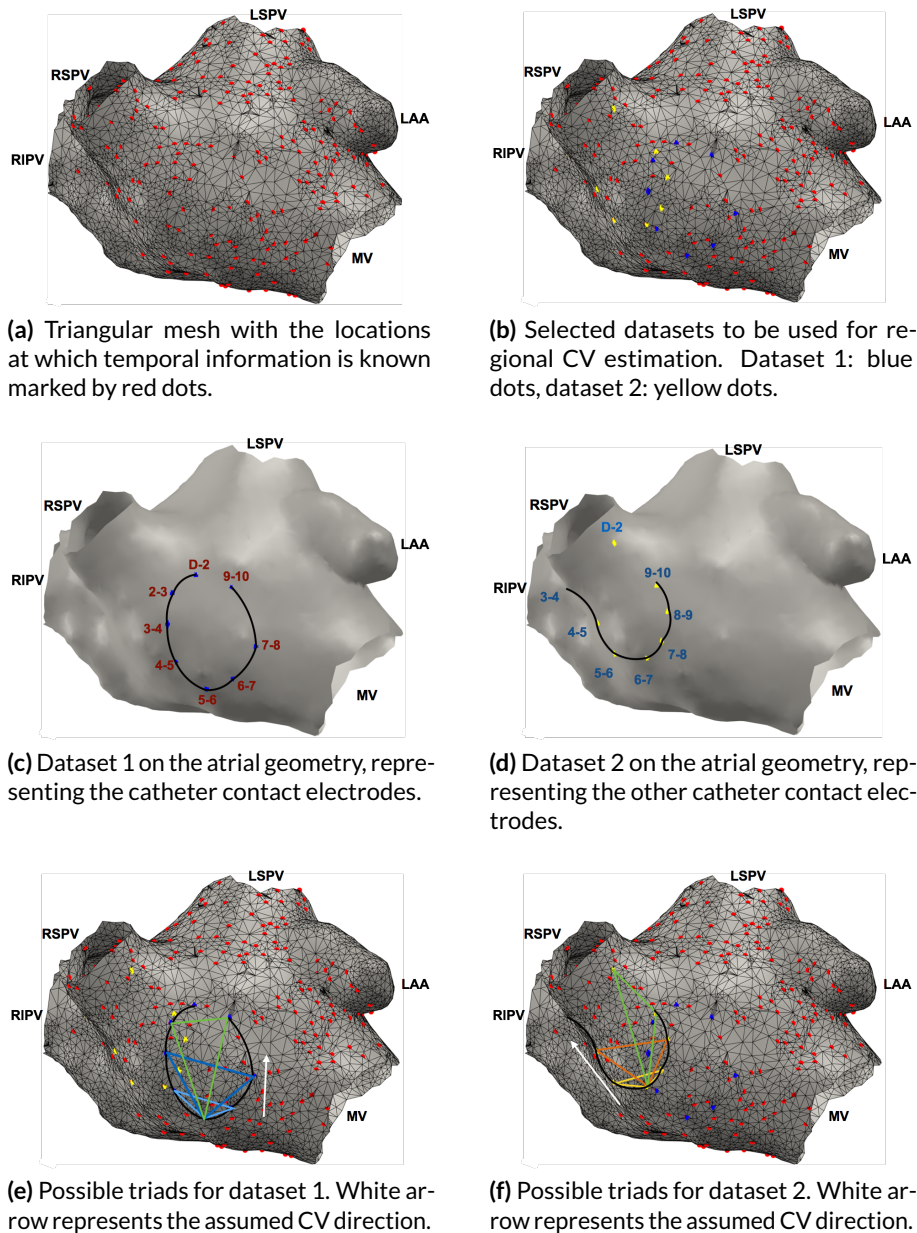


Figure 10.9: CV estimation for selected datasets. The selection is done based on the clinical data and spatial and temporal assumptions.

preprocessing for the fibrillation clinical cases. For this type of data, the spatiotemporal information was divided into various datasets and used for CV estimation (i.e., $L \leq T$ and D exist). The dataset segregation depends on the parameters such as clinical conditions, data types, catheter contact etc. The dataset is the simultaneously acquired data in the form of bipolar electrograms, for one specific stable catheter position. The mathematical formulas as specified in the sections 10.2.2 were used with the same assumption but instead of all triads, triads for respective datasets were considered. The electrophysiological reasoning of

doing so is explained in section 10.4.2 under the clinical CV estimation. The few examples of the datasets and the triads used for CV estimation are represented in Figure 10.9. Since these data were obtained using the 10 pole or 20 pole LASSO catheter, therefore for the represented two (out of the 4) catheter positions the electrodes from D-2 to 9-10 annotations are represented that were used for CV estimation. These electrodes and shape of catheter could vary with the type of catheter. For a 20 pole LASSO the shape is different and up to 20 electrodes can be observed having the endocardial contact. For a specific dataset the spatial coordinate with least temporal value was taken as node O and the other as A and B respectively with increasing LAT value. For the CV estimation, the intermediate nodes were used for estimating the distance travelled by a propagating wave over the geometry and the triad was assumed to be planar for angle determination. Since for the stable catheter positions, the number of contact electrodes varies from 3 up to 10 or 20 respectively depending upon the catheter used, therefore, more than one triad were possible for a particular dataset. Thus, more than one CV could be estimated for the respective dataset (stable catheter position) as represented in Algorithm 10.1. The results associated with this CV estimation are discussed and represented in the result section of this thesis.

10.3 CV Estimation for Simulated Cases

Simulations are done to mathematically replicate the clinical scenarios in an idealistic and controlled way. This can give an insight into the mechanism responsible for changes by various physiological parameters separately. By changing the parameters in simulations, the various parametric analysis can be performed. There exist various simulation software and models to replicate the depolarisation wavefront propagation over the atrium and also to analyse the ion concentration effects [135] [136]. A lot of parametric analysis can be performed with respect to the in-vivo study. In simulations various parametric conditions are included, which are modelled to behave similar to the clinical environment. As per the interest of the researcher, these parameters can be analysed one by one, to understand the effect of an individual electrophysiological parameter. During the course of this thesis, the propagation speed is taken as a test parameter on the atrial geometry. The simulations were required to produce the spatiotemporal information on a given 3D atrial geometry so as to get the excitation propagation over the atrium for various homogeneous and heterogeneous scenarios. This was later on used to benchmark the algorithm of CV estimation using the ground truth values available for simulations. The global and regional CV was estimated on the clinically obtained 3D geometries. Therefore, the algorithm was developed keeping the clinical applications in mind. This part of the thesis represents how the CV estimation algorithm was applied for various types of datasets. The simulations are done for five cases namely:

1. Homogeneous propagation (i.e., $L=T$ and $L<T$ and D does not exist, as mentioned in Figure 10.5 and Figure 10.6)
2. Heterogeneous propagation (i.e., $L=T$ and $L<T$ and D does not exist, as mentioned in Figure 10.5 and Figure 10.6)
3. Stable catheter positions (i.e., $L\leq T$ and D exist as mentioned in Figure 10.5 and Figure 10.6)
4. Biatrial geometry (i.e., $L=T$ and $L<T$ and D does not exist, as mentioned in Figure 10.5 and Figure 10.6)
5. 2D triangular patch data (i.e., $L=T$ and $L<T$ and D does not exist, as mentioned in Figure 10.5 and Figure 10.6)

Table 5.1 also gives an insight into the various simulation scenarios under analysis, for which the CV estimation was done and analysed. For all the above stated five cases the CV estimation was done using the modified triangulation method and the method was divided into two sections namely:

1. Using all nodes having spatiotemporal coordinates, and
2. Using the specific datasets having spatiotemporal coordinates.

10.3.1 Using all Nodes having SpatioTemporal Coordinates

The 2D and 3D CV estimation was done using the modified triangulation method. The CV estimation for 2D data, was done for the simulated LAT map for the triangular patch as represented in Figure 13.3. Whereas, the CV estimation for 3D data was done for the clinically obtained geometries with simulated LAT maps as represented in chapter 13. The various clinical geometries used to simulate the LAT are represented in Figure 5.1. Since the requirement was to get the excitation propagation pattern for homogeneous and heterogeneous cases for 2D and 3D data, therefore, the FaMaS method was used as explained in Chapter 5. For both 2D and 3D simulations, the speed of propagation depending on the various tissue types as assigned on the clinical geometries are also explained in chapter 5. The input speeds are the ground truth for the CV estimation algorithm. Table 5.1 and Table 5.2 give insight into the various tissue classes used for the clinical and simulated biatrial geometries, i.e. the different sets of the ground truth input speeds. As explained before, the Eikonal equation was used for the LAT simulation using the FaMaS method. With these simulations, the depolarisation wavefront propagation patterns were modelled for

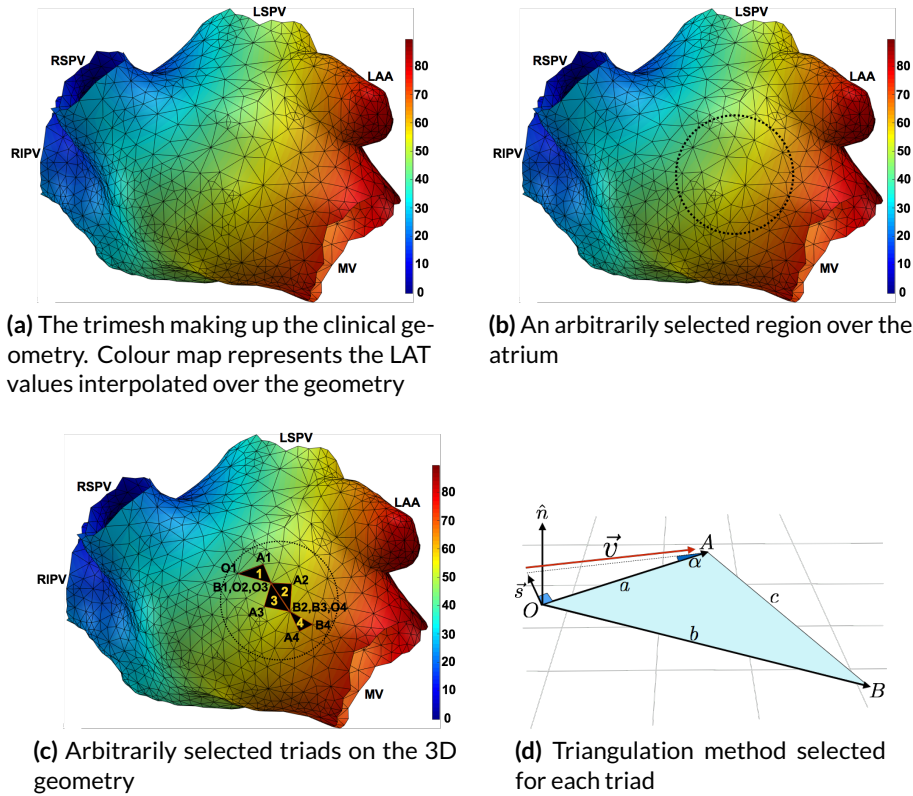


Figure 10.10: CV estimation for selected datasets. The selection is done based on the spatiotemporal information that makes up the 3D geometry. Time of colour bar in *ms*.

idealistic scenarios and used for CV estimations.

From simulation, the spatiotemporal coordinates were available for all the vertices of the triangular mesh in case of both the 2D or 3D geometries therefore, the CV estimation was done using the original triangulation method as explained in section 10.2.1, assuming the triad belonging to a plane. The spatial coordinates are the vertices of the triangle of the atrial geometry while the temporal coordinates are the LAT values simulated at each node. A diagrammatically step wise description of the method is presented in Figure 10.10. The propagation starts from blue region where the trigger node is manually selected and then it moves forward until it covers the entire atrial surface. Regions with heterogeneous propagation were manually selected for LAT simulation and later the regional CV has been calculated. The calculated CV for both the homogeneous and heterogeneous cases have been visualised on the respective geometries.

The visualisation of the CV on the respective geometry gives an insight into the regional behaviour of the atrial substrate. The results obtained for the 2D and 3D homogeneous, heterogeneous and biatrial simulations along with the accuracy of the algorithm and the

associated parametric analysis has been explained in the result section of this thesis.

To get the accuracy and robustness of the algorithm, the analysis was done changing the resolution of the available triangular mesh, by introducing and removing the nodes respectively. To do this, the mesh refinement was done as explained in chapter 7. The next analysis was done introducing gaussian noise to the simulated LAT map. The CV estimation was done for the spatiotemporal data with and without noise. The corresponding results are explained and discussed in chapter 16.

10.3.2 Using Selected Clinical Positions on Simulated LAT Map

Simulations are the idealistic conditions imitating the clinical scenarios. One step forward in the CV estimation is to use the clinically obtained electrode positions on the simulated LAT map to get the accuracy of the method and to benchmark the results with respect to the ground truth values. In this section, the simulated LAT maps for the stable catheter positions were taken into consideration for CV estimation. This is to benchmark the algorithm and to estimate the regional CV for respective depolarisation wavefronts. The CV estimation method explained in section 10.2.3 was used since here the various catheter positions were taken into consideration for CV estimation. Each catheter position was assumed as a dataset as represented in Figure 10.9. The simulated LAT on the clinical geometry and some of the various clinically obtained catheter positions are presented in Figure 10.11. This represents the simulated LAT over the geometry and Figure 10.11*a* to *f* gives some of the catheter positions that build the various datasets on the simulated LAT map. The triad consideration for two catheter positions has been demonstrated in Figure 10.9*e* to *f*. Similarly the triads are taken for other catheter positions in the incremental LAT values. The modified triangulation method taking the intermediate nodes, was used for CV estimation and the results are explained and presented in the result section of this thesis. The comparison of estimated CV and the ground truth value was done along with other parametric analysis.

10.4 CV Estimation for Clinical Cases

There are various types of clinical and canine data recorded for CV estimation. A brief introduction of these is given in Table 10.1. The various types of clinical data under analysis for CV estimation are namely:

1. CV estimation for AFlut data from RHYTHMIA mapping system, Boston Scientific, USA (i.e., $L=T$ and $L<T$ and D does not exist, as mentioned in Figure 10.5 and Figure 10.6)

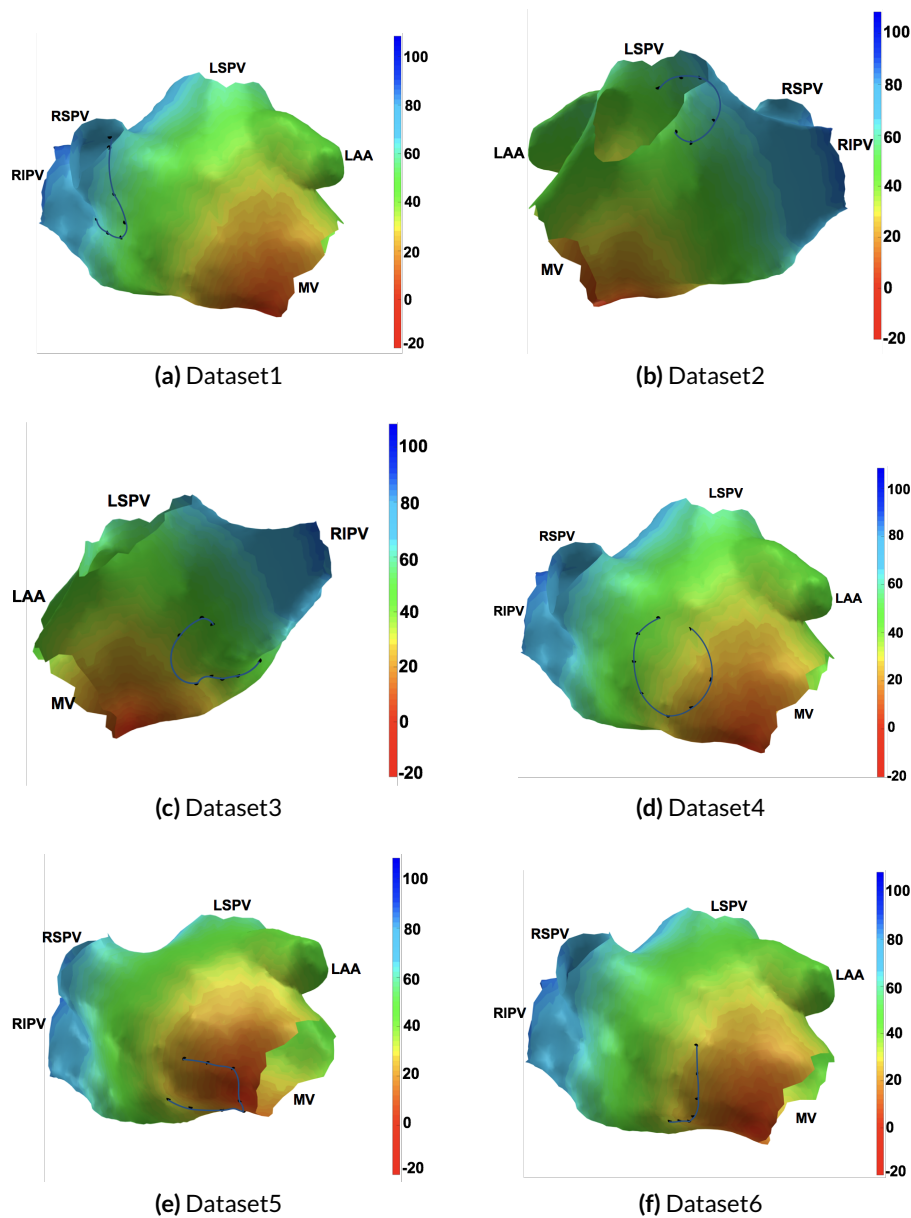


Figure 10.11: The simulated LAT map interpolated over the clinical geometry. Red gives the early activation and blue gives the late activation. The various catheter positions as the catheter gets in contact with the endocardium. Each position represents a new dataset used for CV estimation with arbitrarily selected catheter electrodes in contact inside the atrium.

2. The stimulus protocol clinical data obtained from Velocity mapping system, St. Jude Medical, USA (i.e., $L < T$ and D exist, as mentioned in Figure 10.5 and Figure 10.6)
3. Canine data obtained using the patch catheter, Unimap system. (i.e., $L = T$ and $L < T$ and D does not exist, as mentioned in Figure 10.5 and Figure 10.6)

Table 10.1: Different possibilities of clinical cases and the data availability.

| S.No. | | Low density map | High density map |
|-------|--|-----------------|------------------|
| 1 | Flutter Cases | ✓ | ✓ |
| 2 | Stimulus protocol SR mapping | ✓ | |
| 3 | Stimulus protocol AFib mapping (Human) | ✓ | |
| 4 | Canine data mapping | ✓ | ✓ |

Since the data were obtained using different modalities, therefore different preprocessing measures were taken into consideration to obtain the spatiotemporal information. The modified triangulated algorithm was used for CV estimation using these data, but the assumptions differed depending on the type of data under analysis. A brief introduction of the preprocessing of the clinical cases is given before the CV estimation method description for each of the above stated case.

Moreover the recording was done voluntarily by the physicians depending upon the region to be mapped. Therefore the recorded locations were different from the triangular mesh vertices and were included in the triangular mesh without altering the available triangular mesh so as to keep the curvature information intact. The locations with the temporal information were then included into the available triangular mesh and the CV estimation was done.

10.4.1 CV Estimation for Flutter Case

AFlut and AFib are problems due to abnormal heart rate and rhythm. In case of fibrillation, there is a chaotic depolarisation wavefront pattern. While in case of flutter, there is an abnormal depolarisation wavefront propagation pattern which is repetitive in nature. Due to the periodic nature, it can be assumed that the activated sites have the same pattern, even if the recording is done for more than one depolarisation wavefront. Thus, instead of dividing the data into various datasets, the entire data and all the vertices were taken into consideration for CV estimation. For the regional and global CV estimation for flutter case clinical data, the spatiotemporal coordinates were needed. Using the RHYTHMIA mapping system, the LAT map was obtained along with the triangular mesh information. The LAT values were obtained after smoothening from the mapping system. Since the data were obtained as LAT map, but not electrograms, the feature extraction and preprocessing steps were not needed for dealing with these data. The triangular mesh was available with endocardial LAT values as represented in Figure 10.12c and Figure 10.12d. LATs were available for all the vertices of the triangular mesh. The depolarisation wavefront propagation is from blue to red region being the early and late activation sites respectively. The triangulation method from section 10.2.1 was used for CV estimation. The resolution and density of the recording points was very good compared to the data obtained using the LASSO catheter. Very interesting results for CV magnitude and direction, clearly showing the slow and fast propagation and the

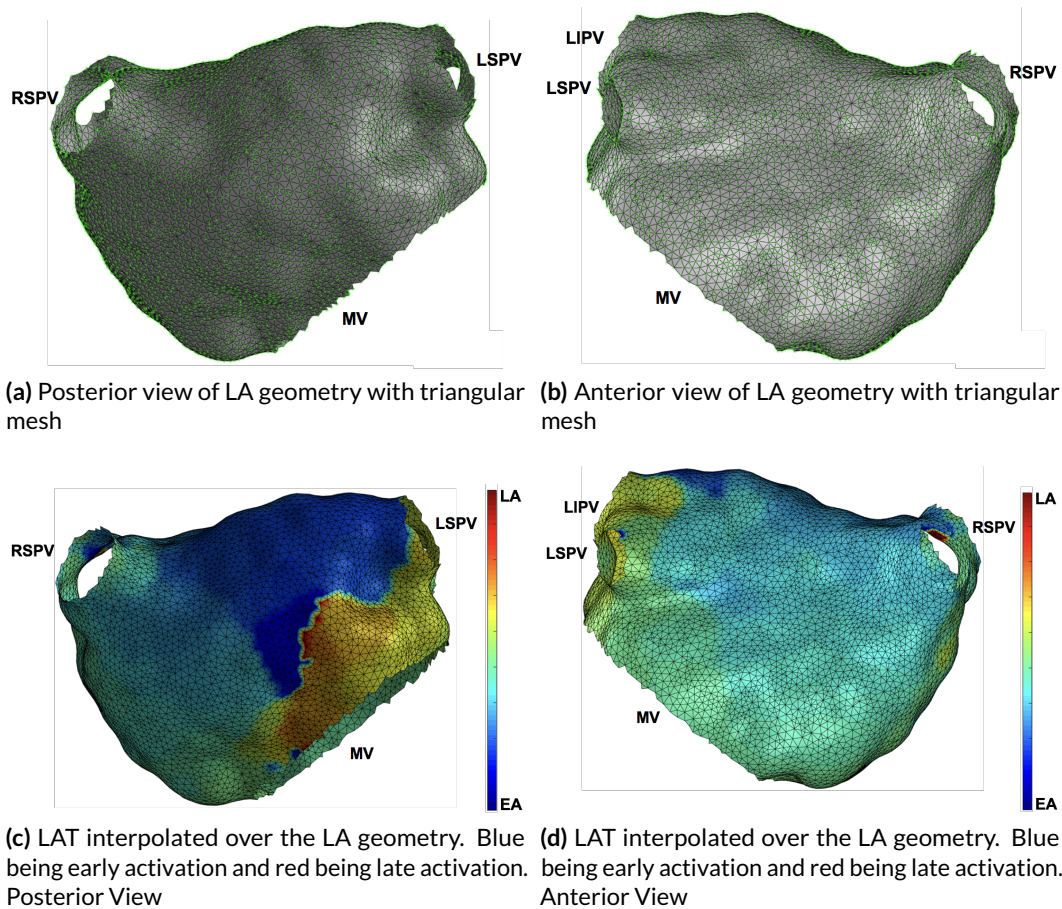


Figure 10.12: Posterior and anterior view. Representation of the clinical left atrial geometry and the LAT map with the triangular mesh geometry.

collision and dispersion of depolarisation wavefront were obtained with this set of clinical data and are discussed and represented in the result section of this thesis.

10.4.2 CV Estimation for Fibrillation Case Mapped during SR

During AFib the depolarisation wavefront propagation pattern is chaotic in nature. With every trigger the depolarisation wavefront might or might not take the same propagation path and pattern to cover the atrium. This highly depends on the arrhythmogenic substrates present on the atrium [130]. The slow conducting region alters the propagation pattern by partially allowing or hampering the propagation of the depolarisation wavefront [124]. The total of four clinical fibrillation cases were under analysis with the stimulus protocol for CV estimation. The mapping and recording of all the cases was done during sinus rhythm. The details about all the clinical cases along with the type of data obtained using an electroanatomical mapping system have been explained and represented in chapter 6 of this thesis.

The clinical cases were acquired after stimulation, the stimulus protocol used for the clinical cases were $400 - 350ms$ and $380 - 320ms$ as represented in Figure 8.2 and Figure 8.1 and were explained in detail in chapter 8 of this thesis. The mapping for all the four cases was done during sinus rhythm (SR) and for S1 stimulation and S2 stimulation. Therefore, three types of atrial depolarisation wavefronts were analysed for all the clinical cases namely:

1. Triggered by SR
2. Triggered by S1 stimulus
3. Triggered by S2 stimulus

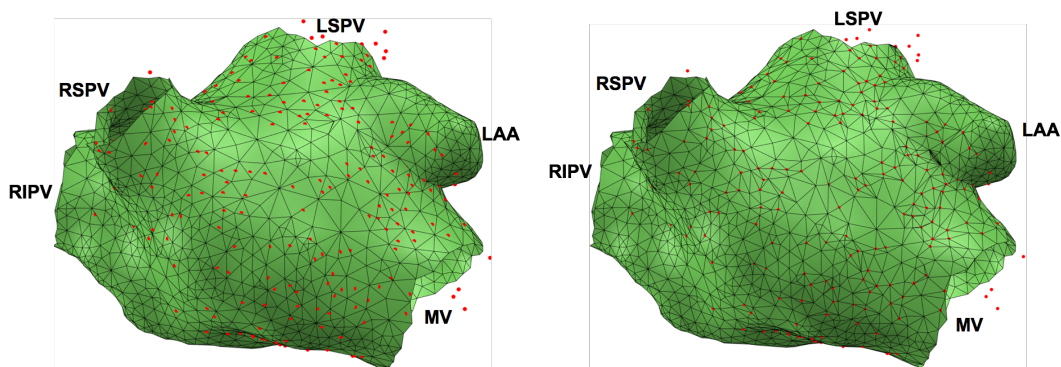


Figure 10.13: The triangular mesh obtained by mapping the atrium during routine procedure with locations (red dots) at which electrograms are recorded and the geometry with these locations included in the triangular mesh. a). The surface points on the atrial geometry with the triangular mesh and recorded locations (red dots). b). The recorded locations included in the existing triangular mesh.

Therefore, at all atrial locations, three activities should be present on the electrograms in idealistic conditions, i.e when there are no artefacts and with the catheter in good contact with the endocardium. The electrograms were recorded with a sampling frequency of $2.0345 kHz$. And the electrograms of $1.5 seconds$ were recorded at all the locations. These $1.5 second$ long atrial electrograms had three different types of atrial complexes as represented in Figure 8.3 and Figure 8.4 for the aligned and non aligned atrial complexes. The CS catheter atrial complexes were used as the reference and the depolarisation wavefront propagations due to all the triggers were analysed separately as explained in chapter 8. This gives in total 12 depolarisation wavefronts that were considered for CV estimation. Before estimating the CV for the 12 depolarisation wavefronts, the preprocessing of the clinical data was required to obtain the spatiotemporal information at the atrial locations. The various steps for preprocessing are briefly described in the following steps:

Step 1: Extracting the physician-selected segments out of entire data sets using markers voluntarily selected by the physician based on his expertise and experience. The atrial complexes in the extracted segments depend on the data type. For stimulus protocol data, the segments contained SN activities, S1 trigger artefact, S1 triggered atrial activity complex, S2

trigger artefact and S2 triggered atrial activity complex.

Step 2: Finding the offset between the recorded locations and the location of the recorded segment. The various locations could also be extracted from the 3D electroanatomical mapping data. The red dots in Figure 10.13a, represent the recorded locations. The triangular mesh is the geometrical information obtained from the electroanatomical mapping system.

Step 3: The triangular mesh and the recorded locations are compared and included in to the triangular mesh geometry. A refinement of the triangular mesh was done till the smallest distance between surface points and closest triangular mesh node became $< 0.2\text{mm}$. Up to 5 iterations were done to get the desired condition. This has been represented in Figure 14.5.

Step 4: Removing the artefacts obtained from the system generated due to no contact electrode or no connection with the mapping system. To do this, the P2P amplitude threshold was kept to be 0.08mV . The electrograms with overall P2P amplitude $< 0.08\text{mV}$ were discarded from CV estimation. The other artefacts were different types of noise. These were removed using the high pass (HP) and low pass (LP) filters with the 30Hz and 300Hz filtering frequencies respectively. The 50Hz noise was also removed using the notch filter.

Step 5: The recorded locations without artefacts were then included in the triangular mesh using MATLAB. The included recording locations within the triangular mesh are presented in Figure 10.13b.

Step 6: The coronary sinus (CS) catheter signals were used to mark the stimulus. Out of the four electrodes on the CS catheter one was selected to be used as reference. This was done by comparing the bipolar electrograms from all of them. This comparison is done based on their activation complexes. Out of the four bipolar signals the one is selected with clear activation complexes. This electrode also corresponds to be the same which was used for stimulation.

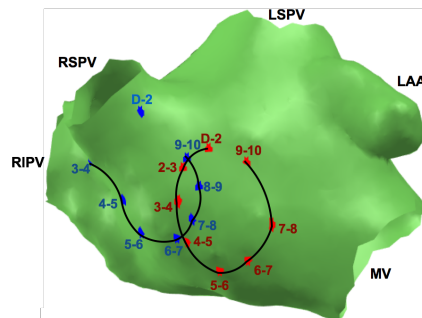


Figure 10.14: Two stable catheter positions of the 10 pole LASSO catheter inside the atrium. Annotated are the bipolar electrodes in contact with the endocardium.

As output of the preprocessing steps, the clinical electrograms are free from various noise and artefacts with corresponding spatial coordinates. These electrograms were used for LAT estimation using NLEO [64] as described in detail in chapter 9 of this thesis. The three activities termed as S1, S2 and SN are separated and analysed for CV estimation using the spatiotemporal coordinates.

During fibrillation, due to the presence of arrhythmogenic substrates and high fibrosis, there is a very high probability of changes in the path and the pattern of the depolarisation wavefront with every trigger since the propagation is chaotic in nature. Thus, for CV estimations the spatiotemporal coordinates could not be used as explained in section 10.2.2 of this thesis. Unlike the flutter case, in fibrillation (mapped during SR), datasets were formed that were from one single depolarisation wavefront. These datasets were then used for CV estimation.

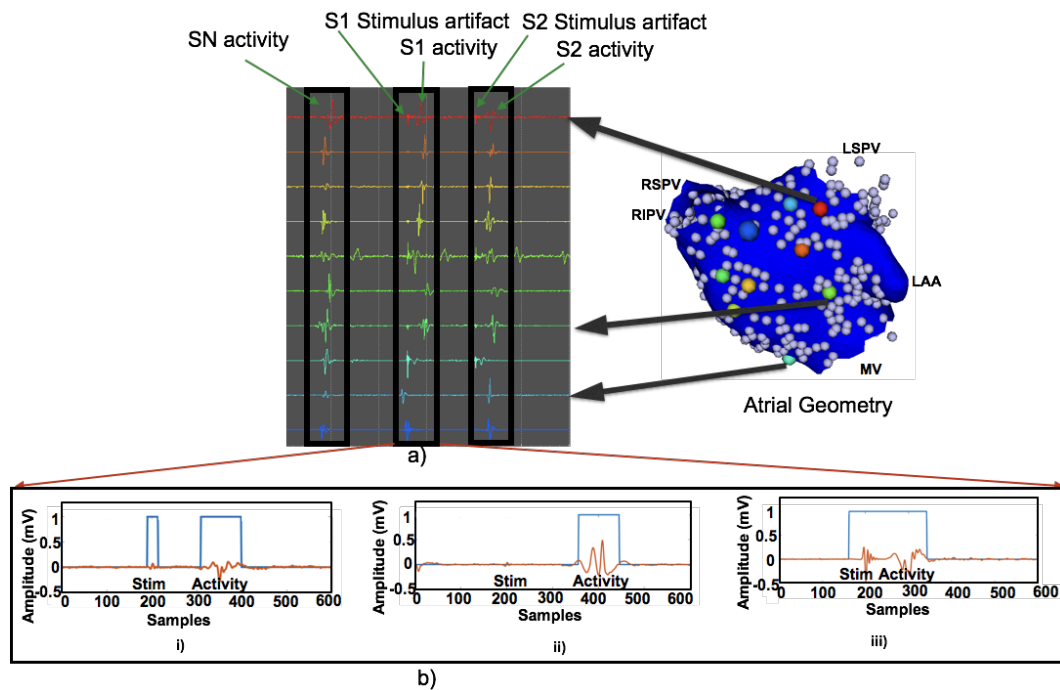


Figure 10.15: Representation of the magnitude of the activity that can be small or comparable with the stimulus artefact magnitude depending upon the recording location

As the catheter moves, the shape of the catheter and the wall contact changes throughout the recording. This is done to obtain a better coverage of the atrium. Few from the various possibilities for various catheter shapes and contact electrodes have been represented in Figure 9.15 to Figure 9.20. When the depolarisation wavefront triggers from SR, S1 or S2, depending upon the coverage and type of electrograms obtained, the stable catheter positions record the electrogram for the respective trigger in all the electrodes having contact with the endocardium. After recording at one catheter position, the catheter is moved to a

new location and the recording is done for other locations as well. Therefore, the electrograms corresponding to one stable catheter position are assumed to belong to one trigger and corresponds to one depolarisation wavefront. While the electrograms obtained using the two stable catheter positions might or might not correspond to the same depolarisation wavefront propagation pattern. Therefore, for CV estimation by merging the spatiotemporal information of two different catheter positions as represented in Figure 10.14, might record the instants from 2 triggers which could in-turn result in wrong CV estimation. Once the various catheter positions are extracted, these are classified as various datasets and the CV estimation was done as explained in section 10.2.3 of this chapter.

When taken separately and removing the artefacts, there exist cases where the magnitude of the activity can be small or comparable with the stimulus artefact magnitude depending upon the recording location (Figure 10.15). Also, the temporal distance between the activities and the artefacts changes. In this situation too the NLEO window was used to separate the atrial complexes from the stimulus artefacts and for ventricular far field (VFF) removal.

The bipolar EGMs and the stable catheter positions on the triangular mesh were the inputs obtained from the mapping system. The LATs were estimated from these bipolar EGMs using the non-linear energy operator (NLEO) [64] at all the locations. In NLEO, the energy of the atrial activity is defined as $E = abs(x^2 - x_{n+1}x_{n-1})$. The time of maxima of the NLEO obtained after low pass filtering is called LAT. From the available contact electrodes, the selection of electrodes to be considered in a triad was based on their LATs. In Figure 10.16, the nodes marked as p to w , are those stable locations at which the catheter is in contact with endocardium and at which the bipolar EGMs were recorded. There could be a number of triad combinations from these locations. But in our case, the node with the smallest LAT is marked as the initial node p . Then, the different triads possibilities were obtained in the direction of LAT incremental values. The different triads in this case are namely: pqr , psw and ptv as represented in Figure 10.16b. At least 3 contact electrodes are required from the stable catheter position giving three LATs for one CV calculation. The least delta LAT was kept $4ms$ and the maximum intermediate nodes were kept 29. This was done because of the different possibilities during mapping such as, when the contact electrodes touches and records the EGMs on either side (say anterior or posterior) of the atrial wall or when the wavefront reaches two out of three locations at the same time (or within $4ms$). These facts were checked and taken into account during the preprocessing steps of the analysis.

For each triad and over the triangular mesh, the distance between two stable catheter locations was calculated using the Dijkstra shortest path algorithm as represented in Figure 10.16e and Figure 10.16f, considering all the intermediate nodes. Since the depolarisation wavefront travelled over the atrial surface, it was important to take into consideration the distance travelled by the wavefront to reach from one catheter location to the other instead of just the Euclidean distance. To calculate the angle (θ , α and β) at any point on the triad, the

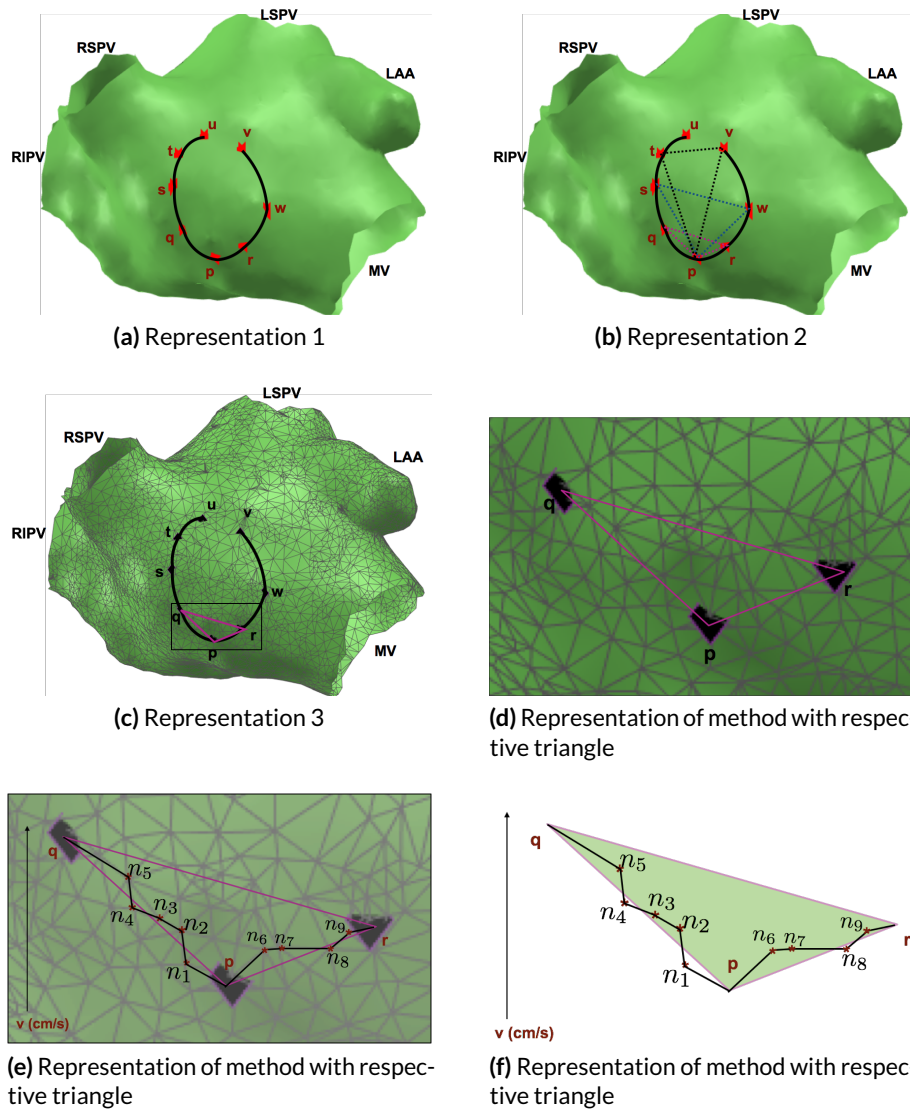


Figure 10.16: Selection of triads for the CV estimations using the incremental LAT pattern.

displacement was taken into consideration as represented in Figure 10.16c. The results obtained from the CV estimate have been represented and discussed in the result section of this thesis.

Graphical User Interface

The graphical user interface (GUI) provides a user friendly environment where the applications of any analysis could be done just by click-control and parameter selection, eliminating the real need to learn the language or commands associated with it.

Chapter 9 and 10 explain the various feature analysis and extractions using the spatiotemporal information obtained from the electroanatomical mapping system. These features were used for the regional and global CV estimation and were also used to mark the arrhythmogenic areas on the atrium. During the course of this research, a GUI was developed using MATLAB to make it easy for any other user to analyse the results obtained for features extracted using the various techniques as explained in the respective sections.

Two GUIs were developed as part of this research project that take the user inputs in terms of the clinical database folder location or the *.mat* file containing LAT map along with the clinical geometry information. The preprocessing and feature determination algorithms were included during the development of the GUI. As an output, the magnitude or the map of the features could be obtained depending on the user interest and selection. This makes it very easy for other users who want to analyse the data without getting into the hassle to understand the logic behind.

11.1 Conduction Time Analysis

As explained, the clinically obtained electrograms were analysed to get the substrate properties beneath the recorded electrodes. Figure 11.1 represents the first GUI developed that can help the user to select the parameters as per interest and has following options that can be utilised during analysis:

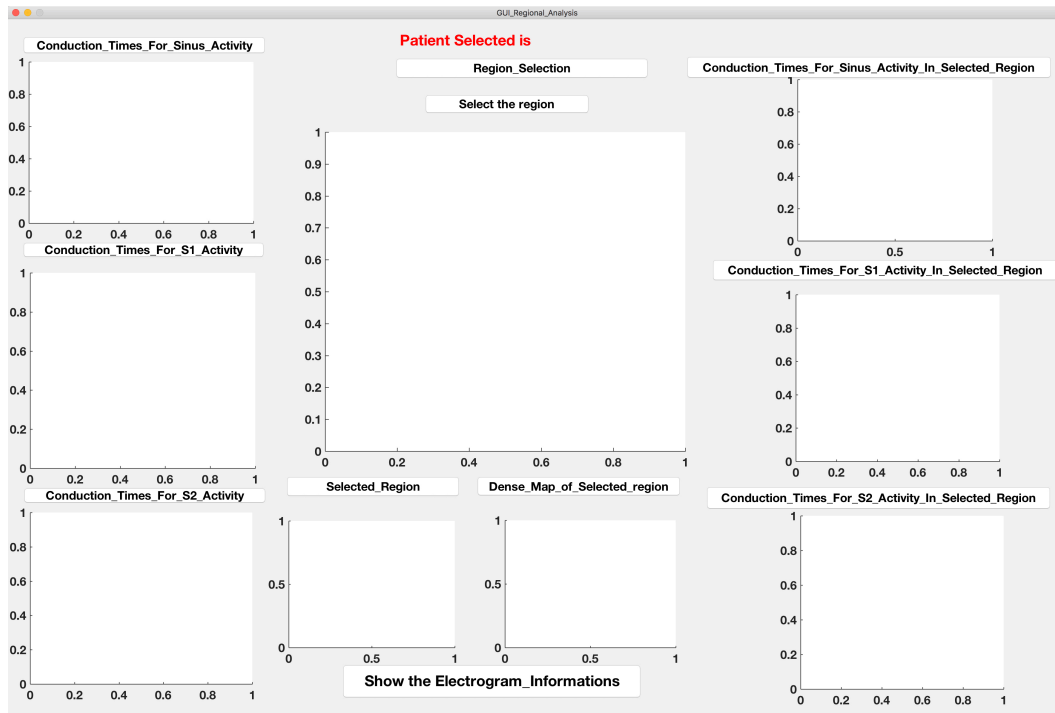


Figure 11.1: Representation of the blank GUI with all the options enlisted

1. Patient selection
2. Region selection
3. Conduction time during sinus rhythm (SR) for the selected patient
4. Conduction time for S1 triggered wavefront for the same selected patient
5. Conduction time for S2 triggered wavefront for the same selected patient
6. Selected region representation with the original triangular mesh
7. Selected region representation with the refined triangular mesh
8. Conduction time during SR for the selected region
9. Conduction time for S1 triggered wavefront for the selected region
10. Conduction time for S2 triggered wavefront for the selected region
11. Electrograms at all the recorded locations inside the selected region

Conduction time in the above GUI represents the local activation time (LAT) interpolated on the atrial geometry. The LAT time is estimated from the electrograms obtained using the NLEO as explained in chapter 9. Figure 11.2 represents the interpolated LAT on the atrium which were imported by selecting the options given in first column of the GUI. The early activation is represented by red and late activation by blue colour. It can be observed that two directions (triggered from SN and CS catheter) of wavefront propagation are represented by these three plots (SN, S1 and S2 respectively) namely the SR and the activities triggered using the coronary sinus (CS) catheter. In order to get the regional information, the next click

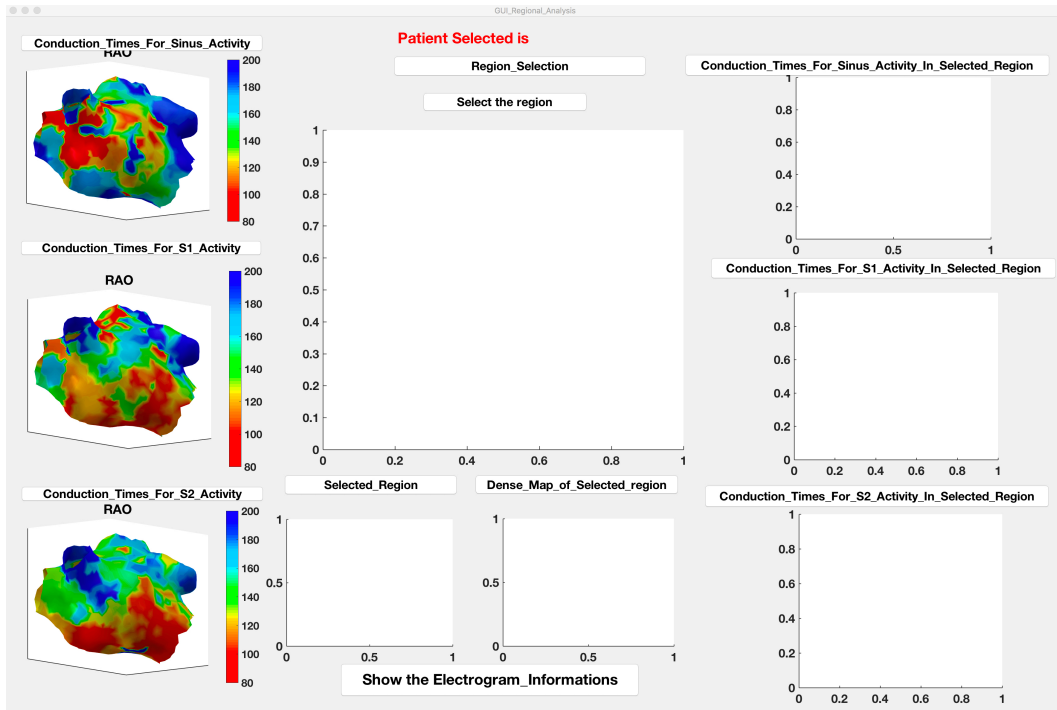


Figure 11.2: GUI with 3D geometries selected. The LAT times are interpolated on the geometry for the respective cases.

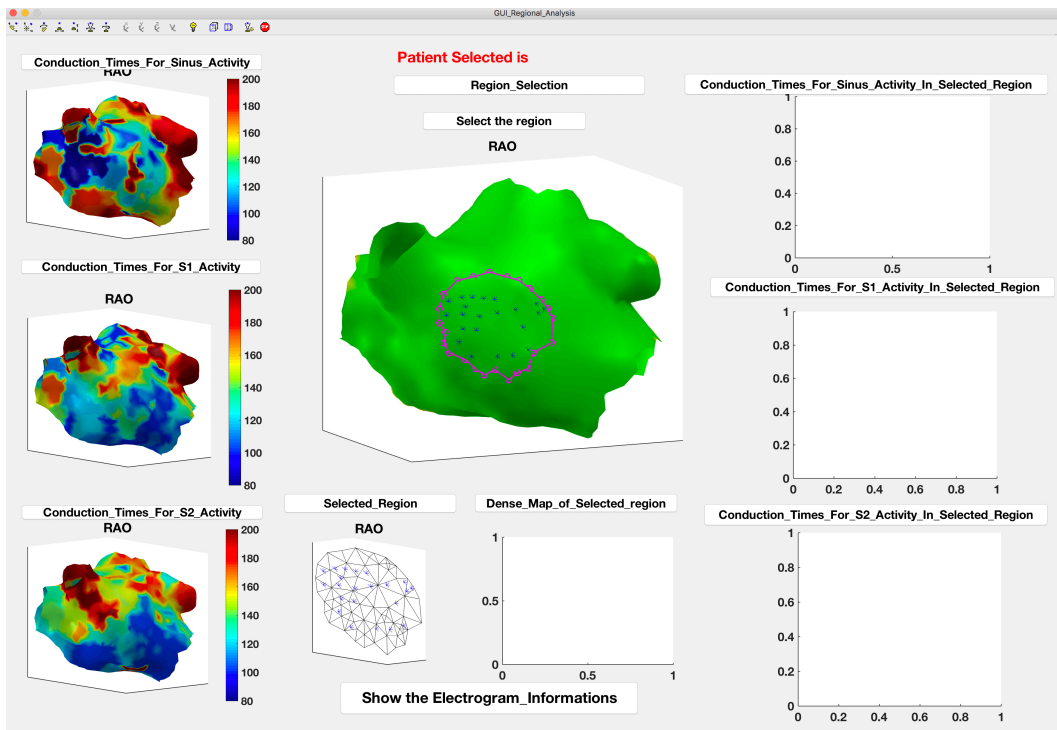


Figure 11.3: A region selected on the geometry. As represented the original triangular mesh and the recorded locations can be observed.

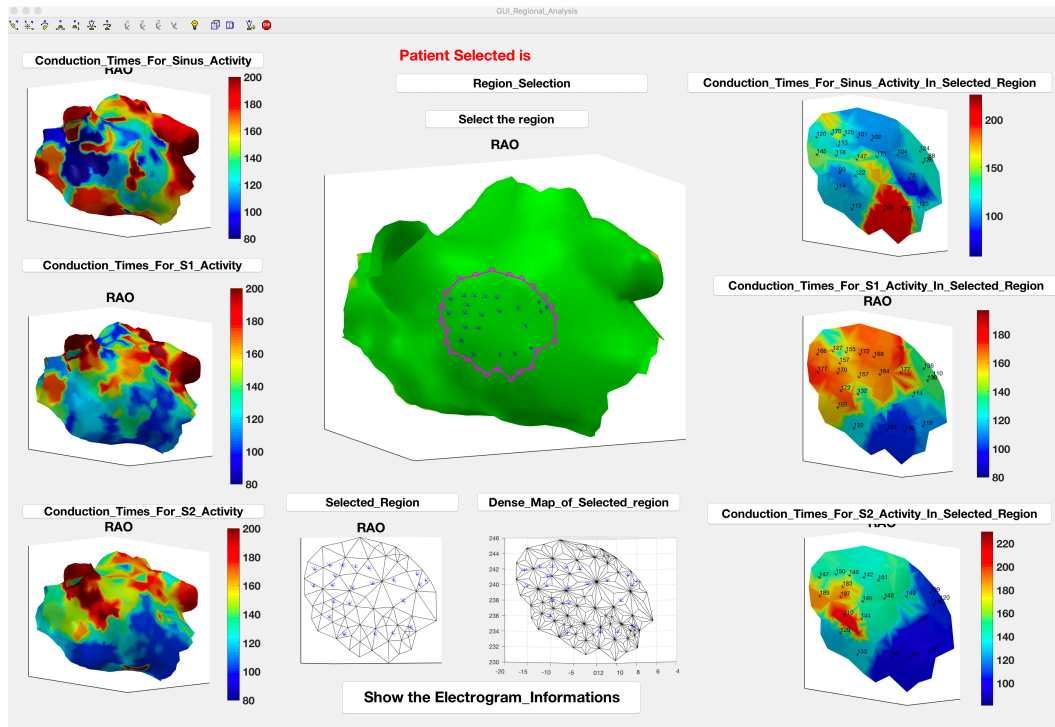


Figure 11.4: Representation of the regional information obtained for the selected region on the atrium. The electrograms can also be displayed if selected.

was used instead of understanding the region selection algorithms running in the background.

Figure 11.3 represents the selected region. The rotational option is also included in the GUI as a feature, so that the 3D view can be observed. The user can select a region by clockwise or anticlockwise selection. The selected region can also be seen in the subfigure of the GUI with the original mesh information as represented in row 3 column 2. The option of mesh refinement is also included in this GUI and the refined mesh can be obtained with all the recorded locations represented by dots on the selected region.

Figure 11.4 represents the GUI when all the options are selected. The regional depolarisation conduction patterns can be clearly observed for the selected region of the atrium along with the LAT at all the recorded points. The last option on this GUI is for getting the electrograms recorded within the selected region. All the unipolar, bipolar filtered and raw electrograms are displayed if the electrogram representation is clicked. They are represented along with the NLEO curves all together as well as segregated activation complexes (depending on the trigger).

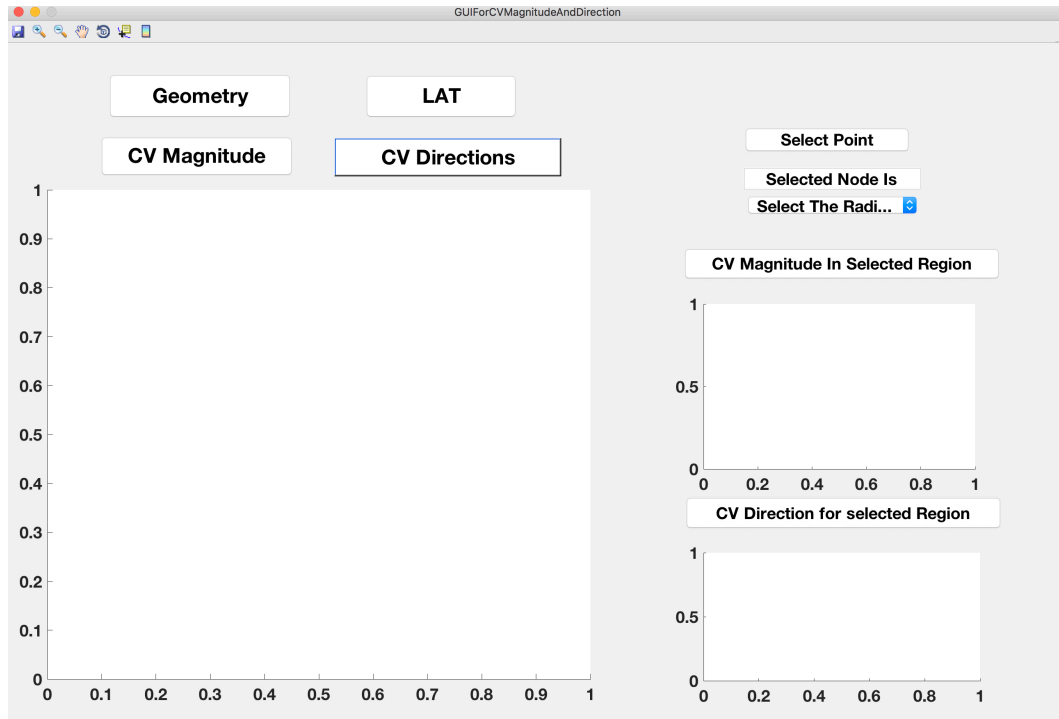


Figure 11.5: Representation of the blank GUI with all the options enlisted

11.2 Regional CV Estimation

Chapter 10 deals with the CV estimation and the results associated with it. The GUI was developed for the regional analysis of the geometry curvature along with the estimated CV magnitude and direction vectors in the proximity of the selected regions.

As represented in Figure 11.5, there are options to select from. The geometry and the LAT map can be selected and depending on the selection they are displayed on the axes available. The 3D rotation of all the subfigures is possible to get the 3D view. The magnitude and the CV direction vectors can then be imported into the GUI from the *.mat* file.

As per the choice of the user, any node on the triangulated mesh can be selected using the select point click. The radius around the point can then be selected from 1 mm to 20 mm range and then represented in Figure 11.7, the regional information can be displayed. Along with these, the direction vector window as represented in Figure 11.8 can also be obtained.

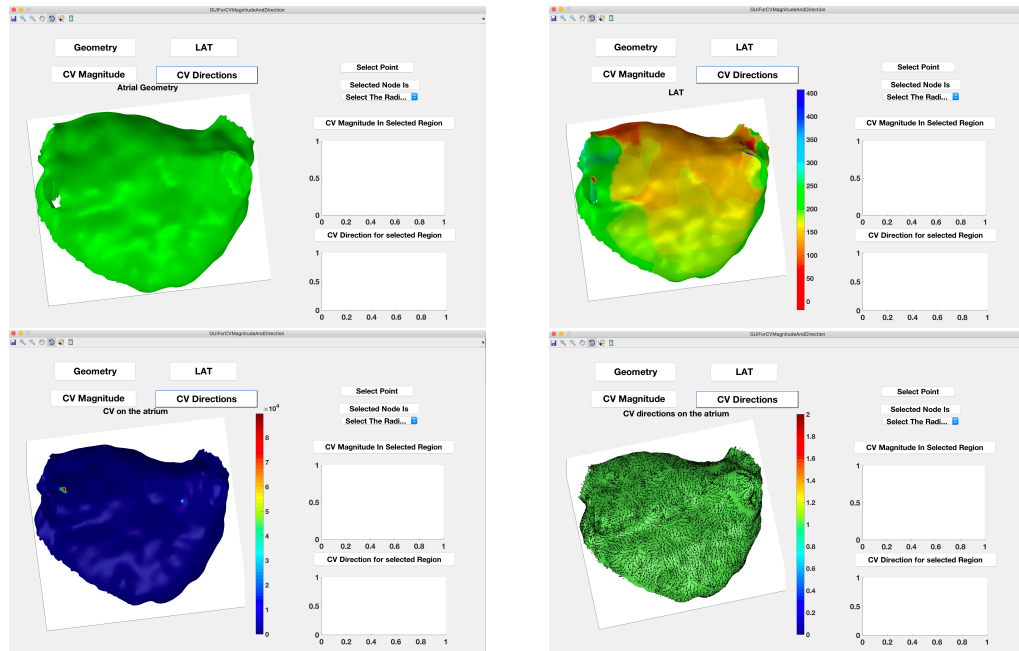


Figure 11.6: Representation of a) Geometry imported for CV estimation. b) The LAT map of the geometry. c) Estimated CV magnitude on the geometry. d) Estimated CV direction vectors on the geometry.

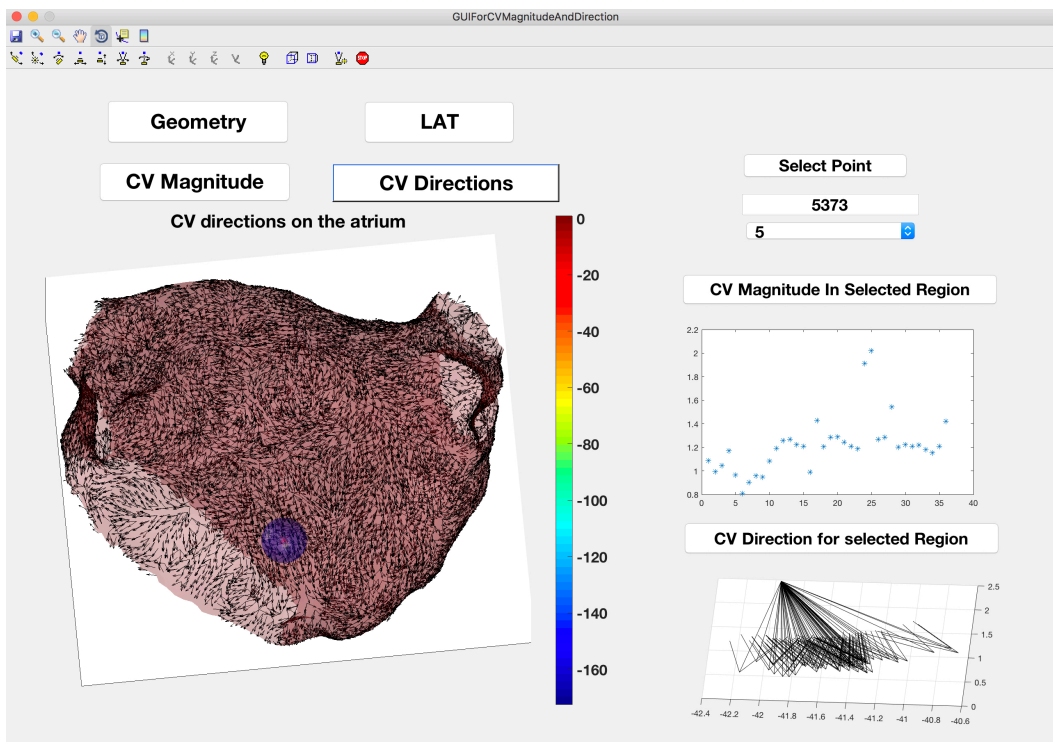


Figure 11.7: Representation of the regional information obtained for the selected region on the atrium.

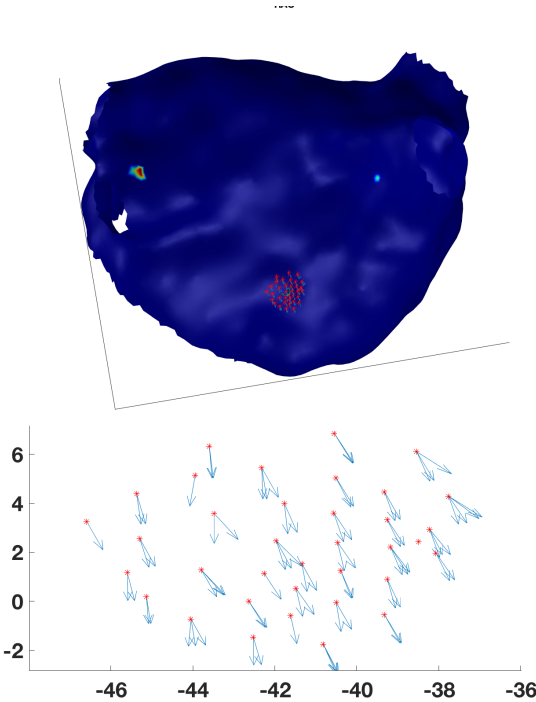


Figure 11.8: Representation of the regional information obtained for the selected region on the atrium displayed with the GUI in Figure 11.5.

Canine Data

12.1 Introduction

The canine data were recorded at the Feinberg School of Medicine, Northwestern University, Chicago, USA. This study is done in collaboration with Dr. Jason Ng. The Unimap system was used to acquire the epicardial data using a triangular patch catheter. The epicardial high-density electrogram maps obtained during fixed rate pacing and sinus rhythm (SR), were studied for electrophysiological parameter analysis.

It is well known that rapid pacing for a long time period can induce persistent atrial fibrillation (AFib) [74]. Also, fibrosis develops in the atria with heart failure. For the canine heart used for analysis, the mapping was done for paced and non-paced scenarios i.e. during the SR and during the pacing cycle length. The baseline data was obtained during SR, before pacing the heart. After this, the continuous rapid ventricular pacing was done at a rate of 600 bpm for 3 weeks to introduce fibrillation. The second recording was done, after AFib was induced in the heart. The epicardial electrograms were recorded at posterior left atrium (PLA) or left atrial appendage (LAA), using a patch catheter at a sampling rate of 1 kHz .

The recording has been done for 200 ms , 300 ms , 400 ms and 500 ms paced sequences during sinus rhythm (SR) and for induced fibrillation. The various recording scenarios are namely:

1. Recording at LAA for 200 ms pacing
2. Recording at LAA for 300 ms pacing
3. Recording at LAA for 400 ms pacing
4. Recording at LAA for 500 ms pacing
5. Recording at PLA for 200 ms pacing
6. Recording at PLA for 300 ms pacing
7. Recording at PLA for 400 ms pacing

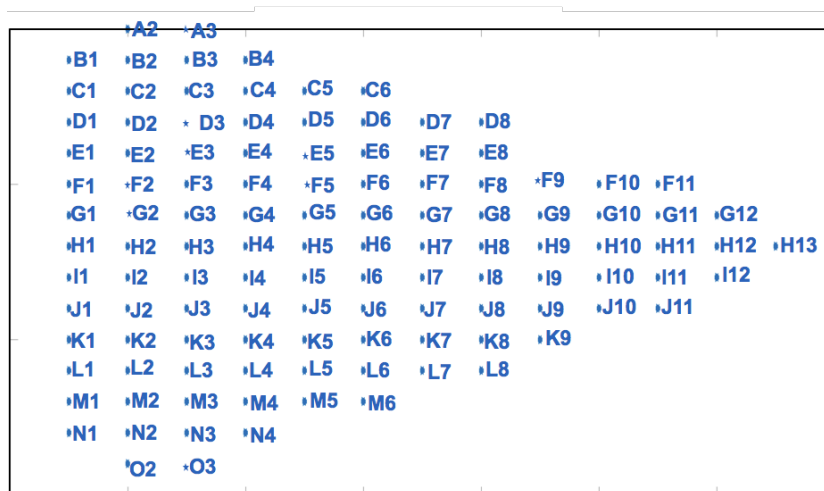


Figure 12.1: Patch catheter used to record (epicardial mapping) the depolarisation propagation at PLA and LAA location in the dog heart. The annotation of all the 117 electrodes are mentioned with the respective electrode. At each electrode of the catheter, 10 second long bipolar electrograms were recorded during SR and also during the paced rhythm after inducing the fibrillation.

8. Recording at LAA for 500ms pacing
9. Recording at LAA for SR
10. Recording at PLA for SR

The size of the patch catheter used for recording was $2.5\text{ mm} \times 2.5\text{ mm}$ and the number of electrodes were 117 as represented in Figure 12.1. At each electrode a 10 second long bipolar electrogram was recorded and analysed. Assuming the region under the patch to be flat, the 2D epicardial activities were recorded using the 2D patched catheter. The electrodes having good contact with the epicardial tissue gave good quality electrograms with clear activation complexes and high peak-to-peak (P2P) amplitudes as represented later in this chapter.

Since it is 2D recording on the atrial surface, therefore, the atrial geometry was taken as a flat surface. This is in comparison to the endocardial mapping using the electroanatomical mapping system, where the curvature of the geometry was an important parameter while analysing the depolarisation wavefront propagation over the atrial geometry (explained in section 14.5).

The recorded electrograms were used to compute the local activation time (LAT) values and to estimate the conduction velocity (CV). Six of the different electrograms giving the epicardial activity information are represented in Figure 12.2 to Figure 12.7.

During preprocessing, filtering was done to remove the unwanted frequency components (such as baseline wander and other high and low frequency components). The filtering frequencies of 30Hz and 300Hz (HP and LP respectively) were used. After removing the

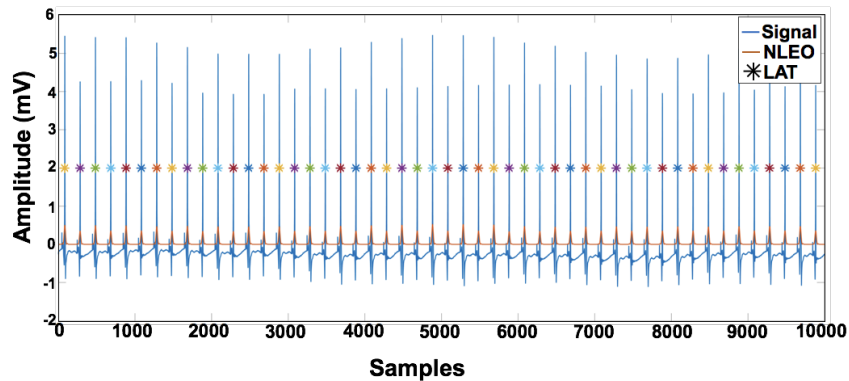


Figure 12.2: Representation of the 10 second long bipolar electrogram with clear activation complexes. Blue electrogram is the one recorded using the electrode on the patch catheter. The NLEO curve is represented by orange. All the LATs are marked by the stars. Sampling frequency: 1 kHz

artefacts during preprocessing stage, the next step was to estimate the LAT and the CV for the epicardial data obtained using the catheter. The recordings containing noise and artefacts (throughout the 10 second long segment) were discarded before selecting a window for LAT estimation.

Figure 12.2 represents a good quality bipolar electrogram with clear activation complexes and having P2P amplitudes of 6 mV . This electrogram is from the SR recording. In this electrogram, the LATs are marked for the respective activation complexes. These were computed using the maxima of the non-linear energy operator (NLEO) (as explained in chapter 9).

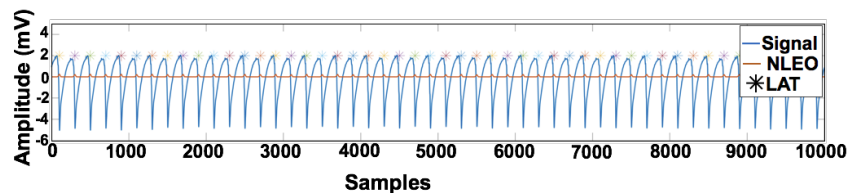


Figure 12.3: Representation of the unipolar electrogram with clear activation complexes. In some cases, instead of bipolar, the unipolar electrogram is recorded using the patch catheter. All the LATs are marked by stars.

As explained in chapter 6, the bipolar electrograms are obtained by subtracting two unipolar electrograms. In some cases, only one of the electrodes was capable of recording the electrophysiological activities, in these specific cases, instead of bipolar electrograms, the unipolar electrograms were used for analysis, as represented in Figure 12.3. The reason of getting a unipolar electrogram could be because of fatty tissue existence, electrode positioned above vein or artery or no contact (for one electrode) with the epicardium or because of a connection problem. The NLEO was used to get the LAT information (in unipolar electrograms as well) similar to the LAT estimation using the bipolar electrograms. These information were then

used for CV estimation as explained in the next section.

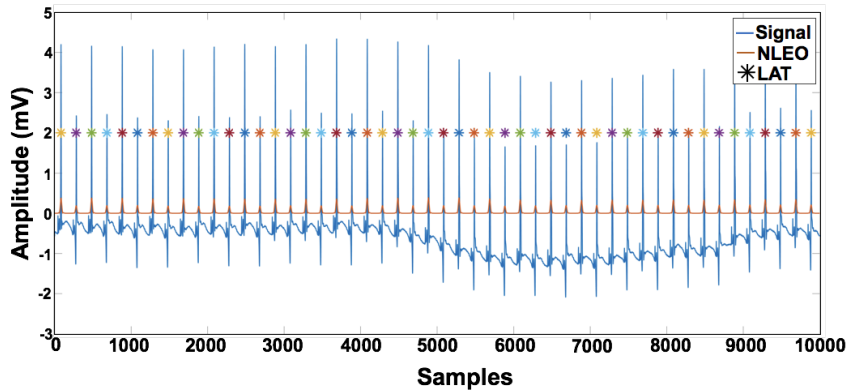


Figure 12.4: Representation of the bipolar electrogram with clear activation complexes. The alternans and the baseline wander can be seen clearly and prominently. All the LATs are marked by the stars.

There were some cases in which alternans were observed in the electrograms as represented in Figure 12.4, Figure 12.5 and Figure 12.6. The alternans can be observed due to changes in the genetics of the ion concentration. The alternans could be in the beginning, in between or in the end of the electrogram segment. In Figure 12.4, the clear baseline wander as well as the alternans are visible. Like the above mentioned cases, in this case also the NLEO was used to get the LAT information.

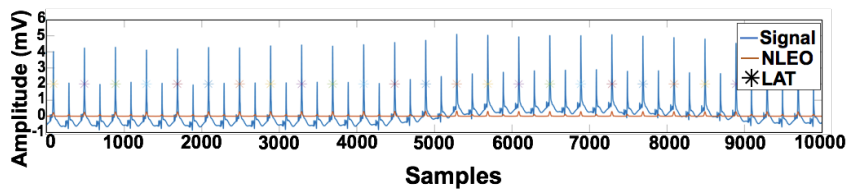


Figure 12.5: Representation of the bipolar electrogram with clear activation complexes. The increase in amplitude can be observed from 1.8 mV to 3.8 mV. The baseline wander can also be observed. All the LATs are marked by the stars. The alternans were observed in the electrograms.

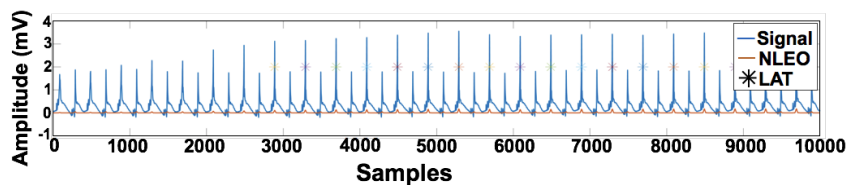


Figure 12.6: Representation of the bipolar electrogram with clear activation complexes. The baseline wander can also be observed. All the LATs are marked by the stars. The high amplitude-low amplitude-high amplitude pattern points towards the alternans presence.

When the recording electrode does not record any signal due to before said reasons, at these locations only noise was obtained in the electrogram, as represented in Figure 12.7. These locations and the electrograms were not used for LAT and CV estimation and were discarded from subsequent analysis.

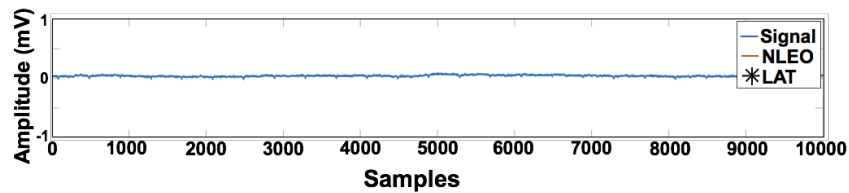


Figure 12.7: A 10 second long segment representing only noise.

The analysis was carried out in MATLAB (version *MATLAB_R2016b*). The locations having LAT information were then used to create the triangular mesh geometry. This was done using the Delaunay function. This generated mesh and the estimated LATs after preprocessing were used for CV estimation.

Figure 12.8 represents the various temporal windows selected (5 electrograms taken as an example, from arbitrary locations of the catheter) based on the LATs for CV estimation. The window selection and LAT estimation were done after preprocessing. For the represented segments, 16 possible windows were marked for the electrograms. Clear activation complexes could be observed in the selected window of the segments with P2P amplitude varying from 6 mV to 12 mV . Similar to this, the respective LATs were taken from all the 117 electrodes. Each vertex of the triad had spatial as well as temporal values, which were used for CV estimation as explained in section 14.3.1 (but for 2D data). The 2D implementation of the modified triangulation method is represented in Algorithm 12.1.

The results corresponding to the signal filtering for all the above mentioned cases, are represented in the result section (chapter 17) of this thesis. The method used for CV estimation on the simulated as well as clinical cases, are explained in the respective section below.

12.2 CV Estimation for Simulated Data

As introduced in the section above, for the canine heart epicardial data (electrograms), the propagation direction and magnitudes had to be determined. Before estimating the CV using

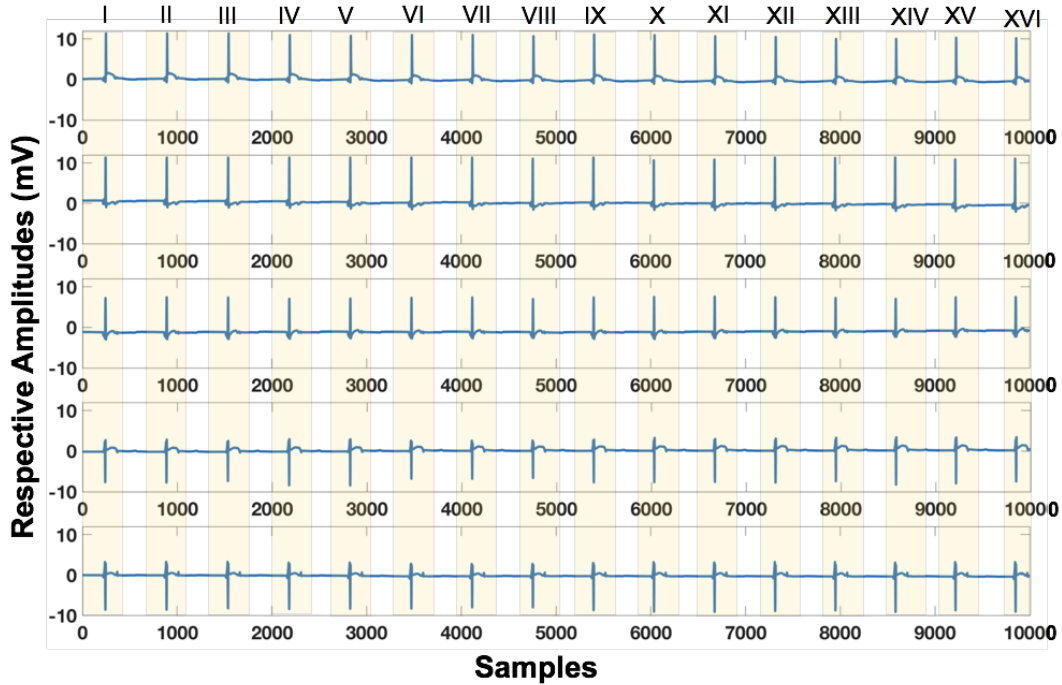


Figure 12.8: Representation of the various windows selected for CV estimation. The 10 second long segment contains the activities for the various excitation propagation, obtained over the period of time. Depending on the activation complex appearance, these are divided into various windows as marked from *I* to *XVI*.

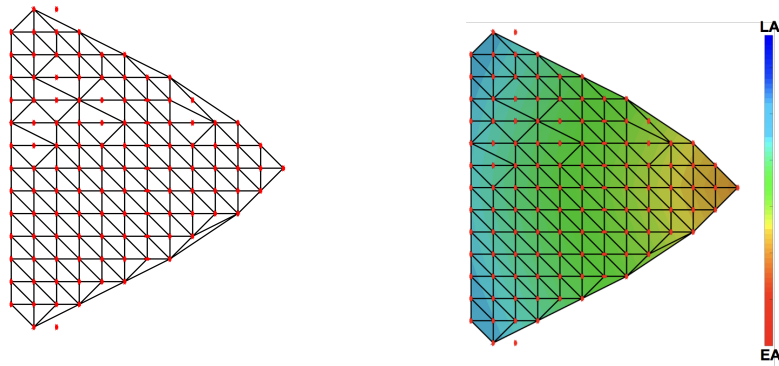


Figure 12.9: Representation of the triangular mesh generated using the electrodes with good contact to the epicardium. a). Using the electrodes with good contact to the epicardium and the simulated LAT. b). Simulated LAT map on the triangular mesh generated using the electrodes with good contact to the epicardium. Red is the early activation (EA) and blue is the late activation (LA).

the experimental spatiotemporal information, the analysis was done using the simulated data.

A 2D triangulated patch was used to determine the simulated LATs using the FaMaS tool [57]. The basics of the FaMaS simulation are explained in chapter 3.2. In this the geometry and excitation speeds were given as the input and the LATs were computed at each node of the triangular mesh using the Eikonal equation. Figure 12.9a represents the locations of

Algorithm 12.1 The triangulation in 2D for CV estimation

if $size(OA, 2) == 1$ **then**

$$\theta = \cos^{-1} \left(\frac{OA^2 + OB^2 - AB^2}{2(OA)(OB)} \right) \quad (12.1)$$

$$\alpha = \tan^{-1} \frac{\frac{t_{OB} OA}{t_{OA} OB} - \cos \theta}{\sin \theta} \quad (12.2)$$

$$\beta = (\theta + \alpha) \quad (12.3)$$

$$CV = \frac{OB}{T_{OB}} (\cos \theta \cos \alpha + \sin \theta \sin \alpha) \quad (12.4)$$

$$d_{OA} = \frac{A - O}{norm(A - O)}$$

$$d_{OB} = \frac{B - O}{norm(B - O)}$$

 $syms\ x\ y$

$$S = solve((x * (d_{OA_x})) + (y * (d_{OA_y})) \quad (12.5)$$

$$= \cos \alpha, (x * (d_{OB_x})) + (y * (d_{OB_y})) == \cos \beta) \quad (12.6)$$

$$d_v = [S.x\ S.y] \quad (12.7)$$

end if

the electrodes for which the electrograms were obtained. All the red dots are the spatial locations of the 2D catheter electrodes having good contact with the epicardium. The nodes at which the good quality electrograms were available after preprocessing were involved in the triangular mesh. Locations with only noise, were discarded from the analysis. The triangular mesh was created using the automatic Delaunay function of MATLAB.

For simulation, the location from where the excitation propagation started called as the trigger point, was manually selected using Paraview. For this simulation the right tip of the catheter represented in Figure 12.9 was manually selected as the trigger location. The estimated LATs are represented in Figure 12.9b. The clear activation can be seen propagating from the right to left region. The CV estimation was done using the method explained in Algorithm 12.1 and section 14.3.1. The points O , A and B in the algorithm represent the 3 nodes of the triad. The node with least LAT was assumed to be O and rest two as A and B . The nodes A and B were named arbitrarily. The LAT difference between O and A was termed as t_{OA} similarly between O and B was termed as t_{OB} . The angle between OA and OB vector is θ and, α and β are the angles that the excitation wave was assumed to make with A and B respectively. Then the CV magnitude was mathematically defined as

$$CV = \frac{OB}{T_{OB}} (\cos \theta \cos \alpha + \sin \theta \sin \alpha) \quad (12.8)$$

and the direction vector was calculated using d_{OA} and d_{OB} , CV direction vectors as represented in Equation (12.7). This was done to get the estimation with the known ground truth values and in order to benchmark the algorithm for 2D data.

12.3 CV Estimation for Canine Data

As explained in the introduction section above, the canine data was obtained as 10 *seconds* long electrograms from the electrodes of the triangular patch catheter. The CV estimation was done using the respective spatial and temporal information. Figure 12.8 represents that for such a long segment there exist a couple of excitation pattern propagating through the region over time. Therefore, more than one CV estimation was performed for the possible excitation patterns using the various LAT values obtained from the paced sequences (depends upon the number of temporal windows as represented in Figure 12.8).

The corresponding results for the CV estimation using the electrograms recorded at PLA and LAA, and for all the excitations are explained in the result section (chapter 17) of this thesis.

PART III

RESULTS

Simulated Data Results

The idealistic replication of simple, known and existing phenomena is done using the simulations as explained in chapter 5. The simulation of the homogeneous and heterogeneous depolarisation wavefront propagation was done using the fast marching simulation (FaMaS) method for given input propagation speeds, depending on the goal of simulation. The FaMaS method is able to solve the Eikonal equation on triangulated surfaces [137]. The Eikonal equation governs the spread of an activation wave in a medium resulting in a scalar local activation time (LAT) field and can be solved efficiently using the fast marching (FaMa) method. The trigger node was selected manually on the triangular geometry near the Bachmann bundle (BB). From the trigger point, the propagation starts on the triangulated surface in all the directions. As simulation output, each node was assigned the LAT value depending on the depolarisation propagation. The basics of the method and input parameters used for simulation have been explained in chapter 5. As part of this thesis, it was required to have the simulated LAT maps that can be used to understand the depolarisation wavefront propagation for various scenarios. After this, the ground truth values used for simulations were used to benchmark the conduction velocity (CV) estimation algorithms. The CV estimation algorithms were later on used for estimation of the depolarisation wavefront propagation for the clinical atrial flutter (AFlut) and atrial fibrillation (AFib) cases. The results obtained from various scenarios are explained in the respective sections below.

Table 13.1: Homogeneous simulation details

| S.No. | Clinical case | Input propagation speed (m/s) | Trigger location |
|-------|-----------------------|-------------------------------|----------------------------|
| 1 | 1 | 0.507 | |
| 2 | 2 | 0.507 | Near |
| 3 | 3 | 0.507 | BB |
| 4 | 4 | 0.507 | |
| 5 | 1 (with refined mesh) | 0.507 | |
| 6 | 1 | 0.507 | Near CS catheter electrode |

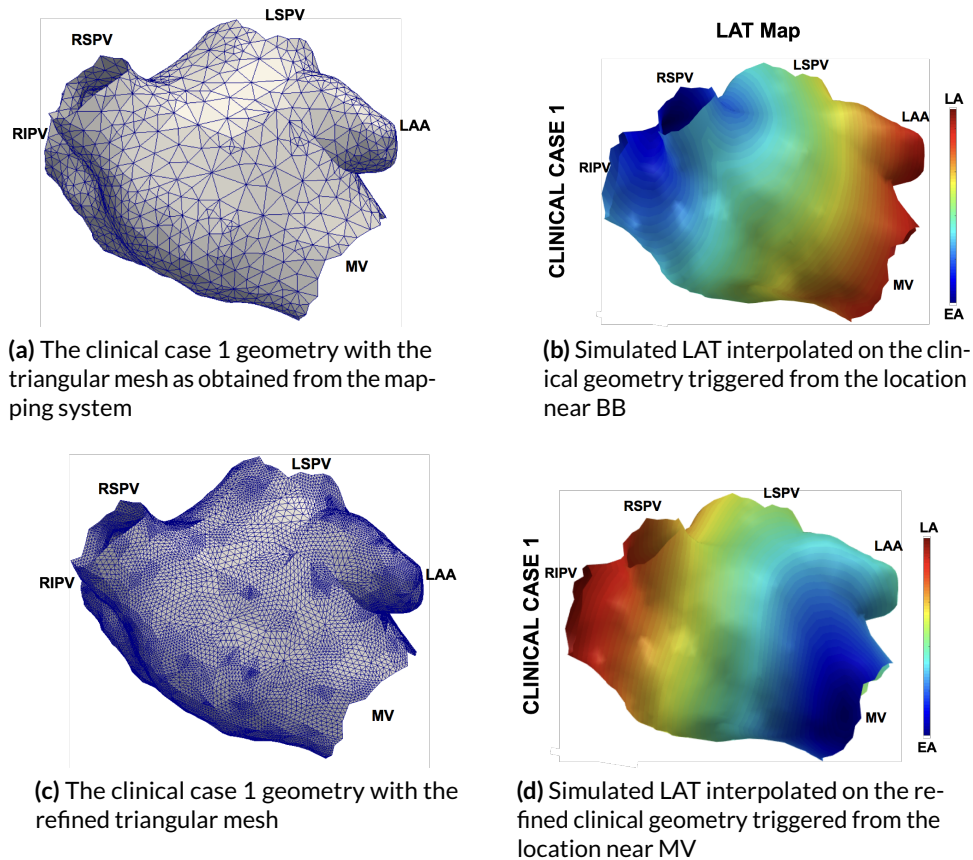


Figure 13.1: Simulated LAT for homogeneous depolarisation propagation on the given clinical case geometry. EA- Early activation, LA- Late activation, LSPV- Left superior pulmonary vein, LIPV- Left inferior pulmonary vein, RSPV- Right superior pulmonary vein, RIPV- Right inferior pulmonary vein, LAA- Left atrial appendage, MV- Mitral valve

13.1 Homogeneous Propagation Simulation

The homogeneous propagation of the depolarisation wavefront was the simplest of the depolarisation wavefront propagation over the clinical geometries. In this the single input speed was given as input parameter to the simulation environment. Table 13.1 gives a brief introduction to the various input for simulation. As a result of simulation, the LAT were obtained at all the nodes of the triangular mesh. As explained in chapter 5, the trigger was selected manually using Paraview software. The results for the homogeneous cases are divided and explained in the sections below.

13.1.1 For 3D Clinical Left Atrial Geometries

For the LAT simulation on the 3D clinically obtained geometries, the FaMaS tool was used as explained in chapter 5. The trigger was selected at the location near coronary sinus and near the BB. The triggering was chosen at these points so as to get closer to the clinical

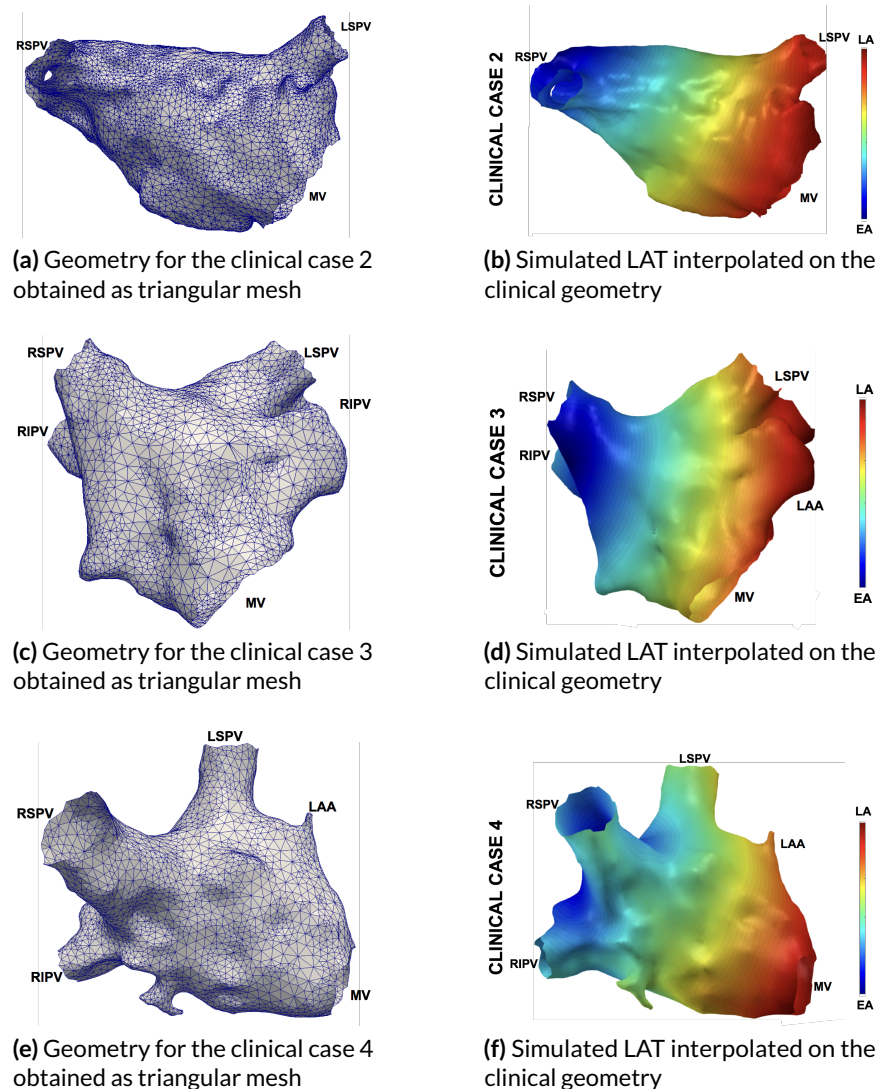


Figure 13.2: Simulated LAT for homogeneous depolarisation propagation on the triangular mesh of given clinical geometry. EA- Early activation, LA- Late activation, LSPV- Left superior pulmonary vein, LIPV- Left inferior pulmonary vein, RSPV- Right superior pulmonary vein, RIPV- Right inferior pulmonary vein, LAA- Left atrial appendage, MV- Mitral valve

analysis. The BB is the location from where the depolarisation wavefront enters the left atrium (LA). In the clinic, the artificial stimulation is usually given from the coronary sinus (CS) catheter, therefore, this location was also chosen as the other triggering point in the simulation environment. Once the trigger (the point from which the depolarisation wavefront initiates) is assigned, the propagation travels outwards into all the directions. The input speed given to FaMaS was 0.507 m/s for all the homogeneous cases. Using the five cases, as represented in chapter 5, the various depolarisation patterns were obtained in terms of LAT maps. The LAT maps along with the geometries are represented in Figure 13.1 and Figure 13.2. As clearly stated, in Figure 13.2 the trigger was at the BB. While in Figure 13.1,

the trigger was once from the CS catheter electrode and once from the approximate location of BB. The refined mesh can also be observed in this. The refinement of the mesh was done by introducing various new nodes on the clinical geometry without disturbing the existing mesh. As presented in both the figures, the propagation goes from blue to red region, blue being the early activation and red being the late activation region. These LAT maps along with the triangular mesh details were then used for the regional and global CV estimation.

13.1.2 For 2D Patch

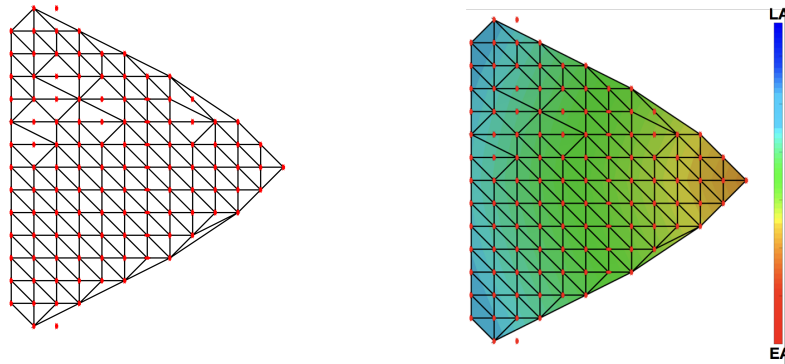


Figure 13.3: Simulated LAT for homogeneous depolarisation propagation on a 2D patch. a). 2D patch used for FaMaS LAT simulation, b). LAT map obtained on a 2D patch. EA- early activation and LA- late activation.

In this case, the 2D simulation patch was used as input for FaMaS method. The trigger was manually selected at the tip of the catheter. The LAT map obtained after the 2D patch simulation is presented in Figure 13.3. The propagation starts in red region and goes to the blue region as represented by the colour map.

13.2 Heterogeneous Propagation Simulation

For the clinically obtained geometries, various regions were selected manually as explained in chapter 5 and chapter 11 using the graphical user interface (GUI) developed during the course of this thesis. The various heterogeneous depolarisation propagation scenarios were obtained by manually selecting the various regions, as diagrammatically presented in Figure 13.4 to Figure 13.6. These regions were given individual propagation speeds to get the different propagation patterns as specified in Table 13.2. The variable speed introduces the heterogeneity in terms of propagation pattern over the atrium. The various regions were marked with different colours in all the respective figures. Figure 13.4 to Figure 13.6

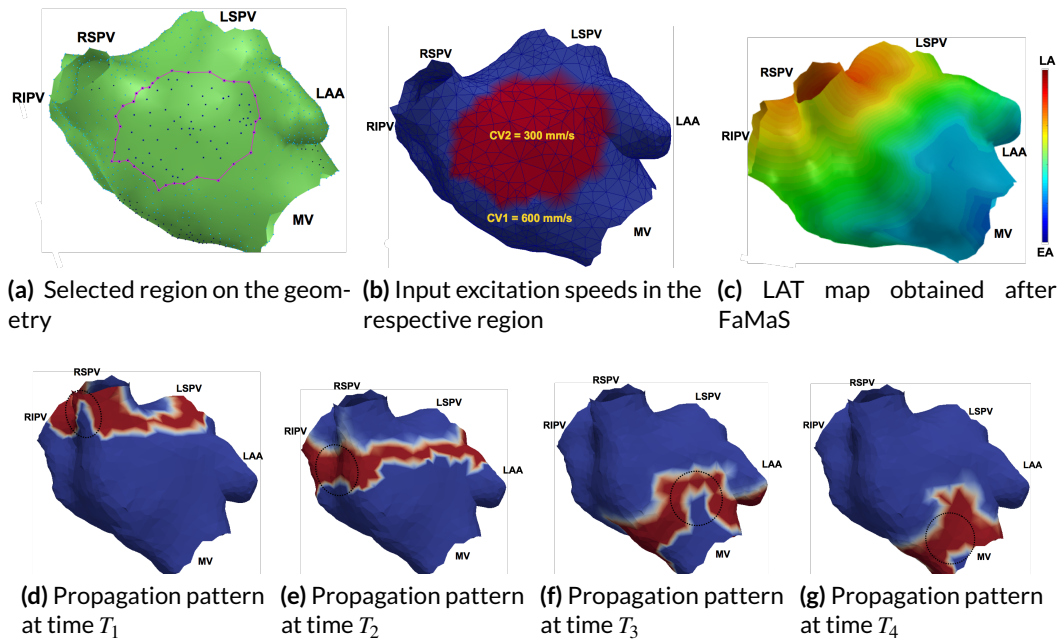


Figure 13.4: Simulated LAT for heterogeneous depolarisation propagation on the given clinical case geometry. EA- early activation, LA- late activation, LSPV- left superior pulmonary vein, RIPV- left inferior pulmonary vein, RSPV- right superior pulmonary vein, RIPV- right inferior pulmonary vein, LAA- left atrial appendage, MV- mitral valve. Two different regions are represented that were given to get the LAT at all the nodes accordingly. d-g). The depolarisation wavefront propagation pattern over time $T_1 < T_2 < T_3 < T_4$.

represent the posterior and anterior views along with the LAT map for the subsequent cases.

For Figure 13.4, the trigger was chosen close to the CS, while for the other simulations, the trigger was chosen near BB. The various permutations and combinations of the propagation speeds used for the two and four heterogeneous regions are mentioned in Table 5.1. This was done to get a step closer to the clinical scenarios where, due to various tissue types and substrates types, the depolarisation propagation pattern varies in different regions. The LAT map was obtained as a result of FaMaS simulation of various input speeds on the triangular mesh. The simulated depolarisation wavefront propagation pattern over time is represented in Figure 13.4 d to g. These temporal values were thereafter used for benchmarking the CV estimation algorithm.

The interesting part was to analyse the depolarisation wavefront behaviour on the boundary regions (boundaries of the selected heterogeneous regions). As an output of the simulation the LAT maps were obtained for all the input speeds. Comparison of Figure 13.2 and Figure 13.4 clearly represents the change in the propagation pattern as the input parameter (speed) changes. Similarly, Figure 13.6 represents the other propagation patterns in comparison to the one already explained.

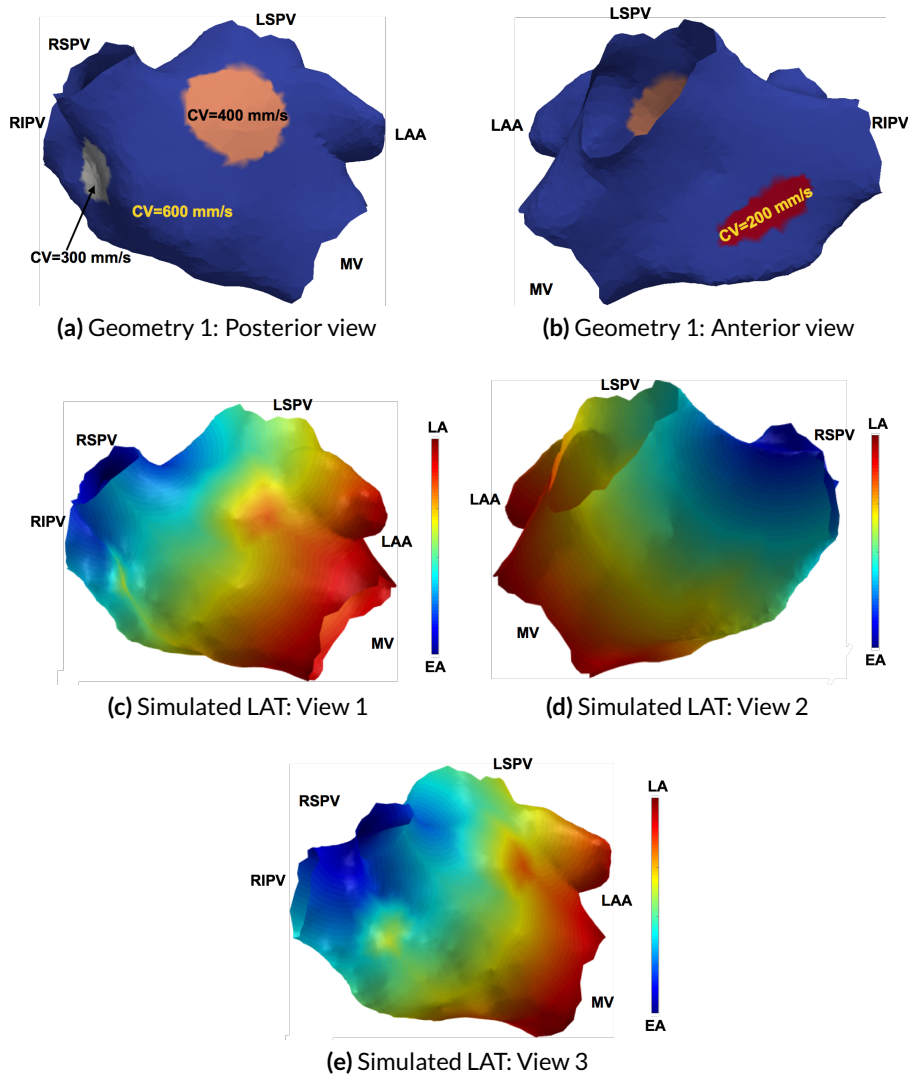


Figure 13.5: Simulated LAT for heterogeneous depolarisation propagation on the given clinical case geometry. EA- early activation, LA- late activation, LSPV- left superior pulmonary vein, LIPV- left inferior pulmonary vein, RSPV- right superior pulmonary vein, RIPV- right inferior pulmonary vein, LAA- left atrial appendage, MV- mitral valve. Four different speeds were given as input to the simulation, as represented in *a* and *b*.

13.3 Biatrial Simulation

The single layer biatrial simulation was done using a high resolution biatrial geometry composed of 357471 nodes. This has been generated by registering the CT scan and MRI images as explained in [67]. The details of various tissue classes (various atrial regions) are enlisted in Table 5.2. The trigger was selected manually at any arbitrary location in the left atrium. The depolarisation starts from this trigger and cover the atrium thereafter.

Table 13.2: Heterogeneous simulations details

| Serial Number | Clinical case | Regions for heterogeneity | Input propagation speed (m/s) | Trigger location |
|---------------|---------------|---------------------------|-------------------------------|------------------|
| 1 | 1 | 2 | 0.6 and 0.300 | near |
| 2 | 1 | 4 | 0.6, 0.4, 0.3, 0.2 | BB |
| 3 | 1 | 4 | 0.2, 0.4, 0.6, 0.8 | |

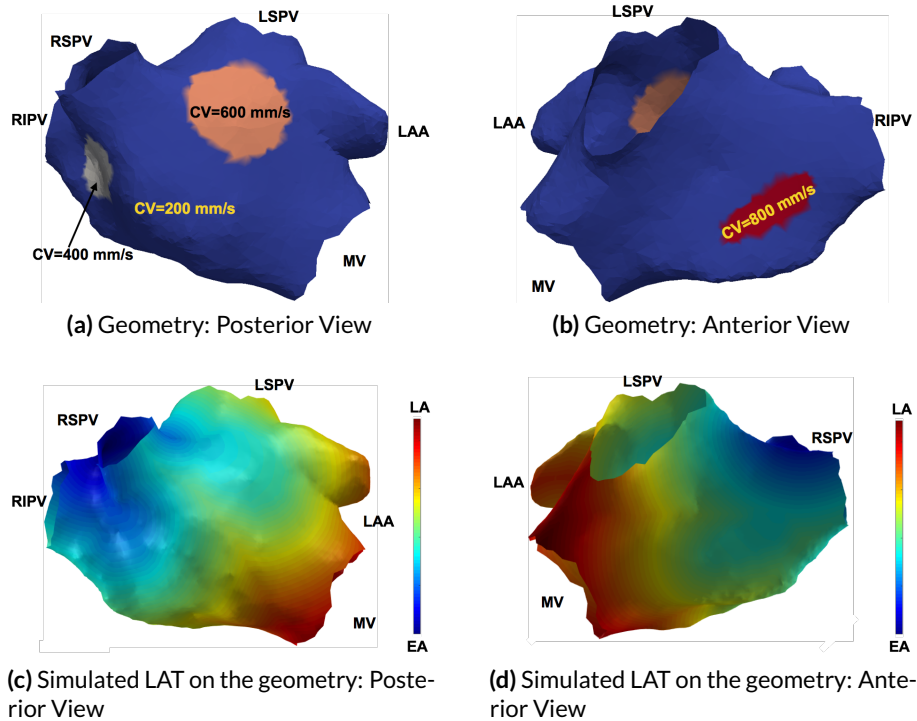


Figure 13.6: Simulated LAT for heterogeneous depolarisation propagation on the given clinical case geometry. EA- early activation, LA- late activation, LSPV- left superior pulmonary vein, LIPV- left inferior pulmonary vein, RSPV- right superior pulmonary vein, RIPV- right inferior pulmonary vein, LAA- left atrial appendage, MV- mitral valve. Four different speeds were given as input to the simulation, as represented in *a* and *b*.

With the given depolarisation wavefront propagation speeds in all the assigned regions in the FaMaS algorithm, the LAT maps for the entire geometry were simulated. The various tissue classes have been assigned the different propagation speeds, so as to analyse the propagation pattern accordingly. 2 sets of input speeds were given to get two different propagation patterns on the atrium as outlined in Table 13.2. Fast propagation speeds were given in the vena cava and the left atrial appendage (LAA) and right atrial appendage (RAA) as compared to the LA and right atrium (RA) respectively. The blood was given 0 propagation speed, as there is no propagation in blood. This simulation was done in order to use the obtained LAT map for benchmarking the CV estimation algorithm on the later stage.

The more the heterogeneity, the closer the propagation is assumed to be to the clinical propagation pattern. Therefore, the analysis can be used with the personalised atrial model. The biatrial tissue classes and the LAT map have been represented in Figure 13.7.

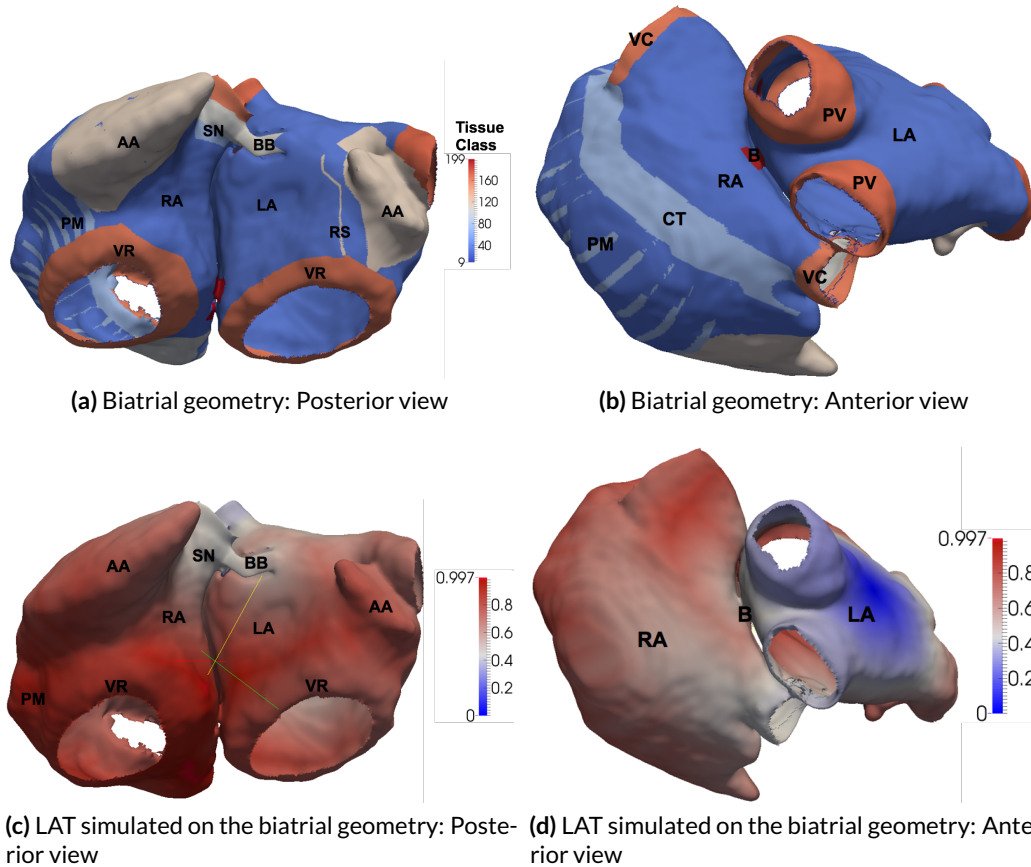


Figure 13.7: Simulated LAT for heterogeneous depolarisation propagation on the biatrial geometry. The various annotations are LA- left atrium, RA- right atrium, SN- sinus node, LAA- left atrial appendage, RAA- right atrial appendage, RS- revitalize scar, CT- crista terminalis, PM- pectinate muscle, BB- Bachmann bundle, VC- vena cava, B- bridges, PV- pulmonary vein.

Feature Extraction

As explained in chapter 9, during the electrophysiological and statistical parametric analysis of the intracardiac signals, the relevant features were extracted from the recorded bipolar and unipolar electrograms along with the spatial information. These features could include the region specific information or global analysis with respect to the analysed parameters. Figure 14.1 represents the recorded clinical geometry. The information obtained from the clinic were the triangular mesh and the electrograms at the recorded locations (marked by red dots). These recorded locations were selected by the physicians based on their experience and expertise. The recorded electrograms were utilised for electrophysiological and statistical parameter analysis to get better understanding of the clinical data. Compared to the simulated electrograms, the clinical electrograms are more fractionated and also have a lot of artefacts. The uncertainties in the clinical electrograms makes them difficult to analyse.

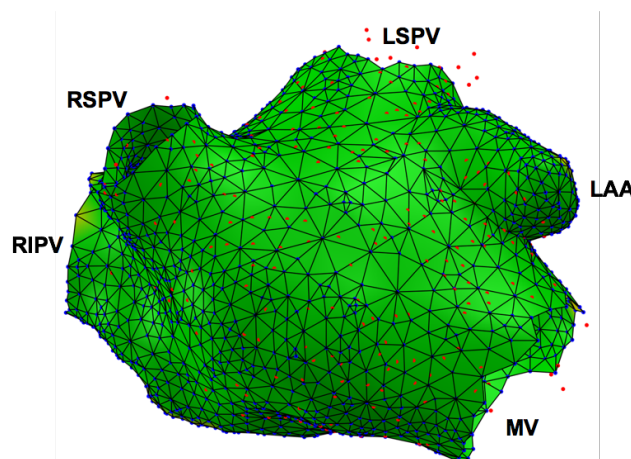


Figure 14.1: Representation of the triangular mesh and the electrogram recorded locations (red dots) for one of the clinical case. MV- mitral valve, LAA- Left atrial appendage, LSPV- left superior pulmonary vein LIPV- left inferior pulmonary vein, RSPV- right superior pulmonary vein, RIPV- right inferior pulmonary vein.

The results obtained from the parametric and geometrical analysis of the clinical data are discussed in the respective section below.

14.1 Catheter Coverage

During electroanatomical mapping, the data was collected in the form of electrograms at various locations. The catheter moves inside the atrium and records the data. The density of the recorded locations varies depending on the coverage by the catheter. Therefore, the coverage map was generated taking the surface traces with respect to a reference, that can in-turn give the information about the mapping densities. For interpolation of the coverage map, the radius around the recorded point was taken into consideration. 5 mm around the mapping location were interpolated as green, 5 mm to 10 mm were interpolated by yellow and away from 10 mm were interpolated by red. As explained in chapter 7, the region of the valve cut were marked and removed. The recordings in those regions were of no interest and thus removed as represented in Figure 7.1 and Figure 7.2. Figure 7.2 is a comparison of the two regional coverage maps interpolated for the same clinical patient. The posterior and the anterior view of the atrium for the same geometry is represented in Figure 14.2. A very good coverage of $\approx 99.5\%$ is achieved as all the points are lying in the vicinity of 10 mm from the electrode recording location. The encircled regions are the ones where comparatively less denser recordings was done.

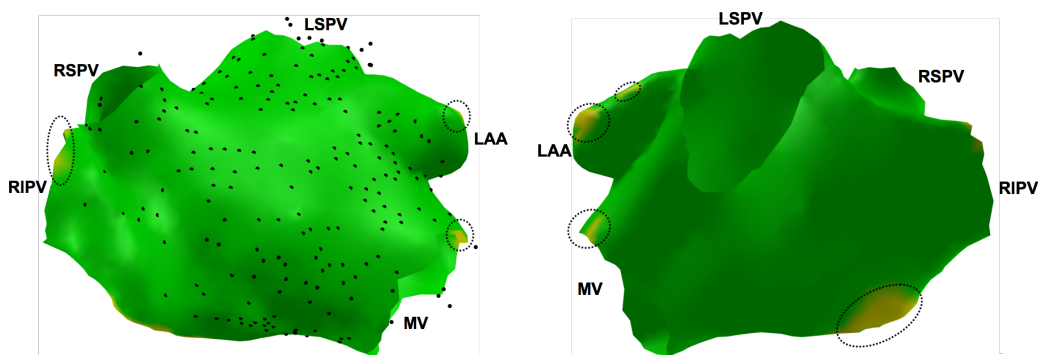


Figure 14.2: Coverage map for the atrium. a) Posterior view of the atrium with coverage interpolation, b) anterior view of the atrium with coverage interpolation (for annotation see Figure 8.1)

Various types and shapes of catheters were used for mapping therefore, getting the coverage map for those recorded locations can give the percentage of the net spatial coverage by the catheter inside the endocardium. During the recording this map takes all the physician selected recording points to represent the resolution in various atrial regions.

This coverage map is specifically helpful to get the coverage of the catheters such as Basket catheter, LASSO catheter, ORION catheter or PentaRay catheter. In this research, mainly

the intracardiac data from the 10 and 20 pole LASSO catheter were used. The coverage area varied from 80% to 99.9% for the clinical cases under analysis. Along with this, one clinical case was also mapped using the ORION catheter. The recording for the canine data (chapter 12) was obtained using a triangular patch catheter. No coverage map was generated for this case since it was the regional recording at 2 locations.

14.2 Location Specific Analysis

As explained above, the coverage map was generated using the recorded locations on the atrium. In chapter 6, it was explained that the intracardiac data recording was done as segment data. These segments correspond to the location saved as the *surface xyz*. The electrograms recorded at these locations were called as the *rov traces*. The location information of the recorded signals were saved in the file called as the *location.csv* as *rovtrace xyz* (marked as red dots in Figure 14.1). The analysis was done to find (if there exist) a correlation between the two location arrays, one that is obtained from segment data called as *surface xyz* and the other that is obtained from the triangular mesh called as *rovtrace xyz*. These both information have been recorded during the routine procedures. Since in our analysis the bipolar electrograms were used for all the evaluations and calculations, therefore the mean location of the bipolar electrograms were used for analysis.

The x – axis, y – axis, and z – axis were taken separately to find the correlation. This was done using the least square transformation method as explained mathematically in chapter 7. The curve in Figure 14.3a represents that after the least square transformation, there was no exact correlation obtained for these locations. The three curves correspond to the x , y and z coordinates of bipolar electrograms respectively, locations obtained after transformation and the given *rovtrace* locations. As a result of the transformation implementation, no exact correlation was found i.e. the transformation did not fit together using least square transformation method. Therefore, it was concluded that instead of using the projection of the *surface xyz* locations on the 3D electroanatomical geometry, these points will be included in the existing triangular mesh and used for further analysis. The error in the location fit obtained was in the range of 0.2mm to 7mm as represented in Figure 14.3b.

14.3 Extraction of the Selected Segment

With the advancements in the mapping systems, locating the sites of interest has become more easy for the physicians as compared to the past decade. The mapping procedures are known and well organised and their exist protocols for the ablation procedure. The exposure to radiation has also decreased and the 3D electroanatomical geometries are available with the regional electrograms. These are of great help for the physicians and reduced the procedure

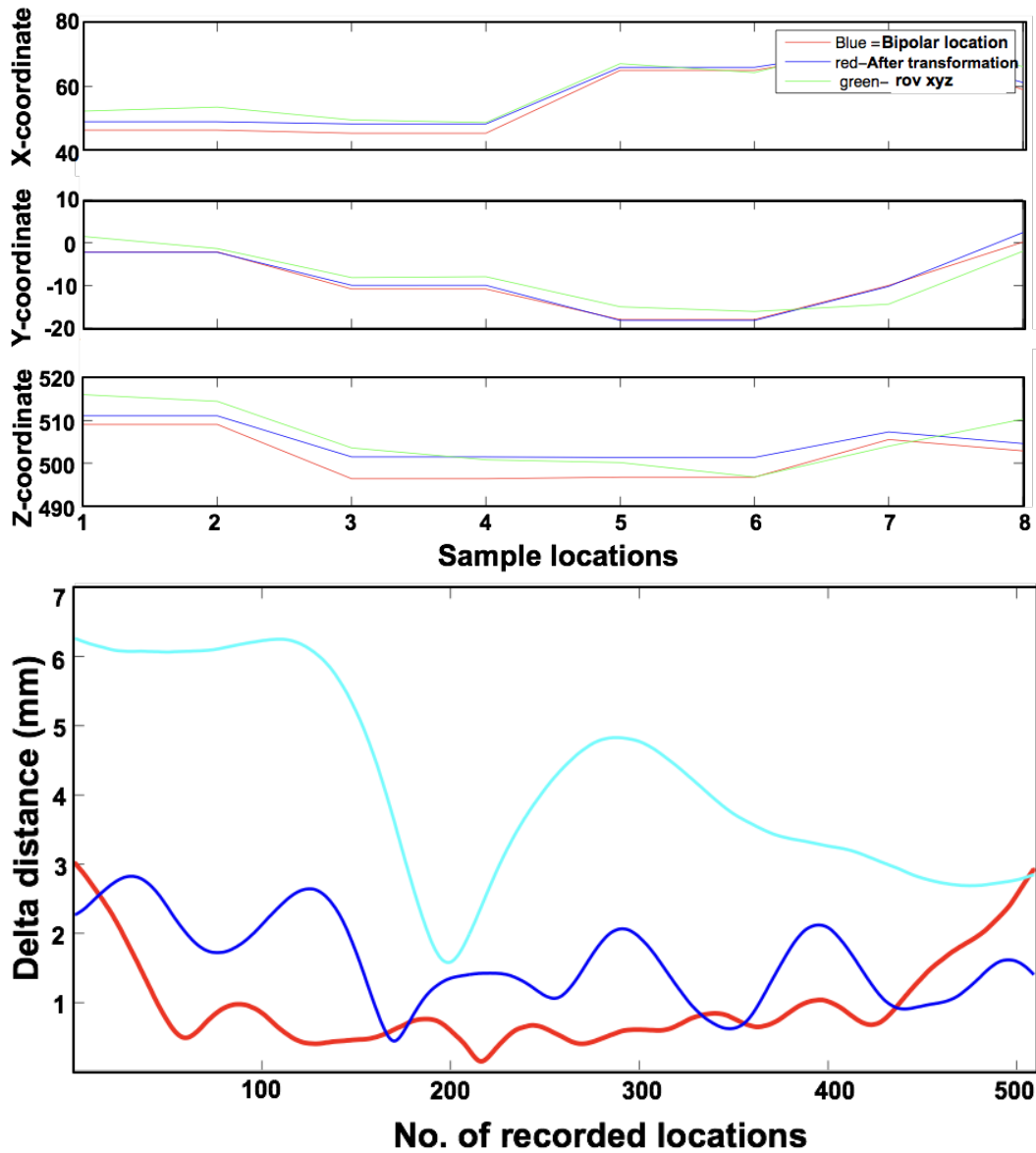


Figure 14.3: a). The linear transformation obtained for x , y , and z coordinates of the atrial location denoted that the segment data and the bipolar electrograms locations are not related using the least square transformation. b). Error obtained from the least square transformation.

time drastically. Although there have been a lot of advances in the intracardiac mapping, still the success rate of the ablation procedure depends on the experience and expertise of the physicians. It is $\approx 40\%$ after first ablation and increases for up to $\approx 70\%$ after the third and fourth ablation.

In the clinical context many decisions are based on the experience and expertise of the physicians. During the electroanatomical mapping and recording the physicians mark some locations and electrograms of interest. One of the first task was to extract those segments from the entire dataset. This has been done by taking the *rovtraces* (recorded electrograms)

and finding these from the segment data using temporal details. Based on the two types of analysis, two categories of segment selection were done in this research namely:

1. Physician selected segment without stimulus protocol
2. Stimulus protocol based electrogram extraction at various locations

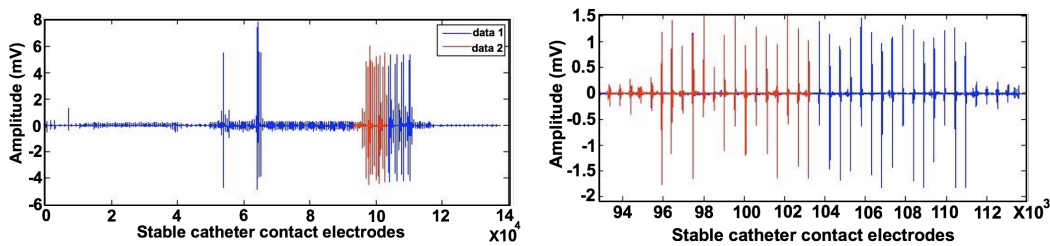


Figure 14.4: a) Selected segment (5 second) superimposed on the entire data segment(70 second). b) Zoomed representation of 5 second selected segment on superimposed on the entire data segment (refer section 7.6 for details).

Figure 14.4a represents the 70second long segment (blue electrogram) that was recorded during the regular mapping procedure. From this electrogram, the physician selected segment was extracted using the temporal information, this physician selected 5second segment is represented by red electrogram. Once these segments were segregated, they were analysed using temporal and spatial information. The atrial activities could be seen clearly in the recorded electrograms. These selected electrograms were then analysed for the other statistical parameters (such as local activation time, fractionation duration, peak-to-peak amplitudes and for the conduction velocity). These are explained in the upcoming section.

14.4 Mesh Refinement

The 3D electroanatomical geometry obtained from the mapping system has the triangular mesh structure. Depending upon the region, the average length of the edges on the triangular mesh varied. Figure 14.5a represents the valve cut geometry for one of the clinical case. The points outside the geometry as represented in Figure 14.5b were removed during preprocessing stage of analysis. The recorded locations (red dots) were included into the triangular mesh as represented in Figure 14.5c. This has also been represented in Figure 10.13. Since the triangular mesh obtained after including recorded locations is also sparse. The edge distances obtained from the various triads was 0.6mm with an inter quartile ratio (IQR) of 0.19mm as represented box-plot 1 of Figure 14.5d.

During the course of this research, the CV estimation of the depolarisation wavefront was done. The CV magnitudes were estimated as explained in chapter 10 and 16. To get the

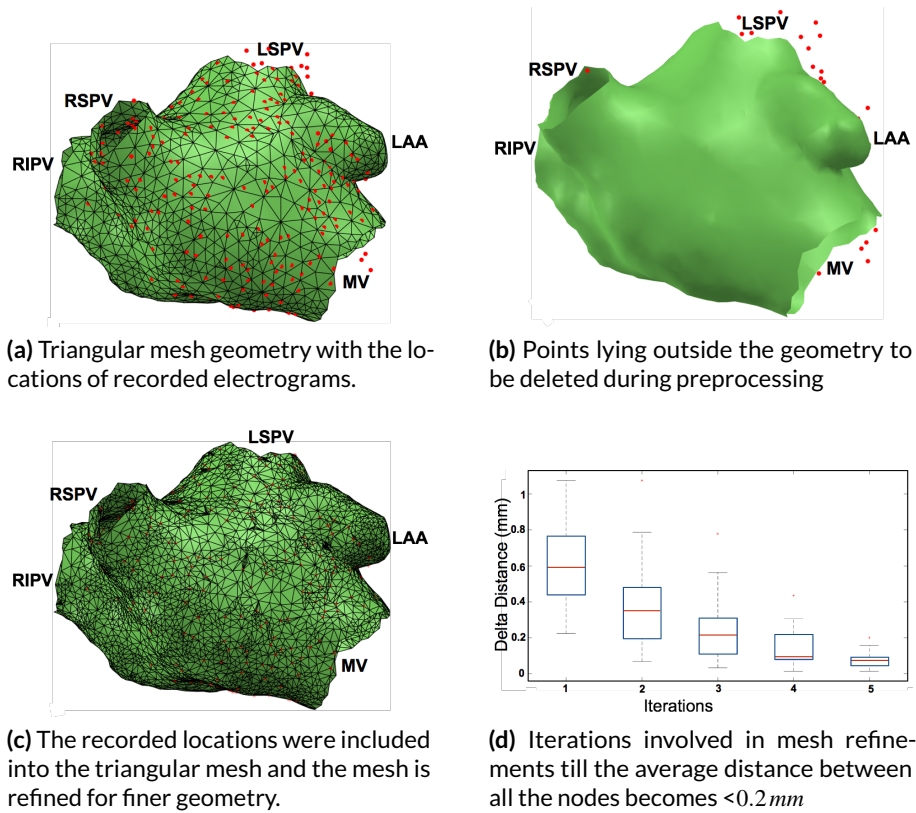


Figure 14.5: Representation of the mesh refinement algorithm. The recorded locations are included into the triangular geometry. New intermediate nodes are included to get the refined geometry.

propagation speed of the depolarisation wavefront, the distance travelled and the time difference between the two recorded locations on the atrium were required. Also in case of fast marching simulation (FaMaS), to get the smoother propagation, the refined triangular mesh was one of the prerequisite.

Therefore, the successful attempt was made for the refinement of the available triangular mesh after including the recorded locations. As explained in chapter 7, the two methods that could be used for mesh refinement were namely:

1. Including the centroid of the triad, or
2. Including the centre of each edge into the triad.

The centre of each edge of the triad was selected as the method for refinement as represented in Figure 7.6. The final geometry obtained after mesh refinement is represented in Figure 14.5c. To reach to the average distance between the nodes of the triad to be $< 0.2\text{ mm}$, up to 5 iterations were done. With every iteration, the average distance between the nodes of the triangular mesh is decreased, leading to the accuracies with respect to the location

information as represented clearly in the box-plot in Figure 14.5d.

The final mesh was then used for CV estimation for the clinical as well as the simulated scenarios. The FaMaS simulation was used to estimate the LAT map on the original mesh and also on the refined mesh to analyse the depolarisation wavefront propagation pattern. The results of all these are explained in the respective section of this thesis. The comparison of the results obtained for the original geometry and the refined geometry was also done and the results are discussed.

14.5 Curvature of the Atrial Geometry: 2D/3D analysis

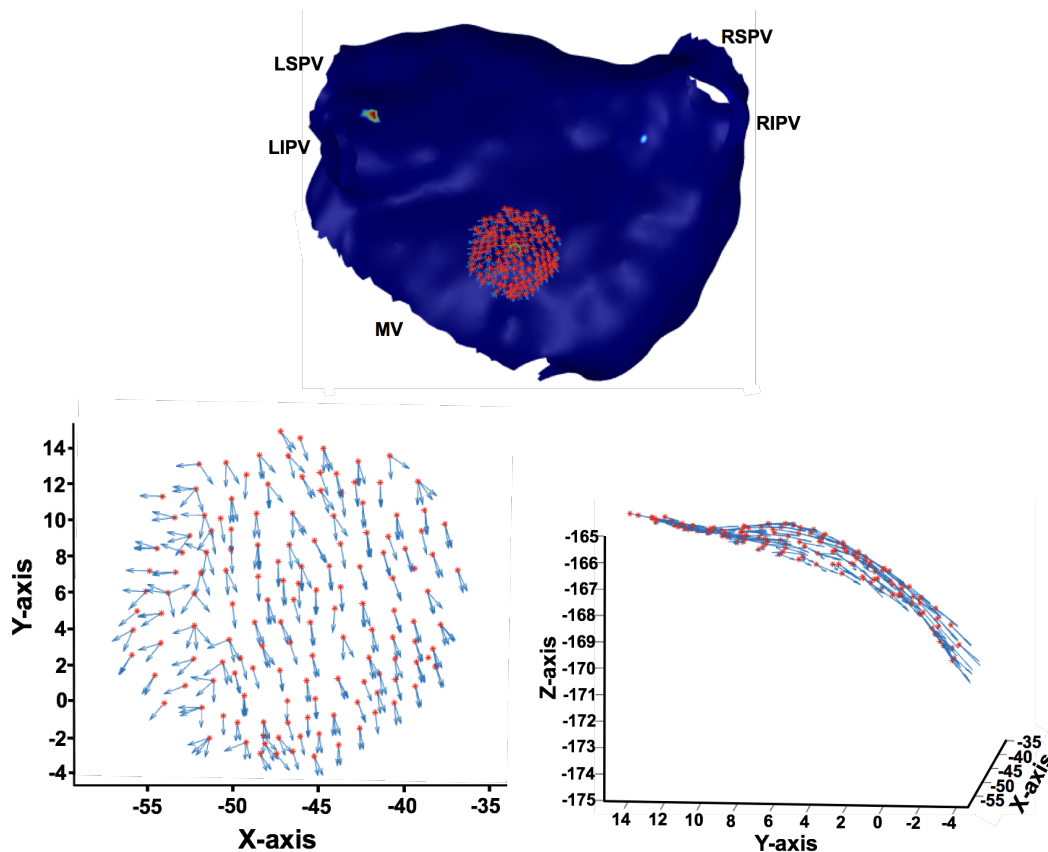


Figure 14.6: Representation of the curvature view of the region selected on the atrial geometry. a). The region around the green circled point is selected (in 5 mm proximity) and the CV vectors are represents at two different views. b). For XY plane, c). representation of the curvature in the geometry.

As explained in the above section, the spatial and temporal information were used for regional and global CV estimation. To do so, the coordinates of the recorded locations and the LAT

time from the electrograms were extracted. Along with these, one more information was very important and that was the pathway followed (distance travelled) by the depolarisation wavefront over the atrium. As represented in Figure 14.6*b* and Figure 14.6*c*, the wavefront in 2D representation might not give the exact pathway information travelled by the depolarisation wavefront as it could be obtained using the 3D geometrical information. The distance travelled by the excitation propagation is more clearly estimated over the geometry in 3D. Therefore, the correct estimation of the pathway that takes the curvature of the region into consideration was important to get the correct CV estimation.

In this research the CV estimation method was done for 2D and 3D geometries separately. This was because the curvature of the geometry is to be taken into consideration while calculating the distance travelled by the depolarisation wavefront over the atrial surface. The regional analysis in canine data was done using a 2D patch while using the 3D analysis the global atrial analysis for the (human) clinical cases were done. Chapter 10 and chapter 16 represent the CV estimation for 3D and 2D data. The CV was estimated using the LAT and the spatial location of the geometrical region under consideration for respective cases.

14.6 Correlation between Bipolar and Unipolar Electrograms

This section presents the correlation analysis between the unipolar and bipolar electrograms obtained from the electroanatomical mapping system. As represented in Figure 6.2 the unipolar and bipolar electrograms can be obtained in raw and filtered electrogram from the electroanatomical mapping (EAM) systems. The bipolar electrograms can be obtained from the unipolar electrograms by subtracting two unipolar electrograms (as explained in section 6.1.2).

The high pass and low pass filtering frequencies for the unipolar electrograms were 2Hz and 300Hz respectively. While for the bipolar electrograms the high pass (HP) and low pass (LP) frequencies were 30Hz and 300Hz respectively. The bipolar electrograms obtained from the unipolar electrograms were filtered with 2Hz and 300Hz HP and LP filter respectively. This section deals with finding the morphological correlation between the unipolar and bipolar electrograms (raw and filtered) as presented in Figure 14.7. The two unfiltered unipolar electrograms (Figure 14.7*a* and *b*) were subtracted to get the bipolar electrogram (Figure 14.7*c*). The resultant was then filtered at the HP and LP filtering frequencies of 30Hz and 300Hz . The electrograms now obtained are called as the filtered bipolar electrogram (Figure 14.7*d*), which were correlated with the given filtered bipolar electrogram (Figure 14.7*e*). The correlation of 99% and above was obtained at all the locations.

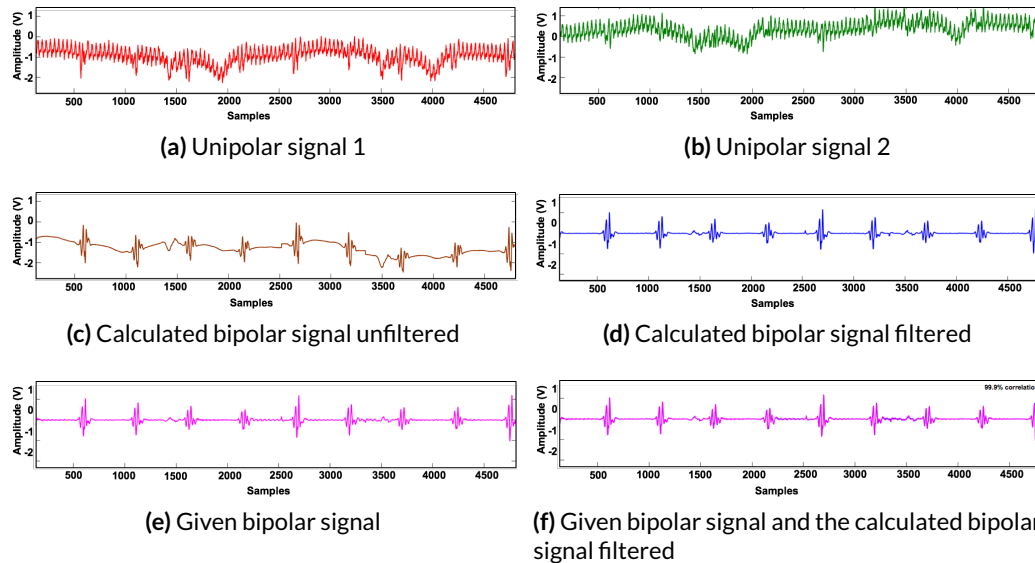


Figure 14.7: Illustration of the correlation between the calculated bipolar electrogram and the given bipolar electrogram.

This proves that either of the electrograms (bipolar or unipolar) could be used for analysis and the filtering frequency range is also 30 Hz and 300 Hz for HP and LP filtering respectively. Since the bipolar electrograms are free from the local artefacts, therefore, in this research the bipolar electrograms were used throughout in most of the analysis.

14.7 QRS Complex Detection

As explained in section 9.1, the *QRS* complex represents the ventricular depolarisation. During this research, the *QRS* complex detection was done in collaboration with Dipl.-Ing. Gustavo Lenis, using the stationary wavelet based transformation technique. The *ECG* signals were used along with the intracardiac signals to mark and identify the ventricular far field (VFF) present. This has been represented in Figure 14.8. Similar to the intracardiac signals, the *ECG* signals also have many artefacts, therefore, instead of using the steepest slope or *R* peak detection method and adequate filtering frequency, the wavelet transform method was used for *QRS* complex detection.

Another application of the *QRS* complex detection is with the πCA method done in collaboration with Dr.-Ing. Tobias Oesterlein. During the πCA method, the ventricular activities recorded in the atrial electrograms were removed by the low amplitude segment. This is similar to the maternal and fetal *ECG* separation according to their periodicity. This section is explained in detail in Chapter 9. For the paced sequence data, the VFF in intracardiac electrograms corresponds to the *QRS* complexes in *ECG* signals, these are separated by selection a window of 200 ms around the stimulus artefact location as represented in Figure 14.8.

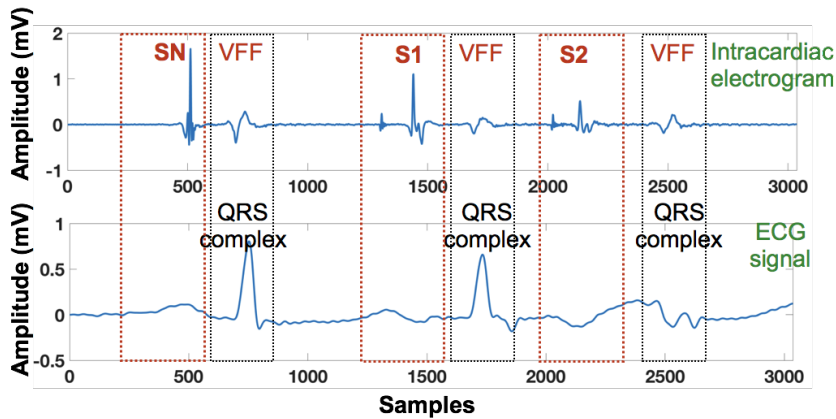


Figure 14.8: Illustration of *QRS* complex annotation in *ECG* and corresponding VFF in intracardiac signals obtained for the paced sequence data.

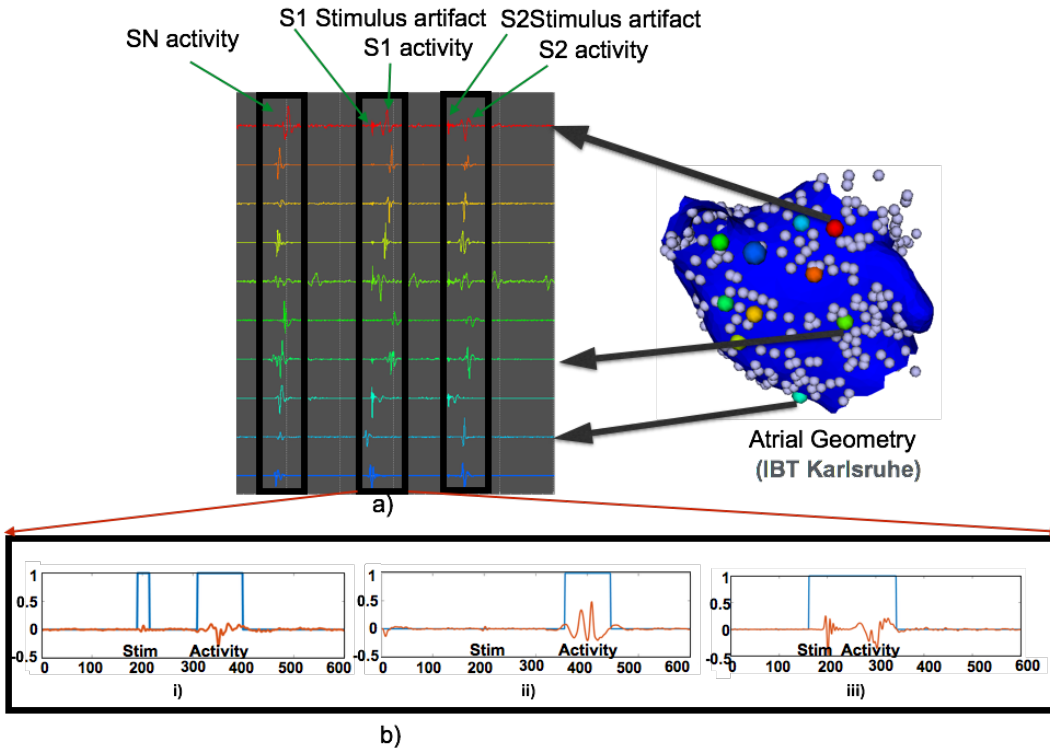


Figure 14.9: Illustration of atrial activity at various locations.

14.8 Atrial Activity Detection

As explained in section 9.2, the analysis was done to get the desired atrial activity complexes separated from the artefacts or alternans that could be present with the depolarisation wavefront information. As the depolarisation wavefront travels through the tissue beneath the electrode of the catheter, this information gets reflected in the electrograms by either positive

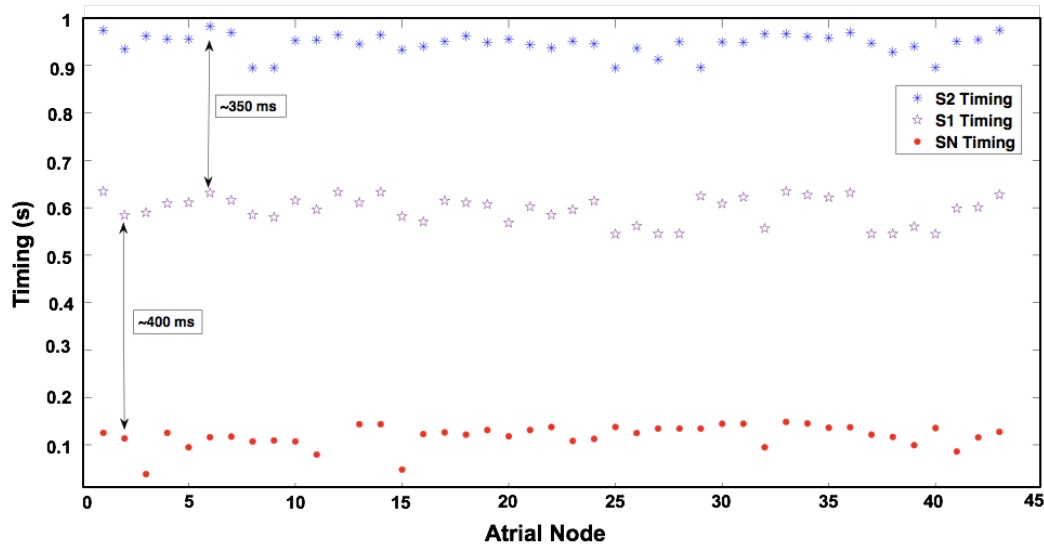


Figure 14.10: Illustration of atrial activity one after the other.

or negative deflections. To find the active atrial segments from the recorded electrogram, the non-linear energy operator (NLEO) were used during the course of this research. The activities are then marked as the *SN*, *S1* or *S2* depending on their temporal location (type of trigger) in the preprocessing stage. At respective location, the electrograms are represented using the KaPAVIE tool (Figure 14.9a) [75]. The three activities can be seen clearly along with the *S1* trigger and *S2* trigger as annotated.

The reference signals from the coronary sinus (CS) catheter were used for temporarily locating the stimulus artefacts and for alignment of the various activities with respect to it. It is important to get the atrial activities separated from the stimulus artefacts as represented in Figure 14.9b. Since the stimulus protocol was given in sinus rhythm (SR), and thus the trigger *S1* and its resulting activity appeared after *SN* triggered activity and similarly *S2* triggered activity appeared after *S1* triggered activity as represented in Figure 14.10, i.e. the SR activity is followed by the *S1* activity and that is followed by *S2* activity). At some locations it was also observed that one type of activity was present while the others were absent, this depends on the tissue substrate.

14.9 Peak-to-Peak Value Estimation

Once the atrial activities are detected the peak-to-peak (P2P) amplitudes were then estimated using the signals inside the selected atrial activation complexes as represented and explained in section 9.5. This is a very important parameter as it gives the information about the strength of the signal along with the electrode and endocardial wall contact information. As the electrode goes far from the tissue the signal strength in terms of its P2P amplitude

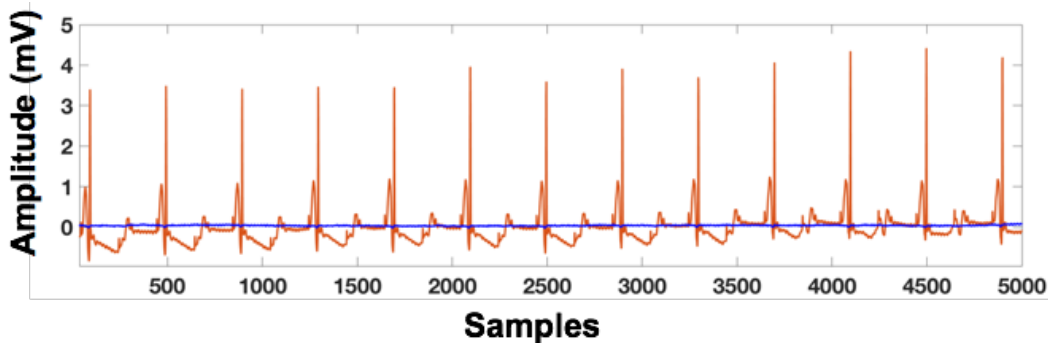


Figure 14.11: Illustration of normal electrogram vs electrograms with only noise. The P2P value for the healthy electrogram recording was up to 6 mV .

decreases, also when the electrode has no contact the P2P amplitudes are extremely low (or zero). During analysis the signals with P2P amplitude less than 0.08 mV are considered as either noise or no contact points.

One such example of the no contact signal (blue) with respect to the normal contact signal (orange) from the canine data is represented in Figure 14.11. In general there is no particular method available in text to find whether the electrode is in contact with the endocardium or not. In practice the physician make a decision looking at the electrograms (by the strength of the activities on the electrograms) and the recorded location information. In the 3D EAM systems, the catheters movement can also be seen inside the atrium.

The slow conducting region, scar regions, highly fibrotic regions, and the arrhythmogenic regions have tendencies of lower P2P values as compared to the normal tissue. Therefore, while estimating the region of interest the P2P amplitude can give a good approximation. Figure 14.12 represents the P2P amplitude variations for the stimulus protocol data for activities at 42 arbitrary locations. Depending on the site the P2P amplitude varied from 0 mV to 5 mV .

The analysis was done for the complete left atrium. Figure 14.13 represents the P2P value visualised on the atrium for two clinical cases. The 0 mV to 3 mV scale was used during visualisation. The clinical cases taken into consideration were the stimulus protocol data as explained in chapter 8. The P2P amplitude was estimated for the SR, S1 triggered depolarisation wavefront and S2 triggered depolarisation wavefront respectively.

At recorded locations the electrograms were obtained for respective depolarisation wavefronts. The NLEO was estimated and then the P2P amplitudes were calculated using the activities inside the step function of 0.1 times the NLEO maxima energy (as explained in section 9.5). In Figure 14.13, the respective row represents the SR activity, S1 triggered

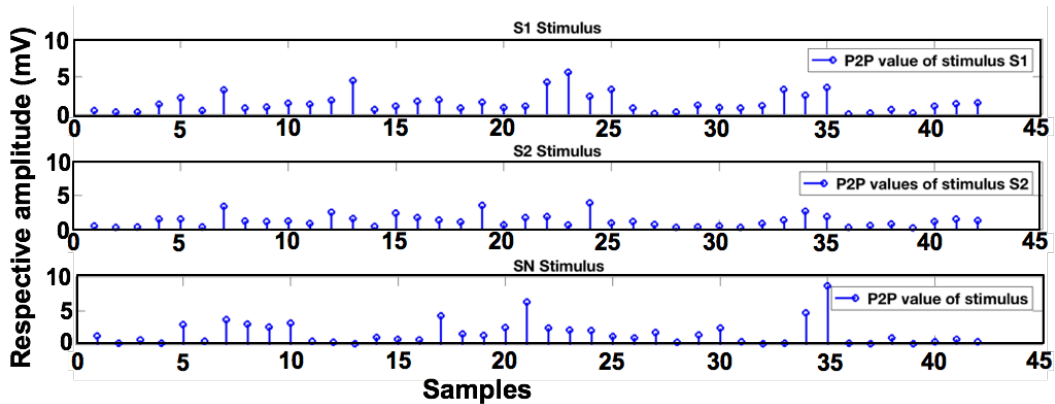


Figure 14.12: Variation of P2P values for various activities for a patient

activity and S2 triggered activity respectively. The region with high P2P amplitudes are assumed to be the healthy regions, while the regions with low P2P amplitudes are assumed to be either representing noise or no contact of the electrode with the endocardium or these could be the arrhythmogenic regions.

The clinical cases under analysis were unhealthy patients. The obtained results were discussed with the physicians. In our case high P2P amplitudes were obtained in the region near the appendages and low P2P amplitudes were obtained near the pulmonary vein (PV) which is in regard to the clinician expectations. To make any other opinion using the P2P values, it was analysed along with other statistical parameter. The detailed explanation and their relation with other statistical parameter is done in chapter 9.

14.10 Fractionation Duration

Similar to P2P amplitudes, the fractionation duration (FD) is another statistical parameter analysed from the atrial activities marked using the NLEO. The estimation of FD is explained in section 9.4. The term FD is also linked to the complexity in the atrial electrograms. The higher FD value measured from an activation complex represents the slow propagation of the depolarisation wavefront in the tissue beneath the recorded electrode. Therefore, higher FD along with the low P2P magnitudes points toward the regional arrhythmogeneity.

The estimate of the FD was done for stimulus protocol data (12 possible depolarisation wavefronts) namely: SR (SN triggered activity), S1 triggered activities and S2 triggered activities. Figure 9.7 is the representation of the FD estimation for the atrial complexes obtained using the stimulus protocol. 0.1 times the maxima of the energy from the NLEO complex was used to get the FD (also called activity duration). The estimated FD values were visualised on the respective geometry to get the regional information and are represented in Figure 14.14. Low FD values with high P2P amplitudes represents healthy tissue having fast

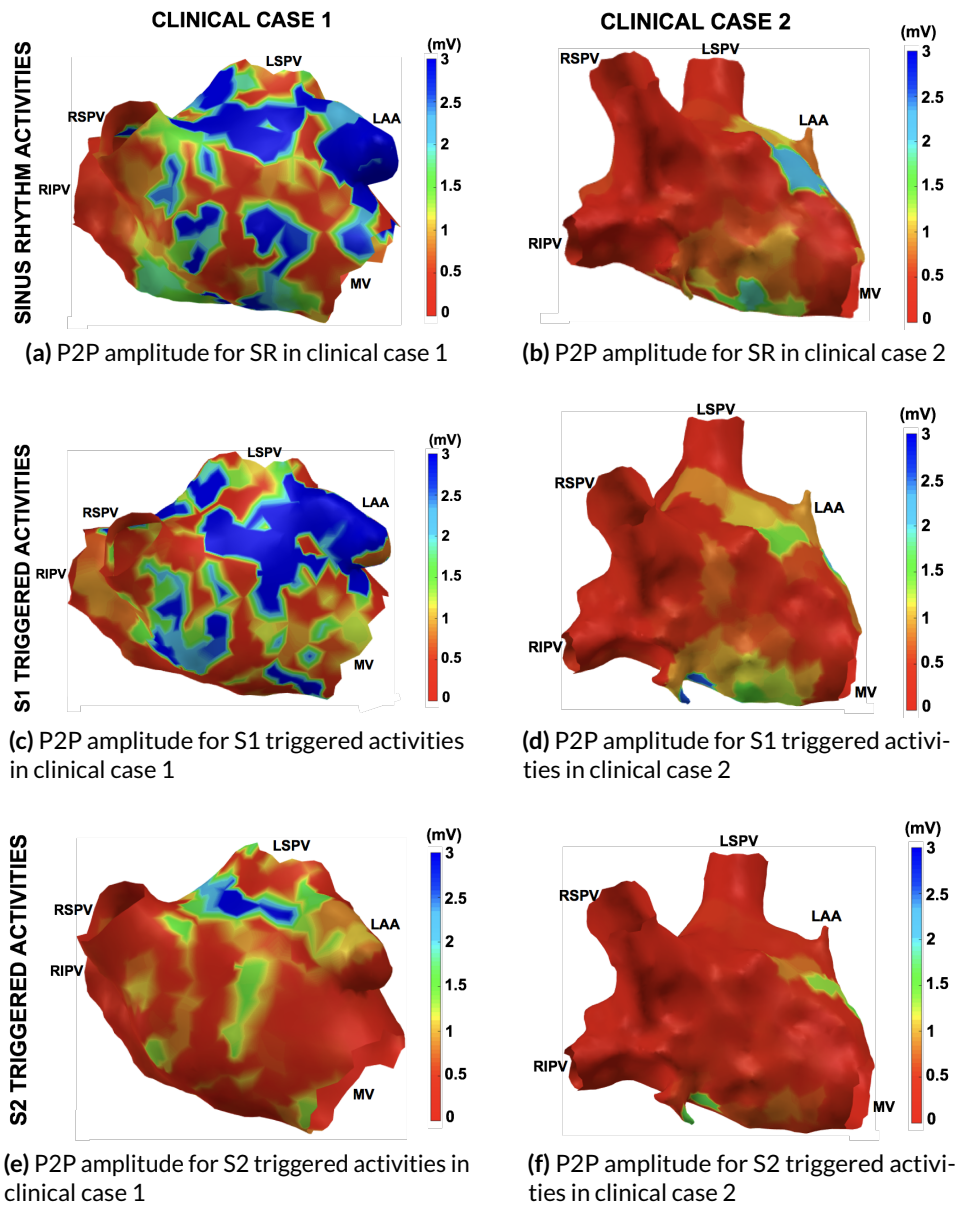


Figure 14.13: P2P amplitude for SN, S1 and S2 triggered activities visualised over the atrial geometry for clinical case 1 and clinical case 2. EA- Early activation, LA- Late activation, LSPV- Left superior pulmonary vein, RIPV- Right inferior pulmonary vein, RSPV- Right superior pulmonary vein, LAA- Left atrial appendage, MV- Mitral valve. Blue region is the region with high P2P amplitude and therefore suspected to be healthy.

propagation of the depolarisation wavefront. Higher the values of FD along with complex morphology represent the slower propagation of the depolarisation wavefront along with more fibrosis.

In Figure 14.14, the region near the PV have higher estimated FD values. Therefore, these are compared with the P2P values and the CV propagation directions to get the result of

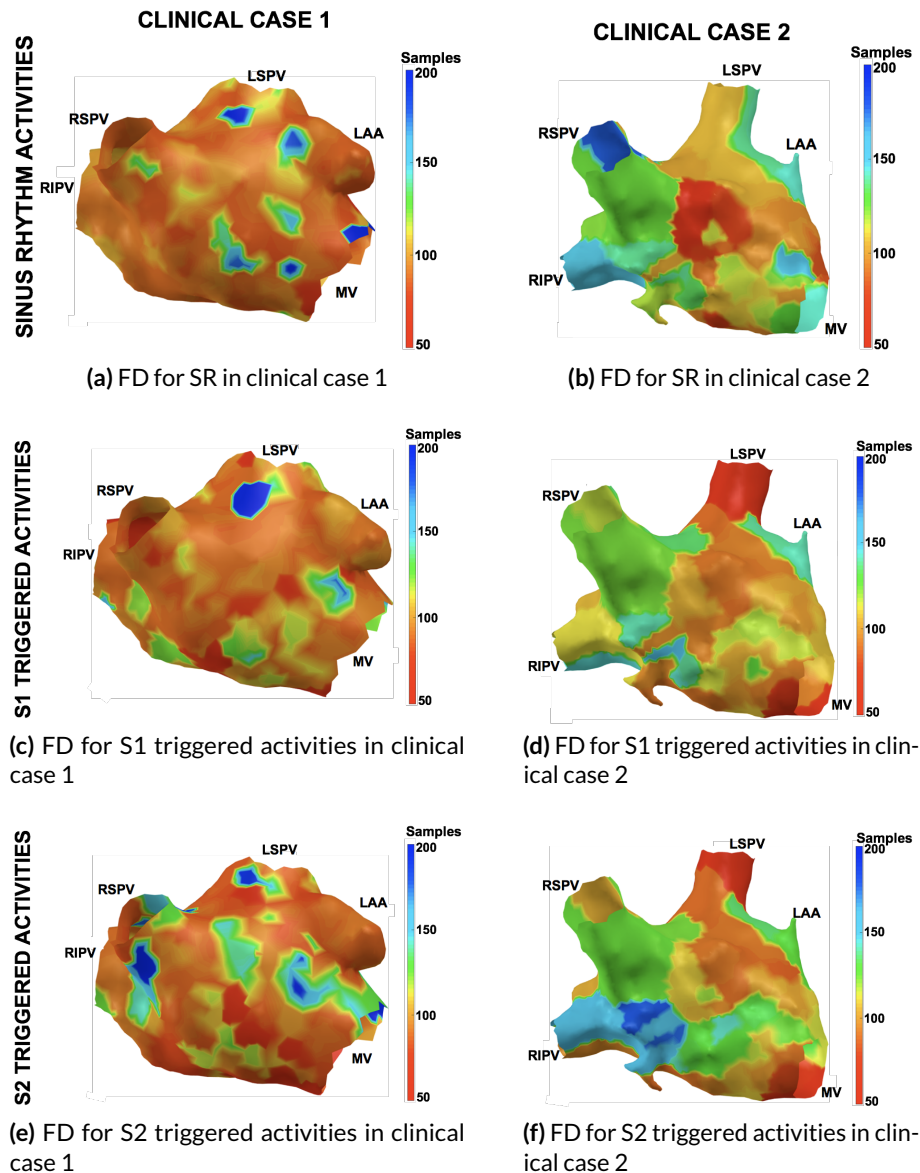


Figure 14.14: FD for SR, S1 and S2 triggered activities visualised over the atrial geometry for clinical case 1 and clinical case 2. EA- Early activation, LA- Late activation, LSPV- Left superior pulmonary vein, LIPV- Left inferior pulmonary vein, RSPV- Right superior pulmonary vein, RIPV- Right inferior pulmonary vein, LAA- Left atrial appendage, MV- Mitral valve. Blue region is the highly fractionated region and therefore suspected to be slow conducting region.

arrhythmogenic substrate marking on the atrial geometries. The comparison of the FD along with other statistical parameters such as CV can give an information about the regional substrates.

14.11 Morphological Correlation

The morphology of the atrial complexes contains a lot of information. In the clinical environment during the electroanatomical mapping, it is difficult to get the orientation information of the catheter. The deflections in the atrial complexes vary as the depolarisation wavefront approaches or leaves the recorded electrode. This also varies with the orientation of the catheter.

In the clinical environment this information (catheter orientation) was difficult to obtain. In this work, the stimulus protocol was used to understand the depolarisation wavefront propagation. From the stimulus protocol, 3 depolarisation wavefronts were obtained in each clinical case. As explained before SR activity was triggered from the SN, while the external stimuli were given from the CS catheter resulting into the S1 and S2 triggered activities. These S1 and S2 activities were triggered from the same location. Due to the same location triggering, in healthy heart and in normal situations it was expected for both the excitation propagation to take the same pathway on the atrium.

The relation between the morphologies of these activities were analysed using the morphological correlations. The $SN - S1$ triggered activity morphological correlation was estimated and is presented in Figure 14.15a. Similarly the $S1 - S2$ triggered activity morphological correlation was estimated and is presented in Figure 14.15c.

It was expected to get a low morphological correlation for $SN - S1$ triggered, since the pathways were different. While for $S1 - S2$, the morphological correlation was expected to be high, since these were triggered from the same locations and therefore, should take the same pathways.

The result represented in Figure 14.15, shows that $SN - S1$ has the $\sim 69\%$ correlation while $S1 - S2$ has the $\sim 90\%$ correlation. These were then visualised over the atrial geometries to get the regional information as represented in Figure 14.15b and d. In Figure 14.15b, the region with high values of correlation are the region of interest while in Figure 14.15d, the region with low value of correlation are of interest.

14.12 LAT Determination

Local activation time marks the temporal arrival of the depolarisation activation at the respective location on the atrium. It is an important electrophysiological parameter for annotating the depolarisation wavefront propagation pattern over the atrium. The local activation time (LAT) information can be extracted from the bipolar or unipolar electrograms using any of the method explained in chapter 9. Once calculated, the LAT values are interpolated on the

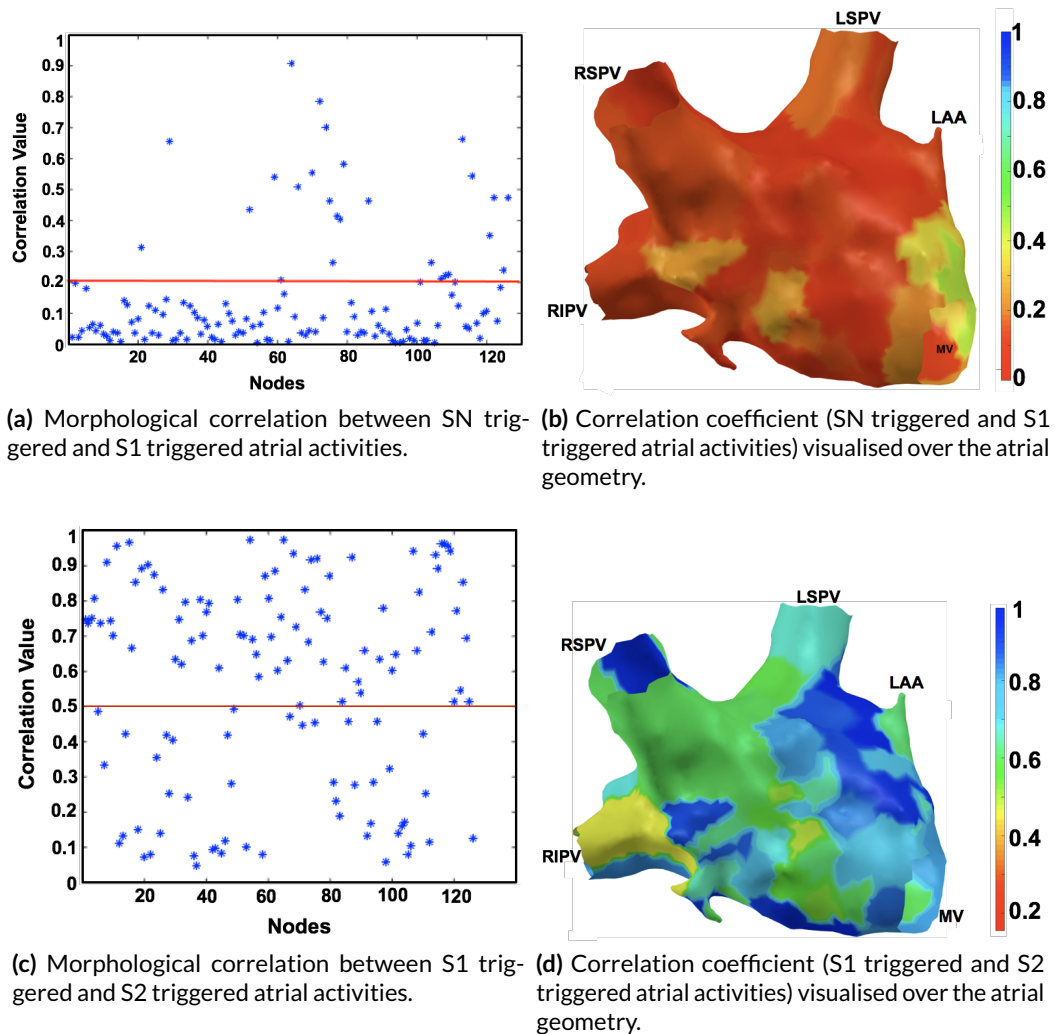


Figure 14.15: Morphological correlation for SN, S1 and S2 triggered activities visualised over the atrial geometry for a clinical case. EA- Early activation, LA- Late activation, LSPV- Left superior pulmonary vein, LIPV- Left inferior pulmonary vein, RSPV- Right superior pulmonary vein, RIPV- Right inferior pulmonary vein, LAA- Left atrial appendage, MV- Mitral valve.

triangular mesh and the LAT map was generated for better visualisation purpose.

During the research the LAT estimation was done using the NLEO as represented in Figure 9.12 and Figure 9.13. In both the cases, the atrial complexes were used to get the NLEO curve and then the maxima of NLEO was marked as the LAT. In case of the stimulus data, the stimulus artefacts were used as the reference. Figure 9.13b represents the LAT estimate between the stimulus artefact and the respective atrial complexes.

Similar to the above cases, the estimation was done for SR, S1 triggered depolarisation and S2 triggered depolarisation wavefront and LAT values, visualised over the atrial geometry, are

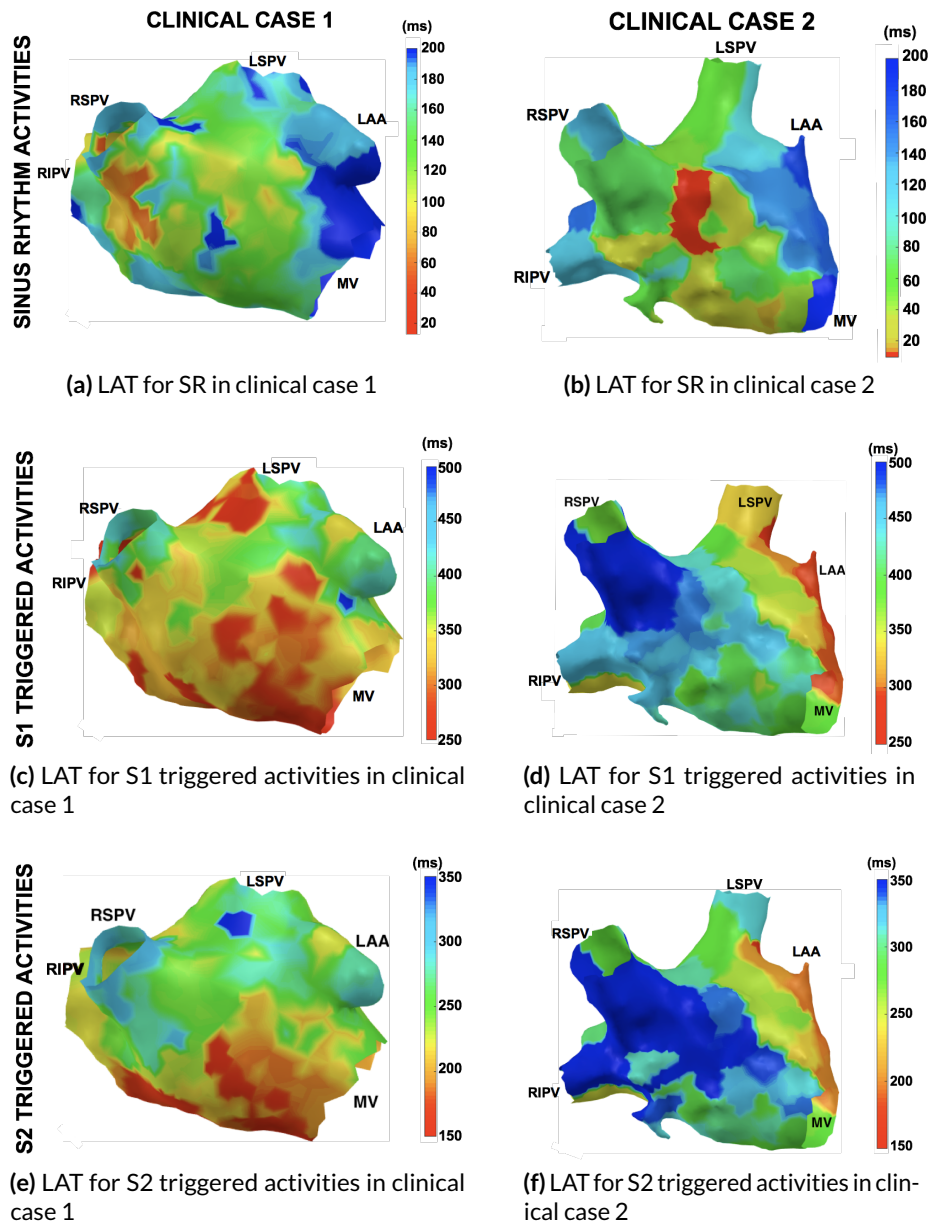


Figure 14.16: LAT for SN, S1 and S2 triggered activities visualised over the atrial geometry for clinical case 1 and clinical case 2. EA- Early activation, LA- Late activation, LSPV- Left superior pulmonary vein, RIPV- Left inferior pulmonary vein, RSPV- Right superior pulmonary vein, RIPV- Right inferior pulmonary vein, LAA- Left atrial appendage, MV- Mitral valve. Red is the early activation region and blue is the late activation region.

represented in Figure 14.16. In Figure 14.16a and b it can be observed that the depolarisation propagation started near the BB. Where in Figure 14.16c to f, it can be observed that the depolarisation propagation started near the CS catheter positions. These results represent the LAT estimated from the clinical data (unhealthy atria). As observed the propagation obtained is not very smooth over the atrium. The obtained LAT maps were analysed along with the

FD and P2P values to find the region with arrhythmogenic substrates as explained in chapter 9.

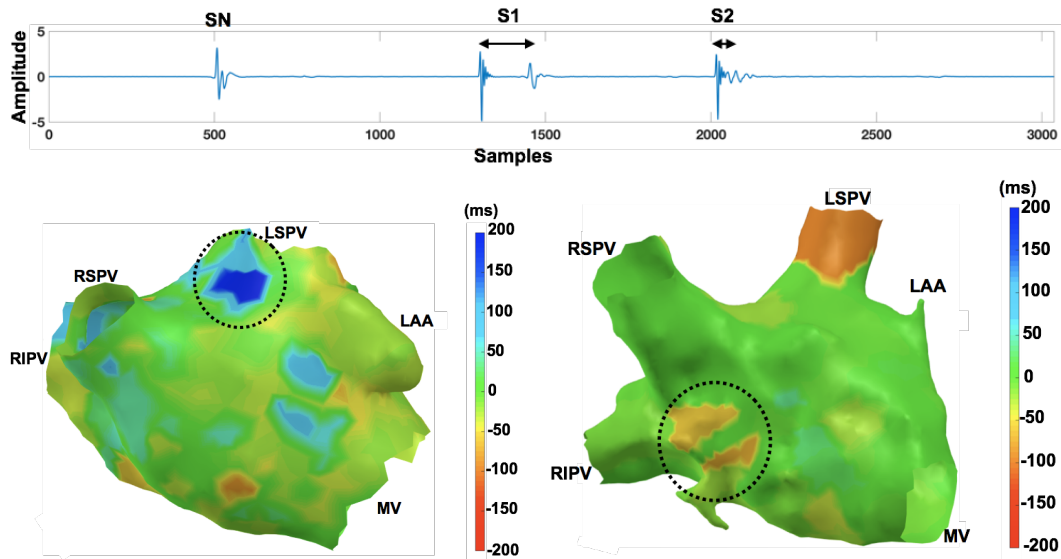


Figure 14.17: Illustration of LAT differences for S1 and S2 triggered activities. a). Electrogram obtained at any arbitrary location on the atrium representing the S1 and S2 span are different. b). The differences between LAT times obtained from S1 and S2 triggered activities for clinical case 1. c). The differences between LAT times obtained from S1 and S2 triggered activities for clinical case 2.

Since S1 and S2 triggered activities initiated from the same location, therefore by comparing the pathways by the respective depolarisation wavefront, the region of interest can be marked. The region of interest based on the LAT could be the one in which the propagation pattern differed. Figure 14.17a is an electrogram from an arbitrary location on the atrium. In this it can be clearly seen that the S1 span (time taken by the wavefront to reach the particular location) is greater than S2 span. This points to the fact that either the wavefront was faster for S2 triggered depolarisation excitation or took some other pathway to reach that location.

Figure 14.17b and c represent the LAT time difference map on the atrium for respective cases. From this it can be observed that although the S1 and S2 stimulus got triggered from one location after a considerable gap of 350ms, there were differences in the path and the time taken by the depolarisation wavefront. This could be because of the arrhythmogeneity present.

The LAT estimation was also done for the canine data. This has been represented in the separate section in chapter 17, since that was the 2D patch data of 10second long segment recorded during SR and various stimulus cycles.

14.13 Region of Interest Determination

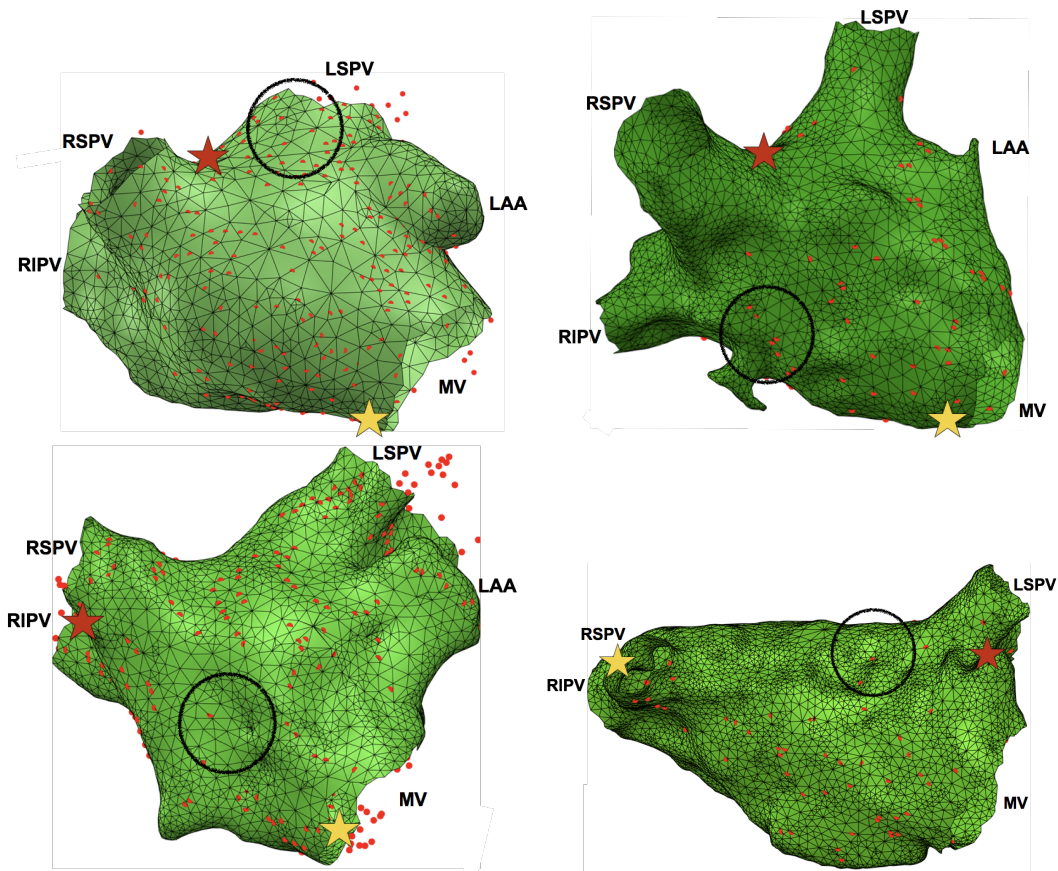


Figure 14.18: Selected region of interest on all the clinical geometries

P2P amplitudes, LAT, FD, morphological correlation were calculated and visualised over the atrial geometry. Regions having small P2P amplitudes, higher FD, low morphological correlations could be observed in the region of arrhythmogenic substrates. Thus, for marking the region of arrhythmogenic substrate, the respectively analysed parameters were taken together.

Heart is a heterogeneous tissue; therefore there are slow and fast conduction areas. The quantitative electrophysiological parameter under scrutiny were the activity instants, also called as the LAT, the amplitude variations called as P2P values and the duration of the activity complexes called the FD. Combining Figure 14.13 to Figure 14.17, the region of interest are marked in Figure 14.18. The activity due to S1 and S2 triggers were compared to see the region in which the propagation direction of the depolarisation wavefronts changes. The encircled region represents the region with differences in the depolarisation wavefront propagation pattern and therefore, could be an indication for the arrhythmogenic substrate. The region of interest basically is finding the target sites for the ablation therapy analysing the

clinical electrograms quantitative. These region of interest give a suspected region which has low voltage signals along with larger fractionated complexes. Therefore, these are marked as the suspected regions. In the upcoming section these ROI have also been linked to the conduction velocity (CV).

Although the ablation of the complex fractionated sites have proven some clinical efficacy, still the complex fractionated electrograms are non specific markers of important target sites because they can be generated by passive mechanisms that play no role in fibrillation maintenance.

Stimulus Protocol Results

As explained in chapter 8, stimulation is the process of applying an external trigger (called stimuli or stimulus) at any location on the cardiac tissue. This could be done by providing adequate amount of energy (above threshold) to the cardiac tissue. This energy threshold is defined by the strength-duration curve (Figure 2.9). Mathematically this is explained using the Weiss equation (Equation 2.9).

During this research various feature analysis was done on the clinical data obtained after stimulation. The special stimulus protocols were used to stimulate the atrium and to get more than one depolarisation wavefront excitation pattern and pathway over the atrium. The special clinical protocols used for stimulation were $400 - 350ms$ and $380 - 320ms$ and the external trigger were applied from the catheter positioned in the coronary sinus (CS). The depolarisation wavefront initiated from this point thereafter covered the entire atrium. During stimulation, all the safety measures were taken into consideration. Figure 8.1 represents the approximate location of the stimulus (yellow star) and the location near Bachmann bundle (BB) from where the normal sinus rhythm (SR) entered the left atrium (LA).

Figure 8.2 represents some electrograms (from any arbitrary location) obtained for the respective clinical cases, along with the atrial activities and their respective stimulus artefacts. It could be observed that the stimulus artefacts and the activities thereafter always appeared after the SR activities. In our case since the $400 - 350ms$ and $380 - 320ms$ protocols were used therefore, the approximate temporal difference between the S1 and S2 artefact were $350ms$ or $320ms$ respectively. While, the temporal difference between SN and S1 were $400ms$ or $380ms$ respectively.

The recordings were done during SR and the segments to be recorded were manually marked by the physicians. As the catheter moved inside the atrium, the endocardial electrograms representing the activation complexes for various catheter positions were recorded. During

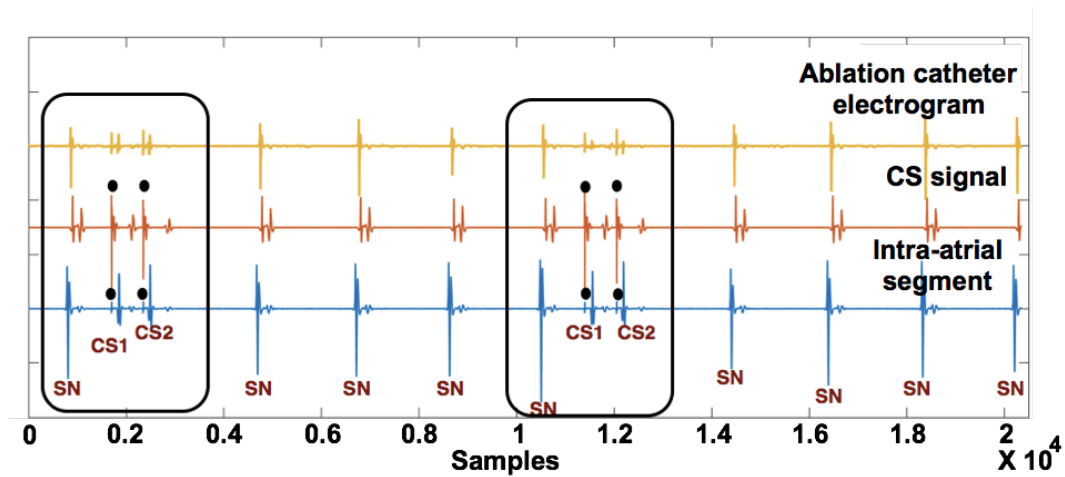


Figure 15.1: Representation of signals from various catheters during endocardial mapping. The clear stimulus artefact with maximum amplitude can be observed in the CS signal. Corresponding to this, the signals can also be observed in the ablation catheter and the mapping intracardiac catheter.

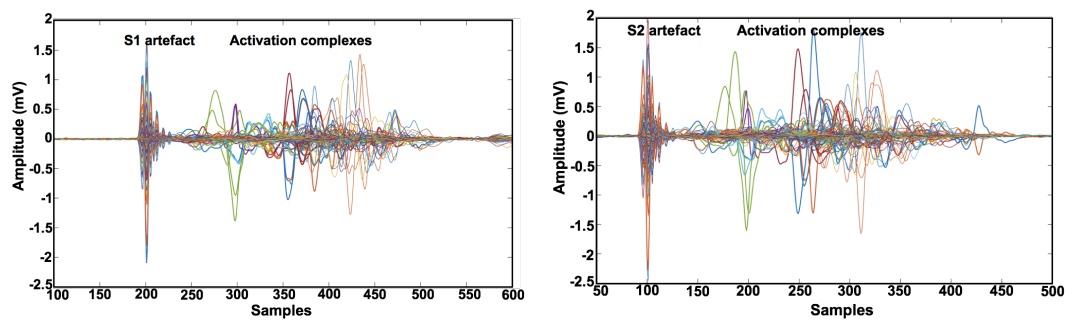


Figure 15.2: S1 and S2 segments segregated from 1.5 second long segment. The selected signals are 500 samples and 450 samples long (corresponding to 245 ms and 220 ms respectively). a). All the segments from various locations superimposed on each other. The stimulus artefacts having different morphologies are marked along with the activation complexes for S1 triggered activities. b). All the segments from various locations superimposed on each other. The stimulus artefacts having different morphologies are marked along with the activation complexes for S2 triggered activities.

the procedure, the recordings were done for all the stable catheter positions. Figure 15.1 represents a segment obtained using electrodes of the LASSO catheter, ablation catheter and the CS catheter respectively. There is a variable number of SN activities present before and after the stimulus activities, SN represents the SR activity triggered from the SN. The stimuli were given after the stable SR. The stimuli were given from the CS catheter and therefore, in the respective CS signal (orange) a high amplitude and clear activation complexes can be observed, marked by black dots. The corresponding signals were also recorded by other catheters as represented for the ablation catheter, but the magnitude was variable in the respective catheter. The temporal information of the stimulus signals from CS catheter was used as a reference to mark the temporal existence of the stimulus artefact in the intracardiac electrogram. This is represented by black dots in CS signal and the intracardiac signal (Figure 15.1). Various types of artefacts such as ventricular far field (VFF), noise, baseline

wander etc. were also present in the electrograms.

Since the three triggers (SN, S1 and S2) resulted into three different depolarisation wavefronts, therefore, these were analysed separately. The first stage of analysis was to get the segments containing the three activities at various recorded locations. This was done using the location and temporal information from the mapping system. Figure 8.3 and Figure 8.4 represent the electrograms at various locations on the atrial geometry.

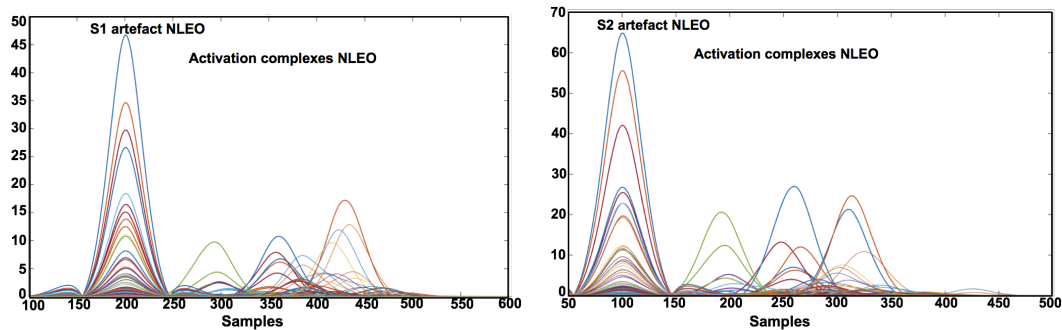


Figure 15.3: NLEO curve for S1 and S2 segments segregated from 1.5 second long segment. The selected signals are 500 *samples* and 450 *samples* long, corresponding to 245 *ms* and 220 *ms* respectively. First peak is the stimulus artefact peak and second peak of respective signal corresponds to the respective atrial activation complex. a). NLEO curve for all the segments from various locations superimposed on each other. First peak is the stimulus artefact peak and second peak of respective signal corresponds to the atrial activation complex S1. b). NLEO curve for all the segments from various locations superimposed on each other. First peak is the stimulus artefact peak and second peak of respective signal corresponds to the atrial activation complex S2.

In the next stage of analysis, the three SN, S1 and S2 activities were then separated as represented in Figure 8.3. Figure 8.5 also represents all the activities superimposed on each other. The section having the SN, S1 and S2 activities were then segregated based on their temporal existence. Figure 15.2 represents the S1 and S2 triggered artefacts along with the respective activities (superimposed on each other) for all the locations. The pre-processing of these signals was then done to remove the unwanted artefacts and to get the relevant information from the given segment. Since these are the bipolar signals, the low pass and high pass filtering of 300 *Hz* to 3 *Hz* respectively were used to remove the unwanted high frequency contents and the baseline wander from the signals. The temporal alignment of the S1 and S2 artefact was done to remove any temporal offset (if present). The maxima of the NLEO curve were used for temporal alignment and offset removal around the stimulus artefact. For this the NLEO was estimated for the CS catheter signal and the intracardiac signal. Then the maxima of the NLEO of CS catheter electrograms were aligned with the maxima of the NLEO of the stimulus artefact of the intracardiac electrogram.

The selected signals segments are 500 *samples* and 450 *samples* long, corresponding to 245 *ms* and 220 *ms* respectively for S1 and S2 triggered activities respectively. To select the

segment for analysis, the temporal information was used. At each location, 100 *samples* before the stimulus artefact and 400 *samples* after the stimulus artefact were selected. Thus giving the 500 *samples* long segment for analysis.

Figure 9.7 clearly represents the VFF lying outside the selected window. In the same figure, the first peak is the stimulus artefact peak and second peak is the energy of the respective signal corresponding to the respective atrial activation complexes. Subtracting the time of the maxima of NLEO activation complex with the maxima of NLEO of stimulus artefact gives the time that each activity took to reach the particular location. This time is then regarded as the local activation time (LAT) of the respective location. The NLEO of all the activities superimposed on each other is represented in Figure 15.3. It can be clearly observed in Figure 15.3a and Figure 15.3b, that the maxima of all the stimulus artefacts are perfectly aligned, even if their morphologies were different.

The data obtained for all the depolarisation wavefronts were individually taken for CV estimation as represented in chapter 10 and 16. Since the stimulus protocol endocardial mapping was done for 4 clinical cases, thus in total 12 depolarisation wavefronts were analysed. For all the cases, the LAT estimation was done in the same way. Two types of stimulation (400 – 350 *ms* and 380 – 320 *ms*) cases were analysed during the course of this research, the method of LAT estimation was the same for both.

The other stimulus protocol data analysis was used with the canine data. In this case, the continuous pacing was done for 3 weeks to induce atrial fibrillation in the dog heart. The detailed description and explanation of the canine data is done in chapter 12 and 17 respectively.

Estimated Conduction Velocity

CV is an important electrophysiological parameter in understanding the heterogeneities of the atrial substrate. Getting the information of the slow and fast conducting regions, presence of scar and having the propagation pattern can help the physicians in better diagnosis and a successful ablation procedure. In this thesis, the conduction velocity (CV) estimation for the clinical and simulated data was done using the modified triangulation method as explained in section 10.2. This chapter includes the results obtained for the global and regional CV (magnitude and direction). The estimation was done using the spatiotemporal information on the atrial surface. The FaMaS method was used to obtain the simulated local activation time (LAT) data. In the clinical data, the LATs were estimated using the bipolar electrograms after preprocessing and the clinical geometries were obtained from the electroanatomical mapping system. The LAT estimated using the non-linear energy operator (NLEO) were the temporal coordinates and the recorded locations were used as the spatial coordinates for CV estimation. The simulations were done to benchmark the proposed CV estimation algorithm, which could then be used with the clinical data.

The homogeneous and heterogeneous excitation simulations were done with prescribed input speed (known golden truth). As explained in chapter 10 (Figure 10.5 and Figure 10.6), the CV estimation was divided into three approaches, depending on the number of triangular mesh vertices (T), number of nodes for which the temporal information was available (L), and if selected datasets of the temporal nodes (D) exist. If the nodes with temporal information are divided into datasets (example, in atrial flutter (AFlut) cases), then the number of datasets is expressed as D . But if the temporal coordinates are not divided into datasets (example, in AFib cases), then D does not exist. The three approaches are:

1. CV estimation using all the triangular mesh nodes (i.e., when $L=T$), as explained in chapter 10. That was, when the spatiotemporal information was available at all the vertices of the triangular mesh.

Table 16.1: Results of homogeneous excitation propagation simulations done using FaMaS.

| S.No. | Clinical case | Given propagation speed for simulation (m/s) | Trigger Point location | CV calculated in non collision region (m/s) | Percentage error |
|-------|---------------|--|------------------------|---|------------------|
| 1 | 1 | 0.507 | near | 0.507 ± 0.011 | $\sim 2\%$ |
| 2 | 2 | 0.507 | BB | 0.507 ± 0.019 | $\sim 4\%$ |
| 3 | 3 | 0.507 | | 0.507 ± 0.014 | $\sim 3\%$ |
| 4 | 4 | 0.507 | | 0.507 ± 0.012 | $\sim 2\%$ |
| 5 | 1 | 0.507 | Near CS | 0.507 ± 0.010 | $\sim 2\%$ |

2. CV estimation using some of the triangular mesh nodes (i.e. when $L < T$), as explained in chapter 10. That was, when the spatiotemporal information was available at some of the vertices of the triangular mesh.

3. CV estimation using a selected dataset obtained from clinically processed data (i.e. when $L < T$ and D exist), as explained in chapter 10. That was when the spatiotemporal information was available at some of the vertices of the triangular mesh and was divided into various datasets.

Approach 1 and 2 can be used when the data were obtained as a high resolution map from any electroanatomical mapping system, when the CV estimation is to be done for patched data (example, Chapter 12, canine data CV estimation) or for flutter cases. In this all the triads were respectively taken into consideration for CV estimation. The homogeneous and heterogeneous scenarios and the flutter case data are explained in this thesis. The results obtained are stated and explained in the respective section below for all the cases. The next section of this chapter deals with the CV estimation for stable catheter positions. Most of the mapping catheters (eg. LASSO or PentaRay catheter) give low density maps. Additionally the temporal resolution of these catheters is not very high. The physicians voluntarily move the catheter and change its shape and orientation to get a better coverage map. A successful attempt has been made to calculate CV for this scenario as explained below in the respective section.

16.1 CV Estimation for Simulated Data

Simulated environments are often used to analyse the idealised and controlled scenarios. To get an understanding of the depolarisation wavefront propagation for homogeneous and heterogeneous speeds, the simulated LAT maps were generated using FaMaS as explained in chapter 5. These LAT maps were later used to get the CV speed and direction for the homogeneous as well as heterogeneous depolarisation wavefront propagations. In chapter 13, the simulated LAT maps are represented for all the cases. This chapter deals with the CV estimation results obtained using the modified triangulation method for all the simulated

cases explained in chapter 10. Since this was a controlled environment, these results were later used to benchmark the algorithm and to statistically obtain the accuracy of the algorithm. Table 5.1, gives the details of the various simulations done and their respective results are explained in Table 16.1.

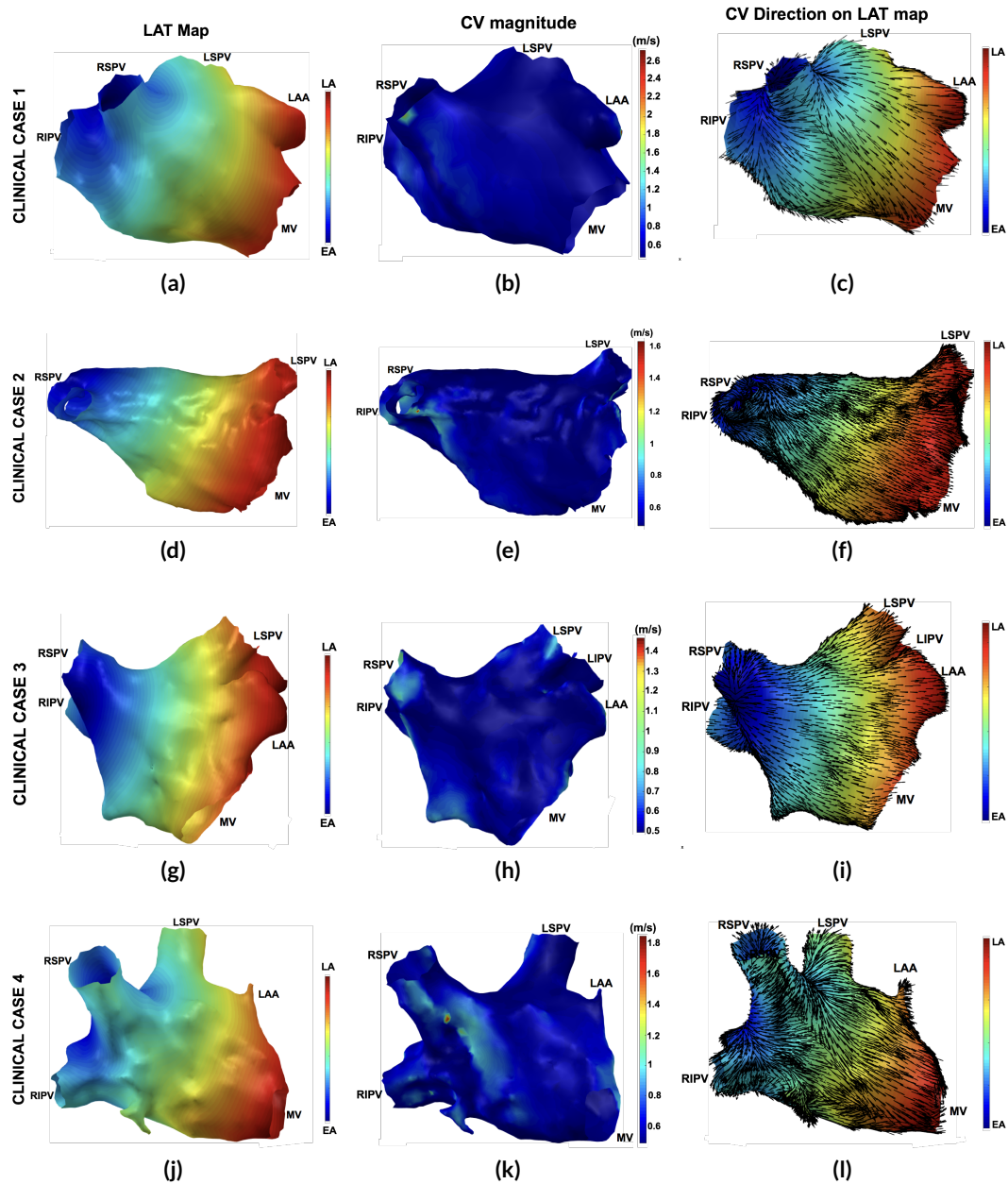


Figure 16.1: Estimated CV for homogeneous depolarisation propagation on the given clinical case geometries. EA- early activation, LA- late activation, LSPV- left superior pulmonary vein, LIPV- left inferior pulmonary vein, RSPV- right superior pulmonary vein, RIPV- right inferior pulmonary vein, LAA- left atrial appendage, MV- mitral valve.

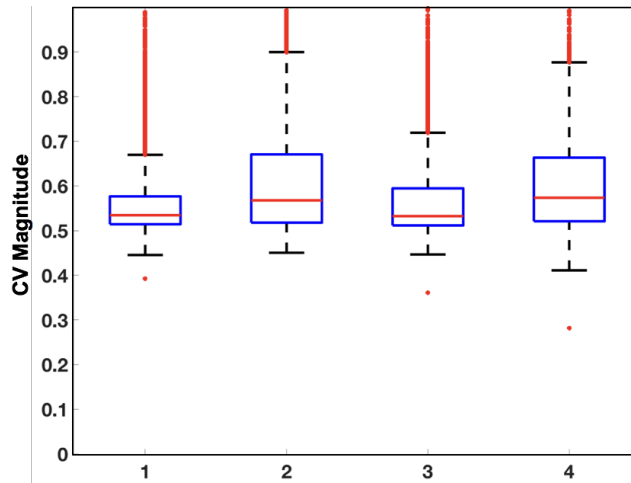


Figure 16.2: CV magnitude (m/s) for all the four cases represented in Figure 16.1. Slightly higher than the expected CV was obtained with the percentage error represented in Table 16.1. The outliers are in the region of wavefront collision as seen by the CV interpolated on the atrium.

16.1.1 Homogeneous Propagation Simulation

The term homogeneous means that the excitation propagation speed was uniform (single speed) on the atrial surface, irrespective of the curvature or the region on the atrium. The geometries for homogeneous propagation simulation and their corresponding LAT maps are represented in chapter 13. Table 16.1 gives the details about the various propagation speeds. The first column in Figure 16.1, represents the simulated depolarisation propagation pattern using LAT interpolation over all the four clinical geometries. Blue represents the early activation (EA) and red represents the late activation (LA). For all the cases, the propagation speed used as input was 0.507 m/s . The CV were estimated and visualised on the respective left atrium geometries using the simulated LATs and their respective geometries. The CV estimation was done as explained in section 10.2.1. The magnitude is visualised on the atrium and is represented in column 2 of Figure 16.1 for respective clinical cases. Also Figure 16.2 is the box-plot representation of CV magnitudes for all the four clinical cases. The direction of the CV has been visualised over the LAT map for the respective clinical case and represented in column 3 of Figure 16.1.

A percentage error of up to $\approx 3\%$ was observed. There exist few outliers in the CV magnitude as represented in the box plot (Figure 16.2). These outliers are observed in the regions of wavefront collision only. For all the cases, the higher CV magnitudes were obtained in the collision regions as represented in column 2 of Figure 16.1. These were the region where the time difference between two vertices of the triad was too small. This is because of the fact that

$$Speed = \frac{\Delta x}{\Delta t}$$

Table 16.2: Results of heterogeneous excitation propagation simulations done using FaMaS

| S.No. | Clinical case | Heterogeneous regions | Given propagation speed for simulation (m/s) | Trigger Point location | CV calculated in non collision region (m/s) | Percentage error |
|-------|---------------|-----------------------|--|------------------------|---|--------------------------------|
| 1 | 1 | 2 | 0.6 and 0.3 | | 0.3 ± 0.013 and 0.6 ± 0.014 | $\sim 2.33\%$ $\sim 4.33\%$ |
| 2 | 1 | 4 | 0.6, 0.4, 0.3 and 0.2 | near BB | 0.6 ± 0.016 | $\sim 3\%$ |
| 3 | 1 | 4 | 0.2, 0.4, 0.6 and 0.8 | | 0.20 ± 0.013 | $\sim 7\%$ |

If time approaches zero, the speed shoots up to a very high value. The changes in *distance* and *time* are the mutually independent spatial and temporal coordinates. Their ratio, is also not the same and the $CV-\Delta time$ shares the inverse proportionality relationship. This also makes the statistical estimation of the CV magnitude error with respect to the spatial and temporal coordinates difficult using the available data. It has also been observed that the CV magnitude median is slightly higher than the known golden truth of $0.507 m/s$, but at the same time the spread is very low. The magnitude lies in the range of $\approx 10\%$ of the expected value, making it a robust and reliable method for CV estimation.

16.1.2 Heterogeneous Propagation Simulation

Similar to the homogeneous excitation propagation cases, the CV estimation was done using all the vertices of triangular meshes for the heterogeneous excitation propagation. The various geometries and their respective LAT maps for heterogeneous excitation propagation are represented in chapter 10. Different speeds were given to the manually selected regions and the LAT maps were simulated using FaMaS method, as enlisted in Table 16.2. This was done with the changing excitation propagation speed (with respect to the assigned region). The CV estimation for this case was done using the method as explained in section 10.2.1. The simulated LAT maps on the clinical geometries were used as the temporal information for CV estimation. The robustness of the CV estimation algorithm was analysed in the boundary region where the propagation speed changes. Figure 16.3, Figure 16.4 and Figure 16.5 represent the results for some of the heterogeneous cases. The estimated CV magnitudes are visualised on the atrial surface and CV direction vectors are visualised on the LAT maps.

Figure 16.3 represents the CV estimation for two types of excitation speed ($0.3 m/s$ and $0.6 m/s$). Figure 16.3a represents the manually selected region on the atrial geometry. This selection was done using MATLAB software, the various input speeds are represented in Figure 16.3b. Figure 16.3c and d represent the CV magnitude and the direction vectors representing the propagation direction of the depolarisation wavefront visualised over the

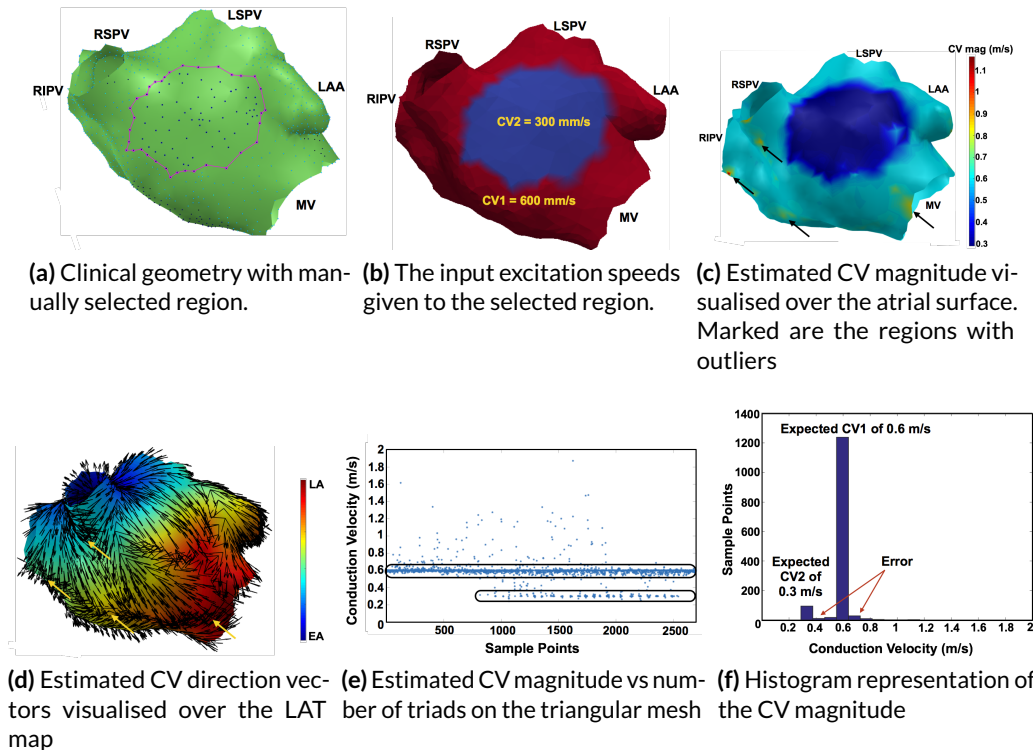


Figure 16.3: Estimated CV for heterogeneous excitation propagation on the given clinical case geometry. EA- early activation, LA- late activation, LSPV- left superior pulmonary vein, LIPV- left inferior pulmonary vein, RSPV- right superior pulmonary vein, RIPV- right inferior pulmonary vein, LAA- left atrial appendage, MV- mitral valve.

atrial surface and on the LAT map respectively. It can be clearly seen in Figure 16.3c that the slow propagating region has the estimated CV ($\approx 0.3 \text{ m/s}$), while the rest of the atrial surface has a higher CV magnitude, as expected ($\approx 0.6 \text{ m/s}$). Clear boundaries of these two regions are obtained. Along with this, slight offsets are also obtained in CV magnitude as represented in Figure 16.3e and f. The nodes with error are small in number as compared to the number of nodes at which the CV estimation was done. As represented in Table 16.2, the percentage error in CV magnitude is up to 7%.

Zooming into the excitation propagation over the atrial surface, the observed pattern is as represented in Figure 16.4. This represents the propagation at various time stamps. The encircled region in Figure 16.4a to d are the regions in which the wavefront collision is taking place. If compared with Figure 16.3c, it can be clearly seen that these are the regions with CV magnitude outliers. The similar effect was observed in all other homogeneous and heterogeneous excitation propagation cases. Thus, it is stated that in the region of wavefront collision, the algorithm gives outliers. At the same time, these outlier regions are very small compared to the entire atrial region. Also the method is giving the exact CV direction vectors, therefore the CV direction vectors are reliable for any region on the atrial surface. The other benefit of this method is that it calculates the CV magnitude and direction irrespective of

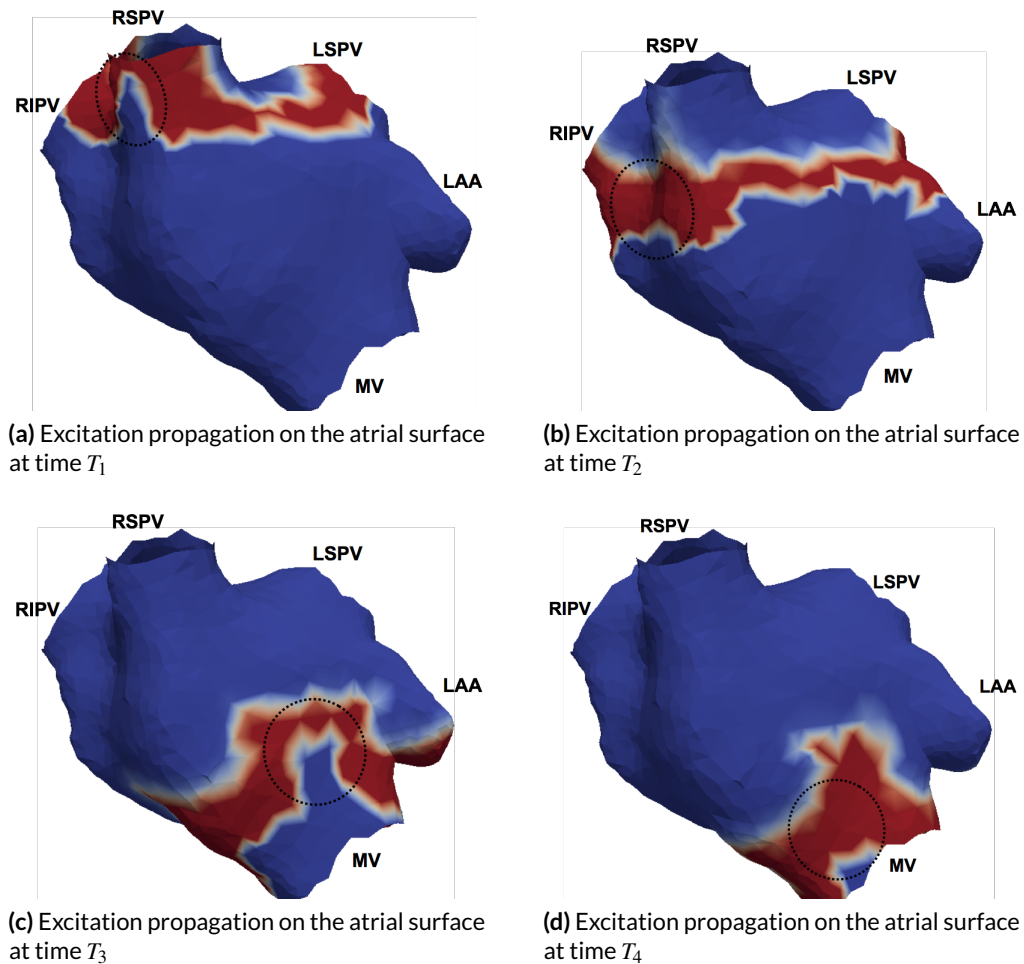


Figure 16.4: Estimated CV collision for heterogeneous excitation propagation on the given clinical case geometry. Encircled is the region of wavefront collision ($T_1 < T_2 < T_3 < T_4$). EA- early activation, LA- late activation, LSPV- left superior pulmonary vein, LIPV- left inferior pulmonary vein, RSPV- right superior pulmonary vein, RIPV- right inferior pulmonary vein, LAA- left atrial appendage, MV- mitral valve.

the type of excitation. This method works good with the planar wavefront, at location of the trigger or with respect to the sink region of the excitation propagation.

A similar analysis was done for the atrial geometries having up to 4 types of tissue classes with different excitation speeds. Depending on the four input excitation speeds ($0.2m/s$, $0.3m/s$, $0.4m/s$ and $0.6m/s$), the LAT map was generated. The regions were manually selected and also the trigger point (starting point of excitation propagation) was manually selected near the Bachmann bundle (BB) in left atrium before the FaMaS simulation. The various tissue classes having variable speeds are enlisted in Table 16.2. This can also be clearly observed in Figure 16.5 (column 1 is the posterior and anterior view). The CV magnitude and directions were estimated using the proposed method and are represented in column 2 and 3 respectively of Figure 16.5. The CV magnitude vs the triangular mesh vertices is represented in Figure 16.5d. Outliers are again present in the region of wavefront

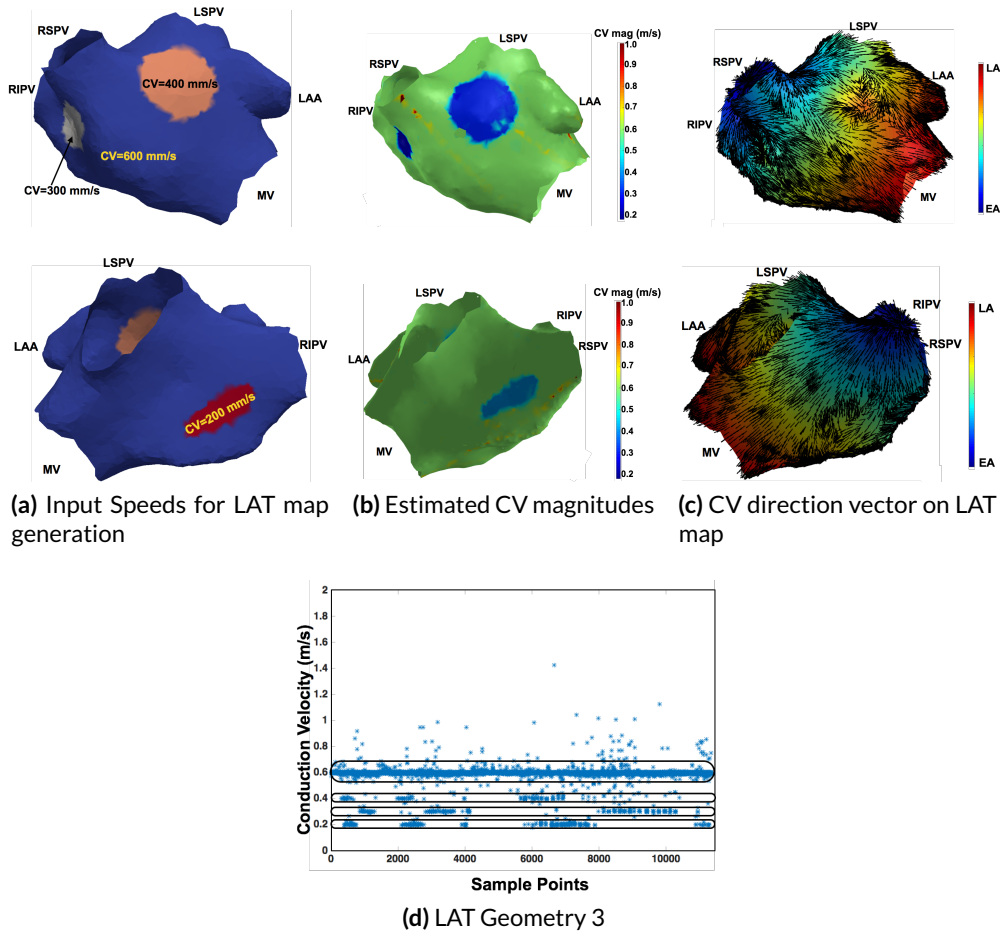


Figure 16.5: Estimated CV for the 3 region depolarisation propagation on the given clinical case geometry. EA- early activation, LA- late activation, LSPV- left superior pulmonary vein, LIPV- left inferior pulmonary vein, RSPV- right superior pulmonary vein, RIPV- right inferior pulmonary vein, LAA- left atrial appendage, MV- mitral valve.

collision.

The CV estimation and interpretation results from the simulated LAT map on the clinical geometries, having a resolution of around 5000 points. The next CV estimations were done for the biatrial geometry as represented in Figure 16.6, having approximately 357471 vertices on the triangular mesh.

The various tissue classes marked on this biatrial geometry are similar to the human atrium. The various regions were given the input excitation speeds as represented in Table 5.2. The trigger was selected manually in the left atrium using the Paraview software. The excitation starts from this trigger and propagates over the entire atrium. The CV estimation was done using the LAT map of Figure 16.6c and d. The corresponding CV magnitudes are represented in Figure 16.6e and f. Very good CV estimates were observed for the biatrial geometry as

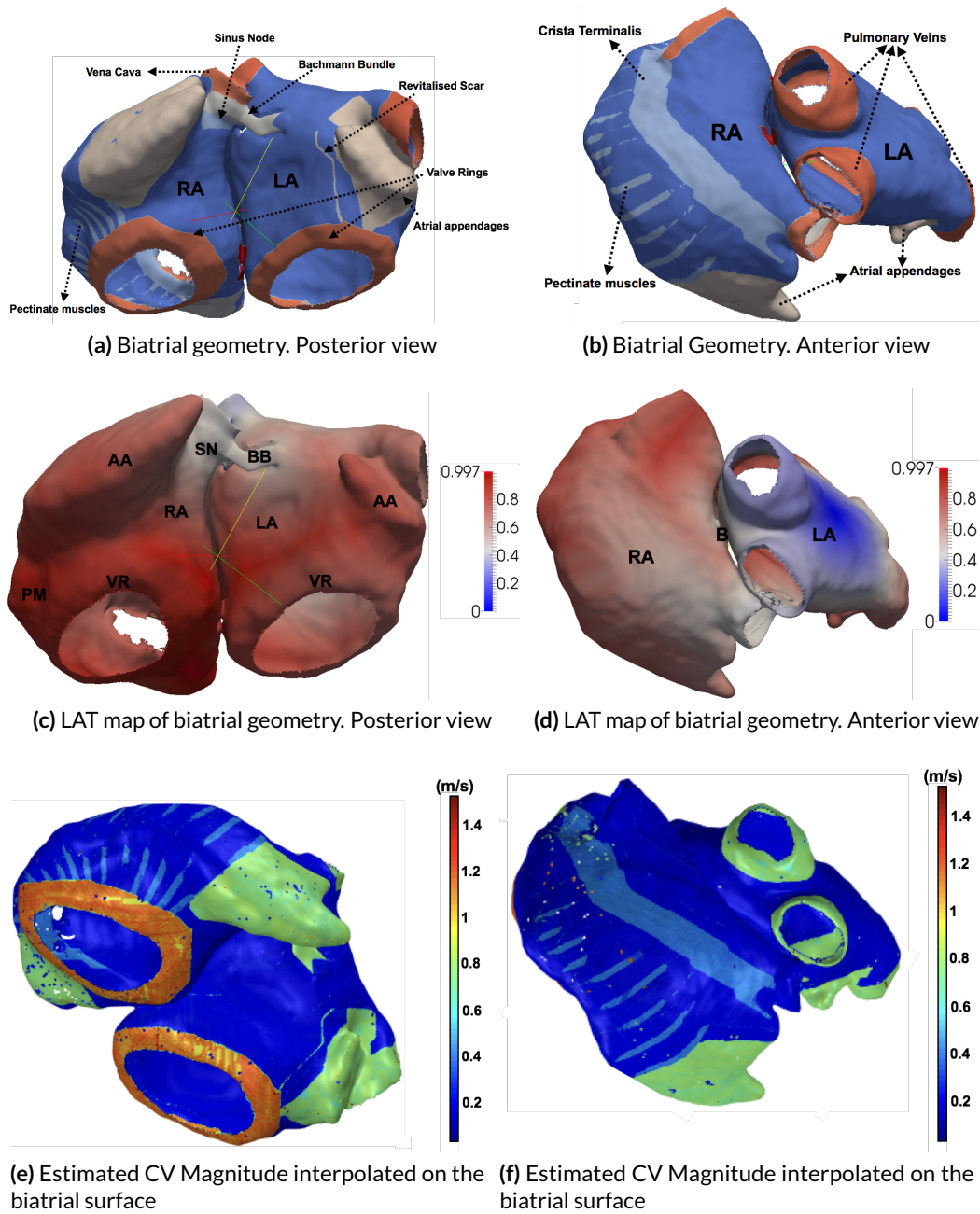


Figure 16.6: Estimated CV for biatrial geometry. Left is the posterior view, right is the anterior view.

well. All the regions can be seen clearly. The revitalised scar (Figure 16.6a) which was given low input excitation speed also was visible on the estimated CV (Figure 16.6e). This case can be considered as a step ahead in estimating the CV using the personalised biatrial model.

Since the triads were used for CV estimation and the geometry is very dense, due to this at some locations the time difference between the triad locations was too small resulting in outliers at certain locations. These can be seen as dots in Figure 16.6*f*.

16.1.3 CV Estimation for Stable Catheter Positions in Simulated Data

Some of the results of CV estimation from simulated data were explained in the above section, where the temporal information was available at all the vertices of the triangular mesh. That was the case when the LAT map was available or when a very high density mapping was done. But in the clinical scenarios, the information available are the electrograms and the geometry which are usually mapped using the catheters such as LASSO or PentaRay. In such cases, as the catheter moves inside the cardiac chamber, the endocardial mapping is done. The recorded locations (where electrograms are recorded) are far less than the number of nodes in the triangular mesh (3D geometrical locations). Also, in fibrillation cases, due to various degree of heterogeneity and fibrosis, the depolarisation wavefront most likely takes variable pathways in certain regions of the atrium. Therefore, if the regional mapping is to be done, the triggered activity might not take the same excitation propagation. Thus, for those cases it is better to calculate the regional CV using the activities recorded by respective trigger/ beat, that is recorded by the stable catheter positions. To do this the various stable catheters were first segregated from the clinical recordings using their temporal information. These stable catheter positions are represented in Figure 9.15 to Figure 9.20.

After the stable catheter positions were selected, using the approach of modified triangulation method mentioned in section 14.2.3, the CV estimation was done. Here, each stable catheter position is regarded as one dataset. Figure 16.7*b*, *c* and *d* represent the estimated CV direction vectors (posterior and anterior view) and magnitudes respectively interpolated on the LAT map of the left atrium. The ground truth speed used for simulating the LAT map (Figure 16.7*a*) was 0.5m/s , and the estimated CV magnitude obtained was 0.54m/s with an inter quartile ratio (IQR) of 0.22. This is a good estimate for such sparse points. The point of interest were the regions with highly curved surfaces (eg, near pulmonary veins and appendages). In these regions too, the propagation directions were obtained as represented by the LAT map. This good estimation of CV benchmarks the algorithm as usable for the clinical cases.

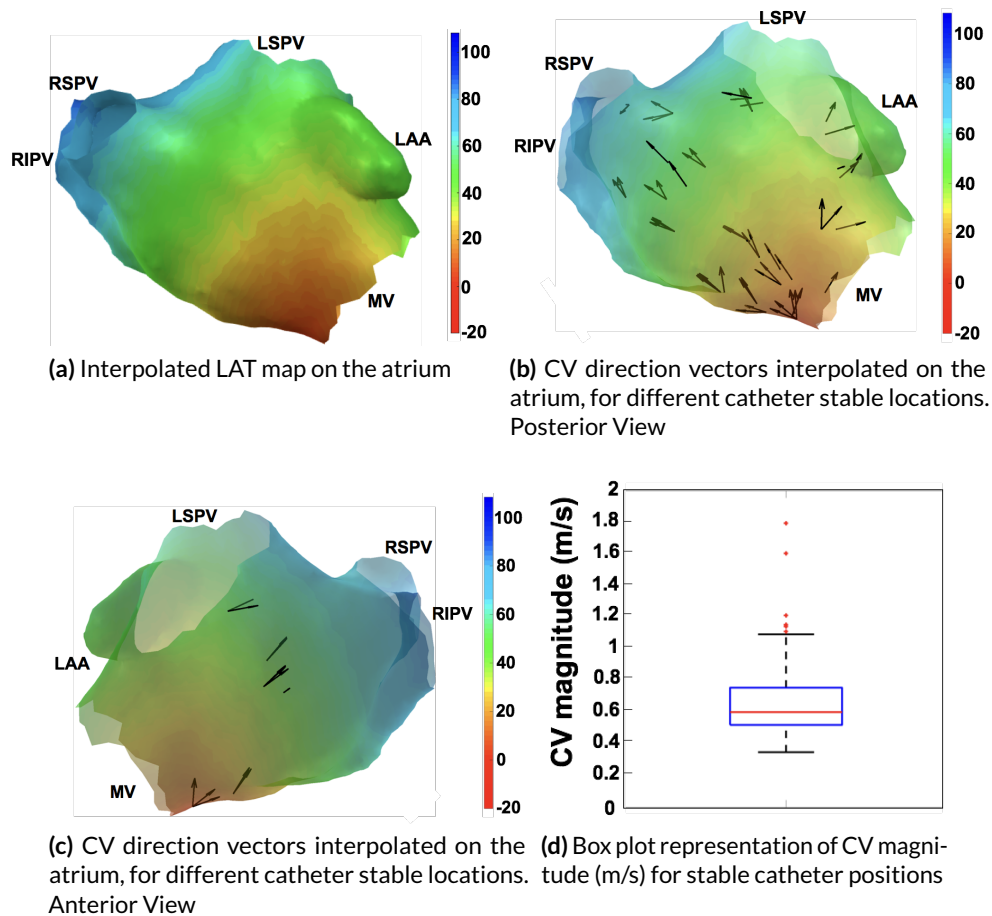


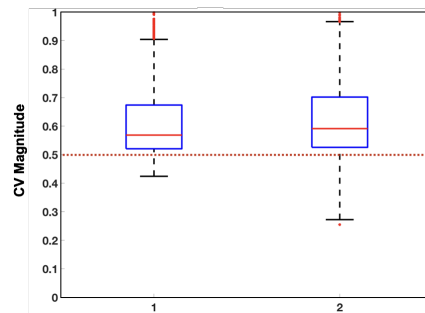
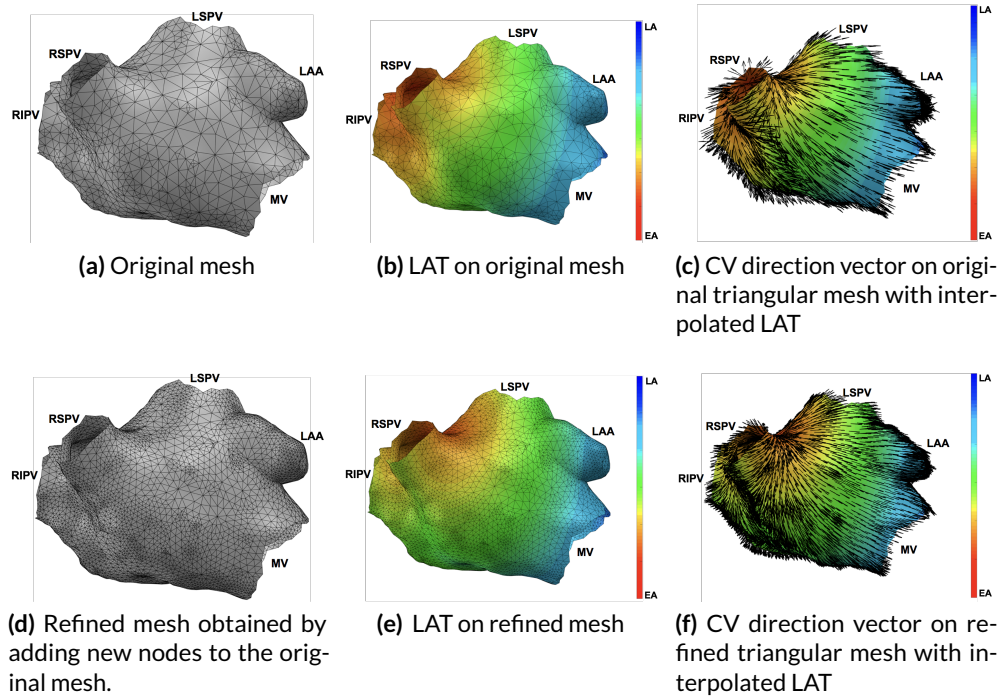
Figure 16.7: Estimated CV for simulated LAT map on the clinical geometry for stable catheter positions. *a* to *c*: Red to blue colour shows the early to late activation respectively.

16.2 Effect of Grid-Size and Noise on CV Estimation

This section deals with the effect of the triangular mesh grid size on the estimated CV. At the same time the effect of noise on the CV estimation was calculated. The results are explained in the respective section below.

16.2.1 Effect of Triangular Mesh-Size on the CV Estimation

This section deals with the estimation of the effect of changes in the triangular mesh on the CV estimation. As the resolution of the triangular mesh changes, the estimated CV magnitude also gets affected. This is analysed and the results obtained are represented in Figure 16.8 for homogeneous propagation of the depolarisation wavefront.



(g) CV magnitude (m/s) comparison using box plot. The ground truth value is represented by the dashed line. Box plot 1 represents the CV on original mesh, 2. represents the CV on refined mesh.

Figure 16.8: Representation of the effect of triangular mesh size on the CV estimation. As the resolution of the triangular mesh changes the CV magnitude changes. Denser the mesh is, less would be the time difference between the vertices of a triads, therefore the CV median shifts slightly away from the ground truth values. But for both the cases, correct CV directions are obtained.

Figure 16.8a and d are the same clinical geometry with different triangular mesh resolution. Figure 16.8b and e are the LAT maps obtained for the respective cases using the trigger at the same location. The excitation propagation goes from early activation (red) to late activation (blue). Figure 16.8c and f represent the CV direction vectors on the atrial surface. Figure 16.8g represents the box plot for the CV magnitudes for both cases. The ground truth speed of excitation for both simulations was kept to be 0.507 m/s . As represented in the box plots, for both cases, magnitudes slightly higher than the ground truth value were

obtained. This was explained in the previous section of this chapter. Comparing the two magnitudes of the box-plot, the median shifts away from ground truth in the denser mesh. Also the spread in the magnitude increases. This is because with a denser mesh the time difference between two vertices of the considered triad gets smaller and also the region of collision points increases. This can be observed comparing Figure 16.8c and *f*. The spread in magnitude depends on the collision regions.

From this analysis, it is observed that changing mesh size does affect the CV magnitude significantly. If the mesh size is reduced, the CV median magnitude gets lower and closer to the ground truth, while for denser mesh the CV median magnitude shifts towards higher values.

16.2.2 Effect of Noise on CV Estimation

This section deals with the effect of noise on the estimated CV done in collaboration with the bachelor student Benedikt Ebener. Various levels of noise were introduced in the estimated LATs obtained using FaMaS (represented in Figure 16.8a). For both the cases, the same CV estimation algorithm was used.

With the increment of variance (σ) representing the gaussian noise by a factor of 0.2 from 0 to 2, the CV estimation was done. As the noise level increases the error in CV estimation and the spread increases. Figure 16.9a is the box plot representation of CV magnitude for all the noise levels. It was observed that the spread in the CV value increases, and the median of the estimated CV also becomes smaller with increasing noise. While on the other hand, the RMSE increases rapidly both in value and spread as represented in Figure 16.9b.

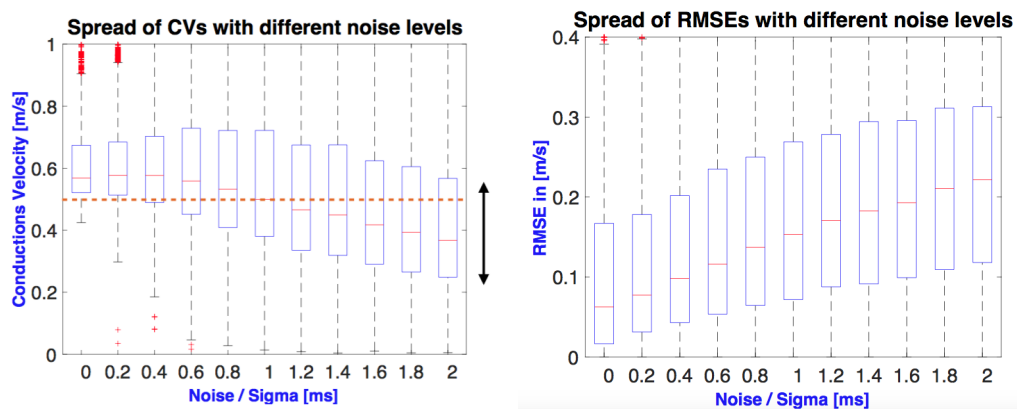


Figure 16.9: Representation of the effect of noise on the CV estimation. Increase in noise increases the spread in estimated CV values. a). Increment in the spread in CV as the introduced error is increased. b). The changes in the RMSE for the increased noise level. The ground truth value is represented by the dashed line.

Therefore, it can be stated that the noise does have impact on CV estimation. By adding noise, the spread in CV magnitude is increased and the RMSE increases. However this effect is small, as with adding σ equal to 2 the RMSE median changed from 0.05 m/s to 0.21 m/s .

16.3 Comparison of Polynomial Fit and the Modified Triangulation Method

The comparison was done between the polynomial fit and modified triangulation method in collaboration with the bachelor student Benedikt Ebener as a part of his thesis. The modified triangulation method was used for CV estimation throughout this thesis. But for the simulated data, the polynomial fit method was used to get the CV estimation for homogeneous propagation. The results from both methods are compared in this section. The CV estimation was done for the triangulation and the polynomial fit method with and without noise. The box plot in Figure 16.10 represents the CV estimation done using the modified triangulation and the polynomial fit method with and without noise. The noise added was of the same level as represented in Figure 16.9. The ground truth for estimating the simulated LAT was 0.507 m/s .

It has been observed that with no error and high resolution the CV estimation with polynomial fit is slightly better than the modified triangulation method. But the polynomial fit method performance reduces drastically as the error is introduced. The drop of CV magnitude is represented in Figure 16.10*b*. The clinical data always contain various types of artefacts, therefore, a more robust method is required which is less prone to errors and artefacts.

Therefore, during the course of this thesis, the modified triangulation method was used and considered. Figure 16.10*b* represents the varying noise level effect on the CV estimation using the polynomial fit or the triangulation method (Figure 16.10). In polynomial fit method, the absolute value and the width of box are always smaller than the modified triangulation method. This represents that the polynomial fit is more robust for estimation with noise but less accurate without noise, while triangulation was more accurate but less robust.

16.4 CV for Clinical Data

Calculating the regional and global CV for the clinical data is one of the most challenging tasks because of the various types of heterogeneities and anisotropies. As explained in chapter 10, existing methods to estimate the CV have their limitations dealing with the clinical scenarios when the catheter contact and shape are changing. The modified triangulation method was used for CV estimation after being benchmarked using the simulated data, in the previous section of this chapter. CV estimation can give reliable information about the depolarisation wavefront propagation over the atrial surface. The regions of slow and fast

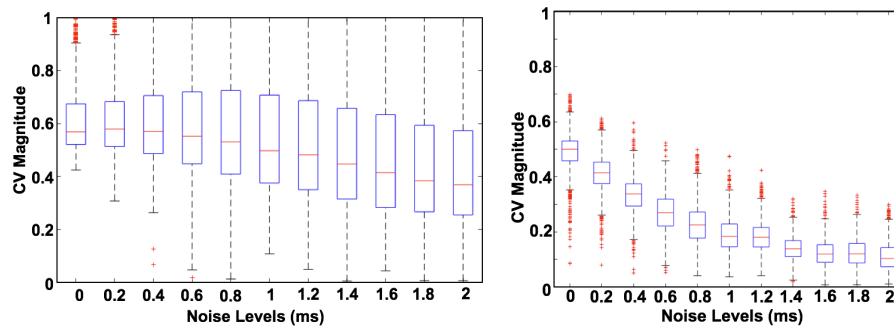


Figure 16.10: Representation of the comparison of polynomial fit and modified triangulation method. Increase in noise increases the spread in estimated CV values (m/s) for triangulation and polynomial fit method. a) Increment in the spread in CV as the introduced error is increased for modified triangulation method, b) for polynomial fit method.

conduction can also be visualised clearly in case of high density LAT map and partially in case of the low density LAT map. The three types of clinical data for CV estimation are presented in Table 10.1. Those were:

1. AFlut high density data,
2. AFib case with stimulus protocol, low density data mapped during SR, and
3. 2D triangular patch data

The CV estimation method used for the respective cases was explained in chapter 14. The results associated with all the cases are detailed below.

16.4.1 CV Estimation for Flutter Case

In AFlut there is a reentering rhythm of a looping excitation resulting in an endless excitation propagation cycle. The possibility of formation of a blood clot increases that could in-turn lead to stroke or heart attack. The estimation of the conduction pathway could be an important information towards the treatment of AFlut.

In this section the results of the regional and global CV estimation for the flutter case are presented. As explained in section 14.3.1, the CV estimation was done using the LAT map (given temporal information at all the vertices of the triangular mesh) and the clinical geometry as represented in Figure 10.12. Since during flutter, the propagation pattern is repetitive in certain regions, the regional CV estimation can provide the conduction pathway which can help the physicians during diagnosis. The CV estimation was done using the modified triangulation and visualised over the atrial geometry as represented in Figure 16.11. The obtained CV magnitudes and directions are visualised on the atrial surface.

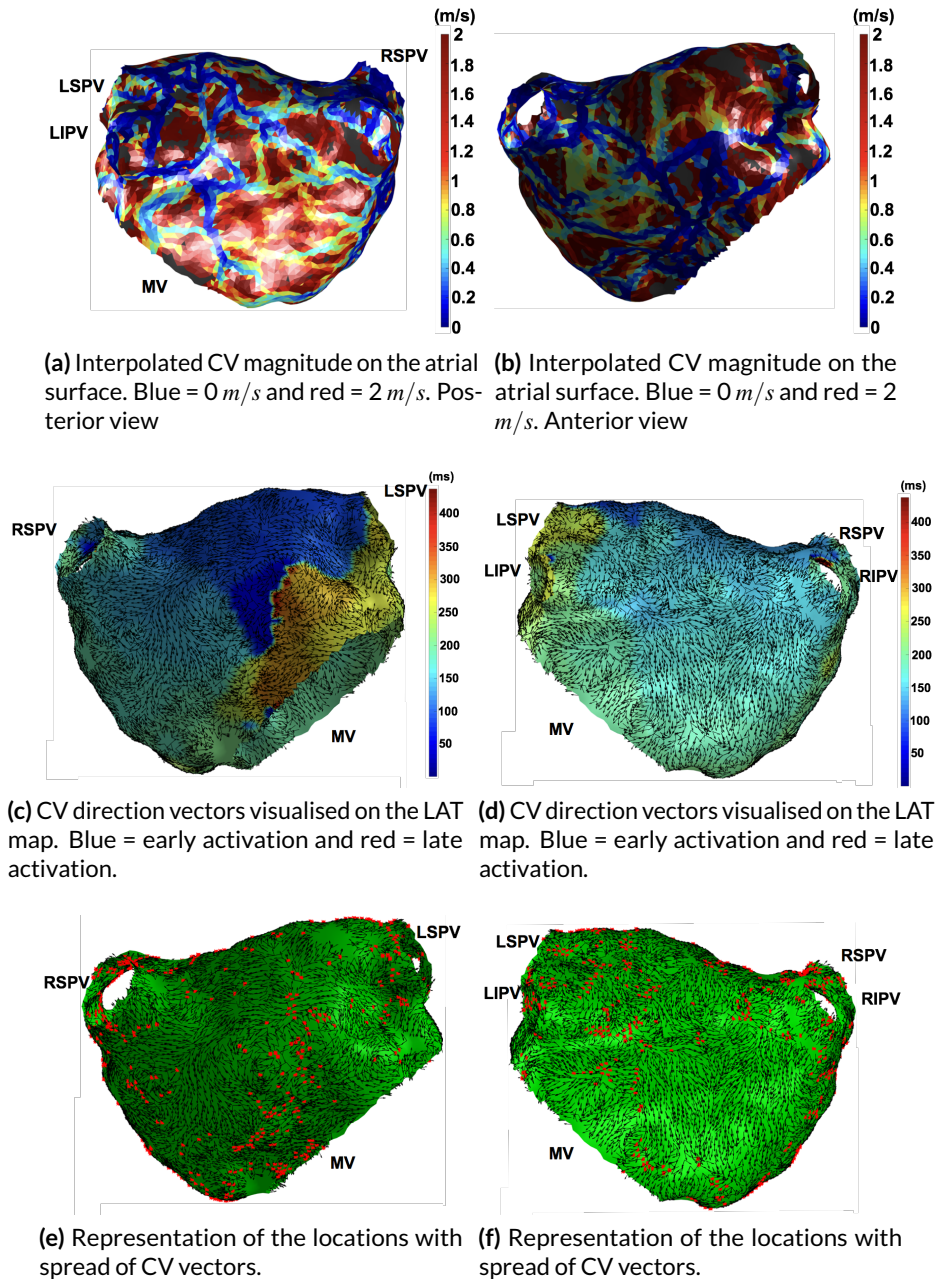


Figure 16.11: Representation of estimated CV for the flutter case. CV magnitude interpolated on the atrial surface and CV direction vector is visualised on the LAT map in posterior view (left) and anterior view(right). The spread of CV vectors are explained in chapter 15.

Figure 16.11a and b represent the estimated CV magnitude visualised on the atrial surface with 0 m/s being the slow conducting region (blue) and 2 m/s being the fast conducting region (red). Very slow conducting lines are visible on the atrium. When zooming into the electrograms of the slow conducting regions, a low peak-to-peak (P2P) amplitude ($< \approx 1$ mV) was observed at respective locations. While the electrograms in the fast conducting regions

were of high P2P amplitude ($> 1\text{ mV}$). This has been represented in Figure 16.12.

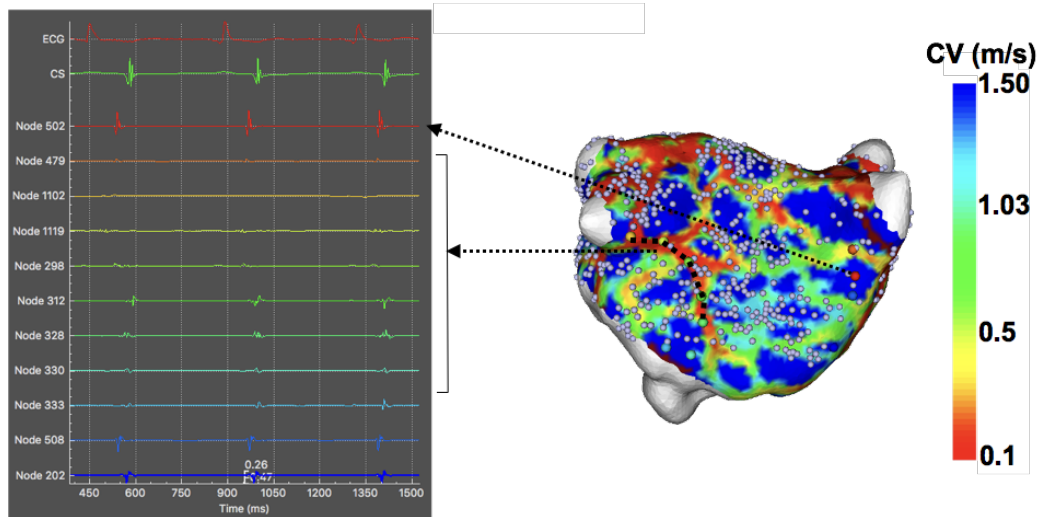


Figure 16.12: Representation of the electrograms at specific locations on the left atrial geometry. It can be clearly observed that the low CV magnitude location had electrograms with larger FD and low P2P amplitudes. While the locations with high CV magnitude have clear activation complexes for large P2P amplitudes and small FD. The visualisation was done using the KaPAVIE tool [75].

Figure 16.11*c, d* represent the estimated CV direction vectors visualised on the given LAT map. The excitation propagation observed from the LAT via colour bar (from blue to red region) and by the estimated CV direction vectors are consistent.

In Figure 16.11*e, f*, the region of the spread of CV direction vectors are marked by red stars. If compared with Figure 16.11*a, b*, these are mostly in the slow conducting regions.

16.4.2 CV Estimation for Fibrillation Case Mapped during SR

During AFib the depolarisation wavefront shows a chaotic pattern. The propagation pattern on the atrium depends on the atrial substrate. The changes in the propagation pattern result in changes in the morphology of the atrial activities at different locations [138] [139]. The atrial electrograms obtained usually have complex fractionated morphologies [140].

For the fibrillation case mapped during SR, the respective stable catheter positions were taken into consideration for CV estimation as explained in section 14.3. This section gives the details about the results obtained for CV estimation. The spatiotemporal information were mapped using the 10 and 20 pole LASSO catheter respectively and were obtained using the electroanatomical mapping system.

The CV estimation was done for 12 depolarisation wavefronts obtained from 4 clinical data. The stimulus protocol (S1-S2) was used with the 4 clinical cases as explained in chapter 10. Since with one clinical case 3 depolarisation waves were available, therefore, for 4 cases in total 12 depolarisation wavefronts were obtained. The temporal alignment of all the atrial activities with respect to the stimulus artefact was done using the CS catheter.

For all the depolarisation wavefronts the temporal information was extracted (after preprocessing) from the bipolar electrograms using the NLEO as explained in chapter 12. After extracting the spatiotemporal information and separating the 12 depolarisation wavefronts, the CV estimation was done. This section explains the results of the estimated CV for SR, for S1 stimulus and for S2 stimulus respectively.

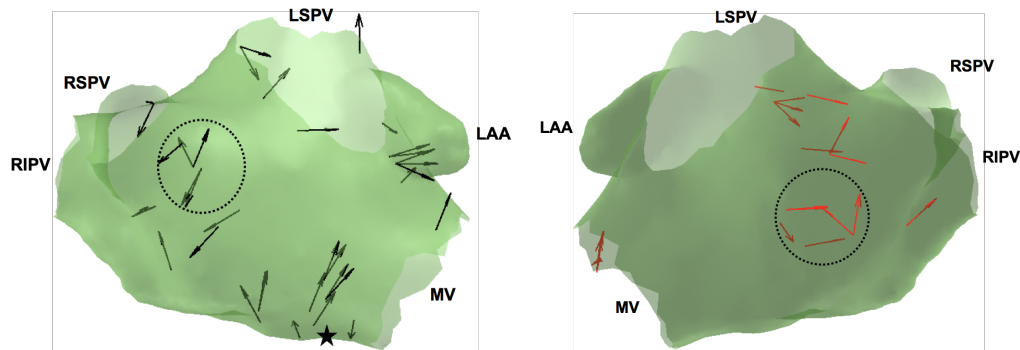


Figure 16.13: Posterior and anterior view of the LA with direction vectors representing the regional CV. These are the CV vectors for S1 triggered activities. Star is the probable position of the stimulus trigger. The region encircled represents a region where the depolarisation wavefront is observed to be different for two stable catheter position. Posterior view (left), and anterior view (right).

All the four clinical cases with the stimulus location (SR and S1 trigger and S2 trigger) are represented in Figure 8.1. Since the S1 and S2 trigger were given from the same location on the atrium, therefore, it was expected that the activities initiated from these two trigger should take the same pathway to travel along the atrial surface during normal cases. Any deviation in the path of S1 and S2 triggered activities could be because of the arrhythmogeneity on the atrial substrate. The results are explained for the CV estimation of S1 and S2 triggered activities in detail. The CV estimation was done for the various stable catheter positions. The various catheter positions for one of the clinical cases are represented in Figure 9.15 to Figure 9.20.

The number of recorded locations with available temporal information was around 66 for this clinical case. In total 17 stable catheter positions were obtained. Therefore, 17 datasets were used separately for CV estimation. The estimated CV direction vectors for S1 triggered activity (initiated from CS) are represented in Figure 16.13. The estimated CV magnitude in this case was $0.29 \pm 0.09m/s$ with few outliers (as represented in box plot 2 of Fig-

ure 16.16). This clearly represents that the depolarisation wavefront started at a point near the CS (marked as star) and covered the entire atrium. Some randomness in the propagation direction was observed in the encircled region. Depending upon the resolution of the data, more or less dense CV vectors could be obtained.

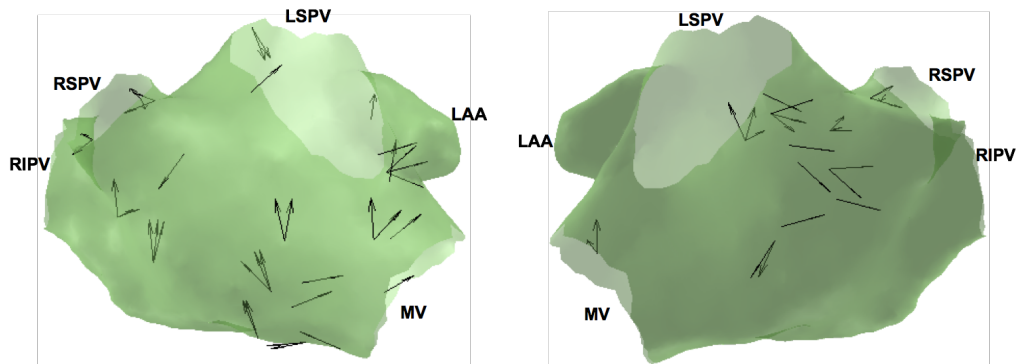


Figure 16.14: Posterior and anterior view of the left atrium with direction vectors representing the regional CV. These are the CV vectors for S2 triggered activities. Star is the probable position of the stimulus trigger. Posterior view (left), and anterior view (right).

Similarly, the estimated CV direction vectors for the S2 triggered activities are represented in Figure 16.14. The estimated CV magnitude in this case was $0.23 \pm 0.14 m/s$ with few outliers (as represented in box plot 3 of Figure 16.16). Here also the depolarisation wavefront started at a point near the CS and covered the entire atrium. There is no discrepancy observed in the CV vectors for S2 triggered activities, between direction vectors from the datasets representing different stable catheter positions for its propagation.

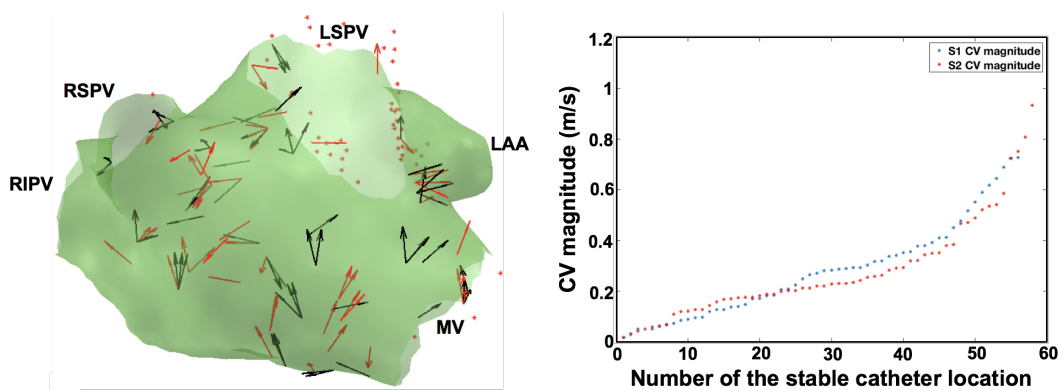


Figure 16.15: Comparison of estimated CV for S1 and S2 triggering. S1 triggered waveform are represented by red arrows while the S2 triggered are represented by black directional vectors. a). Estimated CV for S1 and S2 triggering represented by two different colour arrows. b). Estimated CV magnitude for S1 and S2 depending on the number of the stable catheter location.

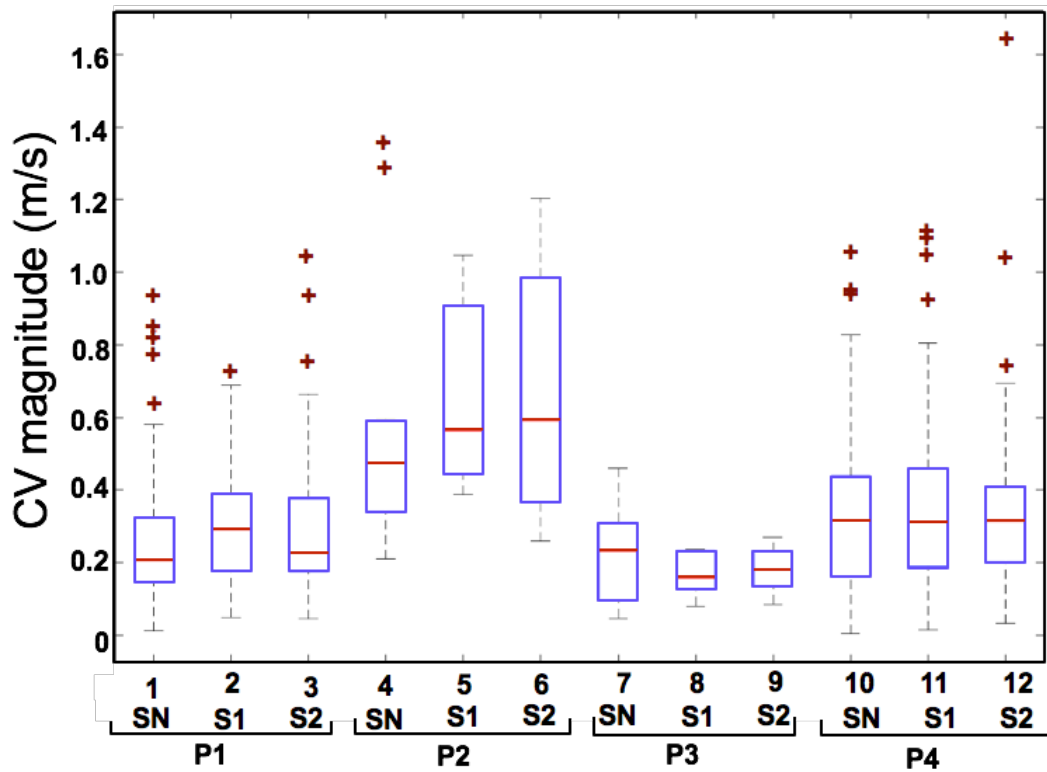


Figure 16.16: Estimated CV for all 12 depolarisation wavefronts box plot representation.

As stated above to get information about the arrhythmogenic region, a comparison of S1 and S2 triggered activities was done. In Figure 16.15a, the direction vectors obtained for S1 and S2 triggered activities were visualised. Red arrows being the S1 triggered activities propagation directions and black arrows being the S2 triggered activities propagation directions. The magnitudes obtained for both cases are also represented in the axis in ascending order for both activities. Manually inspecting and comparing Figure 16.15a (with Figure 9.15 to Figure 9.18) and Figure 16.14 (with Figure 9.19 to Figure 9.20), the encircled region (in Figure 9.15 to Figure 9.20) is the only region which shows a change of pattern. This could be because of the substrate ahead to this region, since the propagation pattern is influenced by all the substrate along the pathway. Changes in path are therefore, a sign of the presence of arrhythmogenic substrate in the atrium.

The estimated CV for all the other 12 cases are represented in Figure 16.16, with the help of box plots. Table 16.3 represents the various CV magnitudes as well as the FD and P2P for all 12 depolarisation wavefronts. All the CV magnitudes obtained are in the realistic range. The median magnitude obtained for the 12-depolarisation wavefronts varied from 0.2 m/s to 0.6 m/s . For a stable catheter position, there has been the possibility of getting more than one triad as represented in Figure 10.11e, f. For different triads, different CV were obtained. The number of possible triads varies depending on the number of contact electrodes, because

Table 16.3: Results of conduction velocity, FD and P2P values for the 12 depolarisation wavefronts. Each clinical case has 3 types of depolarisation wavefront (SN, S1 and S2).

| Serial number | Clinical case | Trigger | CV range (m/s) | Fractionation duration (ms) | Peak to peak values (mV) |
|---------------|---------------|---------|----------------|-----------------------------|--------------------------|
| 1 | 1 | SN | 0.21± 0.12 | 41.76 ± 4.18 | 1.32 ± 1.52 |
| 2 | | S1 | 0.29 ± 0.09 | 41.78 ± 2.95 | 1.13 ± 1.51 |
| 3 | | S2 | 0.23 ± 0.14 | 42.76 ± 8.48 | 0.99 ± 0.71 |
| 4 | 2 | SN | 0.47± 0.12 | 43.25 ± 3.69 | 3.11 ± 2.41 |
| 5 | | S1 | 0.56 ± 0.34 | 41.29 ± 1.48 | 2.43 ± 2.27 |
| 6 | | S2 | 0.59 ± 0.39 | 40.80 ± 2.95 | 2.17 ± 2.09 |
| 7 | 3 | SN | 0.23± 0.08 | 45.22 ± 7.88 | 0.62 ± 0.54 |
| 8 | | S1 | 0.16 ± 0.08 | 48.66 ± 5.90 | 0.62 ± 0.29 |
| 9 | | S2 | 0.18 ± 0.05 | 47.68 ± 7.38 | 0.67 ± 0.46 |
| 10 | 4 | SN | 0.31 ± 0.13 | 43.25 ± 2.83 | 0.97 ± 1.07 |
| 11 | | S1 | 0.31 ± 0.14 | 40.79 ± 2.46 | 1.14 ± 0.75 |
| 12 | | S2 | 0.31 ± 0.10 | 40.79 ± 2.83 | 1.13 ± 0.59 |

only the electrodes in contact with the endocardium were taken into consideration for CV estimation.

A comparison was done between the CV values obtained from different possible triads for the specific stable catheter locations. A manual inspection was done because in clinical geometry, it was not possible to clearly annotate various types of atrial regions and substrates. It has been observed that in the anterior wall, roof, and appendages area, the magnitude of CV remains in close proximity of CV magnitude for all triads. While the magnitude varies for pulmonary vein, posterior side, close to mitral valve area, for stable catheter locations. A low CV magnitude was observed in the appendages and close to the isthmus regions. The changes in the propagation direction at any location could be because of the substrate at that location and of the substrate ahead of it. Therefore, it has also been observed that higher resolution gives better insight in the atrial regions.

16.5 Comparison for S1-S2 Triggered Depolarisation Waveforms

Ideally the activities triggered from S1 and S2 stimulus should take the same path and the same speed to cover the atrium in case of no arrhythmogeneity. But due to various arrhythmogenic substrates (scar region, slow conducting region etc.), variations between respective propagations are observed. This can be clearly seen in Figure 16.17, where the S1

Table 16.4: Comparison for S1-S2 triggered depolarisation waveforms CV magnitudes for some of the stable catheter positions. Same CV magnitude could not be estimated since the algorithm assumptions and requirements were not met (m/s).

| Catheter position | Contact electrode | S1 CV magnitude m/s | S2 CV magnitude m/s |
|-------------------|-------------------|---------------------|---------------------|
| 1 | 6 | 0.45 | 0.36 |
| 2 | 8 | 0.47 | n/a |
| 3 | 9 | n/a | 0.38 |
| 4 | 6 | 0.50 | n/a |
| 5 | 8 | 0.35 | 0.68 |
| 6 | 9 | 0.35 | n/a |
| 7 | 8 | 0.32 | n/a |
| 8 | 9 | 0.73 | n/a |
| 9 | 10 | 0.51 | 0.52 |
| 10 | 10 | n/a | 0.36 |
| 11 | 9 | 0.67 | n/a |
| 12 | 10 | n/a | 0.34 |
| 13 | 6 | 0.38 | n/a |
| 14 | 10 | 0.66 | n/a |
| 15 | 9 | n/a | 0.33 |
| 16 | 8 | 0.40 | 0.52 |
| 17 | 9 | 0.31 | 0.89 |
| 18 | 7 | 0.33 | 0.39 |
| 19 | 10 | 0.35 | 0.71 |
| 20 | 9 | 0.44 | n/a |
| 21 | 6 | n/a | 0.36 |
| 22 | 8 | n/a | 0.32 |
| 23 | 5 | 0.62 | n/a |
| 24 | 7 | 0.42 | n/a |
| 25 | 10 | n/a | 0.32 |
| 26 | 10 | 0.53 | n/a |
| 27 | 9 | 0.82 | 0.46 |
| 28 | 5 | 0.34 | n/a |
| 29 | 8 | 0.67 | n/a |

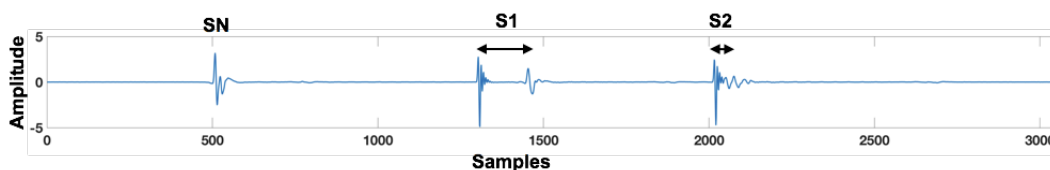


Figure 16.17: Representation of the fact that time taken by S1 and S2 could be variable. This is seen since, the sample distance between S1 artefact and activity is greater than that of S2 artefact and activity. This shows that S2 has fast propagation compared to S1.

span is different from S2 span. While both the complexes belong to the same location, S1 appeared late (after the artefact) in comparison to S2.

The region from where these changes originate can be regarded as arrhythmogenic and are potential ablation sites. Figure 16.15a shows estimated CV with both S1 and S2 triggered depolarisation wavefront CV vector. The magnitude of CV at all catheter positions are

presented in ascending order in Figure 16.15*b*. The same is also represented in Figure 16.16 with the median CV of approximately 0.33 m/s and 0.26 m/s . Table 16.4 represents the various CV magnitudes obtained for S1 and S2 depolarisation propagation for the various catheter positions over the temporal scale. It is to be noted here, that some catheter shapes show the same CV for S1 and S2 triggered activities while for others this varied.

The variations in the wavefront propagation could very well be possible because of the fact that the recordings were done for the unhealthy heart with arrhythmogenic areas, and the depolarisation wavefront might have not taken exactly the same path to cover the atrium. But in both the cases, it can be seen clearly that the depolarisation wavefront started near MV and from the CS catheter and travelled over the atrium thereafter. Also the magnitude of CV for S1 and S2 trigger was almost in the same range and close proximity. The propagation comparison can be done for other clinical cases similarly.

16.6 Comparison of Estimated CV with Statistical Parameters

As explained in chapter 13, with the electroanatomical mapping system along with the triangular mesh, the unipolar and bipolar electrograms were also recorded after preprocessing. These electrograms can be used to estimate other statistical parameters such as the LAT, fractionation in the atrial complexes, the duration of the fractionated complexes, P2P value of the amplitudes in the atrial complexes etc.

For CV estimation, the LAT and the recorded electrogram locations were used. But the analysis was done for other features as well. This section compares the atrial activity duration (also called fractionation duration) and the P2P values with the estimated CV for all the 12 depolarisation wavefronts.

To calculate the atrial activity duration the fractionation in the bipolar EGMs was considered. The step window was estimated based on the NLEO in each electrogram to mark the activity as represented in Figure 9.7. This has been calculated by using a standard deviation σ of 0.1 in respect to the maxima of the NLEO [64]. The atrial activities were marked and within that region the P2P amplitudes were calculated. A comparison of CV with FD and P2P values was done for the stable catheter positions and the results are explained in the respective sections below:

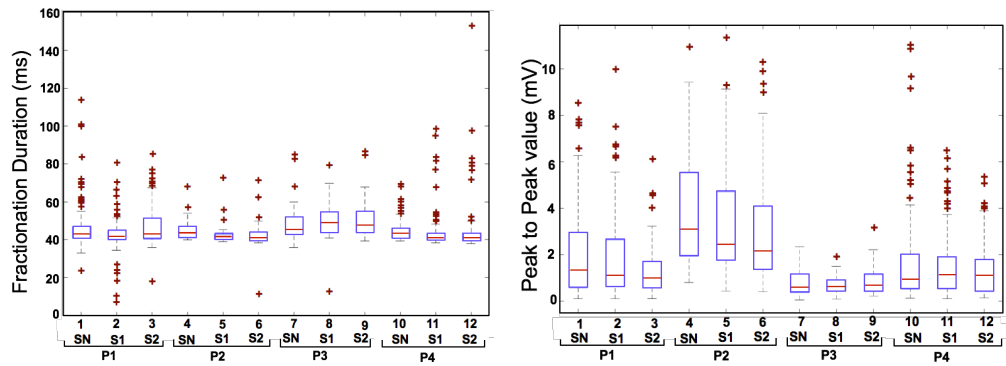


Figure 16.18: Box plot representation of the fractionation duration (left) and peak to peak amplitudes (right), of the selected atrial segments for all the 12 depolarisation wavefronts.

16.6.1 CV vs Fractionation Duration

For all the 12 depolarisation wavefronts, the FDs were estimated for the active segments in the atrial complexes as represented in section 9.4. The NLEO was used to find the atrial activities. The step function was generated using an appropriate threshold of 0.1σ of the maximum energy from the NLEO. The various FD for all the 12 complexes are represented in Figure 16.18a.

The FD was between $40ms$ to $60ms$ for all the cases. The correlation coefficient between median values of CV and FD was 62.26%. Comparing the box plots of CV (Figure 16.16) and FD (Figure 16.18a) nothing can be said about the relation between the two. The consideration is neither high nor low, therefore, it must be stated that no clear correlation was observed between FD and CV. The FD vs CV for all the 12 depolarisation cases are represented in Appendix A.

16.6.2 CV vs Peak-to-Peak Amplitudes

Similar to the FD, the analysis was done for the amplitudes of the atrial complexes. A high P2P amplitude is usually recorded, when the electrode comes in good contact with the healthy tissue. At the locations when the electrodes have bad or no contact with the endocardium, or when the tissue has scar or arrhythmogenity, the amplitude on the electrogram drops to a very low value of around $0mV$ to $0.08mV$. For the electrogram analysis, the lower threshold value of magnitude is kept to be $0.08mV$. The NLEO was used to find the atrial complexes and then the amplitude of the selected segment was estimated. Figure 16.18b represents the box plot for the P2P amplitude of the atrial complexes for all the 12 depolarisation wavefronts, with a median of P2P ranging from $0.62mV$ to $3.11mV$. The correlation between median values of CV (Figure 16.16) and P2P (Figure 16.18b) was 85.59%. Therefore, it is observed that the higher the P2P amplitude, the higher was the magnitude of CV. The P2P vs CV for all the 12 depolarisation cases are represented in Appendix B.

16.7 CV Comparison for Simulated and Clinical Data

As a long term goal, personalised patient specific simulations can help in understanding and finding better solutions for atrial fibrillation diagnosis and treatment. Getting simulated depolarisation wavefronts similar to clinical ones is the first step towards detailed analysis of the realistic propagation. Using simulations, the CV estimation was done:

1. Using the clinical geometries and the LAT (obtained using FaMaS), and
2. Using the stable catheter positions recorded during the routine procedure. The ground truth for the simulation cases was known and used for benchmarking the algorithm and estimate the performance in terms of accuracy and robustness.

In this chapter the homogeneous and heterogeneous depolarisation wavefront was simulated and it was analysed how the modified triangulation method was working with respect to the various regions and especially at the boundary of the regions where the speed was changing. The modified triangulation method was good enough to be used with the clinical data as the percentage error with respect to the simulated data was up to 4 % as seen in Table 16.3. The obtained magnitude of CV was close to the ground truth values. Even if an error was introduced or the triangular mesh size was changed, the CV box plot remained in close proximity of the true value making the algorithm more robust. The very important information of wavefront collision was also obtained. The regions in which very high CV values are obtained are actually the regions with depolarisation wavefront collision. This was also visible with the CV direction vectors. This means that in real clinical scenarios too, interpolating the CV direction vectors and magnitudes over the atrial geometries can give information about the wavefront propagation as well as the collision regions of the depolarisation wavefronts. Taking the stable catheter positions in the simulation like the clinical fibrillation case was the next step towards getting a personalised wavefront propagation scenario for understanding the propagation patterns and CV estimations in real environments.

The same algorithm was applied to the clinical data. The LAT values in clinical data were obtained using the electrograms after preprocessing. The stable catheter positions were segregated and used similar to the simulated data and the CV estimate was done.

Canine Data Results

As explained in chapter 12, the electrogram segments were recorded from a canine heart using the patch catheter. The sampling frequency of 1kHz was used for recording and the recordings were done at the posterior left atrium (PLA) and the left atrial appendage (LAA) locations. The initial recording was done during sinus rhythm (SR) and then after inducing atrial fibrillation (AFib). The second set of data was obtained after 3 weeks of rapid ventricular pacing to induce fibrillation till the heart fails. In comparison to the other clinical data analysed (3D) during the course of this research, this data was 2 dimensional. This was obtained using the Unimap system. This study was done in collaboration with Dr. Jason Ng from the Northwestern University, Chicago, USA.

In the preprocessing stage, the noise and the non-contact points were removed using the appropriate low pass (LP) and high pass (HP) filters with filtering frequencies of 300Hz and 30Hz respectively. The signals with the overall peak-to-peak (P2P) amplitude of $< 0.08\text{mV}$ were regarded as noise and not included in the analysis. These electrode locations (recording noise) were also not included in the triangular mesh generation.

Figure 17.1a represents the raw electrogram from an arbitrary electrode of the triangular patch catheter and Figure 17.1b represents the respective filtered electrogram. The filtered electrograms were used for the local activation time (LAT) estimation using non-linear energy operator (NLEO) (explained in chapter 12). The spatiotemporal information for all the electrodes were later used for the CV estimation.

Figure 17.2a represents the recorded locations (dots), and the locations with noise (stars). For SR case and on the triangular patch electrode location, the location at which the signals with noise are represented by stars in Figure 17.2a. During analysis, the triangular mesh was generated using the recorded locations. The next section represents the results obtained for CV estimation using the simulated and the experimental data.

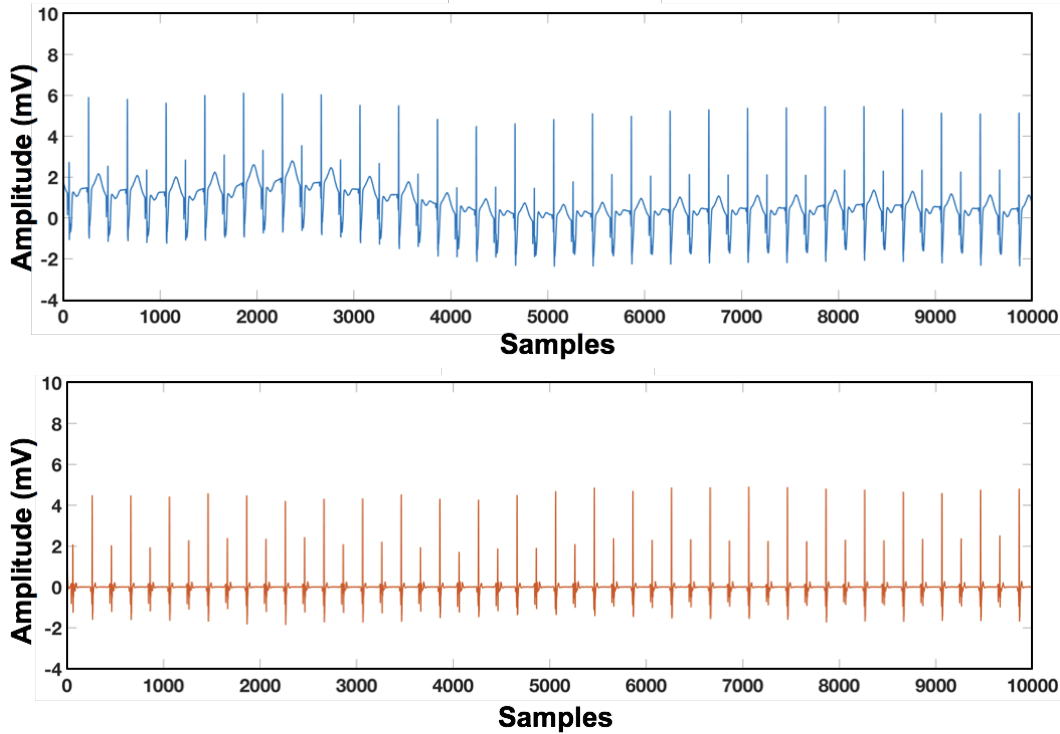


Figure 17.1: Representation of the raw electrogram and the filtered bipolar electrogram obtained after preprocessing. a). Raw electrogram recorded during SR for depolarisation propagation. The base line wander can be seen clearly. b). Filtered electrogram after base line removal at the preprocessing stage

17.1 CV Estimation for Simulated Data

During simulation the fast marching simulation (FaMaS) tool was used for the LAT estimation using a given propagation speed of 0.5 m/s . The triads represented in Figure 12.9a were obtained using the locations presented in Figure 17.2a. The CV estimation was done as explained in section 16.2 using the spatiotemporal information.

Figure 17.3a represents the estimated CV magnitude for the simulated LAT map, and Figure 17.3b represents the estimated propagation direction vectors visualised on the LAT map. The estimated CV magnitude was 0.50 m/s to 0.51 m/s with no outliers. The estimated CV direction vectors were also as expected. The clear propagation could be observed from right to left region. Since the accurate results were obtained for the CV magnitude as well as direction vectors therefore, the same algorithm was used for estimating CV in case of the experimental data.

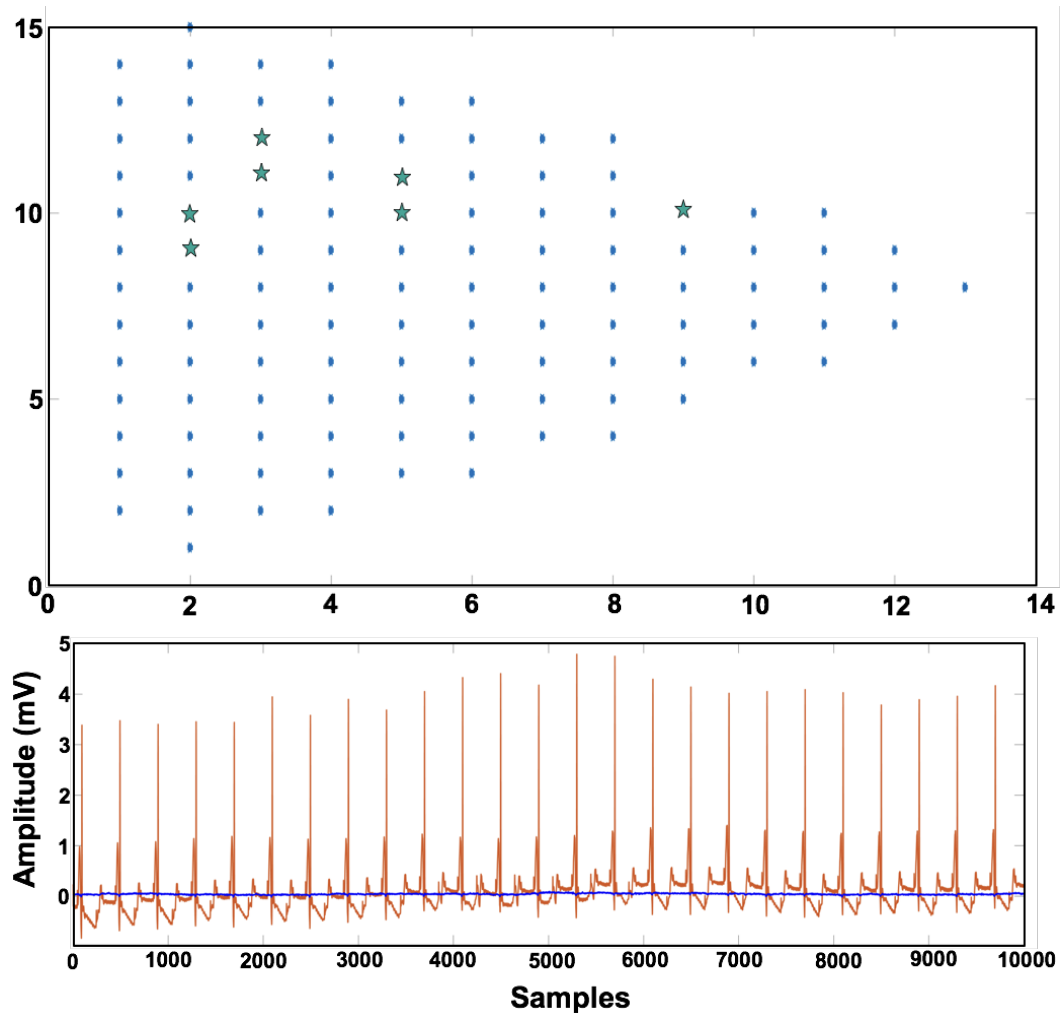


Figure 17.2: Representation of electrograms obtained at various locations. a). Representation of the triangular patch catheter with the electrodes having contact with the epicardium (dots) as well as the electrodes without having contact with the epicardium (stars). b). Representation of a good quality electrogram with respect to noise. Noise (blue electrogram) obtained at one of the location (marked as star), and the good quality signal (orange electrogram) obtained from the location (marked as dot).

17.2 CV Estimation for Canine Data

As represented in Figure 12.8, the temporal LAT window was selected for CV estimation. The LAT corresponding to particular window along with its spatial information were used for CV estimation. The 10 cases analysed for the CV estimation are namely:

1. Recording at LAA for 200ms pacing
2. Recording at LAA for 300ms pacing
3. Recording at LAA for 400ms pacing

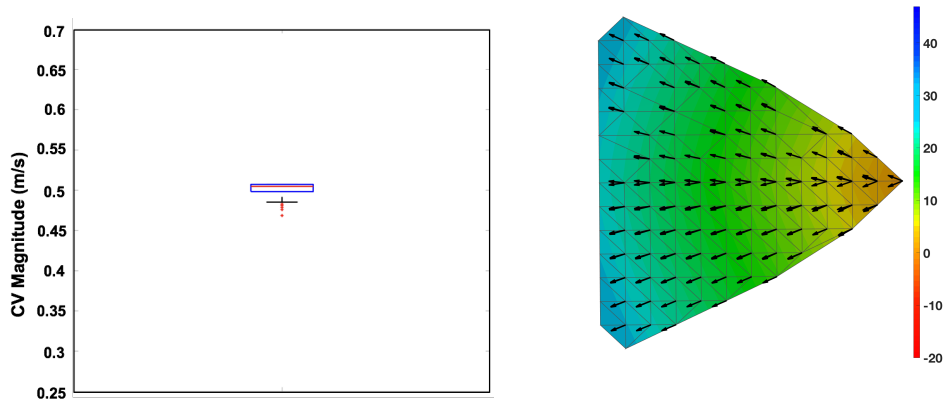


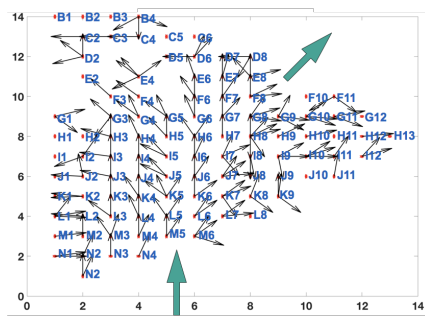
Figure 17.3: Estimated CV representation. a). Box plot of CV magnitude obtained, the ground truth was 0.5 m/s. b). Estimated CV direction vectors interpolated over the simulated LAT map.

4. Recording at LAA for 500ms pacing
5. Recording at PLA for 200ms pacing
6. Recording at PLA for 300ms pacing
7. Recording at PLA for 400ms pacing
8. Recording at LAA for 500ms pacing
9. Recording at LAA for SR
10. Recording at PLA for SR

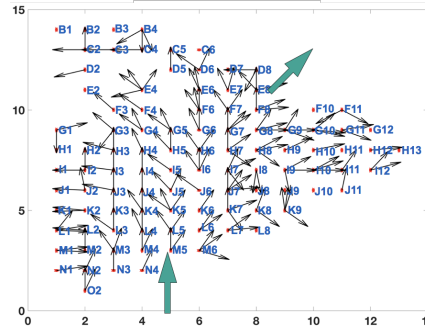
For all these cases, the CV estimation was done before and after inducing fibrillation (at LAA and PLA locations). The number of LAT windows varied from 12 to 47, depending upon the pacing and number of activation complexes present in the electrograms.

As represented in the developed methods (chapter 12) the temporal window was selected for the 10second electrogram and the LATs were computed using NLEO. After estimating the LAT times, these were used along with the spatial locations for CV estimation as represented in Algorithm 12.1. The various CV vectors obtained for the SR data at LAA location for SR are represented in Figure 17.4 for the 10seconds using the various temporal windows. Red dot represents the electrodes and arrows represents the CV direction vectors at each location. The magnitude for the respective excitation are represented in Figure 17.5. It could be observed that the depolarisation wavefront took the same propagation pathway to cover the mapped region.

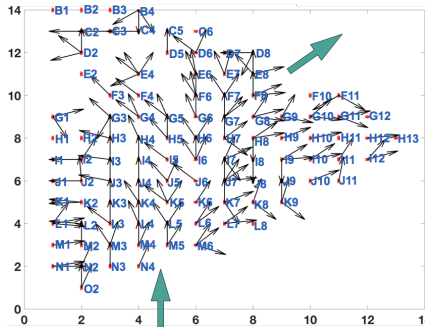
The depolarisation wavefront enters the region (under analysis beneath the catheter patch) from the electrode N4- M5 (Figure 12.1) for all the temporal window. The dispersion of depolarisation can be observed at electrode D7 to L7. For this triangular patch location, the excitation leaves the region from the electrode D7- D8- H1 to K1. For all the cases, the median magnitude of the CV during SR is obtained to be $\approx 0.28m/s$ for all the temporal



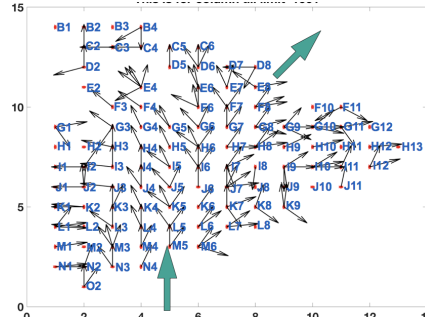
(a) CV direction vector for window on the segment represented in chapter 10



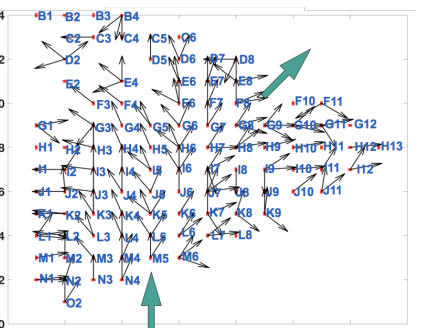
(b) CV direction vector for window on the segment represented in chapter 10



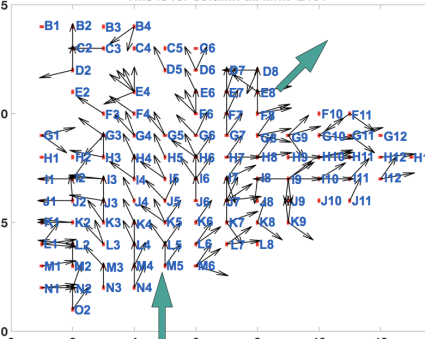
(c) CV direction vector for window on the segment represented in chapter 10



(d) CV direction vector for window on the segment represented in chapter 10



(e) CV direction vector for window on the segment represented in chapter 10



(f) CV direction vector for window on the segment represented in chapter 10

Figure 17.4: Estimated CV direction vector representation for 6 various temporal windows out of the 10second data as represented in Figure 12.8. The green arrows represents the wavefront entry and leaving direction for the respective case

windows.

Similar to this, the CV estimation was done for all the 10 cases, after 3 weeks of fibrillation. For LAA location, the CV vector representation is done in Figure 17.6 and for PLA in

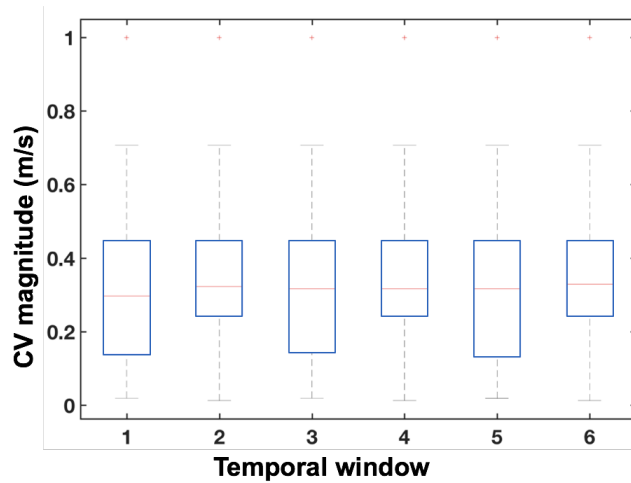


Figure 17.5: CV magnitude for the excitation propagation in SR. The direction vectors are represented in Figure 17.4.

Table 17.1: Depolarisation wavefront underneath the electrodes at location LAA

| Recording location | Pacing cycle | CV median magnitude (m/s) \pm IQR |
|--------------------|--------------|-------------------------------------|
| LAA | 200 | 0.12 ± 0.21 |
| LAA | 300 | 0.24 ± 0.20 |
| LAA | 400 | 0.29 ± 0.12 |
| LAA | 500 | 0.27 ± 0.25 |
| LAA | SR | 0.44 ± 0.17 |

Figure 17.7.

Figure 17.6 represents the estimated CV direction vectors at LAA for various pacing along with SR. Unlike Figure 17.4 where for one particular SR case, the CV estimation was represented (for various temporal windows), here the CV estimation is represented for one temporal window selected for each pacing.

Figure 17.6a represents the CV direction vector for the excitation at 200ms pacing. The depolarisation wave enters from B1 to N1 and leaves the patch from E9 F19 F11 G12 electrode. Similarly the depolarisation directions can be observed for other pacing and excitation propagations. These details of the CV magnitudes and directions are mentioned in Table 17.1.

The median value of the CV magnitude obtained for the respective cases are $\approx 0.12m/s$, $0.24m/s$, $0.29m/s$, $0.27m/s$ and $0.44m/s$ for 200ms, 300ms, 400ms, 500ms and SR at LAA respectively as represented in Table 17.1. The median value of the CV magnitude obtained for the respective cases are $\approx 0.27m/s$, $0.33m/s$, $0.33m/s$, $0.33m/s$ and $0.44m/s$ for 200ms, 300ms, 400ms, 500ms and SR at PLA respectively as represented in Table 17.2. The changes in the depolarisation wavefront propagation can also be observed at respective

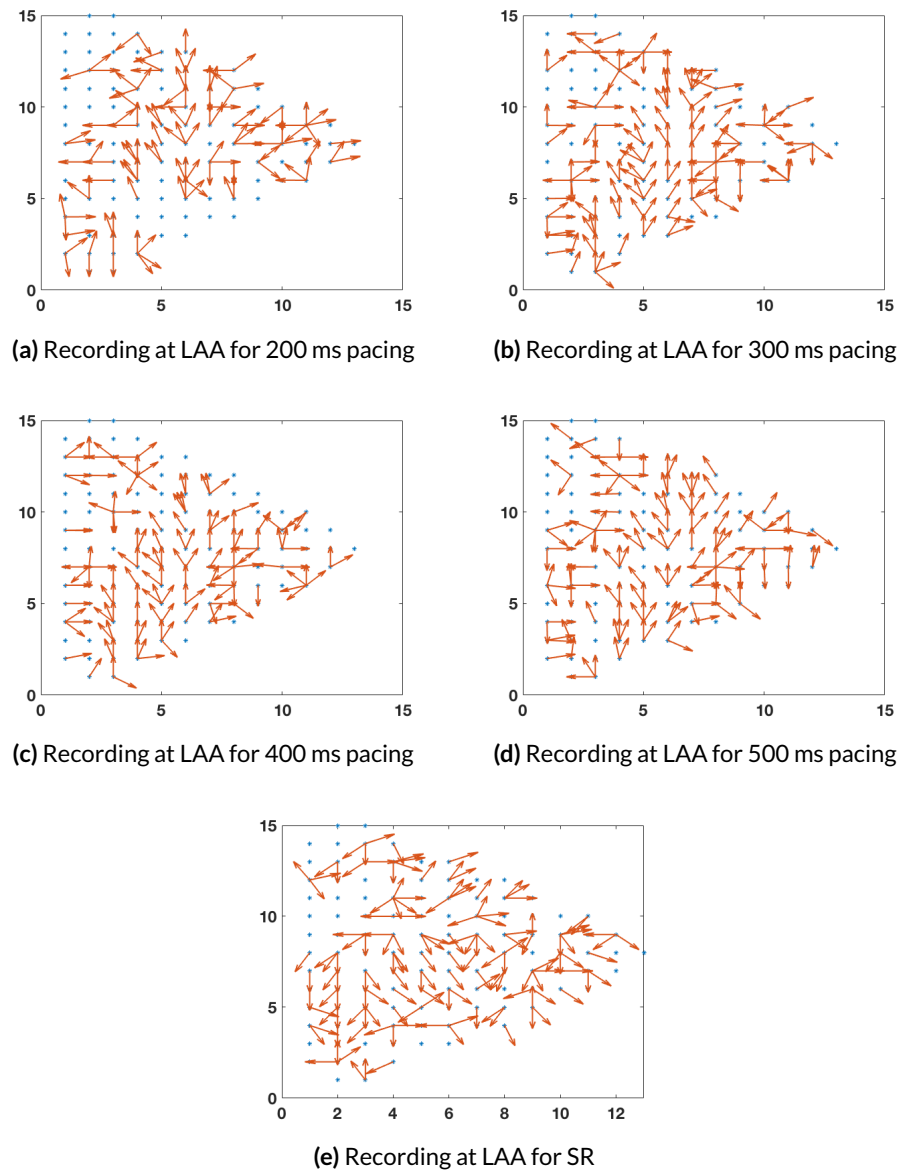


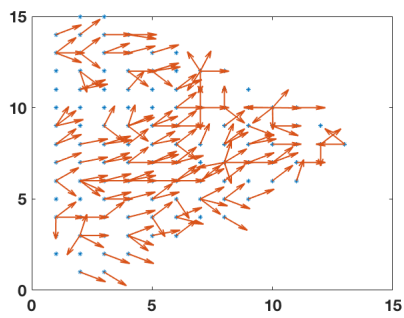
Figure 17.6: Estimated CV direction vector representation for 6 various temporal windows out of the 10 *second* data as represented in Figure 12.8.

location.

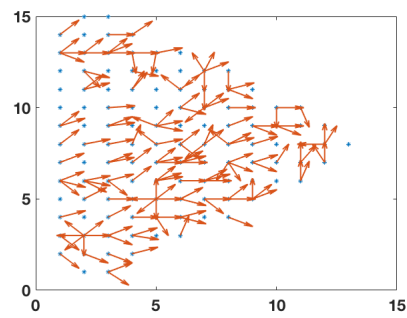
Similar to the above case at LAA, the CV excitation propagation was estimated at PLA. Table 17.2 represents the magnitude and propagation pathway for all the electrodes. The pacing was done in the ventricle, therefore, the changes in the wavefront propagation were not observed in the atrium.

Table 17.2: Depolarisation wavefront underneath the electrodes at location PLA

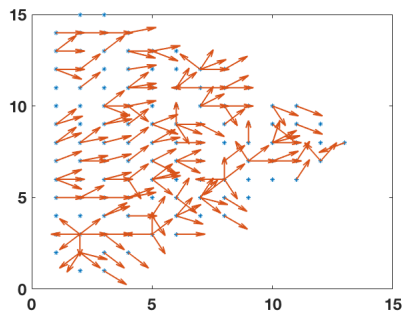
| Recording location | Pacing cycle | CV median magnitude (m/s) \pm IQR |
|--------------------|--------------|-------------------------------------|
| PLA | 200 | 0.27 ± 0.17 |
| PLA | 300 | 0.33 ± 0.14 |
| PLA | 400 | 0.33 ± 0.11 |
| PLA | 500 | 0.33 ± 0.11 |
| PLA | SR | 0.44 ± 0.26 |



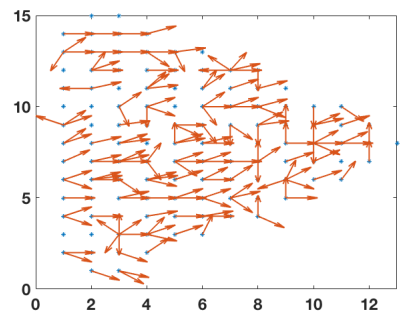
(a) Recording at PLA for 200 ms pacing



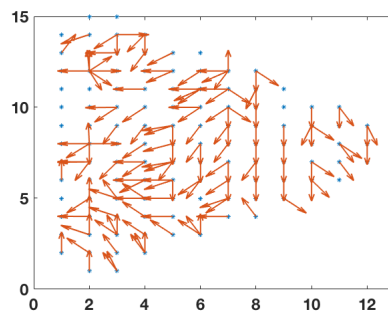
(b) Recording at PLA for 300 ms pacing



(c) Recording at PLA for 400 ms pacing



(d) Recording at PLA for 500 ms pacing



(e) Recording at PLA for SR

Figure 17.7: Estimated CV direction vector representation for 6 various temporal windows out of the 10 second data as represented in Figure 12.8.

PART IV

DISCUSSION AND CONCLUSION

Discussion and Conclusion

18.1 Discussion

Atrial arrhythmia is the most common cardiac arrhythmia [1]. Parameters such as conduction velocity (CV), CV restitution, fibrosis etc. are under analysis in order to understand cardiac arrhythmias [111]. CV represents the magnitude and direction of the propagation of depolarisation wavefronts on the atrium. The functional and anatomical heterogeneities results in a variation of the depolarisation wavefront propagation speed and pattern over the atrium [141]. The analysis of regional CV gives insight into the behaviour of the tissue underneath that region [142] [143]. Regional CV gives the information about the magnitude and direction of the propagating depolarisation wavefronts on the atrium with different types of tissue. The regional CV can provide important quantitative electrophysiological information about the underlying tissue. The estimation of CV is a measure to mark the slow and fast conducting regions on the atrial substrates. Some of the existing CV estimation methods have already been presented and discussed in chapter 10. But the main part of this thesis deals with the proposed CV estimation algorithm obtained by modifying the existing triangulation method, it takes the spatial coordinates and the intracardiac electrograms, obtained from the electroanatomical systems as an input for CV estimation.

When dealing with the clinical electrograms, many artefacts were to be removed and the various features were to be extracted before jumping to the CV estimation. This aspects related to the feature extraction were addressed under the section called as the feature extraction section of this thesis. It was important to understand the stimulus protocol data and to identify the features hidden in those electrograms. This was done during the preprocessing stages which involved artefact removal and filtering of the electrograms.

The bipolar electrograms were used for analysis of the paced scenarios, non paced scenarios and for the experimental data analysis also. The geometrical and signal artefacts were removed at the preprocessing stage. Along with this there were other instances such as

dealing with the electrograms close to the stimulus location at which special measures were taken to estimate the local activation time (LAT). In these cases, along with the bipolar electrograms the unipolar electrograms were also taken into consideration. The depolarisation propagation pattern for stable catheter position was estimated using the LAT obtained from the unipolar and bipolar electrograms and the same pattern was observed using both. The bipolar electrograms and the non-linear energy operator (NLEO) estimation were preferred to find the LAT at all the locations. This was because the unipolar electrograms compared to the bipolar electrograms show local artefacts and the signal to noise ratio is better for bipolar electrograms.

As a part of this thesis, the simulation, clinical and the mathematical basics were explained that were important to understand the processing of multichannel intracardiac electrograms. It was very interesting to determine the CV for the high density atrial flutter (AFlut) map and also to make the comparison between the electrogram features and the CV magnitude. It was observed that the electrograms were having low P2P amplitude and higher FD in the region with slow propagating speed. These parameters were used to mark the region of arrhythmogeneity in the stimulus protocol data.

It was also observed that the density of the various maps that can be recorded using the electroanatomical mapping (EAM) systems can actually affect the analysis. The CV estimation on the high density map can give a better regional substrate information, while in a low density map it is difficult to talk about the substrate properties. Other than the various simulated cases, the clinical cases were addressed for CV estimation. For this thesis the high density LAT map from the flutter case was used for CV estimation. The other case was the fibrillation case where the mapping was done using the 10 pole and 20 pole LASSO catheter. These maps were comparatively sparse in nature. Also the mapping was done for the fibrillation case, although in SR. No assumption was done with respect to the depolarisation propagation pattern, and it was decided to use the respective triggering beat for the stable catheter position. Therefore the data was divided into datasets and used for analysis. The comparison of the activities triggered from the CS catheter was used to find the differences in wavefront propagation. The comparison of the S1 and S2 stimulus CV vectors can give better insight into regional properties in terms of propagation patterns.

Other than the human intracardiac data and the simulated data, the next set of data under analysis was the experimental data obtained from the Northwestern University in collaboration with Dr. Jason Ng. This was the data in which the ventricular pacing was done and the mapping in atria was done at left atrial appendage (LAA) and posterior left atrium (PLA). This data was obtained by the epicardial mapping and the same CV estimation algorithm was used here. A good estimation was obtained with the simulated data and then the analysis was done on the experimental data. The interesting part in these data was the presence of alternans that was observed in some electrograms. The CV estimation before and after pacing was done and observed on the regional locations. The next section concludes this thesis.

18.2 Conclusion

The focus of this thesis was to estimate the depolarisation wavefront propagation speed by analysing multichannel atrial electrograms. The scope of this project was to investigate atrial electrograms during atrial fibrillation to improve the understanding and knowledge of these signals. During the course of this research, the movement of the catheter inside the atrium is mapped inside the atrial endocardium using the electrogram and location coordinates obtained from the EAM systems. In the presented work, the algorithm for CV estimation for atrial fibrillation (AFib) cases (mapped during sinus rhythm (SR)) are demonstrated. The proposed method works for varying catheter shapes and changing wall contact. This method takes the coordinate of the catheter and LAT value at each coordinate to estimate the CV. The depolarisation wavefront propagation pattern over the atrial geometry gives useful information to know the behaviour of the depolarisation wavefront at any location and also to analyse the underlying substrate behaviour. To reach to this goal and to benchmark the proposed algorithm, the simulated as well as the clinical data were analysed and used to reach to the goal of the estimation of CV. The relation between the two are represented in Figure 10.6.

A fast marching simulation solving the Eikonal equation enabled us to get the excitation propagation pattern over the atrial surface by assigning the LAT value at each node of the geometry. This takes the triggering point location information as well as the speed of excitation and returns the LAT value at each node as the output. In this work the regional CV has been calculated for simulated LAT on different 3D clinical geometries. A lot of work has been done regarding the simulated and clinical CV estimation separately. This work puts together the simulated and clinical environment. The CV has been visualised on the respective clinical geometries to get a better view of the regional CV. In the preprocessing step, the removal of geometrical artefacts from the clinical geometries has been done. A good estimation of CV was observed for all the locations with the homogeneous as well as heterogeneous propagation. The higher CV magnitude value was obtained only at the points where the wavefronts collide. The CV directional vectors have also been plotted on the atrial geometry. The triggering point and the spread of the depolarisation wavefront was seen very clearly in all the cases. This is a novel study for regional CV calculation for simulated LATs for the wavefront propagation over clinical geometry. The clinical data have a lot of ambiguity and artefacts in terms of different substrates, tissue properties or thickness etc. This also gets reflected in the electrograms recorded from the endocardium or epicardium. It has also been demonstrated that while calculating the regional CV, great attention is required in order to calculate the LAT information precisely.

In the minimally invasive electroanatomical mapping procedure, the catheter is moved inside the atrium during endocardium mapping and EGM recording. As the catheter moves, the shape of the catheter and the number of electrodes in contact with the endocardium changes.

This is done to obtain a better coverage of the atrium. Few from the various possibilities for various catheter shapes and contact electrodes have been represented in Figure 9.14 to Figure 9.19. Unlike AFlut, in case of AFib, the path taken by the depolarisation wavefront is chaotic. Also, depending upon the arrhythmogeneity of the atrial substrates, the magnitude and direction of the depolarisation wavefronts changes with time. Therefore, for CV calculation, only the stable catheter positions were taken into consideration.

Comparison of LAT obtained as a result of different beats in an unhealthy heart results in wrong CV calculation because the propagation pattern might change with every beat. Presence of the region of scar, slow conduction region, improper ablation points, might be among the reasons that result in the change of the propagation pattern. Therefore, the dynamics of the catheter movement have to be considered for LAT and CV estimation. Due to the presence of heterogeneity, the CV is also variable in the atrium, and changes from one region to the other. The next step to this work would be to calculate the CV from the clinically obtained LAT. This type of study gives an insight and is a step towards the real clinical cases study with respect to the wavefront propagation over the atrium in different scenarios.

During EAM mapping as the catheter moves inside the atrium, the endocardial wall contact changes. The alignment of each atrial activity is done using the CS signals. The VFF always appears after the atrial activity. The removal of the VFF is done with respect to the ECG signals. Double potentials and late potentials were absent in both clinical cases. A considerable duration should be kept between the triggering impulses, so that clear activities can be obtained from different triggers. Looking at the visualisation of the atrial activity durations along with the interpolation of the differences of LAT gave clear indication for the region of arrhythmogenic substrate. This has been observed in both the clinical cases. Since routine clinical recordings have been used to find the arrhythmogenic substrate, this method is easy to integrate into the clinical environment.

The better the recording resolution is, the better the CV propagation estimation can be done. The main interest here was the investigation of the propagation pattern and to find the arrhythmogenic substrate region. This is done by investigating the electrograms and parametrising the regions based on P2P amplitudes, LAT, FD and morphological correlations.

Appendix

A.1 Appendix A

The conduction velocity (CV) vs peak-to-peak (P2P) figures for respective 8 cases. Figure A.1 represents the estimated CV vs P2P for clinical case 1. Similarly Figure A.2 to Figure A.4 represents for the rest of the three clinical cases.

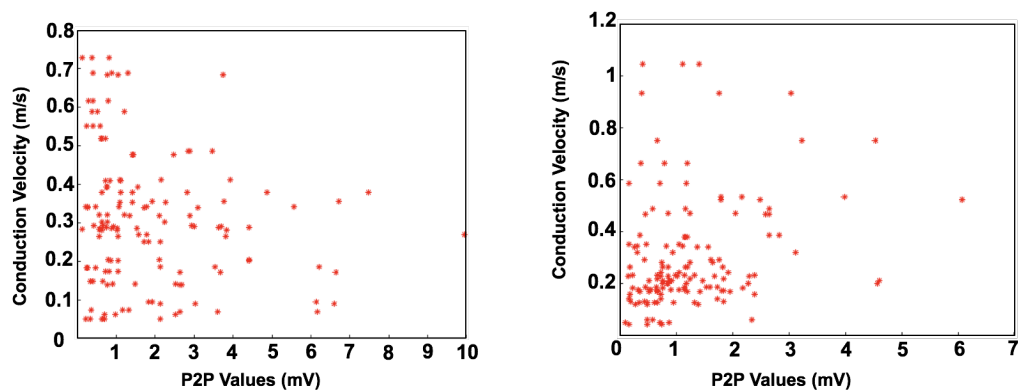


Figure A.1: Representation of CV vs P2P for clinical case 1.

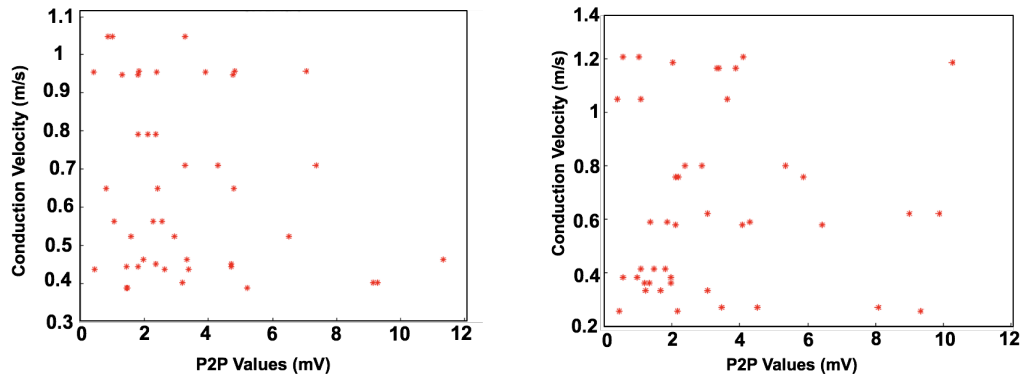


Figure A.2: Representation of CV vs P2P for clinical case 2.

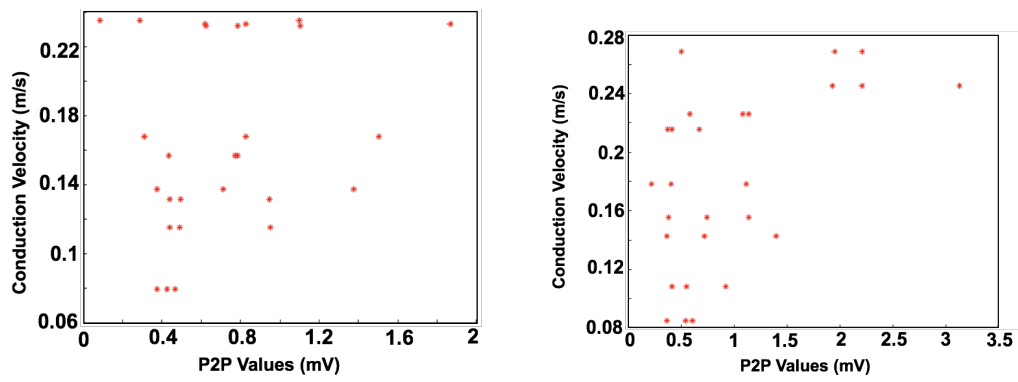


Figure A.3: Representation of CV vs P2P for clinical case 3.

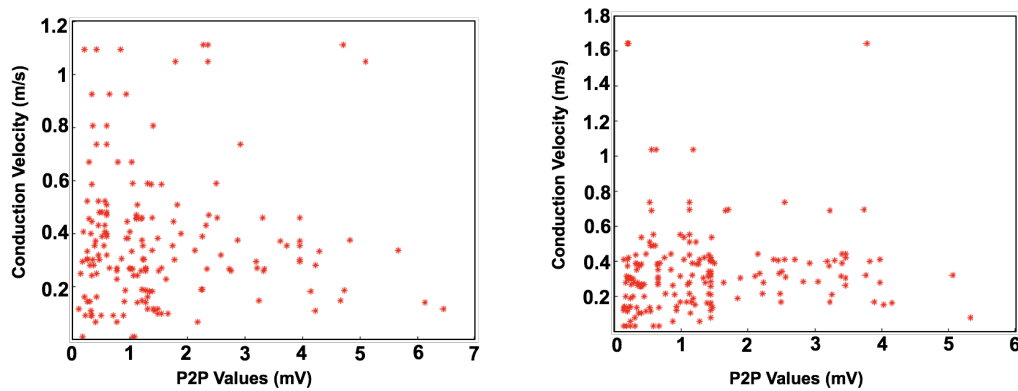


Figure A.4: Representation of CV vs P2P for clinical case 4.

A.2 Appendix B

The CV vs fractionation duration (FD) figures for respective 8 cases. Figure A.5 represents the estimated CV vs FD for clinical case 1. Similarly Figure A.6 to Figure A.8 represents for the rest of the three clinical cases.

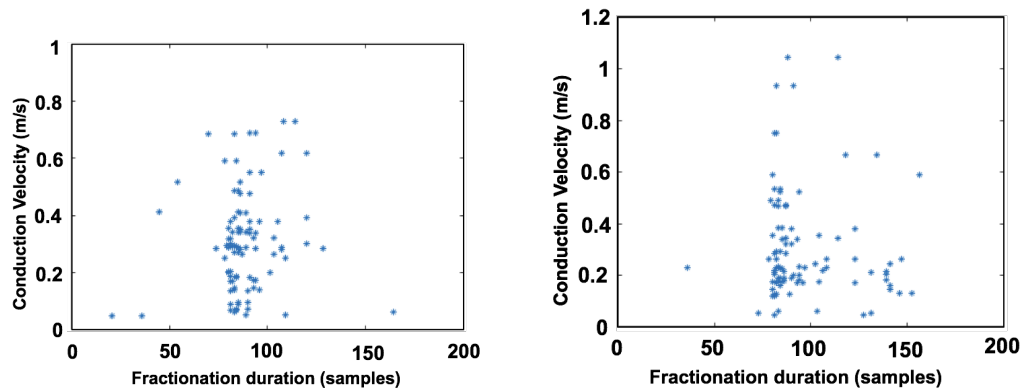


Figure A.5: Representation of CV vs FD for clinical case 1.

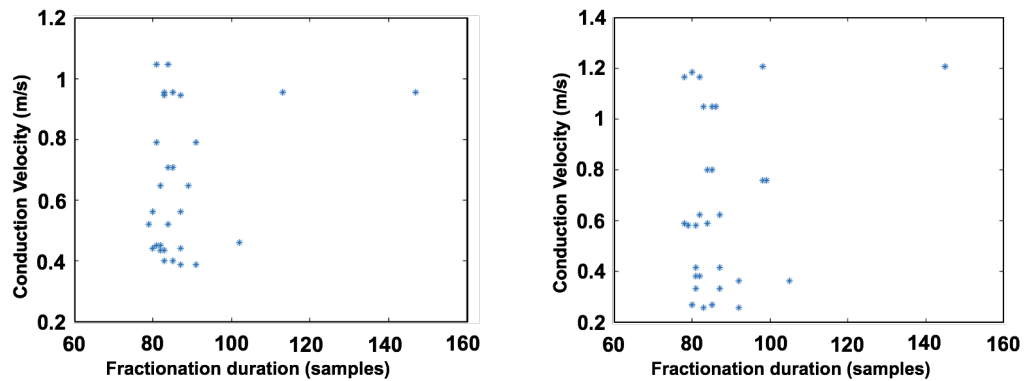


Figure A.6: Representation of CV vs FD for clinical case 2.

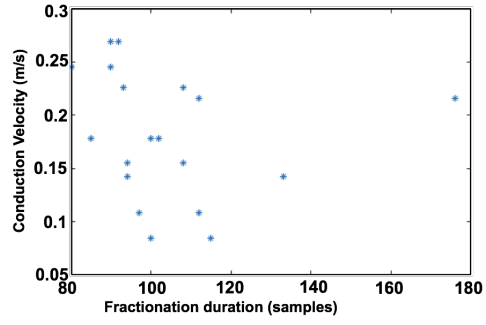
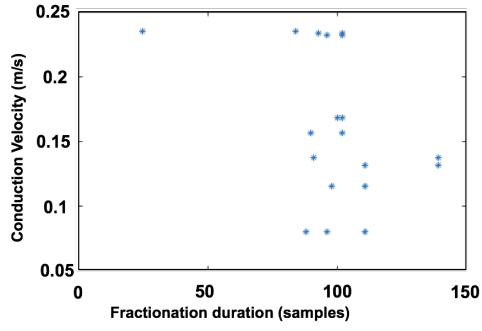


Figure A.7: Representation of CV vs FD for clinical case 3.

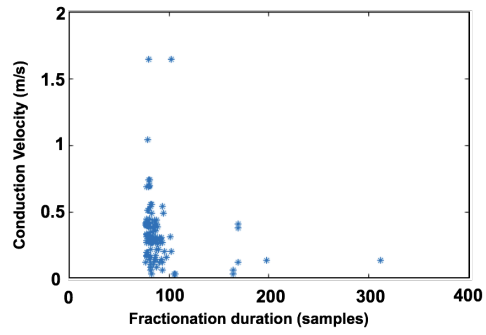
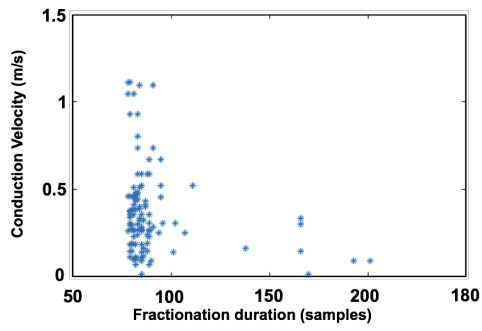


Figure A.8: Representation of CV vs FD for clinical case 4.

References

- [1] S. Nattel, “New ideas about atrial fibrillation 50 years on,” *Nature*, vol. 415, no. 6868, pp. 219–226, 2002.
- [2] H. Calkins, K. H. Kuck, R. Cappato, et al., “2012 hrs/ehra/ecas expert consensus statement on catheter and surgical ablation of atrial fibrillation: recommendations for patient selection, procedural techniques, patient management and follow-up, definitions, endpoints, and research trial design,” *J Interv Card Electrophysiol*, vol. 33, no. 2, pp. 171–257, 2012.
- [3] V. Fuster, L. E. Ryden, D. S. Cannom, et al., “Acc/aha/esc 2006 guidelines for the management of patients with atrial fibrillation: a report of the american college of cardiology/american heart association task force on practice guidelines and the european society of cardiology committee for practice guidelines (writing committee to revise the 2001 guidelines for the management of patients with atrial fibrillation): developed in collaboration with the european heart rhythm association and the heart rhythm society,” 2006.
- [4] D. M. Lloyd-Jones, T. J. Wang, E. P. Leip, et al., “Lifetime risk for development of atrial fibrillation: the framingham heart study,” *Circulation*, vol. 110, no. 9, pp. 1042–1046, 2004.
- [5] E. Ciaccio, A. Biviano, V. Iyer, et al., “Trends in atrial flutter and atrial tachycardia research,” *Informatics in Medicine Unlocked*, vol. 7, pp. 14–22, 2017.
- [6] L. S. Wann, A. B. Curtis, K. A. Ellenbogen, et al., “2011 accf/aha/hrs focused update on the management of patients with atrial fibrillation (update on dabigatran). a report of the american college of cardiology foundation/american heart association task force on practice guidelines,” *Heart Rhythm : the Official Journal of the Heart Rhythm Society*, vol. 8, no. 3, pp. e1–8, 2011.
- [7] S. Bundesamt, “Diagnosedaten der patienten und patientinnen in krankenhäusern (einschl. sterbe- und stundenfälle),” 2011.
- [8] C. Schmitt, I. Deisenhofer, and B. Zrenner, Eds., *EnglishCatheter Ablation of Cardiac Arrhythmias: A Practical Approach*. Darmstadt : Steinkopff, 2006.
- [9] P. Santangeli, L. Di Biase, D. J. Burkhardt, et al., “Catheter ablation of atrial fibrillation: state-of-the-art techniques and future perspectives,” *Journal of Cardiovascular Medicine (Hagerstown, Md.)*, vol. 13, no. 2, pp. 108–124, 2012.
- [10] H. Calkins, J. Brugada, D. L. Packer, et al., “Hrs/ehra/ecas expert consensus statement on catheter and surgical ablation of atrial fibrillation: recommendations for personnel, policy, procedures and follow-up. a report of the heart rhythm society (hrs) task force on catheter and surgical ablation of atrial fibrillation developed in partnership with the european heart rhythm association (ehra) and the european cardiac arrhythmia society (ecas); in collaboration with the american college of cardiology (acc), american heart association (aha), and the society of thoracic surgeons (sts). endorsed and approved by the governing bodies of the american college of cardiology, the american heart association, the european cardiac arrhythmia society,

- the european heart rhythm association, the society of thoracic surgeons, and the heart rhythm society,” 2007.
- [11] H. Gray and W. H. Lewis, *Anatomy of the human body*. Philadelphia: Lea & Febiger, 1918.
- [12] M. Courtemanche, R. J. Ramirez, and S. Nattel, “Ionic mechanisms underlying human atrial action potential properties: Insights from a mathematical model,” *Am. J. Physiol.*, vol. 275, no. 1 Pt 2, pp. H301–H321, 1998.
- [13] R. F. Schmidt, F. Lang, and M. Heckmann, Eds., *Physiologie des menschen: mit pathophysiologie*, Springer-Lehrbuch. Heidelberg: Springer, 2010.
- [14] J. Malmivuo and R. Plonsey, *Bioelectromagnetism: principles and applications of bioelectric and biomagnetic fields*. Oxford University Press, USA, 1995.
- [15] J. Malmivuo and R. Plonsey, *Bioelectromagnetism*. New York; Oxford: Oxford University Press, 1995, ch. Subthreshold membrane phenomena, pp. 44–65.
- [16] F. H. Martini, *English Fundamentals of Anatomy & Physiology*, L. Berriman, Ed. Prentice Hall, Inc. Upper Saddle River, NJ: Benjamin-Cummings Publishing Company, 2006.
- [17] H. JW., S. RC., R. CE., et al., “The heart: Arteries and veins,” *McGraw-Hill, New York*, vol. 7, p. 2274, 1990.
- [18] M. PW. and L. TDV., “Comprehensive electrocardiology: Theory and practice in health and disease,” *Pergamon Press, New York*, vol. 1, no. 1, p. 1785, 1989.
- [19] M. Borggreffe, T. Budde, A. Podczeczek, et al., “High frequency alternating current ablation of an accessory pathway in humans,” *Journal of the American College of Cardiology*, vol. 10, no. 3, pp. 576–582, 1987.
- [20] P. C. Gillette, M. M. Swindle, R. P. Thompson, et al., “Transvenous cryoablation of the bundle of his,” *Pacing and Clinical Electrophysiology : PACE*, vol. 14, no. 4 Pt 1, pp. 504–510, 1991.
- [21] S. Ahmed, A. C. A., and P. A. Gould, *Abnormal heart rhythms*. INTECH, 2015, vol. Chapter 1, ch. Atrial Flutter ; Diagnosis, Management and Treatment, pp. 1–25.
- [22] I. Anguera, J. Brugada, M. Roba, et al., “Outcomes after radiofrequency catheter ablation of atrial tachycardia,” *Am J Cardiol*, vol. 87, no. 7, pp. 886–890, 2001.
- [23] A. Luik, M. Merkel, T. Riexinger, et al., “Persistent atrial fibrillation converts to common type atrial flutter during cfae ablation,” *Pacing and Clinical Electrophysiology : PACE*, vol. 33, no. 3, pp. 304–308, 2010.
- [24] M. D. O’Neill, P. Jais, Y. Takahashi, et al., “The stepwise ablation approach for chronic atrial fibrillation—evidence for a cumulative effect,” *J Interv Card Electrophysiol*, vol. 16, no. 3, pp. 153–167, 2006.
- [25] G. V. Naccarelli, H. T. Shih, and S. Jalal, “Catheter ablation for the treatment of paroxysmal supraventricular tachycardia,” *Journal of Cardiovascular Electrophysiology*, vol. 6, no. 10 Pt 2, pp. 951–961, 1995.
- [26] L. Saxon, J. Kalman, J. Olgin, et al., “Results of radiofrequency catheter ablation for atrial flutter,” *The American Journal of Cardiology*, vol. 11, no. 77, pp. 1014–1016, 1996.
- [27] M. Haissaguerre, F. Gaita, F. Marcus, et al., “Radiofrequency catheter ablation of accessory pathways: A contemporary review,” *J. Cardiovasc Electrophysiol.*, vol. 5, pp. 532–552, 1994.
- [28] H. L. Estner, I. Deisenhofer, A. Luik, et al., “Electrical isolation of pulmonary veins in patients with atrial fibrillation: reduction of fluoroscopy exposure and procedure duration by the use of a non-fluoroscopic navigation system (navx),” *Europace : European Pacing, Arrhythmias, and Cardiac Electrophysiology : Journal of the Working Groups on Cardiac Pacing, Arrhythmias,*

- and Cardiac Cellular Electrophysiology of the European Society of Cardiology*, vol. 8, no. 8, pp. 583–587, 2006.
- [29] M. Rotter, Y. Takahashi, P. Sanders, et al., “Reduction of fluoroscopy exposure and procedure duration during ablation of atrial fibrillation using a novel anatomical navigation system,” *European Heart Journal*, vol. 26, no. 14, pp. 1415–1421, 2005.
- [30] L. Macle, P. Jais, C. Scavee, et al., “Pulmonary vein disconnection using the localisa three-dimensional nonfluoroscopic catheter imaging system,” *Journal of Cardiovascular Electrophysiology*, vol. 14, no. 7, pp. 693–697, 2003.
- [31] L. Gepstein, G. Hayam, and S. A. Ben-Haim, “A novel method for nonfluoroscopic catheter-based electroanatomical mapping of the heart. in vitro and in vivo accuracy results,” *Circulation*, vol. 95, no. 6, pp. 1611–1622, 1997.
- [32] S. Shpun, L. Gepstein, G. Hayam, et al., “Guidance of radiofrequency endocardial ablation with real-time three-dimensional magnetic navigation system,” *Circulation*, vol. 96, no. 6, pp. 2016–2021, 1997.
- [33] D. Krum, A. Goel, J. Hauck, et al., “Catheter location, tracking, cardiac chamber geometry creation, and ablation using cutaneous patches,” *Journal of Interventional Cardiac Electrophysiology : an International Journal of Arrhythmias and Pacing*, vol. 12, no. 1, pp. 17–22, 2005.
- [34] H. L. Estner, I. Deisenhofer, A. Luik, et al., “Electrical isolation of pulmonary veins in patients with atrial fibrillation: reduction of fluoroscopy exposure and procedure duration by the use of a non-fluoroscopic navigation system (navx),” *Europace : European Pacing, Arrhythmias, and Cardiac Electrophysiology : Journal of the Working Groups on Cardiac Pacing, Arrhythmias, and Cardiac Cellular Electrophysiology of the European Society of Cardiology*, vol. 8, no. 8, pp. 583–587, 2006.
- [35] M. Keller, *englischFormation of Intracardiac Electrograms under Physiological and Pathological Conditions*, K. I. of Technology (KIT) Institute of Biomedical Engineering, Ed. KIT Scientific Publishing, 2014.
- [36] D. L. Packer, “Three-dimensional mapping in interventional electrophysiology: techniques and technology,” *Journal of Cardiovascular Electrophysiology*, vol. 16, no. 10, pp. 1110–1116, 2005.
- [37] C. C. Gornick, S. W. Adler, B. Pederson, et al., “Validation of a new noncontact catheter system for electroanatomic mapping of left ventricular endocardium,” *Circulation*, vol. 1999, pp. 829–835, 1999.
- [38] D. J. Abrams, M. J. Earley, S. C. Sporton, et al., “Comparison of noncontact and electroanatomic mapping to identify scar and arrhythmia late after the fontan procedure,” *Circulation*, vol. 115, no. 13, pp. 1738–1746, 2007.
- [39] R. J. Schilling, N. S. Peters, and D. W. Davies, “Simultaneous endocardial mapping in the human left ventricle using a noncontact catheter: comparison of contact and reconstructed electrograms during sinus rhythm,” *Circulation*, vol. 98, no. 9, pp. 887–898, 1998.
- [40] D. Bhakta and J. M. Miller, “Principles of electroanatomic mapping,” *Indian Pacing Electrophysiol J*, vol. 8, no. 1, pp. 32–50, 2008.
- [41] N. M. de Groot, M. Bootsma, E. T. van der Velde, et al., “Three-dimensional catheter positioning during radiofrequency ablation in patients: first application of a real-time position management system,” *Journal of Cardiovascular Electrophysiology*, vol. 11, no. 11, pp. 1183–1192, 2000.

- [42] G. N. Kay, D. H. Mulholland, A. E. Epstein, et al., "Effect of pacing rate on the human atrial strength duration curve," *J Am Coll Cardiol*, vol. 15, pp. 1618–23, 1990.
- [43] M. Wilhelms, H. Hettmann, M. M. C. Maleckar, et al., "Benchmarking electrophysiological models of human atrial myocytes," *Frontiers in Physiology*, vol. 3, no. 487, pp. 1–16, 2013.
- [44] A. L. Hodgkin and A. F. Huxley, "A quantitative description of membrane current and its application to conduction and excitation in nerve," *Journal of Physiology*, vol. 117, pp. 500–544, 1952.
- [45] D. Noble, "A modification of the hodgkin-huxley equations applicable to purkinje fibre action and pace-maker potentials," *Journal of Physiology*, vol. 160, pp. 317–352, 1962.
- [46] A. Nygren, C. Fiset, L. Firek, et al., "Mathematical model of a adult human atrial cell. the role of k+ currents in repolarization," *Circulation Research*, vol. 82, pp. 63–81, 1998.
- [47] D. R. V. Wagoner, A. L. Pond, and P. M. McCarthy, "Outward k+ current densities and kv1.5 expression are reduced in chronic human atrial fibrillation," *Circ. Res.*, vol. 80, pp. 772–781, 1997.
- [48] D. Dobrev, E. Graf, E. Wettwer, et al., "Molecular basis of downregulation of g-protein-coupled inward rectifying k+ current (ik, ach) in chronic human atrial fibrillation: Decrease in girk4 mrna correlates with reduced ik, ach and muscarinic receptor-mediated shortening of action potentials," *Circulation*, vol. 104, no. 21, pp. 2551–2557, 2001.
- [49] U. Schotten, S. Verheule, P. Kirchhof, et al., "Pathophysiological mechanisms of atrial fibrillation: a translational appraisal," *Physiological Reviews*, vol. 91, no. 1, pp. 265–325, 2011.
- [50] N. A. Trayanova, "Mathematical approaches to understanding and imaging atrial fibrillation: significance for mechanisms and management," *Circulation Research*, vol. 114, no. 9, pp. 1516–1531, 2014.
- [51] M. Wallman, N. P. Smith, and B. Rodriguez, "A comparative study of graph-based, eikonal, and monodomain simulations for the estimation of cardiac activation times," *IEEE Transactions on Biomedical Engineering*, vol. 59, no. 6, pp. 1739–1748, 2012.
- [52] M. Wallman, N. Smith, and B. Rodriguez, "Estimation of activation times in cardiac tissue using graph based methods," in *Functional Imaging and Modeling of the Heart*. Springer, 2011, p. 71;79.
- [53] E. Pernod, M. Sermesant, E. Konukoglu, et al., "A multi-front eikonal model of cardiac electrophysiology for interactive simulation of radio-frequency ablation," *Computers & Graphics*, vol. 35, no. 2, pp. 431–440, 2011.
- [54] G. Seemann, *Modeling of electrophysiology and tension development in the human heart*. Universitätsverlag Karlsruhe: Institut für Biomedizinische Technik, 2005.
- [55] R. H. Clayton, O. Bernus, E. M. Cherry, et al., "Models of cardiac tissue electrophysiology: progress, challenges and open questions." *Progress in Biophysics and Molecular Biology*, vol. 104, no. 1-3, pp. 22–48, 2011.
- [56] C. D. Werner, F. B. Sachse, and O. Dössel, "Electrical excitation propagation in the human heart," *Int. J. Bioelectromagnetism*, vol. 2, no. 2, 2000.
- [57] A. Loewe, *Modeling human atrial patho-electrophysiology from ion channels to ecg : substrates, pharmacology, vulnerability, and p-waves*. KIT Scientific Publishing, 2016.
- [58] E. Poremba, *Implementation of a fast simulation c++ framework for the computation of vulnerability to atrial arrhythmias using the fast marching algorithm*, no. Bachelor thesis. Institute of Biomedical Engineering, Karlsruhe Institute of Technology (KIT), 2013.

- [59] M. Sermesant, E. Konukoglu, H. Delingette, et al., *Functional imaging and modeling of the heart*. Springer Berlin / Heidelberg, 2007, vol. 4466, ch. An Anisotropic Multi-front Fast Marching Method for Real-Time Simulation of Cardiac Electrophysiology, pp. 160–169.
- [60] W. Martinez, “Exploratory data analysis with matlab,” *Boca Raton: CRC Press*, 2005.
- [61] U. Kiencke, M. Schwarz, and T. Weickert, *Signalverarbeitung: Zeit-frequenz-analyse und schätzverfahren*. München: Oldenbourg, 2008.
- [62] J. F. Kaiser, “On a simple algorithm to calculate the ‘energy’ of a signal,” *Acoustics, Speech, and Signal Processing, 1990. ICASSP-90., 1990 International Conference on*, pp. 381–384, 1990.
- [63] R. Agarwal and J. Gotman, “Adaptive segmentation of electroencephalographic data using a nonlinear energy operator,” *Circuits and Systems, 1999. ISCAS*, vol. 4, pp. 199–202, 1999.
- [64] C. Schilling, M. P. Nguyen, A. Luik, et al., “Non-linear energy operator for the analysis of intracardial electrograms,” in *IFMBE Proceedings World Congress on Medical Physics and Biomedical Engineering*, vol. 25/4, 2009, pp. 872–875.
- [65] T. Lewalter, C. Weiss, S. Spencker, et al., “Gold vs. platinum-iridium tip catheter for cavotricuspid isthmus ablation: the aurum 8 study,” *Europace : European Pacing, Arrhythmias, and Cardiac Electrophysiology : Journal of the Working Groups on Cardiac Pacing, Arrhythmias, and Cardiac Cellular Electrophysiology of the European Society of Cardiology*, vol. 13, no. 1, pp. 102–108, 2011.
- [66] J. R. Silvaa, H. Pana, D. Wua, et al., “A multiscale model linking ion-channel molecular dynamics and electrostatics to the cardiac action potential,” *PNAS*, p. 11102;11106, 2008.
- [67] M. W. Krueger, *Personalized multi-scale modeling of the atria: Heterogeneities, fiber architecture, hemodialysis and ablation therapy*, Karlsruhe Transactions on Biomedical Engineering, vol. 19. Karlsruhe: KIT Scientific Publishing, 2012.
- [68] S. N. Singh, “Costs and clinical consequences of suboptimal atrial fibrillation management,” *ClinicoEconomics and Outcomes Research : CEOR*, vol. 4, pp. 79–90, 2012.
- [69] M. Zoni-Berisso, F. Lercari, T. Carazza, et al., “Epidemiology of atrial fibrillation: European perspective,” *Clinical Epidemiology*, vol. 6, pp. 213–220, 2014.
- [70] L. Bacharova, R. H. Selvester, H. Engblom, et al., “Where is the central terminal located; in search of understanding the use of the wilson central terminal for production of 9 of the standard 12 electrocardiogram leads,” *Journal Electrocardiology*, vol. 38, no. 2, pp. 119–127, 2005.
- [71] Y. Kumar and G. K. Malik, “Performance analysis of different filters for power line interface reduction in ecg signal,” *International Journal of Computer Applications*, vol. 3, no. 7, pp. 1–6, 2010.
- [72] S. Narayanaswamy, “High resolution electrocardiography,” *Indian Pacing and Electrophysiology Journal*, vol. 2, no. 2, pp. 50–56, 2002.
- [73] G. Lenis, T. Baas, and O. Dössel, “Ectopic beats and their influence on the morphology of subsequent waves in the electrocardiogram,” *Biomedical Engineering / Biomedizinische Technik*, vol. 58, no. 2, pp. 109–119, 2013.
- [74] M. Allessie, J. Ausma, and U. Schotten, “Electrical, contractile and structural remodeling during atrial fibrillation,” *Cardiovascular Research*, vol. 54, no. 2, pp. 230–246, 2002.
- [75] T. G. Oesterlein, J. Schmid, S. Bauer, et al., “Analysis and visualization of intracardiac electrograms in diagnosis and research: Concept and application of kapavie,” *Computer Methods and Programs in Biomedicine*, vol. 127, pp. 165–173, 2016.

- [76] T. Feldman, R. W. Childers, K. M. Borow, et al., "Change in ventricular cavity size: differential effects on qrs and t wave amplitude," *Circulation*, vol. 72, no. 3, pp. 495–501, 1985.
- [77] R. Alcaraz, F. Sandberg, L. Sornmo, et al., "Classification of paroxysmal and persistent atrial fibrillation in ambulatory ecg recordings," *IEEE Transactions on Biomedical Engineering*, vol. 58, no. 5, pp. 1441–1449, 2011.
- [78] M. Benmalek and A. Charef, "Digital fractional order operators for r-wave detection in electrocardiogram signal," *IET Signal Process*, vol. 3, no. 5, p. 381;391, 2009.
- [79] A. M. L. and T. W. J., "Automated high-speed analysis of holter tapes with microcomputers," *IEEE Transactions on Biomedical Engineering*, pp. 651–657, 2007.
- [80] N. M. Arzeno, Z. Deng, and P. C., "Analysis of first-derivative based qrs detection algorithms," *IEEE Trans Biomed Eng.*, vol. 55, no. 2 Pt 1, pp. 478–484, 2008.
- [81] J. Rieta, V. Zarzoso, J. Millet-Roig, et al., "Atrial activity extraction based on blind source separation as an alternative to qrst cancellation for atrial fibrillation analysis," *Computers in Cardiology 2000*, pp. 69–72, 2000.
- [82] G. Lenis, "Automatic detection and classification of ectopic beats in the ecg using a support-vector-machine," PhD thesis, Karlsruhe, 2010.
- [83] M. E. Nygard and L. Sornmo, "Delineation of the qrs complex using the envelope of the e.c.g.," *Medical & Biological Engineering & Computing*, vol. 21, no. 5, pp. 538–547, 1983.
- [84] A. Ligtenberg and M. Kunt, "A robust-digital qrs-detection algorithm for arrhythmia monitoring," *Comput. Biomed.*, vol. 16, pp. 273–286, 1983.
- [85] J. Pan and W. J. Tompkins, "A real-time qrs detection algorithm," *IEEE Transactions on Biomedical Engineering*, vol. 32, no. 3, pp. 230–236, 1985.
- [86] T. Oesterlein, G. Lenis, A. Luik, et al., "Periodic component analysis to eliminate ventricular far field artifacts in unipolar atrial electrograms of patients suffering from atrial flutter," in *Biomedizinische Technik / Biomedical Engineering*, vol. 59, no. s1. Berlin, Boston: Walter de Gruyter, 2014, p. 14.
- [87] J. J. Rieta and F. Hornero, "Comparative study of methods for ventricular activity cancellation in atrial electrograms of atrial fibrillation," *Physiological Measurement*, vol. 28, no. 8, pp. 925–936, 2007.
- [88] G. Lenis, T. Oesterlein, and O. Dössel, "Orthogonal component analysis to remove ventricular far field in non periodic sustained atrial flutter," in *Computing in Cardiology*, vol. 42, 2015, pp. 669–672.
- [89] T. G. Oesterlein, G. Lenis, D.-T. Rudolph, et al., "Removing ventricular far-field signals in intracardiac electrograms during stable atrial tachycardia using the periodic component analysis," *Journal of Electrocardiology*, vol. 48, no. 2, pp. 171–180, 2015.
- [90] F. Castells, P. Laguna, L. Sörnmo, et al., "Principal component analysis in ecg signal processing," *EURASIP J. Appl. Signal Process.*, vol. 2007, no. 1, p. 98, 2007.
- [91] C. Schilling, M. Aubreville, A. Luik, et al., "Pca-based ventricular far field cancellation in intraatrial electrograms," in *Biomedizinische Technik / Biomedical Engineering*, vol. 55, no. s1. Walter de Gruyter, 2010, pp. 49–52.
- [92] R. Sameni, C. Jutten, and M. B. Shamsollahi, "Multichannel electrocardiogram decomposition using periodic component analysis," *IEEE Transactions on Biomedical Engineering*, vol. 55, no. 8, pp. 1935–1940, 2008.
- [93] M. Garibaldi and V. Zarzoso, "Exploiting intracardiac and surface recording modalities for atrial signal extraction in atrial fibrillation," *Conference Proceedings : ... Annual International*

- Conference of the IEEE Engineering in Medicine and Biology Society. IEEE Engineering in Medicine and Biology Society. Conference*, vol. 2013, pp. 6015–6018, 2013.
- [94] R. Llinares, J. Igual, J. Miro-Borras, et al., “Atrial activity estimation using periodic component analysis,” in *International Joint Conference on Neural Networks*. IEEE, 2010, pp. 1–7.
- [95] L. K. Saul and J. B. Allen, “Periodic component analysis: an eigenvalue method for representing periodic structure in speech,” in *Nips*, 2000, pp. 807–813.
- [96] M. P. Nguyen, C. Schilling, and O. Dössel, “A new approach for frequency analysis of complex fractionated atrial electrograms,” in *Conf Proc IEEE Eng Med Biol Soc*, 2009, pp. 368–371.
- [97] N. W. F. Linton, M. Koa-Wing, D. P. Francis, et al., “Cardiac ripple mapping: a novel three-dimensional visualization method for use with electroanatomic mapping of cardiac arrhythmias,” *Heart Rhythm : the Official Journal of the Heart Rhythm Society*, vol. 6, no. 12, pp. 1754–1762, 2009.
- [98] C. F. Pieper, R. Blue, and A. Pacifico, “Simultaneously collected monopolar and discrete bipolar electrograms: comparison of activation time detection algorithms,” *Pacing and Clinical Electrophysiology : PACE*, vol. 16, no. 3 Pt 1, pp. 426–433, 1993.
- [99] M. S. Spach, R. C. Barr, G. A. Serwer, et al., “Extracellular potentials related to intracellular action potentials in the dog purkinje system,” *Circulation Research*, vol. 30, no. 5, pp. 505–519, 1972.
- [100] M. S. Spach and J. M. Kootsey, “Relating the sodium current and conductance to the shape of transmembrane and extracellular potentials by simulation: effects of propagation boundaries,” *IEEE Transactions on Biomedical Engineering*, vol. 32, no. 10, pp. 743–755, 1985.
- [101] B. M. Steinhaus, “Estimating cardiac transmembrane activation and recovery times from unipolar and bipolar extracellular electrograms: A simulation study,” *Circ. Res.*, vol. 64, pp. 449–462, 1989.
- [102] B. Dube, A. Vinet, F. Xiong, et al., “Automatic detection and classification of human epicardial atrial unipolar electrograms,” *Physiological Measurement*, vol. 30, no. 12, pp. 1303–1325, 2009.
- [103] S. Huck, T. Oesterlein, A. Luik, et al., “Preprocessing of unipolar signals acquired by a novel intracardiac mapping system,” in *Current Directions in Biomedical Engineering*, vol. 2, no. 1. De Gruyter, 2016, p. 259;262.
- [104] K. T. Konings, J. L. Smeets, O. C. Penn, et al., “Configuration of unipolar atrial electrograms during electrically induced atrial fibrillation in humans,” *Circulation*, vol. 95, no. 5, pp. 1231–1241, 1997.
- [105] K. Otomo, K. Uno, H. Fujiwara, et al., “Local unipolar and bipolar electrogram criteria for evaluating the transmural depth of atrial ablation lesions at different catheter orientations relative to the endocardial surface,” *Heart Rhythm : the Official Journal of the Heart Rhythm Society*, vol. 7, no. 9, pp. 1291–1300, 2010.
- [106] G. Ndrepepa, E. B. Caref, H. Yin, et al., “Activation time determination by high-resolution unipolar and bipolar extracellular electrograms in the canine heart,” *Journal of Cardiovascular Electrophysiology*, vol. 6, no. 3, pp. 174–188, 1995.
- [107] R. H. Milad El Haddad, “Algorithmic detection of the beginning and end of bipolar electrograms: Implications for novel methods to assess local activation time during atrial tachycardia,” *Biomedical Signal Processing and Control*, vol. 8, no. 6, pp. 981–991, 2012.

- [108] B. Verma, T. Oesterlein, A. Luik, et al., *Current directions in biomedical engineering*. Basel: De Gruyter, 2016, vol. 2, ch. Combined analysis of unipolar and bipolar electrograms for local activation time annotation near the stimulus site of paced rhythms.
- [109] B. Verma, T. G. Oesterlein, A. Luik, et al., “Analyzing the atrial depolarization wavefront triggered from sinus node and coronary sinus for identification of the arrhythmogenic substrate,” in *Computing in Cardiology*, vol. 42, 2015, pp. 897–900.
- [110] B. Verma, T. G. Oesterlein, A. Luik, et al., “Locating regions of arrhythmogenic substrate by analyzing the duration of triggered atrial activities,” in *Current Directions in Biomedical Engineering*, vol. 1, no. 1, 2015, pp. 50–53.
- [111] C. Cabo, A. M. Pertsov, W. T. Baxter, et al., “Wave-front curvature as a cause of slow conduction and block in isolated cardiac muscle,” *Circulation Research*, vol. 75, no. 6, pp. 1014–1028, 1994.
- [112] A. W. C. Chow, R. J. Schilling, D. W. Davies, et al., “Characteristics of wavefront propagation in reentrant circuits causing human ventricular tachycardia,” *CIRCULATION*, vol. 105, pp. 2172–2178, 2002.
- [113] V. G. Fast and A. G. Kleber, “Role of wavefront curvature in propagation of cardiac impulse,” *Cardiovascular Research*, vol. 33, no. 2, pp. 258–271, 1997.
- [114] S. B. Knisley and B. C. Hill, “Effects of bipolar point and line stimulation in anisotropic rabbit epicardium: Assessment of the critical radius of curvature for longitudinal block,” *Ieee Transactions On Biomedical Engineering.*, vol. 42, pp. 957–966, 1995.
- [115] T. Kawara, R. Derksen, J. R. de Groot, et al., “Activation delay after premature stimulation in chronically diseased human myocardium relates to the architecture of interstitial fibrosis,” *Circulation*, vol. 104, no. 25, pp. 3069–3075, 2001.
- [116] O. Dössel, M. W. Krueger, F. M. Weber, et al., “Computational modeling of the human atrial anatomy and electrophysiology,” *Medical & Biological Engineering & Computing*, vol. 50, no. 8, pp. 773–799, 2012.
- [117] D. G. Latcu, S.-S. Bun, F. Viera, et al., “Selection of critical isthmus in scar-related atrial tachycardia using a new automated ultrahigh resolution mapping system,” *Circulation. Arrhythmia and Electrophysiology*, vol. 10, no. 1, 2017.
- [118] T. Itoh, M. Kimura, S. Sasaki, et al., “High correlation of estimated local conduction velocity with natural logarithm of bipolar electrogram amplitude in the reentry circuit of atrial flutter,” *Journal of Cardiovascular Electrophysiology*, vol. 25, no. 4, pp. 387–394, 2014.
- [119] Y. Zheng, Y. Xia, J. Carlson, et al., “Atrial average conduction velocity in patients with and without paroxysmal atrial fibrillation,” *Clinical Physiology and Functional Imaging*, 2016.
- [120] M. Haissaguerre, F. Gaita, B. Fischer, et al., “Elimination of atrioventricular nodal reentrant tachycardia using discrete slow potentials to guide application of radiofrequency energy,” *Circulation*, vol. 85, pp. 2162–2175, 1992.
- [121] F. G. Akar, R. D. Nass, S. Hahn, et al., “Dynamic changes in conduction velocity and gap junction properties during development of pacing-induced heart failure,” *American Journal of Physiology. Heart and Circulatory Physiology*, vol. 293, no. 2, pp. H1223–30, 2007.
- [122] F. M. Weber, C. Schilling, G. Seemann, et al., “Wave-direction and conduction-velocity analysis from intracardiac electrograms—a single-shot technique,” *IEEE Transactions on Biomedical Engineering*, vol. 57, no. 10, pp. 2394–2401, 2010.

- [123] F. M. Weber, A. Luik, C. Schilling, et al., "Conduction velocity restitution of the human atrium—an efficient measurement protocol for clinical electrophysiological studies," *IEEE Transactions on Biomedical Engineering*, vol. 58, no. 9, pp. 2648–2655, 2011.
- [124] P. Kojodjojo, P. Kanagaratnam, V. Markides, et al., "Age-related changes in human left and right atrial conduction," *Journal of Cardiovascular Electrophysiology*, vol. 17, no. 2, pp. 120–127, 2006.
- [125] M. Mase and F. Ravelli, "Automatic reconstruction of activation and velocity maps from electro-anatomic data by radial basis functions," *Conf Proc IEEE Eng Med Biol Soc*, vol. 2010, pp. 2608–2611, 2010.
- [126] M. Mase, M. Del Greco, M. Marini, et al., "Velocity field analysis of activation maps in atrial fibrillation - a simulation study," in *IFMBE Proceedings World Congress on Medical Physics and Biomedical Engineering*, vol. 25/4, 2009, pp. 1014–1017.
- [127] A. R. Barnette, P. V. Bayly, S. Zhang, et al., "Estimation of 3-d conduction velocity vector fields from cardiac mapping data," *IEEE Transactions on Biomedical Engineering*, vol. 47, no. 8, pp. 1027–1035, 2000.
- [128] C. H. Roney, C. D. Cantwell, N. A. Qureshi, et al., "An automated algorithm for determining conduction velocity, wavefront direction and origin of focal cardiac arrhythmias using a multipolar catheter," in *Engineering in Medicine and Biology Society (EMBC), 2014 36th Annual International Conference of the IEEE*, 2014, pp. 1583–1586.
- [129] C. D. Cantwell, C. H. Roney, F. S. Ng, et al., "Techniques for automated local activation time annotation and conduction velocity estimation in cardiac mapping," *Computers in Biology and Medicine*, vol. 65, pp. 229–42, 2015.
- [130] P. V. Bayly, B. H. KenKnight, J. M. Rogers, et al., "Estimation of conduction velocity vector fields from epicardial mapping data," *Biomedical Engineering, IEEE Transactions on*, vol. 45, no. 5, pp. 563–571, 1998.
- [131] G. Salama, A. Kanai, and I. R. Efimov, "Subthreshold stimulation of purkinje fibers interrupts ventricular tachycardia in intact hearts. experimental study with voltage-sensitive dyes and imaging techniques," *Circulation Research*, vol. 74, no. 4, pp. 604–619, 1994.
- [132] J. I. Laughner, F. S. Ng, M. S. Sulkin, et al., "Processing and analysis of cardiac optical mapping data obtained with potentiometric dyes," *American Journal of Physiology. Heart and Circulatory Physiology*, vol. 303, no. 7, pp. H753–765, 2012.
- [133] D. G. Latcu, S.-S. Bun, M. Arnoult, et al., "New insights into typical atrial flutter ablation: extra-isthmus activation time on the flutter wave is predictive of extra-isthmus conduction time after isthmus block," *Journal of Interventional Cardiac Electrophysiology : an International Journal of Arrhythmias and Pacing*, vol. 36, no. 1, pp. 19–25; discussion 25, 2013.
- [134] A. T. Schoenwald, A. V. Sahakian, and S. Swiryn, "A method for determining local activation direction in the atrium," *Proceedings of 16th Annual International Conference of the IEEE Engineering in Medicine and Biology Society*, vol. 1, pp. 1–2, 1994.
- [135] W. E. Cascio, T. A. Johnson, and L. S. Gettes, "Electrophysiologic changes in ischemic ventricular myocardium: I. influence of ionic, metabolic, and energetic changes," *Journal of Cardiovascular Electrophysiology*, vol. 6, no. 11, pp. 1039–1062, 1995.
- [136] Y. Watanabe, "Effects of calcium and sodium concentrations on atrioventricular conduction: experimental study in rabbit hearts with clinical implications on heart block and slow calcium channel blocking agent usage," *American Heart Journal*, vol. 102, no. 5, pp. 883–891, 1981.

- [137] V. Jacquemet, "An eikonal approach for the initiation of reentrant cardiac propagation in reaction-diffusion models," *IEEE Transactions on Biomedical Engineering*, vol. 57, no. 9, pp. 2090–2098, 2010.
- [138] F. Badilini, M. Vaglio, R. Dubois, et al., "Automatic analysis of cardiac repolarization morphology using gaussian mesa function modeling," *Journal of Electrocardiology*, vol. 41, no. 6, pp. 588–594, 2008.
- [139] E. J. Ciaccio, A. B. Biviano, and H. Garan, "The dominant morphology of fractionated atrial electrograms has greater temporal stability in persistent as compared with paroxysmal atrial fibrillation," *Computers in Biology and Medicine*, vol. 43, no. 12, pp. 2127–2135, 2013.
- [140] M. Aubreville, C. Schilling, A. Luik, et al., "Detection of periodicity in complex fractionated atrial electrograms (cfaes)," in *IFMBE Proceedings World Congress on Medical Physics and Biomedical Engineering*, vol. 25/4, Munich, Germany, 2009.
- [141] F. G. Akar and G. F. Tomaselli, "Conduction abnormalities in nonischemic dilated cardiomyopathy: basic mechanisms and arrhythmic consequences," *Trends in Cardiovascular Medicine*, vol. 15, no. 7, pp. 259–264, 2005.
- [142] O. V. Aslanidi, M. R. Boyett, H. Dobrzynski, et al., "Mechanisms of transition from normal to reentrant electrical activity in a model of rabbit atrial tissue: interaction of tissue heterogeneity and anisotropy," *Biophysical Journal*, vol. 96, no. 3, pp. 798–817, 2009.
- [143] O. Anosov, S. Berdyshev, I. Khassanov, et al., "Wave propagation in the atrial myocardium: dispersion properties in the normal state and before fibrillation," *IEEE Trans Biomed Eng*, vol. 49, no. 12 Pt 2, pp. 1642–1645, 2002.

List of Publications and Supervised Theses

Journal Articles

- T. G. Oesterlein, G. Lenis, D.-T. Rudolph, A. Luik, **B. Verma**, C. Schmitt, O. Dössel, *Removing ventricular far-field signals in intracardiac electrograms during stable atrial tachycardia using the periodic component analysis*, Journal of Electrocardiology, 2015, 48 (2): 171-180
- **B. Verma**, T. G. Oesterlein, A. Loewe, A. Luik, C. Schmitt, O. Dössel, *Regional conduction velocity calculation from clinical multichannel electrograms in human atria*, in revision.
- **B. Verma**, T. G. Oesterlein, A. Loewe, A. Luik, C. Schmitt, O. Dössel, *Comparison of conduction velocity from stimulus protocol for dynamic catheter movement inside the atrium*, in preparation.

Refereed Conference Articles

- T. G. Oesterlein, G. Lenis, A. Luik, **B. Verma**, C. Schmitt, O. Dössel, *Removing ventricular far-field artifacts in intracardiac electrograms during stable atrial flutter using the periodic component analysis - proof of concept study*, International Congress on Electrocardiology, 2014, Proceedings: 49-52
- **B. Verma**, T. G. Oesterlein, A. Luik, C. Schmitt, O. Dössel, *Analysing the Atrial Depolarization Wavefront Triggered from Sinus Node and Coronary Sinus for Identification of the Arrhythmogenic Substrate*, Computing in Cardiology, 2015, 42: 897-900
- **B. Verma**, T. G. Oesterlein, A. Luik, C. Schmitt, O. Dössel, *Locating regions of arrhythmogenic substrate by analyzing the duration of triggered atrial activities*, Current directions in Biomedical Engineering, 2015,1: 50-53
- O. Dössel, G. Lenis, A. Loewe, S. Pollnow, M. Rottmann, **B. Verma**, C. Schmitt, A. Luik, and T. Oesterlein, *Atrial Signals & Modeling Meets Biosignal Analysis*, IFMBE Proceedings, 2017, accepted

Refereed Conference Abstracts

- **B. Verma**, T. G. Oesterlein, A. Luik, C. Schmitt, O. Dössel, *Analysis of local activation times and complexity in the intracardiac electrograms*, Biomedical Engineering/Biomedizinische Technik, 2014; 59: s14
- **B. Verma**, T. G. Oesterlein, A. Luik, C. Schmitt, O. Dössel, *Locating regions of arrhythmogenic substrate by analyzing the duration of triggered atrial activities*, Current directions in Biomedical Engineering, 2015,1: 50-53
- O. Dössel, A. Luik, T. Oesterlein, M. Rottmann, **B. Verma**, C. Schmitt, *Computer modeling of the atria and clinical electrograms*, 37th Annual International Conference of the IEEE Engineering in Medicine and Biology Society, 2015, Poster Session
- **B. Verma**, T. G. Oesterlein, A. Luik, C. Schmitt, O. Dössel, *Determination of region with arrhythmogenic substrate based on local activation time and activity duration*, Gordon research conference, 2015.
- **B. Verma**, T. G. Oesterlein, A. Luik, C. Schmitt, O. Dössel, *Combined analysis of unipolar and bipolar electrograms for local activation time annotation near the stimulus site of paced rhythms*, Current directions in Biomedical Engineering, 2016,1: 50-53
- **B. Verma**, T. G. Oesterlein, A. Luik, C. Schmitt, O. Dössel, *Regional Conduction Velocity Calculation based on Local Activation Times: A Simulation Study on Clinical Geometries*, Computing in Cardiology, 2016, 43: 985-988
- **B. Verma**, A. Loewe, A. Luik, C. Schmitt, O. Dössel, *Regional Conduction Velocity Calculation based on Local Activation Times: A Simulation Study on Clinical Geometries*, Current directions in Biomedical Engineering, 2017

Conference Presentations

- **B. Verma**, T. G. Oesterlein, A. Luik, C. Schmitt, O. Dössel, *Analysing the Atrial Depolarization Wavefront Triggered from Sinus Node and Coronary Sinus for Identification of the Arrhythmogenic Substrate*, Computing in Cardiology, 2015, 42: 897-900
- **B. Verma**, T. G. Oesterlein, A. Luik, C. Schmitt, O. Dössel, *Locating regions of arrhythmogenic substrate by analyzing the duration of triggered atrial activities*, Current directions in Biomedical Engineering, 2015,1: 50-53

Awards & Grants

- Bill and Gary Sanders Poster Award: **B. Verma**, T. G. Oesterlein, A. Luik, C. Schmitt, O. Dössel, *Regional Conduction Velocity Calculation based on Local Activation Times: A Simulation Study on Clinical Geometries*, Computing in Cardiology, 2016
- First price for the best poster presentation, PhD Symposium, Karlsruhe Institute of Technology: **B. Verma**, T. G. Oesterlein, O. Dössel, *Analysis of local activation times and complexity in the intracardiac electrograms*, 2014
- Prestigious DAAD Scholarship for doctoral studies, by German Academic Exchange Service
- DAAD scholarship by German Academic Exchange Service, for Master thesis Internship, at Germany
- KHYS Networking Grant, by Karlsruhe House of Young Scientist, (KHYS), 2015
- First price Young Investigator's Award, 41. International Congress of Electrophysiology, 2014: T. G. Oesterlein, G. Lenis, A. Luik, **B. Verma**, C. Schmitt, O. Dössel, *Removing ventricular far-field artifacts in intracardiac electrograms during stable atrial flutter using the periodic component analysis - proof of concept study*

Supervised Student Thesis

- Benedikt Ebener, *Estimation of the Conduction Velocity from Clinical Local Activation Time Maps*, Bachelor Thesis, Institute of Biomedical Engineering, Karlsruhe Institute of Technology (KIT), 2017

